

AD-A269 452 NTATION PAGE

Form Approved
OMB No. 0704-0188

ated to average 1 hour per response, including the time for reviewing instructions, searching existing data sources, reviewing the collection of information. Send comments regarding this burden estimate or any other aspect of this burden to Washington Headquarters Services, Directorate for Information Operations and Reports, 1215 Jefferson Office of Management and Budget, Paperwork Reduction Project (0704-0188), Washington, DC 20503

ORT DATE

3. REPORT TYPE AND DATES COVERED

Final Report 15 Feb 93 - 14 Jan 94

4. TITLE AND SUBTITLE

Spatial light modulators & applications

Organization of the 1993 Photonics Science topical Meetings

6. AUTHOR(S)

Dr Jarus W Quinn

5. FUNDING NUMBERS

F49620-93-1-0181

7. PERFORMING ORGANIZATION NAME(S) AND ADDRESS(ES)

Optical Society of America
2010 Massachusetts Avenue NW
Washington DC 200368. PERFORMING ORGANIZATION
REPORT NUMBER

9. SPONSORING/MONITORING AGENCY NAME(S) AND ADDRESS(ES)

AFOSR/NE
110 Duncan Avenue Suite B115
Bolling AFB DC 20332-000110. SPONSORING/MONITORING
AGENCY REPORT NUMBER

2301/DS

11. SUPPLEMENTARY NOTES

**DTIC
ELECTE
AUG 31 1993
S E D**

12a. DISTRIBUTION/AVAILABILITY STATEMENT

UNLIMITED

12b. DISTRIBUTION CODE

13. ABSTRACT (Maximum 200 words)

The following symposium was held

- Advanced Solid State Lasers
- Compact Blue-Green Lasers
- Integrated Photonics Research
- Nonlinear Guide-Wave Optics
- Optical Amplifiers & Their Applications
- Optical Design for Photonics
- Photonics in Switching
- Quantum Optoelectronics
- Shortwavelength: Physics With Intense Laser Pulses
- Soft X-Ray Protection Lithography
- Ultrafast Electronics & Optoelectronics
- Optical Computing
- Spatial Light Modulators

93-20267



14. SUBJECT TERMS

ES

16. PRICE CODE

17. SECURITY CLASSIFICATION
OF REPORT

UNCLASS

18. SECURITY CLASSIFICATION
OF THIS PAGE

UNCLASS

19. SECURITY CLASSIFICATION
OF ABSTRACT

UNCLASS

20. LIMITATION OF ABSTRACT

UL

SPATIAL LIGHT MODULATORS AND APPLICATIONS

Accession For	
NTIS - CRA&I	<input checked="" type="checkbox"/>
DTIC - TAB	<input type="checkbox"/>
Unannounced	<input type="checkbox"/>
Justification	
By	
Distribution /	
Availability Codes	
Dist	Avail and/or Special
A-1	



Sponsored by
Optical Society of America

Technical Cosponsor
IEEE/Lasers and Electro-Optics Society

POSTDEADLINE PAPERS

MARCH 15-17, 1993
PALM SPRINGS,
CALIFORNIA

SPATIAL LIGHT MODULATORS POSTDEADLINE PAPERS

Wednesday, March 17, 1993

5:15pm-6:15pm

Grand Ballroom Center

5:15pm-5:35pm

PD1 Longitudinal effect PLZT spatial light modulators,
John W. Tully, Vahram W. Biricik, Northrop Corp.

5:35pm-5:55pm

PD2 Depolarization in liquid crystal TV's, J. Larry
Pezzaniti, Stephen C. McClain, Russell A. Chipman,
Shih Yau-Lu, Univ. of Alabama Huntsville.

5:55pm-6:15pm

PD3 Lowered temperature MBE regrowth of LED structures
on high density GaAs circuits fabricated through
MOSIS, Annette C. Grot, Demetri Psaltis, Krishna V.
Shenoy, Clifton G. Fonstad, California Inst. of
Technology.

SUN 3:10

Longitudinal Effect PLZT Spatial Light Modulators

John W. Tully and V. Warren Biricik

Northrop Corporation

Surface and Thin Film Laboratory

One Research Park

Palos Verdes Peninsula, California 90274

Ph. (310) 544-5306

Design and fabrication aspects of a longitudinal effect PLZT spatial light modulator is described.

Experimental data covering the performance in the visible wavelength region is presented.

Longitudinal Effect PLZT Spatial Light Modulators

John W. Tully and V. Warren Biricik
 Northrop Corporation
 Surface and Thin Film Laboratory
 One Research Park
 Palos Verdes Peninsula, California 90274
 (310) 544-5306

This paper presents the design and fabrication aspects of a longitudinal effect PLZT spatial light modulator designed for operation in the visible and near infrared. Included are experimental data showing the electric field induced phase shift characteristics of a 16 x 16 square array spatial light modulator. Nd:YAG laser damage threshold of bare PLZT is also presented. It is concluded that longitudinal effect PLZT spatial light modulators are rugged devices that can be used in adaptive optics, laser beam quality enhancement and beam steering applications.

The following operational parameters were selected as design objectives for the demonstration of the first spatial light modulator:

Number of Elements	16 x 16
Pixel Size	1 mm x 1 mm
Area Fill Factor	> 90%
Reflectance	> 90%
Phase Shift	90°
Frame Rate	> 1 kHz
Operational Spectral Range	500-1000 nm
Laser Damage Threshold	> 0.2 J/cm ²

Design Aspects--A nonferroelectric PLZT material having a quadratic electro-optic and electrostrictive effects was selected to be the modulator material^{1,2}. The spatial light modulator configuration is schematically shown in Figure 1. In this configuration, a PLZT wafer is coated with two conductive electrodes; one electrode is optically transparent and the other is highly reflective. The application of a voltage in between electrodes results in an index and thickness change in the PLZT wafer. The differential phase shift (i.e., the phase shift of light upon reflection from the back phase of PLZT when the applied voltage is zero or V) is given by a simple quadratic expression:

$$\Delta\phi \sim n(n^2R+2M)V^2/\lambda t$$

where n is the index of refraction of PLZT, λ refers to the wavelength of light, and R and M refer to quadratic electrostriction and electro-optic constants. By using reflected light from the second interface a factor of two increase in phase shift is obtained for an applied voltage vs a purely transmissive device. The index of refraction of PLZT (~ 2.5) enters as a multiplier in the phase shift equation. This formula also predicts that the PLZT wafer thickness needs

to be minimized, consistent with voltage breakdown, saturation, and optical-fabrication concerns, in order to provide high phase shifts with the minimum amount of drive voltage, i.e. the device is electric field driven.

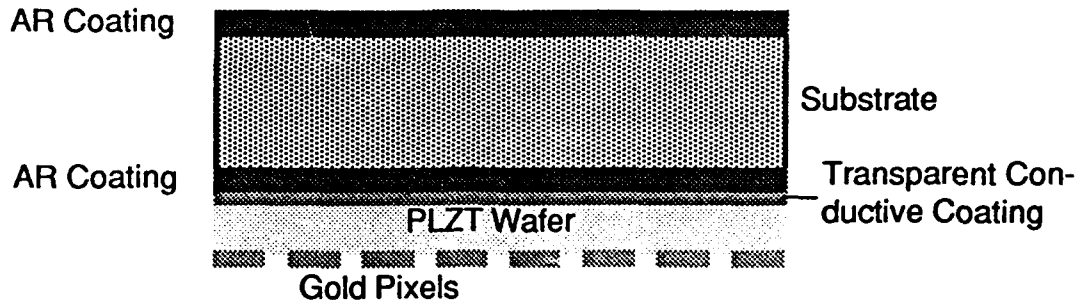


Figure 1. Schematic of a longitudinal effect PLZT phase modulator.

The spatial light modulator, being a pixel addressable phase shift device, requires application and removal of voltages from individual pixels which can be modeled as an array of capacitors. To bring the dynamic voltage levels into an acceptable value, supported by state of the art commercial drivers, and to linearize the response, the spatial light modulator is operated with a biasing electric field. The phase shift between different pixels is then achieved by the application (removal) of differential voltages from the common bias voltage applied to all pixels.

The predicted phase shift as a function of applied voltage for a PLZT wafer having a composition of 9/65/35 and a thickness of 300 microns for visible blue wavelengths indicates a bias voltage of 475 volts and a dynamic voltage of 35 volts for a 90° phase shift. PLZT being transparent in the visible to mid infrared spectral region can be a broadband modulator; its performance being determined by the applied voltage and the optical performance of coatings used in the fabrication of the SLM. Of course, the thickness of the PLZT wafer needs to be so selected as to permit reasonable dynamic voltage levels throughout the spectral region of operation. Longer wavelengths in general require thinner PLZT wafers.

One of the objectives of the SLM design was to maximize pixel area fill factor and thereby the efficiency of the system. Two effects may limit the area fill factor: 1) surface arcing between the adjacent pixels, and 2) pixel to pixel (electrical/mechanical) coupling termed as crosstalk. The first limit was experimentally determined to be not of consequence for fill factors in the neighbourhood of 90%. The latter concern was analyzed through finite element techniques and subsequently validated by experimental measurements. Figure 2, shows the results of a two dimensional finite element electric field distribution analysis conducted for a pixel geometry having an alternating voltages of 400 and 450 volts applied to adjacent pixels. Owing to high dielectric constant (5700) of PLZT, the electric field distribution is nearly constant within each pixel. The high electric field gradients are located near the surface, where voltages are applied. Therefore, very little crosstalk exists between adjacent pixels charged with voltage levels corresponding to a 90° phase shift between them.

This however, pointed out to another potential issue; that of the fatigue crack initiation near the highly stressed areas of PLZT. This issue was experimentally addressed and has shown not to be a problem for the SLM configuration fabricated and tested.

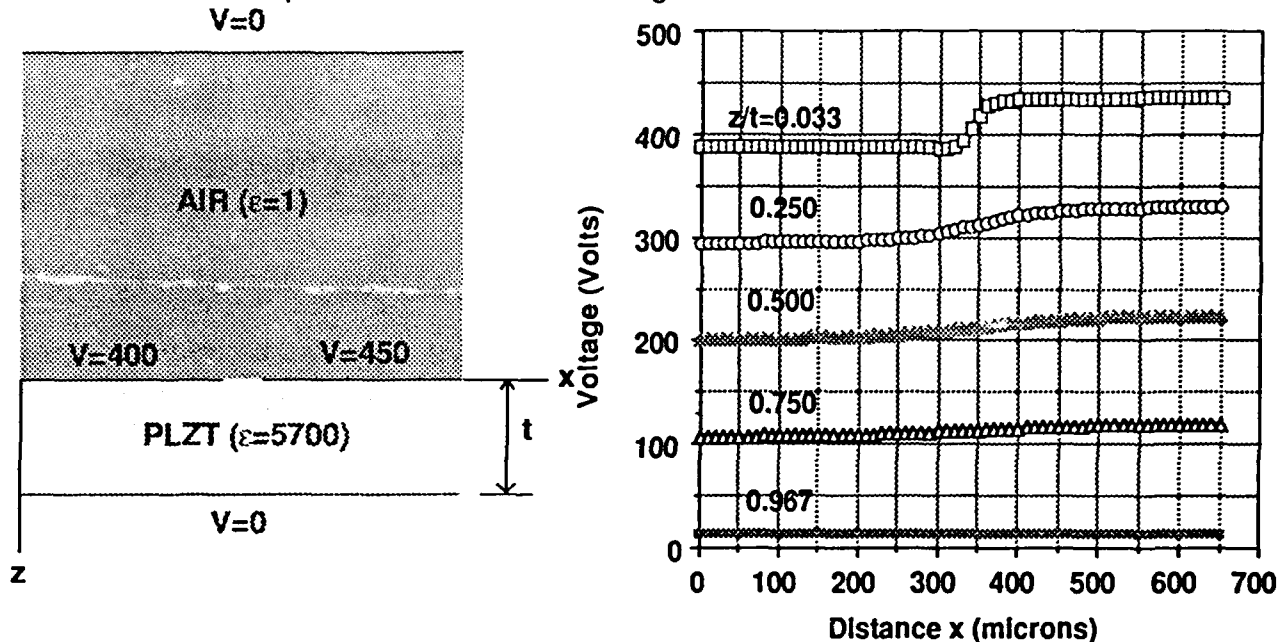


Figure 2. Finite element model configuration and calculated electric field distribution in the PLZT wafer for the case where two adjacent pixels have a 50 volt differential voltage (thickness = 625 microns, pixel spacing = 50 microns).

SLM Fabrication--Fabrication of a longitudinal effect PLZT spatial light modulator uses standard optical polishing, optical thin film coating, and photolithographic techniques. The SLM fabrication used a 2.0 inch diameter PLZT wafer having a thickness of 625 microns which was polished on both sides. The transparent conductive electrode was indium thin oxide (ITO) while the reflecting electrode was gold. ITO was used as the ground plane. The gold coating was patterned using photolithography and chemical etching. Off the shelf electronic drivers and standard attachment techniques were used to make pixel electrical connections. Figure 3 is a photo of the SLM showing a 32 x 32 pixel array. Due to electronics availability, only the central 16 x 16 pixels were activated and used in interferometric tests.

SLM Testing--The spatial light modulator was tested in a commercial HeNe laser interferometer setup. Fringe shifts were measured as a function of applied voltage. For the 9/65/35 PLZT material and at the 633 nm HeNe wavelength, the fringe shift is dominated by electrostriction. Electro-optic effects become important only at high levels of applied electrical field. This is illustrated in Figure 4 which shows the measured fringe shifts as a function of applied voltage. Laser damage threshold of the PLZT was measured under short pulse Nd:YAG illumination. The damage threshold was determined to approximately be 0.4 J/cm².

Concluding Remarks--The longitudinal effect PLZT spatial light modulator has shown to be a rugged device. Its fabrication employs standard optical, coating, electronic processing technologies. This pixel addressable device can provide 90° phase shifts with dynamic voltage levels that can be applied by using standard off-the-shelf drivers. The device is

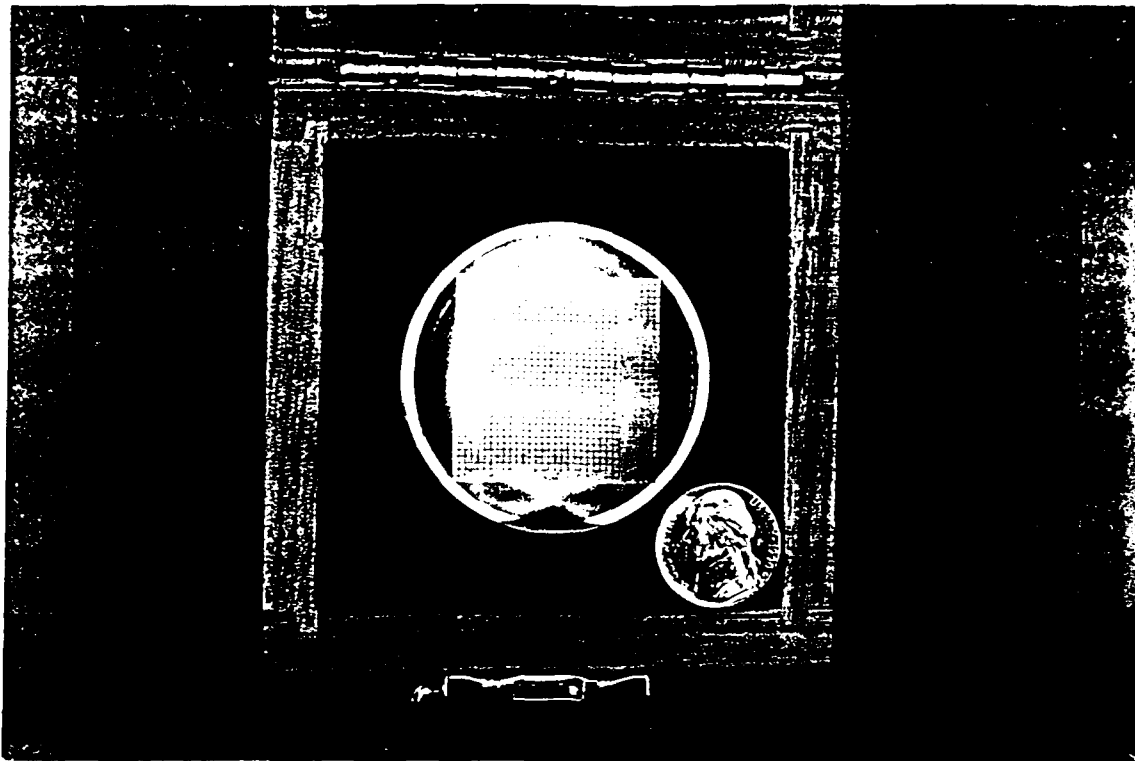


Figure 3. Photograph of a 32 x 32 PLZT spatial light modulator designed for visible-to-near infrared applications.

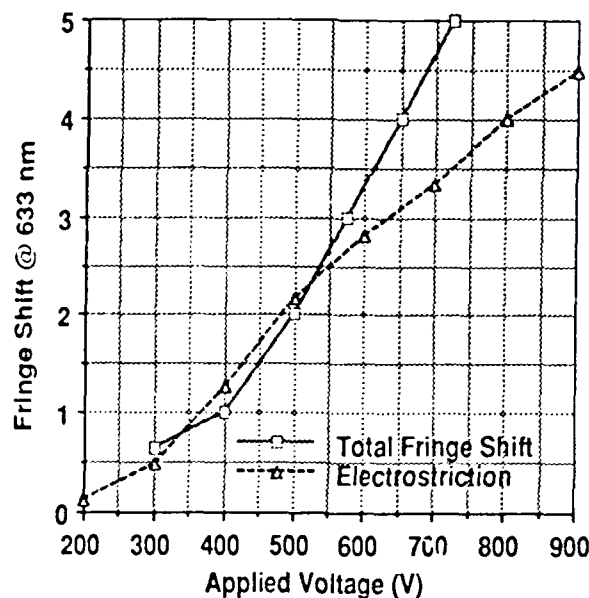


Figure 4. Fringe shift as a function of applied voltage at visible HeNe laser wavelength. Both the electrostrictive component and total fringe shifts are shown.

broadband; its spectral response is only limited by the coatings performance. It can handle reasonably high laser energies and should be useful in a variety of adaptive optical applications.

References:

1. Q. Zhang, et. al., "Electrostrictive and Dielectric Response in Lead Magnesium Niobate-Lead Titanate and Lead Lanthanum Zirconate Titanate under Variation of Temperature and Electric Field," *Journal of the American Ceramic Society*, **72**, 599 (1989).
2. C. E. Land, "Longitudinal Electrooptic Effects and Photosensitivities of Lead Zirconate Titanate Thin Films," *Journal of the American Ceramic Society*, **72**, 2059 (1989).

Depolarization in Liquid Crystal TV's

J. Larry Pezzaniti , Stephen C. McClain

Russell A. Chipman, and Shih Yau-Lu

Physics Department, Optics Building 318

University of Alabama in Huntsville

Huntsville, AL 35899

(205) 895-6417 x318

Abstract:

The depolarization of a TVT-6000 liquid crystal television has been measured to vary between 2-10% as a function of bias voltage, angle of incidence, and incident polarization state.

Depolarization in Liquid Crystal TV's

J. Larry Pezzaniti, Stephen C. McClain
 Russell A. Chipman, and Shih Yau-Lu
 Physics Department, Optics Building 318
 University of Alabama in Huntsville
 Huntsville, AL 35899
 (205) 895-6417

Introduction

The polarization properties of a TVT-6000 liquid crystal television have been mapped as a function of bias voltage to the pixels and angle of incidence using a Mueller matrix imaging polarimeter at 632.8 nm. When operated with the polarizers removed, the LCTV introduces between 2-10% depolarization, depending on the pixel bias voltage, incident polarization state, and angle of incidence. The device acts as an elliptical retarder whose magnitude and form are described.

The polarization properties of LCTV's have been investigated by several authors.[1][2] In those investigations linearly polarized light aligned with the liquid crystal molecular director was incident on an LCTV and the output polarization angle and ellipticity as a function of applied voltage was measured. Our research extends these investigations by measuring Mueller matrices of an LCTV, characterizing all its polarization forms. In addition to linear and circular retardance, the LCTV displays significant amounts of depolarization. Depolarization is the coupling of completely polarized light into partially polarized light.

Measurements of LCTV Depolarization

Figure 1 displays maps of the fraction of unpolarized light F_u (depolarization) in the beams exiting the TVT-6000 liquid crystal TV for six incident polarization states. Each plot shows F_u as a function of angle of incidence and applied voltage. The axes of these plots is as follows. The grey scale addressing each pixel increases from front to back with a grey scale of 0 across the bottom row (horizontal) increasing linearly to 255 across the top row. The angle of incidence increases from -21° along the left side, through 0° up the middle (normal incidence) to 21° along the right side. On all of the plots, the voltage applied to the pixels varies along the vertical y axis, and the angle of incidence varies along the horizontal x axis. The molecular director for the device is horizontal (parallel to the plane of incidence). The light exiting the LCTV is characterized by its Stokes vector $S = [s_0, s_1, s_2, s_3]^T$. The degree of polarization $DOP(S)$ of this beam is

$$DOP(S) = \sqrt{s_1^2 + s_2^2 + s_3^2} / s_0,$$

and the fraction of unpolarized light F_u , the quantity plotted in Fig. 1, is

$$F_u(S) = 1 - DOP(S).$$

The average F_u is 5.5%. This is smallest ($\approx 4\%$) when $\pm 45^\circ$ linearly polarized light is incident. Circular polarized light yields the largest depolarization. Significant variations with bias and angle of incidence are observed.

UAH Imaging Polarimeter

Figure 2 shows the Mueller matrix imaging polarimeter developed at the University of Alabama in Huntsville. The instrument measures Mueller matrices in image form at 633nm and other visible and near IR wavelengths. Mueller matrices images can be acquired across the aperture of a sample, as in the measurements presented here, or in an image plane (polarization point spread functions). The polarimeter may be divided into three sections: a polarization state generator, a sample compartment, and a polarization state analyzer. The polarization state generator includes a spatially filtered and coherence scrambled laser whose power is monitored by a reference detector. A collimated 20mm diameter beam passes through a fixed linear polarizer followed by a $\lambda/3$ wave retarder whose orientation is varied. For

these measurements a cylindrical lens generates a cylindrical wave which is incident onto the sample to allow simultaneous angle of incidence and bias measurement. A second cylindrical lens recollimates the light transmitted through the LCTV. The beam exiting the sample is analyzed by the polarization analyzer, another $\lambda/3$ wave retarder and a fixed linear polarizer. The irradiance distribution at the CCD is recorded for each incident and analyzed state. The CCD is a 512x512 pixel chilled scientific grade detector, with a 14-bit A/D converter.

Mueller Matrix Measurements and Retardance

The liquid crystal TV was positioned such that the molecular director was aligned with the horizontal, and the electrodes addressing the device are on the side the beam exits. The ribbon cable comes out the top of the device. Positive angles of incidence are along clockwise rotations from the normal when viewed from the top. The optics collect a 0.1 numerical aperture beam from the LCTV and reimage the LCTV on the CCD. A set of sixty cylindrical waves with different polarization states are sequentially launched into the LCTV. In these measurements, the center 256x256 pixels were measured. Between subsequent measurements, the first retarder is rotated six degrees and the second retarder is rotated 30 degrees. From these sixty images, the Mueller matrices associated the light path through each pixel is computed. The measured Mueller matrices for the LCTV are shown in Figure 4. Extensive calibration procedures reduce systematic errors due to non-ideal polarization components and drift.[3][4]

Physical quantities, including retardance, depolarization and diattenuation are derived from a measured Mueller matrix. This device is intended to perform as an electrically addressable retarder, and our measurements confirm that this is the dominant polarization effect. Specifying arbitrary elliptical retardance requires three degrees of freedom; for example the magnitude, the orientation of the major axis and the ellipticity. Instead of these, we present the retardance data as follows: δ_0 the horizontal component, δ_{45} the 45° component, and δ_R the right circular component. Retardance δ and (unnormalized) Stokes vector S_F for the fast axis (state) are

$$\delta = \sqrt{\delta_1^2 + \delta_2^2 + \delta_3^2}, S_F = [\delta, \delta_1, \delta_2, \delta_3]^T.$$

Figure 3 shows the retardance components as derived from the Mueller matrix. The retardance increases linearly with voltage and is weakly dependent of the angle of incidence. The retardance is of an elliptical form with $\delta_{45} \approx \delta_R$, so the major axis of the fast axis ellipse is at about 45° with an ellipticity near 0.5.

While a linear increase in retardance with applied voltage is evident in Figure 3, the depolarization in Fig. 1 does not exhibit a similar linear dependence. This indicates that the source of the depolarization is not the same as the source of the polarization rotation. A significant part of the depolarization may result in part from scattering from the regions surrounding the LCTV pixels. Since this scattering may carry light out of the beam, the degree of polarization of the detected beam is expected to depend on the numerical aperture of the detection optics.

Conclusions

Liquid crystal televisions exhibit significant amounts of depolarization, in addition to their desired polarization effects. Up to 10% depolarization was observed in the TVT-6000.

We would like to acknowledge the support of the Air Force Office of Scientific Research (contract #AFOSR-89-0542) for their support of this work.

References

1. T. H. Barnes, T. E. Eiju, K. Matusuda, and N. Ooyama, "Phase-only modulation using a twisted nematic liquid crystal television", *Appl. Opt.* **28**, 4845-4852, (1989).
2. D. A. Gregory, J. A. Loudin, J. C. Kirsch, E. C. Tam, and F. T. S. Yu, "Using the hybrid modulating properties of liquid crystal televisions," *Appl. Opt.* **30**, 1374-1378, (1991).
3. J. L. Pezzaniti, R. A. Chipman, "Imaging polarimeters for optical system metrology," in *Polarimetry: Radar, Infrared, Visible, Ultra-violet, and X-Ray*, Chipman and Morris, Editors, *Proc. SPIE* **1317**, 280-293, (1990).
4. D. B. Chenault, J. L. Pezzaniti, R. A. Chipman, "Mueller matrix Algorithms," in *Polarization Analysis and Measurement*, D. H. Goldstein, R. A. Chipman, Editors, *Proc. SPIE* **1746**, 231-246, (1992).

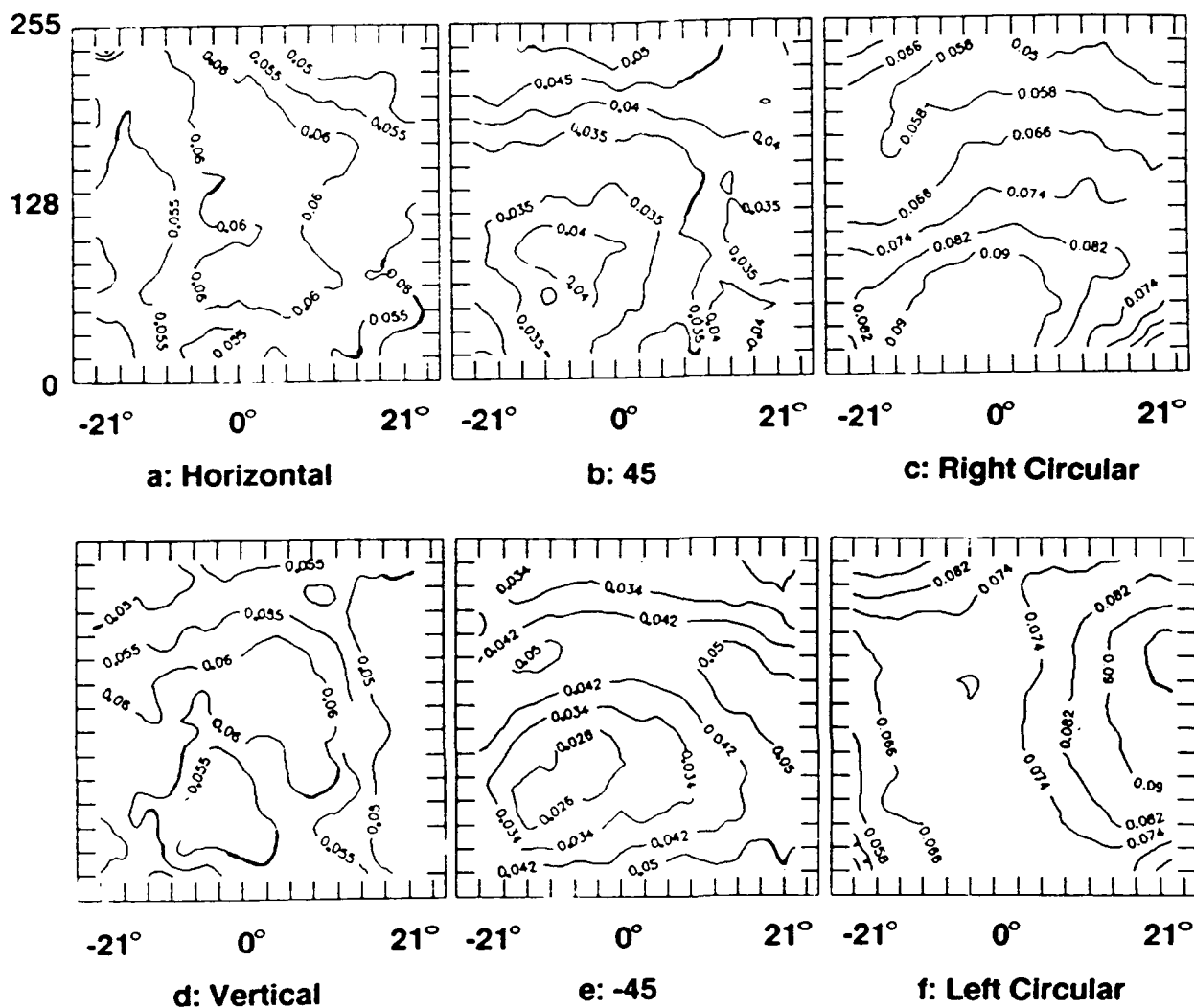


Figure 1. Fraction of transmitted light that is unpolarized for various incident states

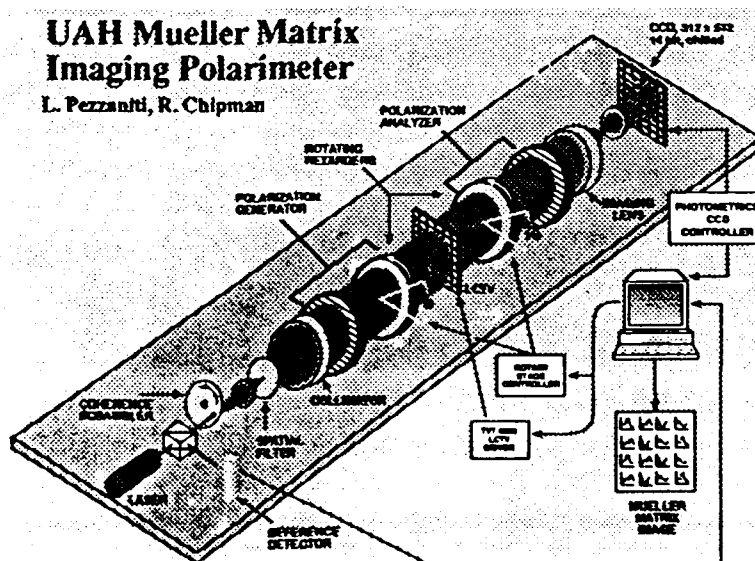


Figure 2.

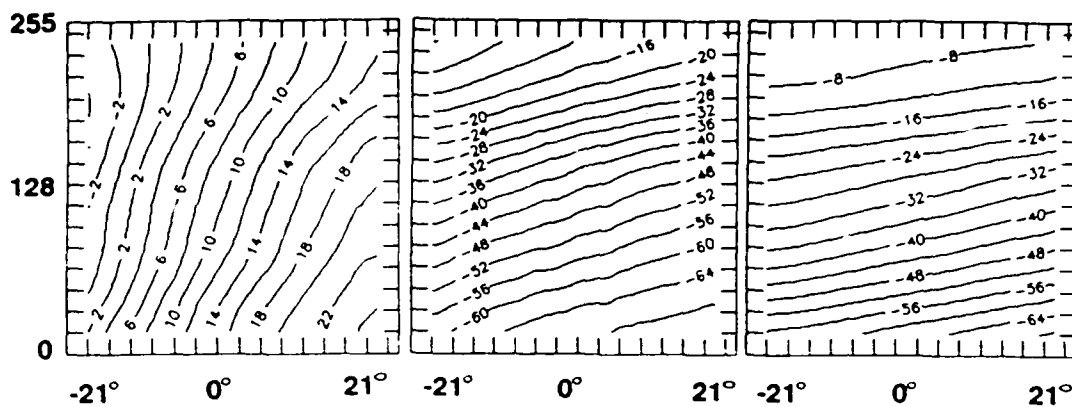


Figure 3. Retardance of LCTV as a function of angle of incidence and applied voltage. a) Horizontal linear retardance, b) 45° linear retardance, and c) Circular retardance.

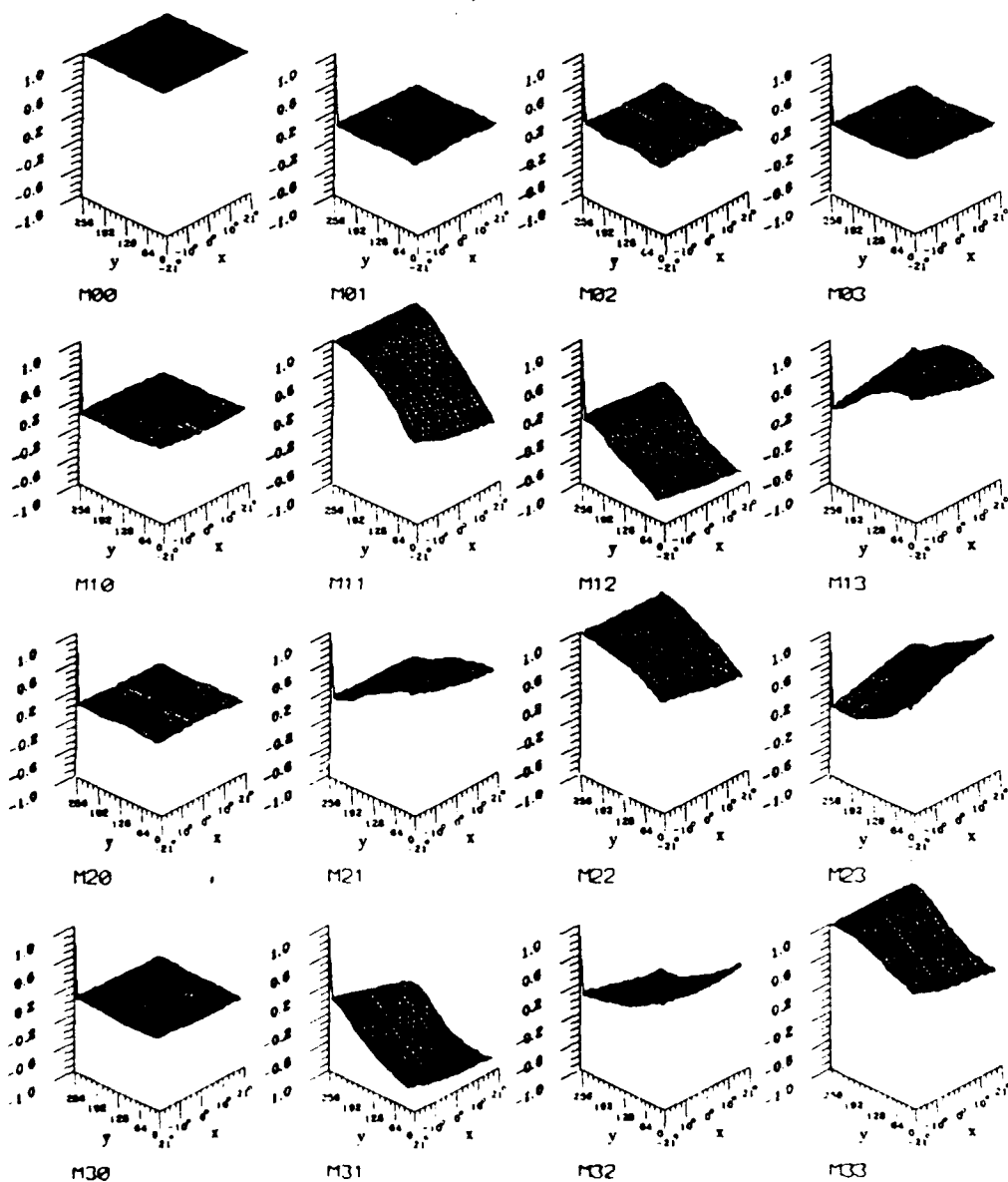


Figure 4. Mueller matrix of the TVT-6000 LCTV as a function of angle of incidence and applied voltage. The Mueller matrix data is used to determine polarization properties including depolarization, retardance, and diattenuation.

Lowered Temperature MBE Regrowth of LED Structures on High Density GaAs Circuits Fabricated through MOSIS

Annette C. Grot and Demetri Psaltis
California Institute of Technology

and

Krishna V. Shenoy and Clifton G. Fonstad, Jr.
Massachusetts Institute of Technology

Abstract

We present results on GaAs/AlGaAs LEDs monolithically integrated by Molecular Beam Epitaxy (MBE) regrowth with GaAs MESFET circuits fabricated through the MOSIS service.

High density GaAs MESFET (Metal-Semiconductor Field Effect Transistor) based circuits are commercially available at an affordable price through the MOSIS (MOS Implementation System) service. Unfortunately, optical sources such as LEDs or laser diodes are not yet part of the standard process. Researchers at Honeywell Systems and Research Center have developed an in-house process where they grow an LED (Light Emitting Diode) structure in semi-insulating GaAs substrate first and then do the ion-implant based MESFET processing, but this technology is not yet available commercially [1]. The transistors circuits available through the MOSIS service are ion-implant based GaAs MESFETs circuits with tungsten-based refractory-metal Schottky gates, nickel-based refractory-metal ohmic contacts and aluminum interconnection metallization and have been shown to be stable with no significant change in the Schottky gate or ohmic contact properties after 3 hours at $525^{\circ}\text{C} \pm 10^{\circ}\text{C}$ [2,3]. Thus, it may now be feasible to regrow optical sources on fully processed MESFET circuitry, to achieve high density optoelectronic circuits, with lowered temperature MBE (Molecular Beam Epitaxy). This allows one to build high density complex electronic circuitry with optical inputs and optical outputs. Such optoelectronic circuits could be used for high speed optical communications, optical computing, or smart pixels.

Our specific circuit application is for optoelectronic neuron arrays in optical neural networks. Each neuron circuit has two photodetectors to receive the optical inputs, electronic circuits to perform a nonlinear thresholding function on the photocurrent and a LED to transmit the output of the neuron. A typical optical neural network has neuron densities of 1×10^4 neurons/cm². This puts stringent requirements on the power dissipation and uniformity of the circuit, but these requirements can be met with an industrial fabrication process [4].

Figure 1 shows the circuit diagram of the circuit we designed and fabricated through MOSIS. Each branch of the circuit accepts two optical inputs, I_1 and I_2 . If I_1 equals I_2 then the gate voltages of both MESFETs are $V_d/2$ which turns both transistors off. The current sinking transistor draws its current entirely from the LED. If I_1 or I_2 are not equal, then the gate voltage on one of the two MESFETs will be high (V_d) turning the transistor on and thus shorting the LED. Therefore the LED is only turned on when $I_1 \approx I_2$. The

photodetectors are enhancement mode MESFETs ($V_T=0.27V$) with the gate connected to the source. These optical FETs provide the nonlinear IV characteristics required. The LED is connected to the circuit after the regrowth.

The entire circuit except for the LED was designed using the MOSIS VITESSE HGaAs2 process and fabricated by Vitesse Semiconductor Corporation. Half the chip was left blank for the LED regrowth. The fabricated chip was electrically tested and then dielectric stack covering the blank area was removed using HF. Once the dielectrics were removed, the chip was degreased and placed in the MBE chamber. The epitaxial structure grown is shown in Figure 2. The superlattice was grown to impede defects from the semi-insulating substrate from propagating upward. The LED structure consists of the double heterostructure nAlGaAs/iGaAs/pAlGaAs layers. The total growth time was nearly 4 hours at the lowered growth temperature of 530°C. The polycrystalline GaAs that covers the portion of the chip where the circuits are, was removed by masking off the crystalline GaAs with photoresist and then etching with a phosphoric etchant, which does not attack the aluminum pads of the circuits. There are cracks visible over the circuits in the overglass layer, but they do not interfere with the operation of the circuits underneath, and can be minimized by reducing the MBE substrate temperature ramp rates.

In order to determine the degradation in the MESFET circuits due to exposure to high temperature for a prolonged period, the circuits were electrically tested after the growth and their performance was compared to the original circuit. Figure 3 shows the before and after I-V curves for a depletion MESFET with its gate connected to the source. This is the current sinking transistor in the circuit. The saturation voltage is the same, whereas the saturation current has decreased by approximately 10%, and the source-to-drain resistance has increased by 40%. Figure 4 shows the I-V characteristics of the optical FETs. The degradation of the performance of the components is marginal and it will not seriously affect the performance of the circuit.

After the electrical testing of the circuits fabricated by Vitesse, the photoluminescence of the epitaxial material was measured and compared with the photoluminescence of a control blank wafer that was grown at the same time. As shown in Figure 5, the strength of the photoluminescence is comparable for the two wafers. LEDs were fabricated on the chip as well as the control wafer. The L-I curves are shown in Figure 6. The efficiency obtained is .01% at 100 μ A and .03% at 1mA. The efficiency is approximately the same on the control wafer.

Acknowledgements ACG acknowledges support from a fellowship from the National Science Foundation and KVS has received fellowship support from the National Science foundation and from the Fannie and John Hertz Foundation.

Bibliography

- [1] M. K. Hibbs-Brenner, S. D. Mukherjee, J. S. Kogan, B. Grung, E. Kalweit, M. P. Bendett, "Design, Fabrication, and Operation of an Integrated Optoelectronic Cellular Array," in Proceedings of SPIE Annual Meeting (1991) vol. 1563, p. 138.

I-V Curve for DFET before and after regrowth

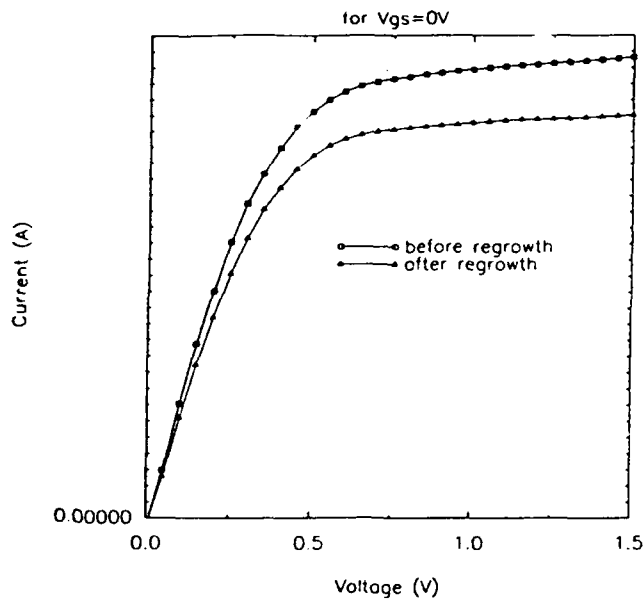


Figure 3 I-V curve for DFET (Depletion mode FET) with $V_{gs}=0V$ before and after regrowth.

I-V Curve for Vitesse EFET Photodetectors

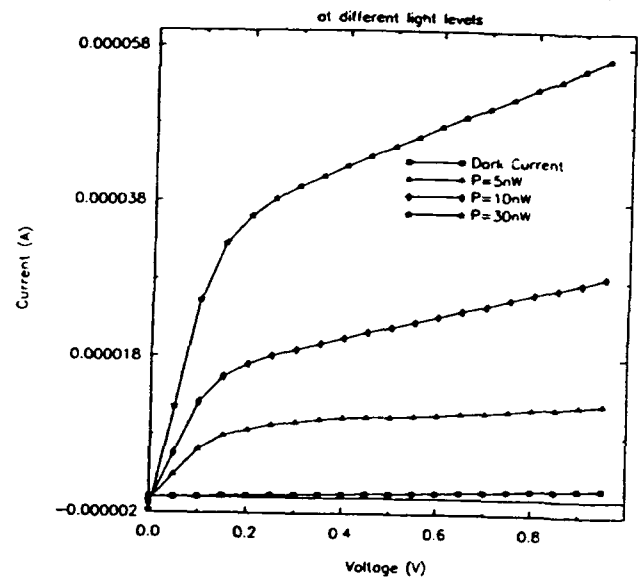


Figure 4 I-V curves for the EFET (Enhancement-mode FETs) as detectors.

Photoluminescence for AlGaAs/GoAs LED structure

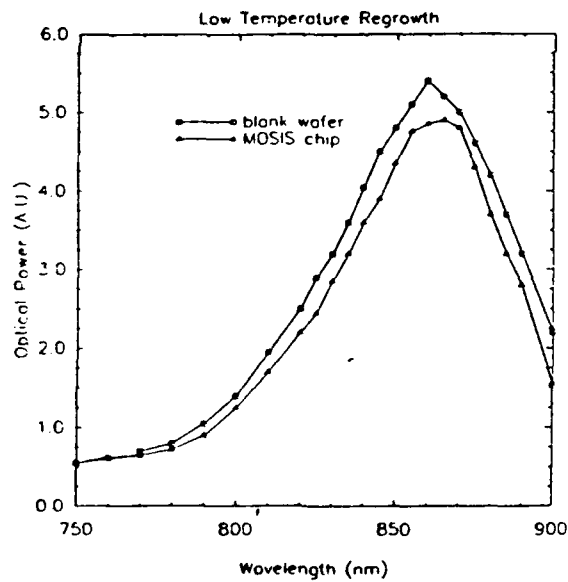


Figure 5 Photoluminescence from regrowth on the blank GaAs wafer and the Vitesse chip.

L-I Curve for LED on Vitesse chip

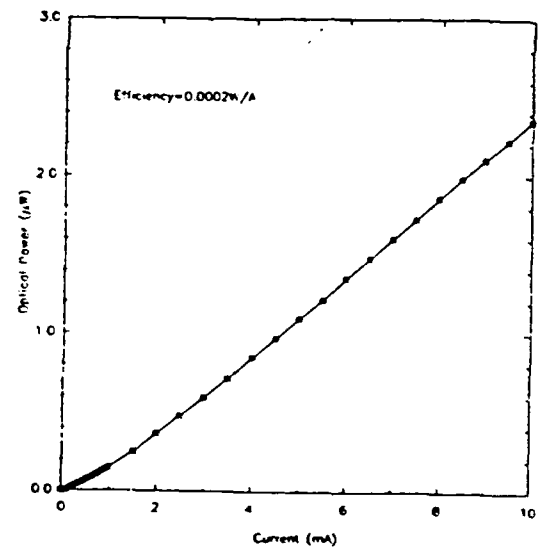
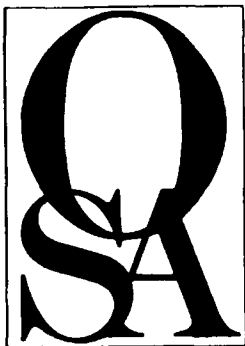


Figure 6 L-I curve for the LED on the Vitesse chip.



Sponsored by
Optical Society of America

Technical Cosponsor
IEEE/Lasers and Electro-Optics Society



Spatial Light Modulators and Applications

*Summaries of papers presented at the
Spatial Light Modulators and Applications
Topical Meeting*

March 15-17, 1993
Palm Springs, California

1993 Technical Digest Series
Volume 6

CONFERENCE EDITION

Sponsored by
Optical Society of America

Technical Cosponsor
IEEE/Lasers and Electro-Optics Society

Optical Society of America
2010 Massachusetts Avenue, NW
Washington, DC 20036-1023

Optical Society of America
1993 Technical Digest Series
Volume 6
Spatial Light Modulators and Applications
Topical Meeting
March 15-17, 1993
Palm Springs, California
STAFF
John W. P. Morgan Manager

Articles in this publication may be cited in other publications. In order to facilitate access to the original publication source, the following form for the citation is suggested:

Name of Author(s), "Title of Paper," in Spatial Light Modulators and Applications Technical Digest, 1993 (Optical Society of America, Washington, D.C., 1993), Vol. 6, pp. xx-xx.

ISBN Number

Conference Edition	1-55752-287-1
Postconference Edition	1-55752-288-X
(Note: Postconference Edition includes postdeadline papers.)	
1993 Technical Digest Series	1-55752-317-7

Library of Congress Catalog Card Number

Conference Edition	92-62846
Postconference Edition	92-62845

Copyright © 1993, Optical Society of America

Individual readers of this digest and libraries acting for them are permitted to make fair use of the material in it, such as to copy an article for use in teaching or research, without payment of fee, provided that such copies are not sold. Copying for sale is subject to payment of copying fees. The code 1-55752-317-7/93/\$2.00 gives the per-article copying fee for each copy of the article made beyond the free copying permitted under Sections 107 and 108 of the U.S. Copyright Law. The fee should be paid through the Copyright Clearance Center, Inc., 21 Congress Street, Salem, MA 01970.

Permission is granted to quote excerpts from articles in this digest in scientific works with the customary acknowledgment of the source, including the author's name and the name of the digest, page, year, and name of the Society. Reproduction of figures and tables is likewise permitted in other articles and books provided that the same information is printed with them and notification is given to the Optical Society of America. Republication or systematic or multiple reproduction of any material in this digest is permitted only under license from the Optical Society of America; in addition, the Optical Society may require that permission also be obtained from one of the authors. Address inquiries and notices to Director of Publications, Optical Society of America, 2010 Massachusetts Avenue, NW, Washington, DC 20036-1023. In the case of articles whose authors are employees of the United States Government or its contractors or grantees, the Optical Society of America recognizes the right of the United States Government to retain a nonexclusive, royalty-free license to use the author's copyrighted article for United States Government purposes.

Printed in U.S.A.

CONTENTS

Agenda of Sessions	v
SMA SLM Technologies: 1	1
SMB Ferroelectric Liquid Crystals SLMs	9
SMC SLM Technologies: 2	31
SMD Smart Pixel SLMs	49
SME Poster Session	73
STuA International Perspective on Liquid Crystal SLMs	105
STuB Silicon-Addressed Hybrid SLMs	121
JTuC Joint Optical Computing/Photonics in Switching/ Spatial Light Modulators Plenary Session	133
SWA Multiple-Quantum Well SLM Technology	149
SWB Asymmetric Fabry-Perot MQW Modulators	165
SWC Optical Interconnects and other SLM Applications	187
SWD New Materials	209
Key to Authors and Presiders	229

SPATIAL LIGHT MODULATORS TECHNICAL PROGRAM COMMITTEE

Arthur D. Fisher, *General Chair*
Micro-Intelligent Systems, Inc.

Sing H. Lee, *Program Chair*
University of California, San Diego

David Armitage
Lockheed RDD

Connie Chang-Hasnain
Stanford University

W. A. Crossland
STC Technology Ltd./BNR, UK

Uzi Efron
Hughes Research Laboratory

Mary K. Hibbs-Brenner
Honeywell, Inc.

Larry Hornbeck
Texas Instruments, Inc.

Tracy Hudson
U.S. Army Missile Command

Kristina Johnson
University of Colorado

I. N. Kompanets
P. N. Lebedev Physics Institute, Russia

Guy Lebreton
Universite de Toulon et du Var, France

John N. Lee
Naval Research Laboratory

Anthony Lentine
AT&T Bell Laboratories

John Neff
University of Colorado

Tomio Sonehara
Seiko Epson Corporation, Japan

Armand Tanguay
University of Southern California

Cardinal Warde
Optron Systems, Inc.

MONDAY, MARCH 15, 1993

GRAND BALLROOM WEST

8:30 am–10:00 am

SMA, SLM TECHNOLOGIES: 1

Arthur Fisher, *Micro-Intelligent Systems, Inc.*, *Presider*

8:30 am (Invited)

SMA1 Microlaser array spatial light sources, J. L. Jewell, G. R. Olbright, R. P. Bryan, W. S. Fu, *Photonics Research Inc.* Spatial light sources have inherent advantages over light modulators in system simplifying and compacting a system. Microlaser array progress and additional issues are discussed. (p. 2)

9:00 am (Invited)

SMA2 Optoelectronic neuron arrays, Demetri Psaltis, Annette Grot, Jiafu Luo, *California Institute of Technology*. We derive the factors limiting the density of optoelectronic neuron arrays and the connectivity they can support. (p. 4)

9:30 am (Invited)

SMA3 Research activities on SLMs in Hamamatsu, Yoshiji Suzuki, Tsutomu Hara, *Hamamatsu Photonics K.K., Japan*; Ming H. Wu, *Hamamatsu Corp.* An overview will be presented of SLM technology at Hamamatsu Photonics and the applications researchers are using our SLMs in various institutes. (p. 5)

10:00 am–10:20 am COFFEE BREAK

GRAND BALLROOM WEST

10:20 am–12:10 pm

SMB, FERROELECTRIC LIQUID CRYSTALS SLMs

John N. Lee, *U.S. Naval Research Laboratory*, *Presider*

10:20 am (Invited)

SMB1 Structures and drive modes for optically addressed ferroelectric liquid crystal SLMs, Garret Moddel, Pierre R. Barbier, *Univ. Colorado*. Structures and drive modes for optically addressed spatial light modulators incorporating ferroelectric liquid crystal light-modulating layers and hydrogenated amorphous silicon photosensors are surveyed. (p. 10)

10:50 am

SMB2 One-transistor DRAM FLC/VLSI SLM, Mark A. Hand-schy, Lise K. Cotter, Jim D. Cunningham, *Displaytech, Inc.*, Timothy J. Drabik, *Georgia Institute of Technology*; Stephen D. Gaalema, *Black Forest Engineering*. We present a 256 × 256 electrically addressed SLM using ferroelectric liquid crystal light modulators atop a VLSI array of one transistor pixels. (p. 14)

11:10 am

SMB3 Chiral smectic liquid crystals for high information content displays and SLMs, Kristina M. Johnson, Douglas J. McKnight, Chongchang Mao, Gary Sharp, Jian-Yu Liu, Anat Sneh, *Univ. Colorado at Boulder*. Results on improvements in liquid crystal on silicon (LCOS) technology that allow for high frame rate operation, analog phase modulation and SLM scalability are discussed. (p. 18)

11:30 am

SMB4 Achromatic intensity modulator, J. E. Stockley, G. D. Sharp, D. Doroski, K. M. Johnson, *Univ. Colorado at Boulder*. Two liquid crystal cells are used to implement an achromatic intensity modulator with a 250-nm bandwidth. A reflection mode device will also be presented. (p. 22)

MONDAY, MARCH 15, 1993—Continued

11:50 am

SMB5 Real-time displacement measurement with ferroelectric liquid crystal (FLC)-SLM by correlation of speckle patterns, Yuji Kobayashi, Tamiki Takemori, Naohisa Mukohzaka, Narihiro Yoshida, *Hamamatsu Photonics K.K., Japan*; Seiji Fukushima, *NTT Opto-electronics Laboratories, Japan*. Real time optical displacement meter with wide measurable range, based on the speckle photography is experimentally constructed by using FLC SLMs. (p. 26)

12:10 pm–1:40 pm LUNCH BREAK

GRAND BALLROOM WEST

1:40 pm–3:00 pm

SMC, SLM TECHNOLOGIES: 2

Cardinal Warde, *Optron Systems, Inc.*, *Presider*

1:40 pm

SMC1 Fabrication and switching sensitivity of the new magneto-optic SLM, William E. Ross, *Litton Data Systems*; David N. Lambeth, *Carnegie Mellon Univ.* This paper reports the design, fabrication, and improved switching sensitivity of the new reflected mode magneto-optic SLM including electrical and optical test results. (p. 32)

2:00 pm

SMC2 New type of SLM with binary phase gratings, L. Buydens, P. Demeester, *Univ. Gent—IMEC, Belgium*. Combining a binary phase grating and materials with a controllable absorption, it is shown theoretically that it is possible to modulate the intensity of the zero order diffraction peak with high contrast ratios. (p. 36)

2:20 pm

SMC3 Optical memory elements based on hetero-nipi superlattice asymmetric cavity SLMs, M. K. Hibbs-Brenner, S. D. Mukherjee, J. Lehman, *Honeywell Systems and Research Center*, P. P. Ruden, J. J. Liu, *Univ. Minnesota*; A. A. Sawchuk, W.-F. Hsu, *Univ. Southern California*. Asymmetric cavity SLMs with hetero-nipi superlattice cavity layers are theoretically and experimentally evaluated for use as short-term optical memory elements. (p. 40)

2:40 pm

SMC4 Amorphous silicon carbide multilayer modulators for silicon smart pixels, Mark A. Neifeld, *Univ. Arizona*. We discuss amorphous silicon carbide multilayer modulators. Features include silicon compatibility, visible wavelength operation, high speed, and fabrication simplicity. We present experimental data from initial multilayers. (p. 44)

3:00 pm–3:30 pm COFFEE BREAK

GRAND BALLROOM WEST

3:30 pm–5:40 pm

SMD, SMART PIXEL SLMs

William Miceli, *Office of Naval Research*, *Presider*

3:30 pm (Invited)

SMD1 Smart and advanced spatial light modulators, J. R. Brocklehurst, *CRL, UK*; N. Collings, *Institute de Microtechnique, Switzerland*; W. A. Crossland, *BNR Europe Ltd., UK*; R. J. Mears, *Univ. Cambridge, UK*; D. G. Vass, *Univ. Edinburgh, UK*; M. R. Worboys, *GEC Marconi Research Centre, UK*. The design of silicon backplane ferroelectric liquid crystal smart spatial light modulators for image processing, neural networks, and telecommunication interconnects is discussed. (p. 50)

MONDAY, MARCH 15, 1993—Continued

4:00 pm

SMD2 Electrically addressed field effect transistor self-electro-optic effect device (FET-SEED) amplified differential modulator array, A. L. Lentine, L. M. F. Chirovsky, L. A. D'Asaro, E. J. Laskowski, S. S. Pei, M. W. Focht, J. M. Freund, G. D. Guth, R. E. Leibenguth, L. E. Smith, T. K. Woodward, *AT&T Bell Laboratories*. We describe a 6×6 array of electrically addressed FET-SEED amplified differential modulators, with voltage gain operating as high as 2 Gbit/s. (p. 54)

4:20 pm

SMD3 VLSI/liquid crystal winner-take-all modulators for optical competitive learning, Timothy M. Slagle, Kelvin H. Wagner, *Univ. Colorado at Boulder*. Second-generation optical winner-take-all modulators have been implemented in VLSI/liquid crystal device technology. These devices will be used as processing elements in an optical competitive learning system. (p. 58)

4:40 pm

SMD4 Multipurpose SLM, Mark A. Handschy, David B. Banas, *Displaytech, Inc.*; Stephen D. Gaalema, *Black Forest Engineering*. An SLM with bidirectional I/O, both optical and electrical, exemplifies the utility of ferroelectric-liquid-crystal over silicon VLSI smart pixel technology. (p. 62)

5:00 pm

SMD5 Optically addressed zero-crossing edge detection SLM, David A. Jared, Kristina M. Johnson, *Univ. Colorado at Boulder*. This paper describes an optoelectronic system that performs zero-crossing edge detection using a VLSI, ferroelectric liquid crystal SLM. Electrical and optical results on the SLM and system are presented. (p. 66)

5:20 pm

SMD6 DANE switching arrays for high-performance computing (HPC) modules, Peter S. Guilfoyle, *OptiComp Corp.*; David E. Grider, *Honeywell, Inc.*; Bart Van Zeghbroeck, *Univ. Colorado at Boulder*. GaAs DANE switching arrays integrated with free-space smart optical interconnects are being utilized in HPC modules. (p. 69)

GRAND BALLROOM CENTER

8:30 pm–10:00 pm

SME, SPATIAL LIGHT MODULATORS POSTER SESSION

SME1 Requirements for SLMs for optical interconnection, Hiroyuki Ichikawa, Neil McArdle, Mohammad R. Taghizadeh, *Heriot-Watt Univ., UK*. The performance of SLMs for optical interconnections is evaluated using ideal models. The poor spatial resolution of the modulators restrict their implementation in practical applications. (p. 74)

SME2 Enhanced performance of AlGaAs/GaAs asymmetric Fabry-Perot reflection modulators, M. A. Gross, R. P. Kenan, T. K. Tran, C. J. Summers, *Georgia Institute of Technology*. Enhanced contrast and passband are predicted and optimized for non-surface normal operation of asymmetric Fabry-Perot reflection modulators incorporating AlGaAs/GaAs quantum wells or heterojunction structures. (p. 77)

SME3 Optical data self-routing system based on MQW modulator and optical bistable matrices, P. Chavel, P. Koppa, J. Taboury, *Centre Univ. Orsay, France*; J.-L. Oudar, R. Kuszelewicz, *FRANCE TELECOM-CNET, France*; J.-P. Schnell, J. Raffy, J.-P. Pocholle, M. Papuchon, *Thomson-CSF, France*. We describe the application of MQW optoelectronic matrices and Damman gratings for address recognition and beam switching in a 64-channel optical serial demultiplexor. (p. 81)

MONDAY, MARCH 15, 1993—Continued

SME4 Space-modulating ferroelectric liquid-crystal light valve and its application to multivalued logic gates, Shigeto Kohda, Yasushi Inaba, Noriyoshi Yamauchi, *NTT Interdisciplinary Research Laboratories, Japan*; M. Hirai, *NTT Communication Switching Laboratories, Japan*. A space-modulating light valve controlled by electronic binary signals is developed using ferroelectric liquid crystal cells. Simple optical multivalued logic gates using these light valves are proposed and demonstrated. (p. 85)

SME5 Retina-like adaptive thresholding in a nonlinear joint transform correlator, K. L. Schehrer, M. G. Roe, L. Schirber, *Rockwell International*; M. Handschy, *Displaytech, Inc.* Simulations show the advantages of a novel retina-like adaptive thresholding scheme implementable in a joint transform correlator with an integrated circuit SLM. (p. 89)

SME6 Polarization behavior of a ferroelectric liquid crystal light valve (FLCLV), W. Xue, N. Collings, *Univ. Neuchâtel, Switzerland*. Effects of device parameters and drive waveform on polarization and intensity characteristics of a FLCLV are discussed. Experimental results are presented. (p. 93)

SME7 Optically addressed liquid crystal phase only modulating SLM, N. Yoshida, N. Mukohzaka, T. Hori, H. Toyoda, Y. Kobayashi, T. Hara, *Hamamatsu Photonics K.K., Japan*. Optically addressed liquid crystal phase only SLM has been developed. The performance parameters and the transfer characteristics of the device are presented. (p. 97)

SME8 Hadamard transforms with ferroelectric-liquid-crystal-over-silicon SLMs, J. Gourlay, P. McOwan, D. G. Vass, I. Underwood, *Univ. Edinburgh, UK*; M. Worboys, *GEC-Marconi Research Centre, UK*. Hadamard transformation is performed by ferroelectric-liquid-crystal-over-silicon SLM. The particular advantages and implications of such novel optical techniques are discussed. (p. 100)

TUESDAY, MARCH 16, 1993—Continued

GRAND BALLROOM WEST

8:30 am–10:00 am

STuA, INTERNATIONAL PERSPECTIVE ON LIQUID CRYSTAL SLMs

Kristina M. Johnson, *University of Colorado, Presider*

8:30 am (Invited)

STuA1 Computer-generated hologram reconstructions using liquid crystal SLMs, Tomio Sonehara, Jun Amako, Hirotsuna Miura, *Seiko Epson Corp., Japan*. We present three CGH reconstructions by using TFT LC-SLMs. They are Lee type for amplitude, Kinoform for phase and wavefront modulation for complex amplitude. (p. 106)

9:00 am

STuA2 Issues in improving the performance of liquid-crystal-over-silicon SLMs, I. Underwood, D. G. Vass, A. O'Hara, D. C. Burns, *Univ. Edinburgh, UK*. We consider some of the critical issues in improving the performance and quality of ferroelectric-liquid-crystal over active-silicon-backplane SLMs. (p. 110)

9:20 am

STuA3 Smectic C* and A liquid crystal light valves: applications to 2-D information processing, J. L. de Bougrenet de la Tocnaye, *ENST de Bretagne, France*. Smectic C* and A liquid crystal light valves are presented. Different addressing modes including VLSI one are described, with applications in neural and signal processing. (p. 114)

9:40 am

STuA4 Liquid crystal SLM for optical image preprocessing, A. V. Partenov, P. N. Lebedev *Physics Institute, Russia*; J. C. Buchholz, *Micro-Optics Technologies, Inc.* Image processing is enhanced by combining transducing and preprocessing functions. Realized preprocessing using an SLM are edge enhancement, selection of nonstationary objects, and image subtraction. (p. 118)

10:00 am–10:30 am COFFEE BREAK

GRAND BALLROOM WEST

10:30 am–12:10 pm

STuB, SILICON-ADDRESSED HYBRID SLMs

Sing H. Lee, *University of California San Diego, Presider*

10:30 am (Invited)

STuB1 Title to be announced, J. Fan, *Kopin Company*. Abstract not available at press time. (p. 122)

11:00 am

STuB2 Bonding of Si thin films to PLZT substrates for SLM applications, M. S. Jin, J. H. Wang, V. H. Ozguz, S. H. Lee, *UC-San Diego*. Silicon films are bonded to PLZT substrates to integrate silicon circuits with bulk PLZT light modulators. The approach and the results of process and device characterization are presented. (p. 123)

11:20 am (Invited)

STuB3 Hybrid silicon/gallium arsenide inverted Fabry-Perot cavity MQW spatial light modulators, Armand R. Tanguay, Jr., Anupam Madhukar, B. Keith Jenkins, *Univ. Southern California*. High bandwidth (>10 MHz) smart pixel SLMs based on the hybrid integration of silicon-based detection and control electronics with gallium-arsenide-based MQW modulators by flip chip bonding are described. The use of an inverted asymmetric cavity design obviates the need for through-substrate vias, and allows for the incorporation of high reflectivity ex situ-deposited dielectric mirrors. (p. 127)

11:50 am

STuB4 Characterization of a free-space optoelectronic interconnect system based on Si/PLZT smart pixels, B. Mansoorian, G. Marsden, V. Ozguz, C. Fan, S. Esener, *UC-San Diego*. The performance characteristics of a prototype parallel free-space optoelectronic communication link utilizing Si/PLZT smart pixels is presented. (p. 128)

12:10 pm–2:00 pm LUNCH BREAK

TUESDAY, MARCH 16, 1993—Continued

GRAND BALLROOM EAST

2:00 pm–5:30 pm

JTuC, JOINT OPTICAL COMPUTING/PHOTONICS IN SWITCHING/SPATIAL LIGHT MODULATORS PLENARY SESSION

B. Keith Jenkins, *University of Southern California*

Joseph W. Goodman, *Stanford University, Presiders*

2:00 pm (Plenary)

JTuC1 Extended generalized shuffle networks, G. W. Richards, *AT&T Bell Laboratories*. This talk discusses how extended generalized shuffle networks are useful in dealing with various constraints that are encountered when implementing switching networks with photonic technology. (p. 134)

2:45 pm (Plenary)

JTuC2 ATM objectives and requirements for next-generation networks, Kai Y. Eng, *AT&T Bell Laboratories*. An overview of ATM networking is described with emphasis on virtual path transport architectures and features. SDH termination, ATM cell processing, and routing are discussed. (p. 138)

3:30 pm–4:00 pm COFFEE BREAK

4:00 pm (Plenary)

JTuC3 Photonics in switching: European systems demonstrators and the long-term perspective, Lars Thylén, *Royal Institute of Technology, Sweden*. Status in the area of photonics-in-switching in Europe, highlighted by systems demonstrators, is reviewed, and the long term perspective for photonics-in-switching is discussed. (p. 142)

4:45 pm (Plenary)

JTuC4 Transition from optical interconnections to optical computing, Richard C. Williamson, *MIT Lincoln Laboratory*. Optical interconnections will be a foot in the door to the next generation of computer systems and provide an evolutionary path toward the use of optics at finer scales. (p. 147)

GRAND BALLROOM WEST

8:30 pm–10:00 pm

STuC, COLLABORATIVE PROGRAMS IN OPTICAL AND OPTOELECTRONIC TECHNOLOGIES FOR COMPUTING

Ravindra A. Athale, *George Mason University, Presider*

Recent developments in optical and optoelectronic technologies have led to a number of exciting devices, such as microlaser arrays, MQW modulators, diffractive optical elements and CMOS-Liquid Crystal devices. Further maturation of these technologies depends critically on developing products incorporating these devices that can lead to a mass market for them. To facilitate this process, it is necessary to make the early prototype devices easily available to potential users and systems developers. One avenue for achieving this involves forming collaborations between industry, universities and government institutions. In U.S., Japan and Europe, several such collaborative efforts are currently under way.

The goals, obstacles, and rewards of such collaborations are the subject of this panel discussion. The panel will consist of representatives from different countries with direct experience in organizing such collaborative efforts. After a brief presentation from the panel members, we will seek inputs from the attendees about their views of the promise and problems regarding such collaborative projects.

WEDNESDAY, MARCH 17, 1993

GRAND BALLROOM WEST

8:30 am-10:00 am

SWA, MULTIPLE-QUANTUM WELL SLM TECHNOLOGY

Anthony L. Lentine, *AT&T Bell Laboratories, Presider*

8:30 am (Invited)

SWA1 Applications and technology of QW SEED arrays, David A. B. Miller, *AT&T Bell Laboratories*. Current status of these device arrays is reviewed, for applications as smart pixels or SLMs in digital or analog optical switching and processing. (p. 150)

9:00 am

SWA2 SLM using semi-insulating MQW material, A. Partovi, A. M. Glass, T. H. Chiu, *AT&T Bell Laboratories*. We describe the use of semi-insulating MQW materials for SLMs. The performance of an optical correlator system based on these materials is discussed. (p. 153)

9:20 am

SWA3 High-contrast SLM using Stark effect tuning and heterostructure acoustic charge transport (HACT) pixel addressing, F. Jain, S. K. Cheung, R. LaComb, *Univ. Connecticut*; T. Grudkowski, R. Sacks, D. Cullen, *United Technologies Research Center*. This paper describes a novel SLM structure which integrates the high-contrast ratio feature of a Fabry-Perot cavity along with Stark effect tuning, and ease of pixel addressing as manifested by the HACT technology. (p. 157)

9:40 am

SWA4 Novel high contrast MQW SLM based on polarization rotation, H. Shen, M. Wraback, J. Pamulapati, M. Dutta, J. Kosinski, W. Chang, P. Newman, *U.S. Army Research Laboratory*; Y. Lu, *Rutgers Univ.* We report on a novel SLM using MQW, anisotropic strain, and polarization rotation to achieve an exceedingly high contrast (330:1) (p. 161)

10:00 am-10:30 am COFFEE BREAK

GRAND BALLROOM WEST

10:30 am-12:10 pm

SWB, ASYMMETRIC FABRY-PEROT MQW MODULATORS

Constance J. Chang-Hasnain, *Stanford University, Presider*

10:30 am

SWB1 Phase characteristics of reflection electro-absorption modulators, Daxin Liu, S. M. Lord, M. Larson, J. A. Trezza, J. S. Harris, Jr., *Solid State Laboratories*; B. Pezeshki, *T. J. Watson Research Center*. The influence of refractive index changes on the phase characteristics of a reflection Fabry-Perot quantum well modulator is discussed and compared with experiment. (p. 166)

10:50 am

SWB2 Ex-situ cavity phase tuning of InGaAs/AlGaAs MQW-based inverted asymmetric Fabry-Perot reflection modulators, Kezhong Hu, R. Cartland, Li Chen, K. Kaviani, P. Chen, A. Madhukar, *Univ. Southern California*. Wafer scale resonant wavelength tailoring with 20 Å accuracy is demonstrated via ex-situ cavity phase tuning in an inverted asymmetric Fabry-Perot reflection modulator affording large scale array. (p. 170)

11:10 am

SWB3 Electroabsorptive asymmetric Fabry-Perot modulators with symmetric coupled QWs, D. S. Gerber, R. Droopad, G. N. Maracas, *Arizona State Univ.* The performance of asymmetric Fabry-Perot modulators based on symmetric coupled QWs is compared to that of similar devices with rectangular QWs. (p. 174)

WEDNESDAY, MARCH 17, 1993—Continued

11:30 am

SWB4 Design model for reflection mode MQW modulators based on minimization of power penalties, C. Fan, M. W. Hansen, D. W. Shih, S. C. Esener, *UC-San Diego*. A model is presented for modulator material and structure design. The performance is evaluated through the contrast ratio and total power penalty (p. 178)

11:50 am

SWB5 Active anti-reflection coating electro-optic modulator, Anjad Obeidat, Jacob Khurgin, Shaozhong Li, *The Johns Hopkins Univ.* A new type of MQW reflection modulator, based on the multilayer active anti-reflection coating is proposed and compared theoretically with a conventional asymmetric Fabry-Perot etalon modulator. (p. 182)

12:10 pm-1:30 pm LUNCH BREAK

GRAND BALLROOM WEST

1:30 pm-3:10 pm

SWC, OPTICAL INTERCONNECTS AND OTHER SLM APPLICATIONS

Uzi Efron, *Hughes Research Laboratory, Presider*

1:30 pm

SWC1 Potential field computation for robotic path planning using a microchannel SLM, Max B. Reid, *NASA Ames Research Center*. A microchannel SLM is employed to demonstrate the optical calculation of potential field maps for mobile robot navigation. The optical calculation time scales favorably in comparison to digital electronic computation. (p. 188)

1:50 pm

SWC2 Generalized dynamic holographic interconnects using SLMs, D.C. O'Brien, T. D. Wilkinson, R. J. Mears, W. A. Crossland, *Cambridge Univ., UK*. Real time binary phase computer-generated holograms are replayed on a SLM. Weighted matrix interconnects are demonstrated, and results discussed. (p. 192)

2:10 pm

SWC3 Implementation of a polarization-sensitive silicon retinula array, Ido Bar-Tana, Kristina M. Johnson, *Univ. Colorado at Boulder*. We describe the implementation of a polarization sensitive silicon retinula array, for material classification based on specular reflection. (p. 196)

2:30 pm

SWC4 Programmable diffractive optical elements, Jeffrey A. Davis, Don M. Cottrell, Robert M. Bunch, Werner V. Brandt, Heidi M. Schley-Seebold, Jarod Guertin, *San Diego State Univ.* Programmable diffractive optical elements can be written onto SLMs. New applications are discussed including anamorphic lenses, derivative lenses, and nondiffracting Bessel function beams. (p. 200)

2:50 pm

SWC5 Self-amplified beam-steering technique for programmable optical interconnections, Hua-Kuang Liu, *Jet Propulsion Laboratory*; Shaomin Zhou, Pochi A. Yeh, *UC-Santa Barbara*. A self-amplified angularly multiplexed beam-steering technique for programmable interconnection and optical computing applications is presented. (p. 204)

3:10 pm-3:30 pm COFFEE BREAK

WEDNESDAY, MARCH 17, 1993—Continued

GRAND BALLROOM WEST

3:30 pm–5:00 pm

SWD, NEW MATERIALS

Tracy D. Hudson, *U.S. Army Missile Command, Presider*

3:30 pm (Invited)

SWD1 Self-assembly SLM for molecular computing, Harold Szu, Ann Tate, David Cullin, Marianne Walch, David Demske, Joseph Garcia, Sonlinh Phuvan, Nicholas Cavaris, *U.S. Naval Surface Warfare Center*. SLM-useful molecular computing is made on a bacteriorhodopsin (BR) molecule film suspended in a viscous liquid medium, similar to a wet photograph but having adaptive and finer pixels. The natural synergism between the thermal diffusion of BR molecule (induced externally by a write-laser) and its photochromism (generated internally by electronic transitions) is demonstrated in an edge-enhanced laser-image application.

(p. 210)

4:00 pm

SWD2 Photoanisotropic organic volume holograms for spatial light modulation, Tizhi Huang, Samuel Weaver, Steve Blair, Kelvin Wagner, *Univ. Colorado at Boulder*. High-resolution dye-polymer holographic films are used as SLMs for incoherent-to-coherent conversion, joint transform correlation, and real-time SAR processing. (p. 214)

4:20 pm

SWD3 Optical data processing with bacteriorhodopsin and its genetically modified variants, C. Bräuchle, N. Hampp, *Univ. München, Germany*; D. Oesterhelt, *Max-Planck-Institut für Biochemie, Germany*. With bacteriorhodopsin and its genetically modified variants, the applicability of biological systems in spatial light modulators and optical pattern recognition is demonstrated.

(p. 218)

4:40 pm

SWD4 Optically driven, optically addressed spatial light modulator (SLM), Janine V. Reardon, Don A. Gregory, *Univ. Alabama in Huntsville*. A dye doped polymer material has been developed that shows promise for use as a SLM modulation medium. Preliminary results will be presented. (p. 222)

5:15 pm

SPDP, POSTDEADLINE SESSIONS

Monday, March 15, 1993

SLM Technologies: 1

SMA 8:30am-10:00am
Grand Ballroom West

Arthur Fisher, *Presider*
Micro-Intelligent Systems, Inc.

Microlaser Array Spatial Light Sources

J.L. Jewell, G.R. Olbright, R.P. Bryan, and W.S. Fu

Photonics Research Inc., 4840 E. Pearl Circle, Boulder, CO 80301

(303) 541-9292

The ability to generate one- and two-dimensional arrays of light beams in arbitrarily redefinable patterns addresses an enormous range of applications. Two basic classes of devices can provide this: spatial light sources (SLS) and spatial light modulators (SLM). In this paper we provide a critical comparison of SLS and SLM technologies. Light sources will generally refer to vertical-cavity surface-emitting lasers (VCSEL) which we are developing, while light modulators will generally refer to semiconductor quantum well modulators which are structurally and operationally the closest comparison to VCSELs.

As its name implies an SLS generates its own light, typically comprising a laser or light emitting diode for each element. The vertical-cavity surface-emitting laser (VCSEL) is particularly well suited for SLS applications. On the other hand, an SLM is not a light source. It modulates light from an external source by any of a number of means such as quantum well electroabsorption. Figure 1 illustrates this fundamental difference between the two classes of devices when used as an input into an optical processing system. In addition to the optical hardware of the SLS system, the SLM-based system requires an external light source, array generating optics, and a lens to direct the light from the light source to the SLM. The increase in size, weight, optical hardware and packaging complexity of the SLM compared to the SLS is profound. It is also fundamental, being implied by the definition of an SLM. A general rule is, therefore, that unless there is a compelling reason to use an SLM, an SLS is preferred.

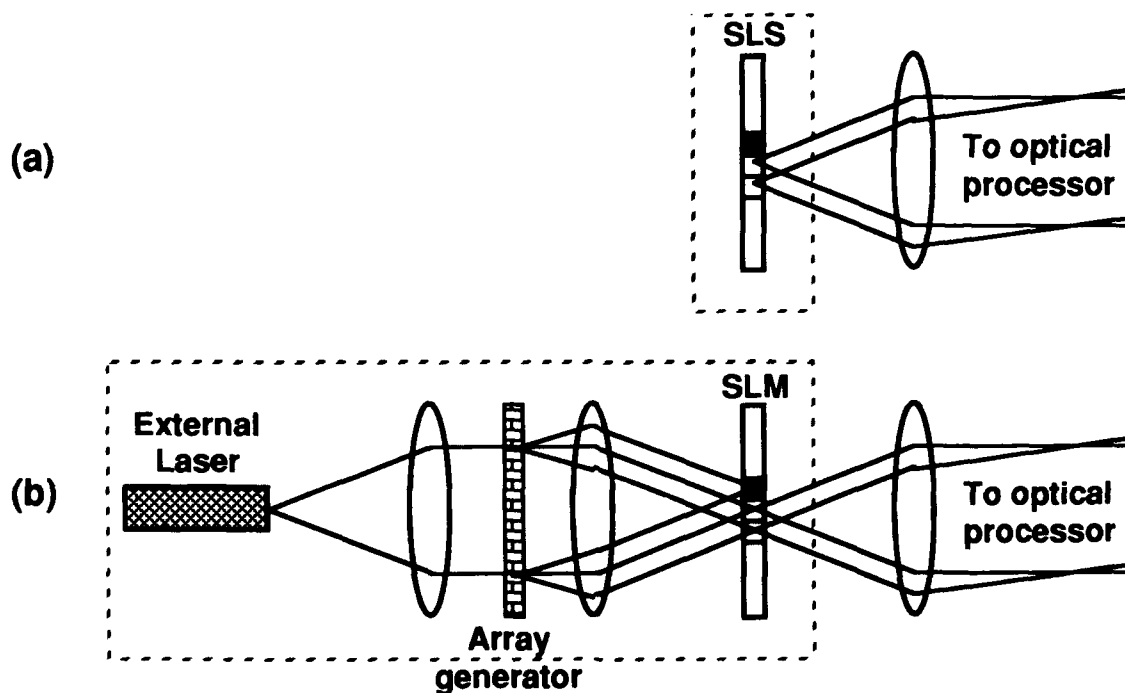


Fig. 1. Comparison of (a) SLS and (b) SLM-based inputs to a system showing the large difference in hardware needed. For optical interconnections or optical computing, a very similar comparison is valid.

There are many other significant differences, not seen in Fig. 1, between SLS and SLM-based systems. The increased bulk in an SLM component adds directly to increased cost. The beam array must be aligned to the SLM. SLM's are either slow, e.g. liquid crystals, require high power, or utilize a resonance to which the external source must be closely matched. Self electro-optic devices for example, use electric field induced absorption by the exciton resonance of semiconductor quantum wells to modulate the light. For proper modulation, the wavelength of the modulated light must be well tuned with respect to the exciton resonance. Since the wavelength of the exciton resonance itself varies with temperature, the overall device is very temperature sensitive with an operating range on the order of 10 degrees Celsius. By comparison, VCSELs have demonstrated less than 20% variation in current threshold over a 75 degree range.

When lasers are used as the sources, SLSs have much higher contrast than SLMs, often greater than 1000:1 compared to ~20:1 for a good asymmetric quantum well modulator. Since there is no optical input to the SLS, there is no issue of optical bandwidth over which this contrast is obtained.

On-chip power dissipation is an area in which modulators have had only a slight advantage over sources, however this advantage is not fundamental. Experiments have demonstrated that VCSELs can be scaled down to sub-half-micron diameters, pointing to the possibility of ultra-low power, high-speed lasers in the future. Although a quantum well modulator could also be scaled down to this size, the difficulty of coupling the externally generated light into the device would almost certainly render the device impractical for systems use.

When spatial coherence is required across the array, SLMs are preferred over SLSs. The natural emission of an independently addressed array of lasers is spatially incoherent. Coherence is generally necessary in performing phase-dependent operations such as Fourier transforms and related analyses. It is possible, however, and sometimes preferable to perform some operations normally associated with coherent optics, such as pattern recognition, using spatially incoherent systems. A compact and robust incoherent pattern recognizer has been demonstrated which is far less sensitive to optical alignment than similar coherent recognizers. Although progress has been made in producing phased arrays of VCSELs, the generation of arbitrary patterns (images) in which all elements are in phase is far more difficult and is not likely to be realized in the foreseeable future.

Modulators have higher reliability and yield than lasers due to the fact that they are field effect devices rather than having current flow through them. As the technologies mature, this will be less of an issue since reliability will be extremely high for both classes of devices.

One of the strongest arguments for SLS development is their extreme versatility in addressing near-term as well as long-term markets. Systems for optical disk memory, barcode scanners and high-speed laser printers require the compactness and high intensity of laser sources. The demands for these near-term applications with identified markets are generally much less stringent than for the more futuristic applications of optical computing and image processing. Addressing the near-term markets for the time being will provide the revenues to further the growth of SLS technology, enabling it to address the far-term applications as well.

We acknowledge the support of DARPA and Rome Laboratory for this work under contract number F30602-92-0091.

Optoelectronic Neuron Arrays

Demetri Psaltis, Annette Grot, and Jiafu Luo
California Institute of Technology
Department of Electrical Engineering
Pasadena, CA 91125

In this paper, we will describe optoelectronic neuron arrays fabricated monolithically in GaAs. Each element of these arrays is a simple thresholding circuit consisting of one or two photodetectors, a MESFET and an LED [1]. It can be shown that the density with which this array can be fabricated is

$$N/A \approx \left[\frac{\eta P_{\max}}{4V\sigma_n\sqrt{C}} \sqrt{3\pi P_e} \right] \quad (1)$$

where N is the number of neurons, A is the area of the array, η is the overall optical efficiency, P_{\max} is the maximum allowable power dissipation per unit area, P_e is the acceptable probability that any neuron will produce an erroneous response, V is the supply voltage of the circuit, σ_n is the standard deviation of the detector noise, and C is the number of connections per neuron.

As an example, suppose we want to build a network with $N=10,000$ neurons and $C=1000$ connections per neuron in an area $A=1 \text{ cm}^2$. Suppose further that $\eta = 5 \times 10^{-4}$, $P_{\max} = 10 \text{ W/cm}^2$, $V=2 \text{ Volts}$, and $P_e=0.1$. Then we must have the capability to fabricate the neuron arrays with sufficient uniformity and low enough noise so that $\sigma_n \approx 1 \text{ nA}$ with a corresponding $P=5 \mu\text{W}$.

The basic trade-off in equation (1) is between density and power. Specifically, the optical power inefficiency of the system must be compensated by electrical power generated on the chip which makes the density proportional to the product ηP_{\max} . It is also interesting to note that the density that we can achieve is also proportional to the ratio of P_e (the accuracy we require) to σ_n (the accuracy the circuit provides). The dependency of the density on C is perhaps the most surprising: the density decrease as the connectivity increases. The principle reason for this is the reduction of the efficiency of the hologram as C increases.

We can also derive an equation for the connectivity that can be supported by the LED circuit,

$$C \approx 3 \left(\frac{\pi P_e}{\alpha} \right)^2 \quad (2)$$

where α ratio of the detector noise current to the mean current. The connectivity that can be supported is proportional to the square of the ratio of the accuracy required (P_e) to the accuracy provided by the circuit (α).

[1] S. Lin, A. Grot, J. Luo, and D. Psaltis, 'GaAS Optoelectronic Neuron Arrays', Applied Optics, March 1993.

Research activities on spatial light modulators in Hamamatsu

Yoshiji Suzuki, Tsutomu Hara

Hamamatsu Photonics K.K., 5000, Hirakuchi, Hamakita-city, Shizuoka, 434,
Japan, +81-53-586-7111

Ming H. Wu

Hamamatsu Corporation, Box 6910, 360 Foothill Road, Bridgewater,
NJ 08807-0910, USA, 908-231-0960

Various systems for optical information processing have been proposed. In these systems, a spatial light modulator (SLM) is one of the essential devices used either as transducer, processor and memory or any combination of these functions. Therefore various types of spatial light modulators have been developed during the last three decades^{1),2)}.

Hamamatsu Photonics K.K. started to develop spatial light modulators in 1980. As the first step, a microchannel spatial light modulator (MSLM), originally proposed by Warde et al. at MIT³⁾, was developed. The MSLM is an optically addressed SLM consisting of a photocathode, a microchannel plate (MCP) and an electrooptic crystal (55 degree cut LiNbO₃) in a vacuum sealed tube as shown in Fig.1^{4),5)}. Photocathode is used as photoreceptor for 2-D photoelectric conversion and the MCP is used to multiply the 2-D photo-electric signal which is imprinted upon the LiNbO₃ crystal for electro-optic modulation. This device has a unique capability of operating at a very low writing light energy and at a high readout light intensity with the same wavelength. It is also intrinsically capable of performing image addition, subtraction, thresholding and memory. These special functional capabilities provide design flexibilities for wide varieties of application such as synchronous detection, logic operation, edge enhancement and optical adaptive processing^{6),7)}.

A variation of MSLM incorporating deflection, rotation and zooming mechanism for images was also developed⁸⁾. This device known as PSLM (Pre-processing Microchannel Spatial Light Modulator) is used

to pre-process optically addressed signals for various applications.

The research on SLM was extended to the electron beam addressed spatial light modulator (EBSLM)⁹⁾. The EBSLM is an electrically addressed SLM consisting of an electron gun for generating an electron beam in proportional to sequential electric signal, and a LiNbO₃ wafer for electro-optic modulating a readout light, as shown in Fig.2. This device is also capable of performing image addition, subtraction, contrast reversal and image storage. The EBSLM is generally useful for interface with electrical signal in real-time electro-optic system for optical signal processing. One of the applications in progress involves electro-holography for reconstructing scanning hologram on real time basis^{10),11)}.

Recently three types of optically addressed liquid crystal spatial light modulators, that is, twisted nematic liquid crystal (TNLC) SLM¹²⁾, parallel aligned liquid crystal (PAL) SLM¹³⁾, and ferro-electric liquid crystal (FLC) SLM^{14),15),16)}, have been developed. The structures of these devices are quite similar, and the typical structure is shown in Fig.3. These devices consist of amorphous silicon (a-Si:H) photo-conducting layer as an addressing material, dielectric mirror and a liquid crystal layer as a modulating material, sandwiched between two transparent conducting layers coated on glass plates. The TNLC-SLM is an intensity modulator as is well documented. The PAL-SLM which employs a parallel aligned nematic liquid crystal layer, is used as a two dimensional phase modulator. In the FLC-SLM, a chiral smectic C liquid crystal layer is used as an

electro-optic layer for bistable operation and memory capability.

Application researches using these SLMs have been performed in many research institutes. These are summarized in Table 1. Continuous efforts in device developments and applications should contribute to bring the current SLM technology one step closer to realization of practical electro-optic system capitalizing the advantages of optics.

References

- 1) A.D.Fisher and J.N.Lee, Proc. SPIE, 634, pp.352-370 (1986).
- 2) J.A.Neff et al., Proc. IEEE., 78, pp.826-855 (1990).
- 3) C.Warde et al., Opt. Lett., 3, pp.196-198 (1978).
- 4) T.Hara et al., Adv. Electron. Electron Phys., 64B, pp.637-647 (1985).
- 5) T.Hara et al., Appl. Opt., 28, pp.4781-4786 (1989).
- 6) C.Warde and J.Thackara, Opt. Eng., 22, pp.695-703 (1983).
- 7) J.A.McEwan et al., Post deadline papers, CLEO, paper1 (1985).
- 8) T.Hara et al., Appl. Opt., 25, pp.2306-2310 (1986).
- 9) K.Shinoda and Y.Suzuki, Proc. SPIE, 613, pp.158-164 (1986).
- 10) T-C.Poon et al., JJAP, 29, pp.L1840-L1842 (1990).
- 11) T-C.Poon et al., To be published in Opt. Lett.
- 12) N.Yoshida and K.Hara, Proc. SPIE, 1347, pp.357-363 (1990).
- 13) N.Yoshida et al., To be presented at OSA Topical Meeting on SLM, (1993)
- 14) S.Fukushima et al., Opt. Lett., 15, pp.285-287 (1990).
- 15) Y.Kobayashi et al., Proc. SPIE, pp.1720 (1992).
- 16) Y.Kobayashi et al., To be presented at OSA Topical Meeting on SLM, (1993).
- 17) A.D.Fisher and C.Warde, Opt. Lett., 4, pp.131-133 (1979).
- 18) S.Isobe et al., ESO Cont.Workshop Proc., 29, (1988).
- 19) F.T.S.Yu et al., Proc. SPIE, 963, pp.322-326 (1988).
- 20) F.T.S.Yu et al., Opt. Commun., 63, pp.371-374 (1987).
- 21) M.B.Reid, SPIE Conf. on Opt. Info. Processing Systems and Architectures, 1772-29, (1992).
- 22) T.Hara et al., Proc. SPIE, 625, pp.30-34 (1986).
- 23) K.Kitayama et al., Proc. SPIE, 963, pp.611-618 (1988).
- 24) Ph.Demaleprade et al., Proc. SPIE, 963, pp.601-606 (1988).
- 25) T.Kurokawa et al., Technical Digest Series on Optical Computing, 9, pp.356-359 (1989).
- 26) Y.Hayashi et al., Proc. SPIE, 963, pp.607-610 (1988).
- 27) H.Suzuki et al., 1990 Topical Meeting on Optical Computing, 9D17 (1990).
- 28) A.D.Fisher et al., Appl. Opt., 26, pp.5039-5054 (1987).
- 29) M.Ishikawa et al., Appl. Opt., 28, pp.291-301 (1989).
- 30) K.Kitayama et al., IJCNN'89, 2, pp.465-471 (1989).
- 31) Y.Hayashi et al., 1990 Topical Meeting on Optical Computing, 10E12, (1990)

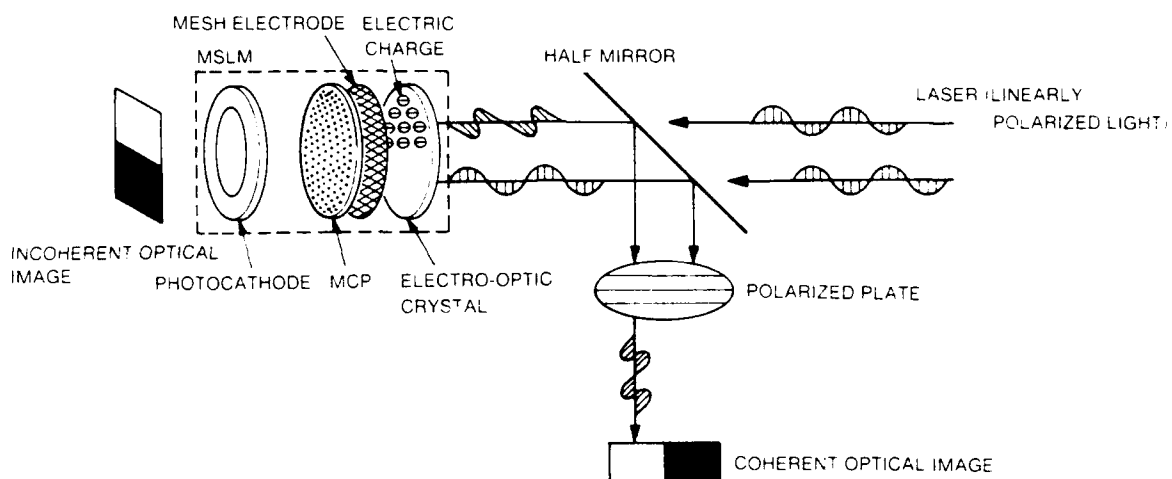


Figure 1 Microchannel Spatial Light Modulator (MSLM).

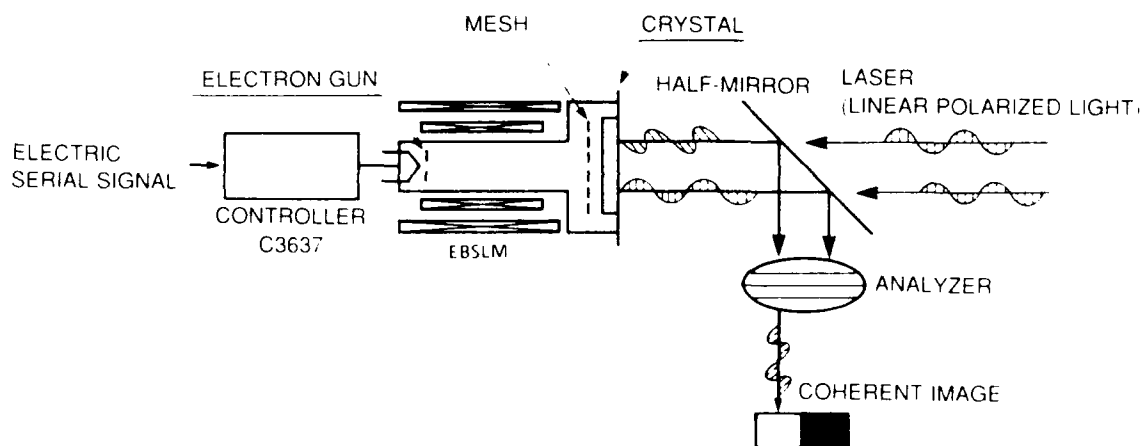


Figure 2 Electro Beam Addressed Spatial Light Modulator (EBSLM).

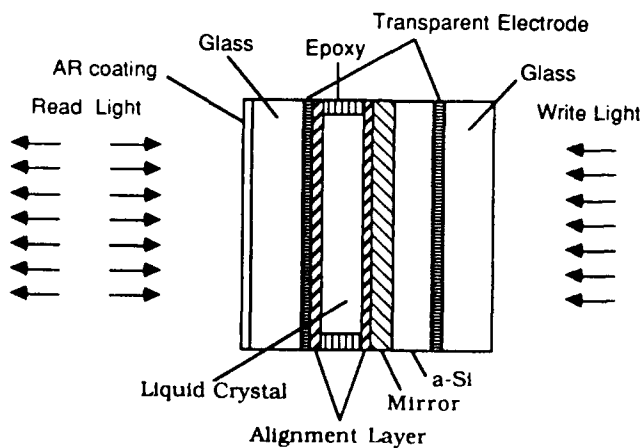


Figure 3

Liquid Crystal

Spatial Light Modulator (LC-SLM).

Analog computing

Application research	Device	Institute	Ref.
Real-time optical phase measurement	MSLM	MIT	17
Speckle observations of double star	MSLM	National Observatory Shizuoka Univ Hamamatsu	18
Real-time joint transform correlation	MSLM	Penn. State Univ. Hamamatsu	19
White light processing	MSLM	Penn.State Univ. Hamamatsu	20
Displacement meter utilizing speckle Photography	FLC-SLM	Hamamatsu- NTT Opto-electron.	15
Real-time optical holography	EBSLM	Virginia Politech. Hamamatsu	10
Optical calculation of potential fields for robotic path planning	MSLM	NASA	21

Digital computing

Application research	Device	Institute	Ref.
Parallel logic operation Programmable parallel processor by polarization encoding	MSLM	Hamamatsu NTT Transmission	22
Sequential logic adder	MSLM	Univ.Tsukuba Institut d'Optique Mechanical Eng.Lab ETL	24
Digital addition and subtraction	MSLM	NTT Opto-electron. NTT Comm.and Info.	25
Space-variant logic operation	MSLM	Univ.Tsukuba ETL	26
Programmable symbolic substitution	MSLM	NTT Comm.and Info.	27

Neuro computing

Application research	Device	Institute	Ref.
Associative networks with adaptive learning capabilities	MSLM	NRL	28
Optical Associatron	MSLM	IPRI Hamamatsu	29
Optical perceptron-like and multiayer neural networks	MSLM	NTT Transmission Hamamatsu	30
Semantic network based on association	MSLM	Univ. Tsukuba ETL	31

Table 1 Application researches on SLMs at various institutes.

Monday, March 15, 1993

Ferroelectric Liquid Crystal SLMs

SMB 10:20am-12:10pm
Grand Ballroom West

John N. Lee, *Presider*
U.S. Naval Research Laboratory

STRUCTURES AND DRIVE MODES FOR OPTICALLY ADDRESSED FERROELECTRIC LIQUID CRYSTAL SLMs

Garret Model and Pierre R. Barbier

Department of Electrical and Computer Engineering and Optoelectronic Computing Systems Center
University of Colorado, Boulder, CO 80309-0425 - model@boulder.colorado.edu - (303) 492-1889

We survey structures and drive modes for optically addressed spatial light modulators (OASLMs) which incorporate surface stabilized ferroelectric liquid crystal (FLC) light modulating layers and hydrogenated amorphous silicon (a-Si:H) photosensors. The devices exhibit response times on the order of 100 μ s, spatial resolution on the order of 70 lp/mm at 50% MTF, write-light sensitivity on the order of 100 nJ/cm², and contrast ratios on the order of 20:1. Hydrogenated amorphous silicon (a-Si:H) has become the most commonly used photosensor in liquid crystal OASLMs [1]. The cross section of an a-Si:H / FLC OASLM is shown in Fig. 1. Electrical power is supplied to the two transparent conducting oxide (TCO) layers. In the reflection-mode device shown, a reflector, usually a dielectric stack, reflects the read light. In transmission mode there is no reflector.

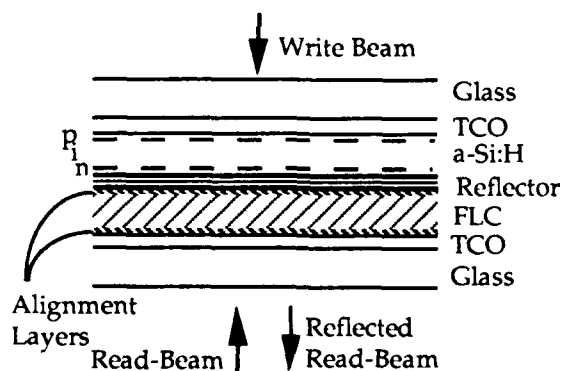


Fig. 1: Cross section of an a-Si:H / FLC OASLM.

PHOTODIODE

Amorphous silicon photodiodes may be formed from p-i-n structures [2], from Schottky barriers, and from metal/insulator/semiconductor (MIS) barriers [3]. In a p-i-n diode the ~200 Å thick boron-doped p-layer blocks electrons from entering the intrinsic region through it from the adjacent TCO electrode. A Schottky barrier is formed by a metal or TCO instead of a p-layer in contact with the intrinsic

a-Si:H, but the rectifying behavior of such barriers is often inferior to that of p-i junctions. In a photodiode under reverse bias, when a photon is absorbed to produce an electron-hole pair in the intrinsic layer, the hole and electron are separated and drift under the action of the internal electric field, and are collected by the p- and n-type contacts, respectively. The blocking contacts stop additional carriers from being injected from the opposite contacts, so that once the carriers have been collected the response is complete. Because the electron is usually the more mobile carrier, and because a-Si:H intrinsic layers are usually n-type the blocking of electrons is more important than the blocking of holes. Therefore p-i or TCO/i structures often suffice rather than p-i-n or TCO/i-n, respectively. In a reverse biased photodiode, the photocurrent varies linearly with the light intensity over several orders of magnitude because one electron-hole pair is collected for each absorbed photon.

Reset Mode

A reset-mode electrical driving scheme [2] and ideal response are shown in Fig. 2. The TCO layer that contacts the liquid crystal is grounded, and a square-wave voltage is applied to the TCO electrode in contact with a-Si:H. With the application of a positive applied voltage, V_+ , the photodiode is forward biased so that all the voltage drops across the FLC with or without the presence of a write-light. This resets the FLC to a state which is defined as off. With a negative applied voltage, V_- , the photodiode is reverse biased, blocking the current in the dark, so that ideally the voltage across and the state of the liquid crystal are unchanged. When a write light illuminates the photodiode, the resulting photocurrent charges the FLC to a negative voltage, switching it on. This voltage is maintained across the liquid crystal until the drive voltage goes positive again, resetting the liquid crystal to its off-state. Thus the reset (erase) operation occurs during the positive voltage period, and the write and read operations occur during the nega-

tive voltage period. The frame rate, which is the frequency of the electrical drive waveform, is sufficiently low that the FLC switches fully off during the positive voltage period. Grey levels have been obtained by charge control [4], temporal averaging [5], and a combination of the two approaches [6].

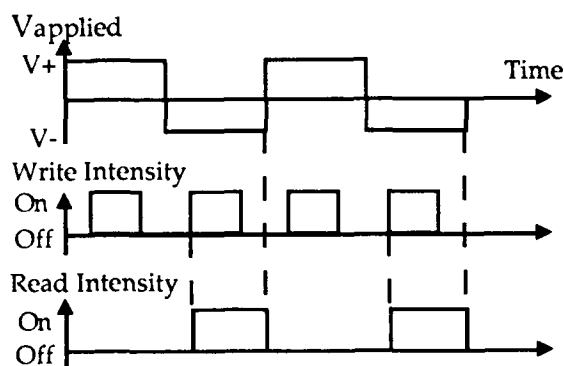


Fig. 2: Ideal photodiode OASLM response in the reset mode (from ref. 2).

Integrating Mode

By driving the OASLM at a higher frequency, an integrating mode is obtained in which the read-out response extends over several driving periods [7]. As shown in Fig. 3, the rise and fall of the output in response to a pulse of write light occur over several driving periods, during which the liquid crystal responds to the time-averaged field. A continuous grey-level response is obtained, but at the cost of sensitivi-

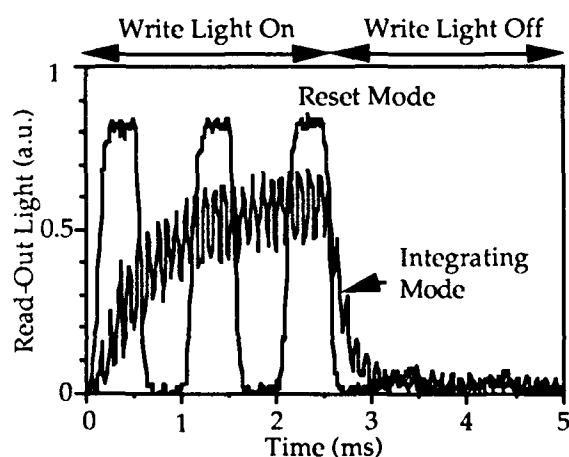


Fig. 3: Response of a photodiode FLC OASLM in the reset (1 kHz electrical drive frequency) and integrating (10 kHz) modes (from ref. 7).

ty and response time when compared to the reset mode. The reset mode is in effect for frame rates of approximately 1 kHz and lower, and the integrating mode for approximately 10 kHz.

PHOTOCONDUCTING DIODE

To form a photoconductor the contacts to the a-Si:H must be ohmic, such that all the applied voltage drops across the bulk. In a sandwich a-Si:H photoconductor, ohmic contacts for electrons are achieved by inserting an i-layer between two thin phosphorus-doped n-layers, which are in contact with the electrodes. One indication of ohmic contacts, and hence the formation of a photoconductor as opposed to a photodiode, is a linear and symmetric current-voltage characteristic. When intrinsic a-Si:H is deposited directly on a transparent conducting oxide, partially blocking Schottky barrier contacts often result, as described above. It is very difficult to obtain a truly ohmic contact to intrinsic a-Si:H without the inclusion of a doped layer at the contact. Many of the TCO/intrinsic a-Si:H photosensors for OASLMs are described as "photoconductors," but perhaps could better be described as "photoconductive diodes," as their contacts are partially blocking. Their current-voltage characteristics are more nearly "symmetric" than those of a photodiode, in the sense that both reverse bias and forward bias currents are low in the dark and significantly larger in the light. This near-symmetry may be used to balance the time-averaged voltage across the FLC to avoid ionic charge buildup, as described below.

Photogenerated electrons contribute to the photoconductor current until they recombine. Consequently large photoconductive gains of up to 10^4 may be obtained with true a-Si:H sandwich photoconductors, but there are several problems in incorporating them into OASLMs. Unless the write-light is absorbed through the entire depth of the photoconductor, a dark, and hence resistive layer impedes the photocurrent. This may be avoided by a compromise between a sufficiently long wavelength, higher than 600 nm [8], and a sufficiently thin film [9]. However, if the film is too thin, undesirable capacitive voltage coupling may result. Another problem involves the dark current, which must be sufficiently low to avoid switching the device within a frame time. This requires the a-Si:H film to be much thicker than 30 μm for video frame rates [9], which is unreasonably

thick. Even if very resistive, but too thin, a-Si:H were used, injected charge would dwarf any photoconductive effect.

Although imperfectly symmetric, the TCO/i photoconductive diode (PCD) has been successfully incorporated into OASLMs. A straightforward operating mode for a bistable FLC / PCD OASLM is shown in Fig. 4. The PCD must be illuminated during the reset (erase) period when a positive voltage is applied to the OASLM. The intensity of illumination during the write period, when a negative voltage is applied, determines whether the liquid crystal attains its stable on-state. If the illumination is insufficient, the device switches off during the read period, during which zero volts is applied. A negative image may be obtained by reversing the polarities described above during the reset and write periods [10]. An ac stabilization voltage may be applied in series with the lower frequency drive voltage to enhance bistability [11].

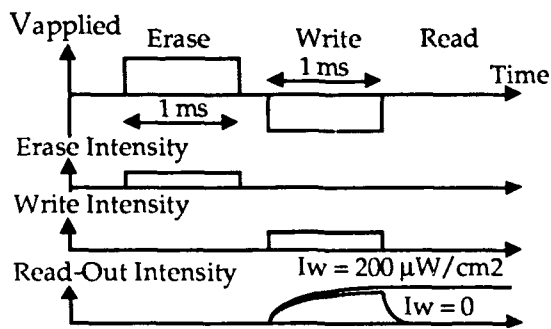


Fig. 4: Basic operating mode for a bistable FLC / PCD OASLM (from ref. 4).

Disadvantages of this simple driving mode are that it does not balance the voltage across the liquid crystal when the erase- and write-light intensities are unequal, and that it requires the PCD to be illuminated during each reset period. A driving scheme which avoids these problems is shown in Fig. 5. After the larger negative and positive voltage pulse pair have been applied, the FLC is reset to its off-state, because even in the absence of a write-light the magnitude of the voltage is sufficient for the capacitively coupled voltage to switch the FLC to the state dictated by the later pulse. This is not the case for the smaller positive and negative voltage pair. It leaves the FLC in an on-state only if the write light is on. With this driving scheme, the voltage is balanced across

the FLC as long as the photosensor has a symmetric enough current-voltage characteristic.

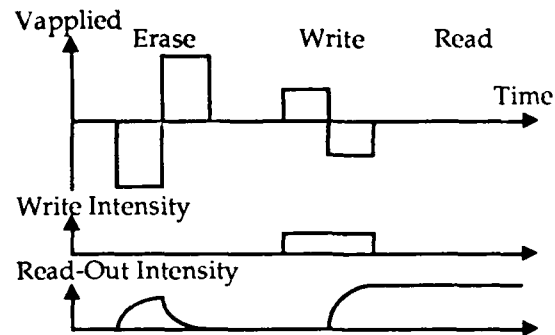


Fig. 5: Operating mode for a bistable FLC / PCD OASLM which provides a time-averaged voltage of zero to the FLC.

BACK-TO-BACK PHOTODIODES

An approach to combining the low leakage current of the photodiode and the symmetry of the photoconductor is to use a back-to-back photodiode structure [9]. An a-Si:H photosensor is deposited in a n-i-p-i-n configuration and incorporated with an FLC into an OASLM. When a voltage of one polarity is applied, one photodiode is reverse biased and the other is forward biased. Reversing the polarity reverses the bias sense on each photodiode. In both cases the current is limited by the reverse-biased diode, and thus by the write light which illuminates it. The operating mode for the back-to-back photodiode OASLM is similar to that of the PCD OASLM.

The first diode must be sufficiently thin that the write light is only partially absorbed in it and penetrates to the second diode. This requirement affects the performance in that the large capacitance associated with the thin diode results in a large voltage which is capacitively coupled to the FLC. Another disadvantage is that the break-down voltage of these structures is low, decreasing with the thickness. These problems limit the operating range of the device.

IMAGE SUBTRACTING OASLMS

The driving scheme of Fig. 4 may be used to subtract one image from another. An image writing on the device during the positive (erase) voltage period is subtracted from the image written originally [12, 13]. OASLMs incorporating a p-i-n-i-p a-Si:H photosensor can subtract

images asynchronously [14] as follows. The top n-i-p photodiode is substantially thicker ($2.5\text{ }\mu\text{m}$) than the buried p-i-n photodiode ($0.5\text{ }\mu\text{m}$). The OASLM is driven with a square-wave voltage, which alternatively forward and then reverse biases each diode. Short wavelength photons are absorbed in the buried p-i-n diode and generate electron-hole pairs which tend to switch the FLC on (excitation). Longer wavelength photons are absorbed dominantly into the top n-i-p diode, and tend to switch the FLC off (inhibition). The short and long wavelength write lights can operate simultaneously, with the dominant one determining the state of the FLC. In Fig. 6 image subtraction is demonstrated in which a continuous image at 633 nm is subtracted from another one at 515 nm . This image subtraction is analog and grey levels may be obtained.

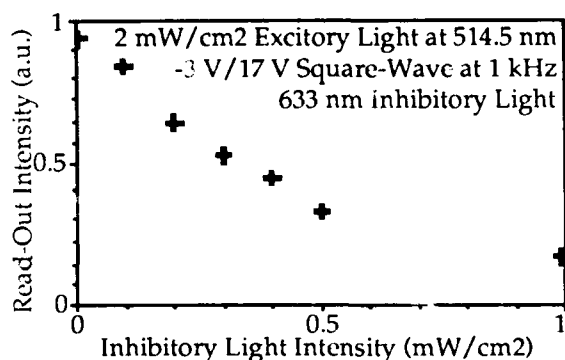


Fig. 6: Experimental inhibitory response of the p-i-n-i-p image subtracting OASLM.

SELF-POWERED OASLM

Generally the photodiode in an OASLM is under reverse bias during the write operation, but if instead the device is short circuited the photodiode operates in a photovoltaic mode, converting the write light into electric power. To obtain a sufficiently high voltage to fully switch an FLC a photovoltaic stack is used [15]. The photodiodes are progressively thicker so that each produces the same photocurrent when the stack is illuminated through the thinnest layer, and the series combination may produce 3 V . The shunt resistances in the photodiode and the FLC are important in allowing the device to switch off quickly, with charge draining through one or both of the resistances. Because the output voltage of the photovoltaic stack is monopolar, a bistable FLC would not switch off. Therefore a monostable FLC is required [16]. A

monostable FLC is one which switches to one of its two saturated states when no electric field is applied. Alternatively, a dc offset voltage can be supplied to the OASLM to aid in switching the device off [15].

REFERENCES

1. Modell, G., "Amorphous silicon for optically addressed spatial light modulators," Ch. 11 in *Amorphous and Microcrystalline Semiconductor Devices: Optoelectronic Devices*, J. Kanicki, ed., (Artech House, Norwood, MA, 1991) pp. 369-412.
2. Li, W., R.A. Rice, G. Modell, L.A. Pagano-Stauffer, and M.A. Handschy, *IEEE Trans. Elec. Dev.* **36**, 2959 (1989).
3. Horikawa, T., S. Tahata, S. Kaho, T. Tasumi, N. Mikami, *et al.*, *MRS Symp. Proc.*, Vol. 219, 203 (1991).
4. Killinger, M., J.L. de Bougrenet de la Tocnaye, and P. Cambon, *Ferroelectrics* **122**, 89 (1991).
5. Landreth, B., and G. Modell, *Appl. Optics* **31**, 3937 (1992).
6. Bone, M., D. Haven, and D. Slobodin, *SID Intl. Symp., Digest of Technical Papers*, Vol. 22, (Playa del Rey, California, 1991), 254.
7. Gabor, A.M., B. Landreth, and G. Modell, in press.
8. Sterling, R.D., R.D. Te Kolste, J.M. Haggerty, T.C. Borah, and W.P. Bleha, *SID Intl. Symp., Digest of Technical Papers*, Vol. 21 (Playa del Rey, California, 1990), 327.
9. Chevrier, J.B., P. Cambon, R.C. Chittick, and B. Equer, *J. Non-Cryst. Solids* **137&138**, 1325 (1992).
10. Fukushima, S., T. Kurokawa, S. Matsuo, and H. Kozawaguchi, *Opt. Lett.* **15**, 285 (1990).
11. Yamamoto, S., T. Ebihara, N. Kato, and H. Hoshi, *Ferroelectrics* **114**, 81 (1991).
12. Robinson, M.G., *Opt. Lett.* **17**, 895 (1992).
13. Yamamoto, S., N. Kato, R. Sekura, J. Yamanaka, and H. Hoshi, *Technical Digest on Spatial Light Modulators and Applications*, (OSA, Washington, D.C., 1990) 105.
14. Barbier, P.R., G. Modell, *MRS 1993 Symp.*, in press.
15. Mao, C.C., B. Landreth, K.M. Johnson, and G. Modell, *Ferroelectrics* **122**, 455 (1991).
16. Zou, Z., N.A. Clark, and G. Modell, 14th Intl. Liquid Crystals Conf., Pisa, Italy, June 21-26, 1992, (Taylor & Francis, London, 1992) 256.

One-transistor DRAM FLC/VLSI SLM

Mark A. Handschy, Lise K. Cotter, Jim D. Cunningham

Displaytech, Inc., 2200 Central Avenue, Boulder, Colorado 80301
(303) 449-8933

Timothy J. Drabik

School of Electrical Engineering, Georgia Institute of Technology,
Atlanta, Georgia 30332
(404) 853-9449

Stephen D. Gaalema

Black Forest Engineering, Colorado Springs, Colorado 80962-2083
(719) 495-0735

The low-power switching characteristics of FLCs make them especially suitable for use in spatial light modulators (SLMs) that will update a frame at a time. In this situation, power dissipation imposes a more restrictive speed limitation than intrinsic response time for most electro-optic materials. If the SLM is to be electrically addressed, the power-dissipation limitation places a premium on low-voltage switching, which further favors FLCs. We report here on SLMs that use FLC light modulators electrically addressed by directly contacted VLSI substrates (FLC/VLSI devices). To achieve maximum pixel density we utilized a pixel circuit based on the one-transistor cell of the familiar dynamic random access memory (DRAM). We have fabricated 256×256 SLMs of two different designs. The first generation device was designed in $2\mu\text{m}$ CMOS rules with pixels on $20\mu\text{m}$ centers. The second generation device utilized $1.2\mu\text{m}$ design rules to give smoother pixels on $30\mu\text{m}$ centers. Both designs along with results from the first generation SLMs are described below; results from the second generation SLM will be presented at the conference.

VLSI design. The electrically addressed SLM functions as an electronically written, optically read memory. Figure 1(a) shows the circuit schematic of an SLM pixel array made from DRAM elements. The large square in each element represents the metal pad that serves both as FLC driving electrode and pixel mirror. The parallel capacitor represents both the primary capacitive load of the FLC modulator and capacitances on the silicon backplane. The transistor in each element acts as a voltage-controlled switch, isolating the capacitor when open (WORD line inactive), and allowing the capacitor charge to the BIT line potential when closed (WORD-line inactive). The voltage-produced change in the state of the FLC overlying the mirror permits optical readout.

Both our SLMs are addressed in a similar way. Data is loaded in eight clock cycles from a 32-bit bus into a 256-element register that then drives the BIT lines. An eight-bit address is decoded to select a word line, which is activated to write the contents of the 256-element register into the corre-

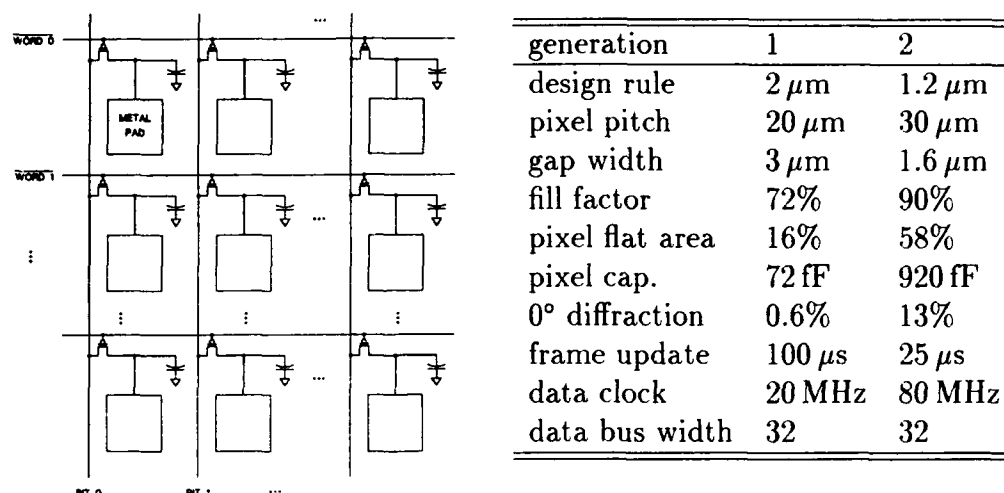


Figure 1: (a) One-transistor DRAM SLM schematic. Each cell comprises an FET pass transistor, addressed by WORD and BIT lines, a charge storage capacitor, and a reflective metal pad. (b) SLM characteristics determined by VLSI design. Diffraction efficiencies represent the fraction of incident intensity diffracted to the brightest (zero) order, off a bare VLSI backplane illuminated in air with $\lambda = 633 \text{ nm}$ light.

sponding pixels of the selected row. Repeating the process 256 times writes an entire frame. The characteristics of our SLMs determined by the VLSI design are summarized in Figure 1(b). Both designs use MOS capacitors in parallel with the mirror. The principal difference between the pixel designs is the amount of area devoted to this capacitor. The first-generation design is close to minimum-geometry; the area free for the capacitor is only 16% of the total pixel area. Shrinking the design rule by a factor of 1.7 and expanding the pixel area a factor of 1.5 lets the pixel area devoted to the capacitor be increased by a factor of eight. Even the smaller capacitor of the first-generation design can store charge adequate to switch FLCs with polarizations up to the 30 nC/cm^2 of the fastest commercial mixtures. The larger capacitance of the second-generation pixel will thus not produce important changes in the available electrical drive. However, it is indicative of improved pixel smoothness, which does have profound implications for both FLC contrast and SLM diffraction efficiency. The patterning of the various conductor and insulator layers in the VLSI process produces surface height variations as large as several microns. This surface topography can disrupt the FLC alignment, lowering achievable contrast ratios. Perhaps more importantly, it can cause the pixel mirrors to be very efficient at diffracting incident light into high orders. Many optical processing applications can use only the light in a single diffraction order, so the light diffracted to other orders represents throughput loss.

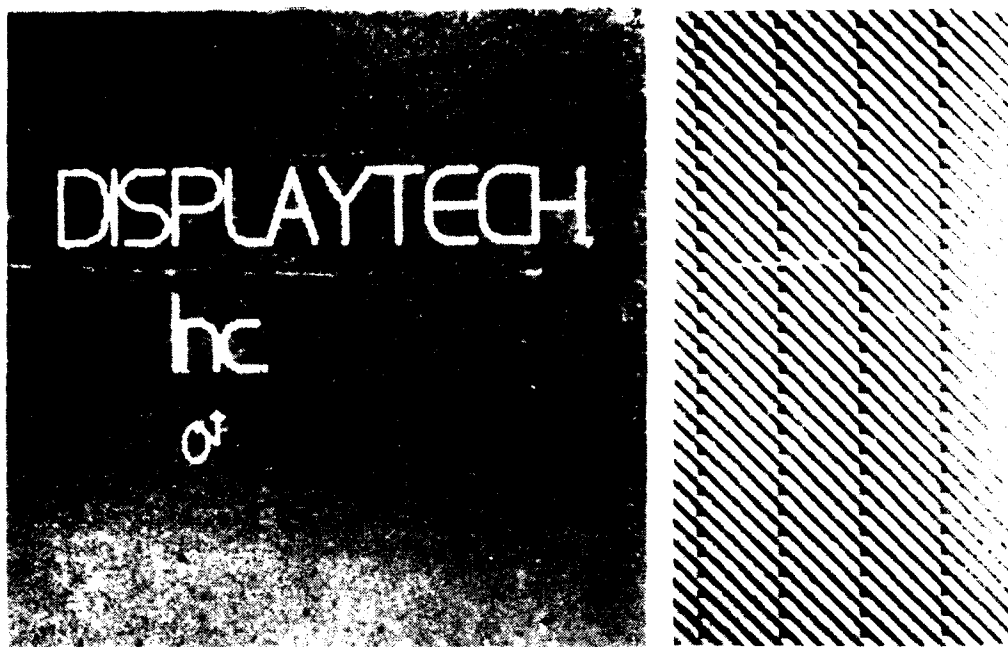


Figure 2: Photographs of first-generation SLM. (a) Full-frame; (b) different pattern, but at same scale as in (a).

Results. Our designs were fabricated by Orbit as Large chips in their *p*-well CMOS process. We packaged the chips ourselves in 81-pin ceramic PGAs (pin-grid arrays) using a resilient die-attach adhesive. FLC cells were formed by assembling the chips to a FTO (indium-tin oxide) coated windows that also carried a rubbed nylon alignment layer. The windows were positioned so that they contacted the chips, and were then glued in place. The highest topography on the chip then set the window-to-mirror gap thickness; passivation glass over this topography prevented short circuits to the window. The cells were vacuum filled with Merck ZLI-3651 at 100 °C, and cooled to room temperature for characterization. The SLMs were driven as described above at a refresh rate of 8kHz; the image data were periodically inverted to preserve DC balance. The window voltage was held constant at 3.0V, half way between the 5V and 1V levels expected on the pixels. We observed the devices using a reflection microscope with crossed polarizers; Figure 2 shows photographs of a first generation SLM. We judged the modulator thickness of the SLM from the FLC birefringence color. The thinnest first-generation SLMs had a magenta color, indicating the first birefringence minimum lay in the green. This would result from an FLC thickness of about 1.8 μm , consistent with topographic heights calculated from the design. The color of the SLM shown varied from magenta near the perimeter, to blue in the center, indicating some thickness variation, resulting mostly from a cupped silicon chip.

To measure the electro optic characteristics, we imaged a 6×6 portion of

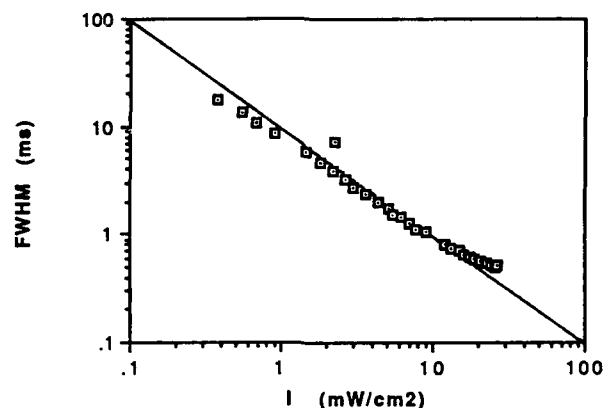


Figure 3: Droop time of first-generation SLM.

the SLM onto a mask that blocked the light coming from the gaps between pixels. The light that passed through the mask was focused onto a silicon photodetector. The infrared light from the incandescent illuminator that would otherwise have leaked through the crossed polarizers was blocked with a filter. We measured a contrast ratio of 29:1, and rise and fall times of 225 μ s. The SLM could achieve a frame rate of 4 kHz while retaining approximately 90% of its achievable peak-to-peak optical response.

The information stored in the one-transistor cell is spontaneously erased by leakage currents. A photogenerated contribution to these currents causes the SLM image to fade at high illumination levels. We characterized fading by orienting the SLM so its pixels were dark in the erased state. We then periodically wrote an all-bright pattern to the SLM, and measured the time from the 50% turn-on point to the 50% fade-off point (FWHM). These data are plotted in Figure 3. At intensities above 10 mW/cm² the 8 kHz refresh rate is inadequate to prevent some image fading. The improved pixel design of the second-generation device has greatly reduced light leakage through the mirrors to the silicon substrate. We have measured single-pixel photocurrents on the second generation device of 10 pA/mW/cm²; with its larger pixel capacitance and higher refresh rate it should then tolerate incident intensities approaching 1 W/cm².

Conclusion. Improved die-attach techniques should soon give optically flat FLC/VLSI SLMs. Improvements in FLC switching speeds foreseeable in the immediate future should permit 6-10 kHz frame rates. High zero-order diffraction efficiencies and FLC contrast ratios above 100:1 should be possible by adopting planarization techniques currently used in advanced VLSI processes. With this improvement, arrays as large as 1024 \times 1024 are feasible within current silicon foundry lithography capabilities.

This work was supported by DARPA, the Department of Commerce through its Advanced Technology Program, and Displaytech.

Chiral Smectic Liquid Crystals for High Information Content Displays and Spatial Light Modulators

Kristina M. Johnson, Douglas J. McKnight*, Chongchang Mao, Gary Sharp, Jian-Yu Liu and Anat Sneh.

University of Colorado at Boulder, Optoelectronic Computing Systems Center, Campus Box 525, Boulder CO. 80309-0525. (303) 492-7967.

*Visiting from the Physics Dept, Heriot-Watt University, Edinburgh EH14 4AS, Great Britain.

1 Introduction—Motivation, and Applications

Although the liquid crystal display market is being driven by the need for a light weight display in computer workstations, laptop computers and notebook computers, there are other applications for high density, high information content displays. These include compact devices for spatial light modulators (SLMs), head up displays (HUDs), high definition television (HDTV) and projection TV displays, virtual reality and three-dimensional data display. A new class of spatial light modulators utilizing chiral smectic liquid crystals (CSLCs) on silicon substrates may meet the need for applications requiring compact, lightweight devices. In addition to providing frame-at-a-time addressing capability, the liquid crystal on silicon (LCOS) technology potentially offers phase, intensity, and color modulation at low operating powers and high frame rates. In order to take advantage of these desirable features, it is necessary to focus on the following technical goals: Achieving high speed operation at CMOS voltages, providing analog phase and intensity modulation, designing the pixel structure for selected applications, understanding the relationship between pixel charge storage time and incident optical illumination, scaling LCOS arrays to high definition television sizes, and fabricating phase flat devices with high quality alignment in the final assembled SLMs. In this paper we present new results on a high frame rate LCOS SLM, and novel methods of analog phase modulation and color generation using CSLCs. Issues concerning pixel design and SLM fabrication and scalability are also discussed.

2 High Frame Rate Operation

In order to achieve higher LCOS SLM frame rates and activate the analog switching chiral smectic A electroclinic mixtures, voltages higher than those available in the CMOS process are required at each pixel modulating mirror. Currently the frame rate of LCOS SLMs is limited to approximately 5 KHz due to the slow response (150 μ sec) of the CSLC to the applied electric fields (typically 1V/ μ m) available with the standard CMOS process. There are three solutions to increasing the response time of these devices: use CSLCs that operate at lower voltages, such as the distorted helix ferroelectrics, use a higher voltage VLSI process, such as BiCMOS, or produce higher voltages in CMOS by lightly doping the transistor drain regions. Our results on the distorted helix materials did not show a drastic improvement in speed, since these CSLCs are inherently slower switching as compared to the smectic C and A materials. Also, a change in voltage not only rotates the optic axis as required for intensity modulation, but also causes a change in the material index of refraction and hence modulates the phase of incident light upon the SLM. The BiCMOS process allows for higher voltages at the metal mirror than the standard CMOS process but dissipates more power.

The maximum pixel transistor voltage is limited by the junction breakdown voltage. The junction breakdown is inversely related to the impurity concentrations of the diffusion regions. This implies that lower doping concentrations for the drains should extend their voltage handling capability. We have designed and fabricated a 64 X 64 VLSI silicon backplane with pixels located on 50 μm centers each containing a lightly doped drain, high voltage n-FET transistor capable of switching 30Volts. This SLM was fabricated in the 2 μm n-well CMOS process through the Metal Oxide Semiconductor Implementation Service (MOSIS) through the USC informaton Sciences NSF/DARPA foundry brokerage. The VLSI processed die were then filled with the CSLC BDH SCE13. The oscilloscope trace in Figure 1 shows 10% to 90% rise and fall times of 70 μsec , the fastest LCOS response time measured to date. The contrast ratio of the entire 64 X 64 array of pixels was measured to be 9:1. This is due in part to the low fill factor of the device. A second generation design with higher fill factor and smaller pixel pitch has been completed and will be presented at the conference.

3 Analog Phase and Color Modulation

We have achieved continuous analog phase modulation using the CSLC smectic A electroclinic in two different alignment configurations; by combining planar aligned electroclinic material with a quarter-wave plate[1] in an asymmetric Fabrey-Perot cavity, and by homeotropic alignment of electroclinic material resulting in direct modulation of the index of refraction seen by the extraordinary eigenmode propagating through the device. The former has the advantage of a wide aperture while the latter is a much simpler design. The device presented in this talk is capable of achieving 250 degrees phase shift (see Figure 3) corresponding to $\alpha = 5$ degrees with 15V/ μm applied field, within 25 μsec using BDH764E electroclinic material.

Using the fast switching smectic C ferroelectric liquid crystals (FLC), it is possible to design a low resolution filter that displays RGB (Red, Green, Blue) saturated colors at frequencies approaching 100kHz. This filter consists of two stages, containing two passive retarders and three FLC devices. Each of the FLC devices is quite thin, ensuring ideal surface stabilized FLC performance. The filter can be used in a color sequential illumination scheme to display color images with the CSLC/silicon devices.

4 Pixel Design Considerations

Small pixels (less than about 20 μm) allow large arrays to fit on smaller and hence cheaper silicon dies which are easier to fill and handle. Applications of LCOS SLMs to optical information processing systems such as optical correlators benefit from smaller pixels because the overall system size scales as the square of the pixel spacing if the same devices are used in the input and filter planes. Fast electronic addressing is easier to achieve in smaller arrays since the signals propagate over smaller distances. On the other hand, larger pixel sizes result in larger fill factors. A correlator using the same SLMs in the input and filter plane has an output signal power that depends on the fourth power of the fill factor. Increasing the fill factor will also increase the display brightness, a critical point for projection display applications. In this paper we discuss the tradeoffs in the design of our 256 X 256 LCOS SLMs with pixels located on 30 μm spacing fabricated in a 1.2 μm CMOS process, as it is, in our opinion, the best compromise between the advantages of small and large pixel pitches.

Charge Storage Time on the LCOS Pixels

An important factor for the operation of these devices is the pixel charge storage time. When the stored charge has leaked from the pixel mirror the FLC will switch into an incorrect state. The

dominant mechanism for charge leakage is through photo-induced leakage currents at the pixel transistors. Recent results of ours show that the leakage current is reduced by only a factor of two as a probe beam of light is moved as far as $10\mu\text{m}$ from a test pixel transistor. This implies that if one were to attempt to completely screen the region of substrate around the pixel transistors from incident illumination one is forced to design a pixel with a smaller fill factor because of the constraints imposed by shielding as much exposed substrate as possible. Our work shows that the fill-factors of a maximally screened $30\mu\text{m}$ pixel and a high fill-factor $30\mu\text{m}$ pixel are 68% and 54% respectively. Note that here we have defined fill factor in terms of only the flat area of pixel mirror. In our 256×256 LCOS SLM we have decided to use minimal screening of the pixels but we intend to refresh the array data every $50\mu\text{secs}$ which is simplified by utilising on-chip clock generation for the array addressing electronics.

[1] Sharp, G. Johnson, K.J. "Chiral smectic liquid crystal optical phase modulator" in OSA Annual Meeting Technical Digest, 1992 (Optical Society of America, Washington, D.C., 1992), Vol. 23, p83.

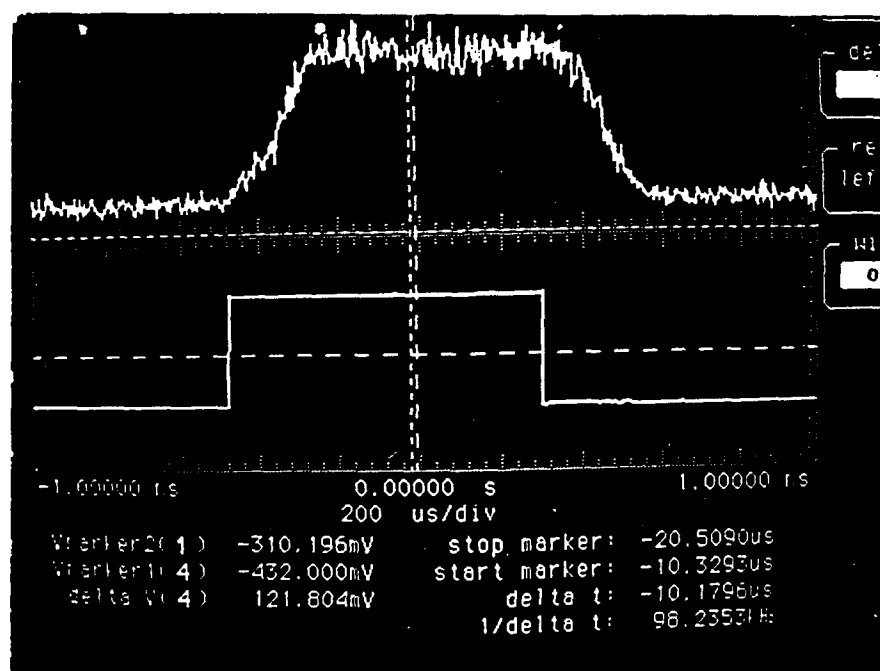


Figure 1. The response of the CSLC BDH SCE13 on the silicon substrate when driven at 30V. The 10% to 90% rise and fall times are $70\mu\text{sec}$.

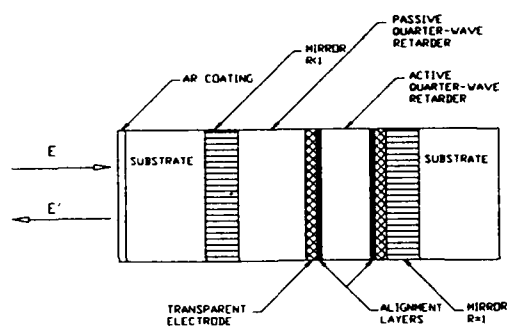


Figure 2. Cross-section of the phase modulator.

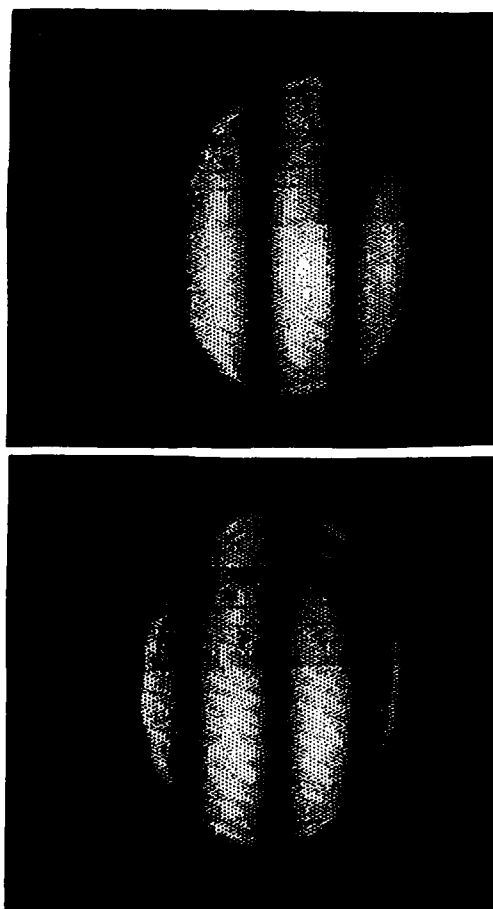


Figure 3. Experimental output of the phase modulator.

Achromatic Intensity Modulator

J. E. Stockley , G. D. Sharp, D. Doroski, and K. M. Johnson

I. Introduction

The limits of polarization rotation as a means of intensity modulation can be significantly improved using a system employing chiral smectic liquid crystals. Chiral smectic liquid crystals exhibit rapid switching speeds. Ten percent to ninety percent rise and fall times of 200 to 300 ns have been measured for experimental mixtures of chiral smectic A (*SmA*) liquid crystals [1]. Polarization diversity systems can be employed to make the modulator independent of the polarization of the incident light [2]. We present here the use of the dispersive properties of *SmA* to implement an achromatic intensity modulator that operates over a 250 nm bandwidth.

SmA liquid crystals are electroclinic or possess analog linear tilt vs. applied field characteristics [3]. Analog tilt corresponds to analog intensity modulation when the device is placed between polarizers. Using two half wave cells filled with commercially available *SmA* that has an 11.25° tilt angle [4] and orienting them such that they tilt in opposite directions provides the required tilt range to achieve a polarization rotation of 90 degrees for light of the design wavelength. At first, using more than a single device to obtain the desired tilt range may seem a disadvantage. However, as is demonstrated below, the second liquid crystal cell may be used to chromatically compensate for the first, thus resulting in a broad band analog intensity modulator.

II. Chromaticity Compensation

It is well known that two birefringent devices of the same retardance have no net effect on the optical field if they are arranged with their axes crossed [5]. Similarly, the ellipticity induced by the first *SmA* device is compensated for by the second device which induces an equal ellipticity of an opposite handedness since its axis is crossed with that of the first.

A broad-band variable attenuator has been designed and demonstrated which illustrates the benefits of two devices in nearly eliminating chromatic effects over very large optical bands. The design utilizes two analog *SmA* devices with a total tilt range of 22.5° . The devices are fabricated to provide a zero-order half-wave retardation at a design wavelength which maximizes the flatness of the transmission function over the visible (450-650 nm). It is well known that two half-wave retarders with angle ψ between their optic axes rotates an arbitrary incident polarization by 2ψ . Since this effect depends only upon the relative orientations of the waveplates, the absolute orientation of the waveplates is arbitrary. This of course requires that the waveplates are exactly half-wave retarders. Using two active electroclinic devices tilting in opposing directions, polarization rotation up to 90° is obtainable.

For the crossed waveplate configuration, the transmission function for a dual *SmA* modulator contained between crossed polarizers can be derived using Jones calculus:

(1)

$$T(\lambda, \alpha) = \sin^2[4\alpha] - \sin^2[\delta/2] \sin^2[4\alpha] - 1/2 \sin^2\delta \sin^2[2\alpha] \left[\cos[4\alpha] + \cos[4\alpha_0] \right].$$

The rotation error induced by chromatic effects is δ and α is the tilt of each device from the smectic layer normal, giving the angle between the optic axes as 2α . The angle α_0 represents the mean orientation of the two retarders, or

$$\alpha = \left[\frac{\alpha_1 - \alpha_2}{2} \right] , \quad \alpha_o = \left[\frac{\alpha_1 + \alpha_2}{2} \right] , \quad (2)$$

where α_1 and α_2 are the absolute orientations of the optic axes. The transmission function of equation 1 is separated into an ideal term (the first expression) and two chromatic transmission terms. It is clear that the two chromatic terms shown above increase in magnitude as the molecular rotation approaches its maximum value of 22.5° . By selecting $\alpha_o = \pm 45^\circ$, the two terms can be made to contribute with opposite sign, nearly cancelling chromatic effects. Substituting this orientation into the above gives

$$T(\lambda, \alpha) = \sin^2[4\alpha] - \sin^2[\delta/2] \sin^2[4\alpha] + \sin^2\delta \sin^4[2\alpha] . \quad (3)$$

In the above equation the transmission is ideal at $\alpha = 0$, and has a loss in transmission of only $\sin^2[\delta/2]$ for the extreme tilt condition. Figure 1 is computer modeling results showing the output transmission spectrum for families of the molecular tilt angle, α .

The transmission spectrum is nearly flat for each output for over 200 nm. The loss at the extreme wavelengths, 450 nm and 650 nm, is less than 3%. The design requires waveplates which are half-wave retarders at the design wavelength 520 nm, indicating the dispersion of the birefringence.

III. Experimental Results

The achromatic intensity modulator has been realized using two *SmA* liquid crystal cells employing BDH 764E electroclinic material designed as half wave retarders at a wavelength of 520 nm. These devices were parallel aligned with polyvinyl alcohol on an indium tin oxide coated substrate pretreated with silane to reduce space charge effects. Two devices oriented to tilt in opposite directions were placed between crossed polarizers and illuminated with a tungsten filament source. The devices were aligned with their axes crossed less 22.5° such that the full tilt range (maximum and minimum applied voltage) resulted in either no change in the state of the input polarization (producing an off state) or a 90° rotation of the state of polarization resulting in complete transmission of the input intensity (neglecting Fresnel losses). Various fields were applied to the devices to change the tilt. A plot of the normalized experimental output intensity as a function of wavelength for various tilts is shown in Figure 2.

Experimental demonstration of the devices compares well to theoretical predictions. The transmission intensity for the on state ($\alpha = 22.5^\circ$) should ideally be 1.0. However, Fresnel losses at the interfaces of the devices result in peak transmission between 85 and 90 percent. The transmission of the on state could be improved with AR coated substrates.

For comparison Figure 3 shows the transmission of a single device between parallel polarizers plotted along with the dual-*SmA* modulator output for the off state. The bandwidth for which the single device has less than 0.5% transmission is approximately 30 nm. The bandwidth for less than 0.5% transmission in the off state for the dual modulator is over 250 nm, or over 8.6 times that of the single device. The two electroclinic devices operate synergistically such that the spectral contrast of the combination is an improvement over the contrast obtained with a single device.

The maximum spectral contrast of the dual modulator is approximately 1000:1 near 600 nm. Here, spectral contrast is the ratio of the maximum to minimum intensities at a given wavelength. Individual devices with higher contrast would result in a higher contrast for the dual modulator.

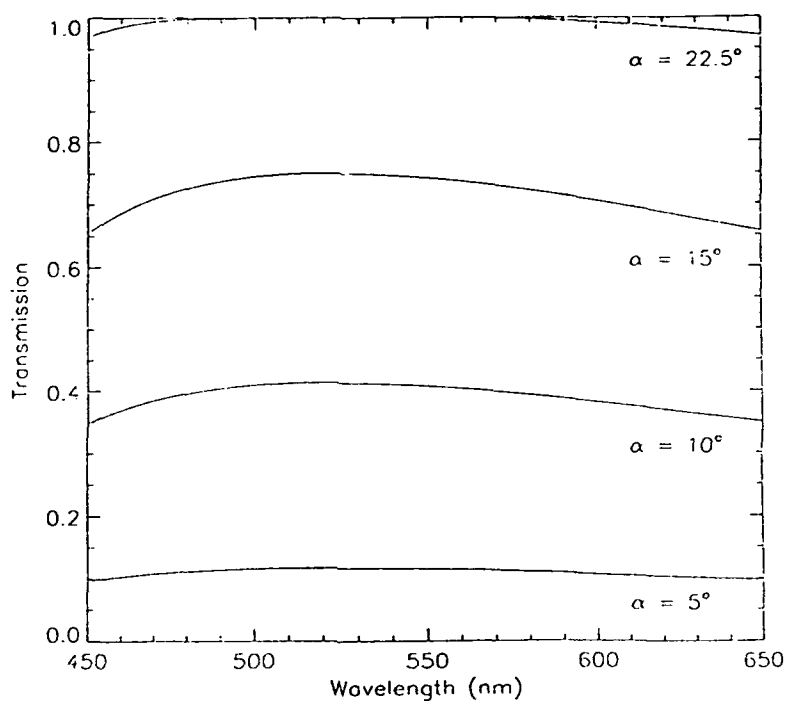


Figure 1. Theoretical transmission spectrum for the dual-SmA* analog intensity modulator, parameterized by the molecular tilt angle, α .

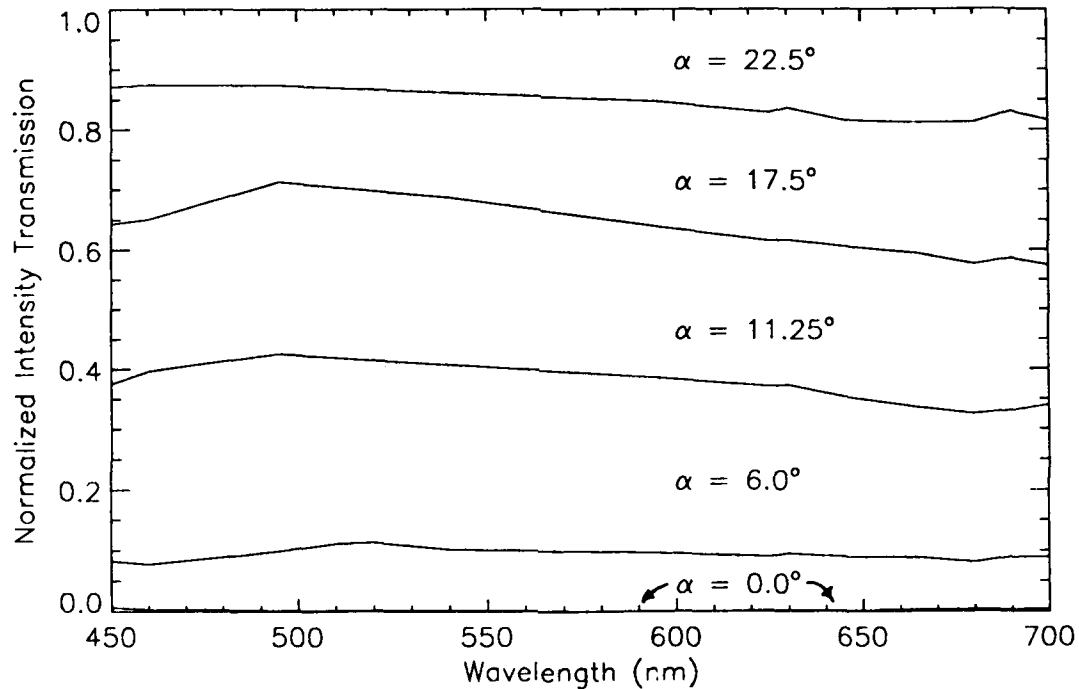


Figure 2. Experimental transmission spectrum for the dual-SmA* analog intensity modulator, parameterized by the molecular tilt angle, α .

IV. Conclusions

A combination of two parallel aligned SmA^* liquid crystal devices has been used to implement an achromatic analog intensity modulator with a bandwidth of 250 nm. Experimental results compare well to theoretical predictions. The combination of two electroclinic devices demonstrate an improvement in bandwidth and contrast ratio over those characteristics obtainable with a single device.

A simpler implementation can be achieved employing a single electroclinic cell, a passive achromatic quarter wave plate, and mirror. This configuration shows promise for implementation as a grey level spatial light modulator. The quarter wave retarder serves to rotate the polarization 90 degrees on reflection, so that the reflected optical field will see the active half wave plate with its optic axis crossed to that orientation seen by the incident light. Results for the reflection mode device will be presented at the conference.

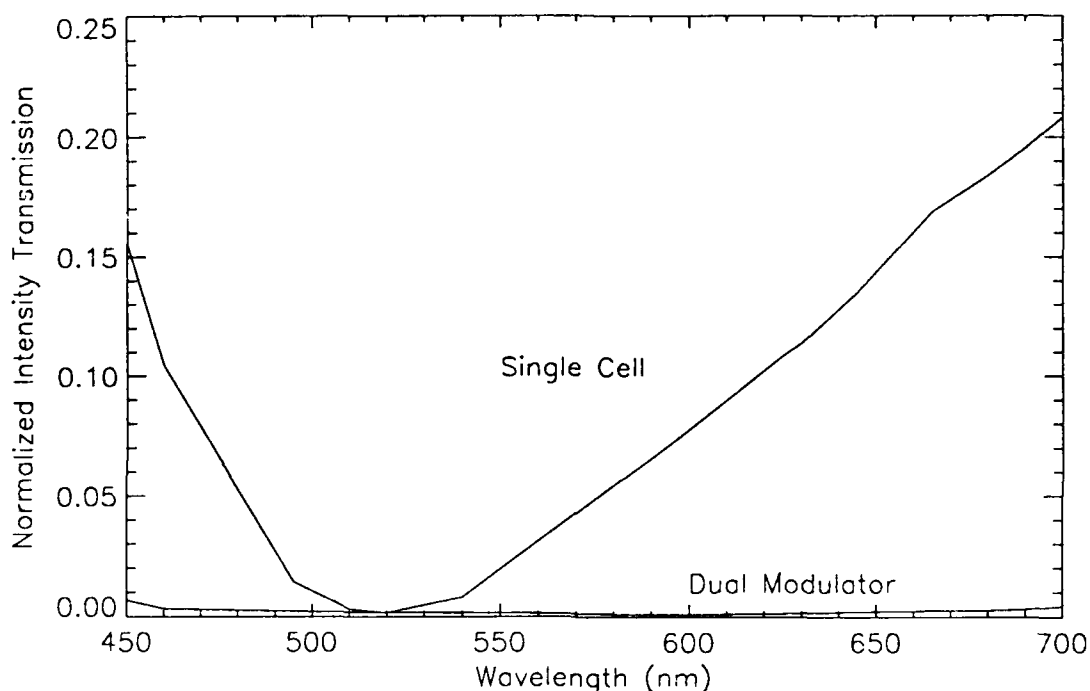


Figure 3. Comparison of the null transmission of the achromatic intensity modulator and a single electroclinic device.

References

1. Ch. Bahr and G. Heppke, *Liquid Crystals*, 2, 825, (1987).
2. K. Bennett and R. L. Byer, *Applied Optics*, 19, 2408, (1980).
3. G. Anderson, I. Dahl, L. Komitov, S. Lagerwall, K. Skarp, and B. Stebler, *Journal of Applied Physics*, 66, 4983, (1989).
4. The British Drug House mixture BDH 764E is available from Merck Ltd., WestQuay Road, Poole, BH15 1Hx, England.
5. I. Filinski, and T. Skettrup, *Applied Optics*, 28, 1720, (1989).

Real time displacement measurement with FLC-SLM
(Ferroelectric Liquid Crystal Spatial Light Modulator)
by correlation of speckle patterns

Yuji Kobayashi, Tamiki Takemori, Naohisa Mukohzaka, Narihiro Yoshida,
Hamamatsu Photonics K.K., 5000, Hirakuchi, Hamakita-shi, Shizuoka, 434, Japan, +81-53-586-7111

Seiji Fukushima
NTT Opto-electronics Labs., 3-1, Morinosato, Wakamiya, Atsugi-shi, Kanagawa, 243-01, Japan,
+81-462-40-3244

1. Introduction

Specklephotography¹⁾²⁾ is effective in the analysis of two-dimensional displacement information. The analysis of the data often requires measurement of the spacing and orientation from numerous fringe patterns³⁾. This is not a real time measurement and therefore appears to be rather time consuming and inefficient.

In order to carry out the displacement measurement for specklegrams on real time basis, we propose a novel approach using the FLC-SLM (Ferroelectric Liquid Crystal Spatial Light Modulator) and the PSD (Position Sensitive Detector) as the key devices based on Joint transform correlation (JTC)⁴⁾⁵⁾.

Utilization of FLC-SLM makes real time Joint transform processing possible. Utilization of PSD enables one to obtain the autocorrelation signals from specklegrams in real time by eliminating scanning procedures. A supporting electronic computing system is employed to adjust the interval of the double-exposure (write-in) time for the FLC-SLM (see Fig. 4) based on the feedback signal from the PSD (see Fig. 3) in order to cope with the problem of space-bandwidth products in the real devices utilized in the experiment. Such storage-time-interval adjustability through feedback scheme, make it possible to extend the measurable range and obtain more accurate position information for the displacements in specklegrams even with some performance limitations in practical devices.

2. FLC-SLM

A structure of the FLC-SLM⁶⁾ is shown in Fig. 1. A 3 μm -thick photoconductive layer of undoped hydrogenated amorphous silicon is deposited on one of the glass plates. The reasonably ohmic or non rectifying property of the photoconductive layer enables the device to be operated with either polarity of driving voltages for a desired contrast (say, positive) and its reversal (negative). Examples of this contrast reversibility are shown in Fig. 2 for both real time (framing) and storage mode. A high reflectivity dielectric mirror is coated on the amorphous silicon layer to isolate the

write-in and readout beams. In particular, when both wavelengths are the same, the isolating for write-in and readout beams also enable the SLM for high optical amplification capability and cascability of SLMs. A chiral smectic C ferroelectric liquid crystal layer of 1 μm is sandwiched between the dielectric mirror and the other conductive and transparent electrode which is coated on a glass plate (see Fig. 1). This liquid crystal layer which serves as an electro-optic modulating medium operates in bistable mode due to surface stabilized condition⁷⁾. The performance characteristics of the FLC-SLM is shown in Table 1.

To perform real time measurement a reference speckle pattern is first written and stored in an SLM. Meanwhile a displaced speckle pattern is superimposed on the stored reference speckle pattern. In the specklephotography the resolvable limit of the displacement is determined by the average speckle size. Generally the speckle pattern has a very high contrast and the temporal resolution is usually limited by the response time of the SLM. These requirements necessitate an SLM with high spatial and temporal resolutions, and binary memory function. The performance characteristics of FLC-SLM as shown in Table 1 appears to be suitable for this application.

3. Experiments

Figure 3 shows the schematic diagram of the experimental setup. The images of diffraction fields from the ground glass resulting from speckle patterns are superimposed in FLC-SLM1 by double-write-in process. The distance from that ground glass to FLC-SLM1 was 170 mm. The ground glass moved within 270 mm distance under constraints of three parameters, namely, acceleration, a , constant velocity, v , and deceleration, $a'=-a$, through the control of a microcomputer. The superimposed speckle pattern written in the FLC-SLM1 is read out and is further written in FLC-SLM2 after Fourier transformation by lens L1. The pattern recorded in the FLC-SLM2 is Fourier-transformed again by lens L2. The resulting first order diffraction pattern is detected by PS-PMT (Position Sensitive Photomultiplier Tube) as a position detective device.

Its light-detecting area was confined to an aperture of 8×1 mm to exclude the zeroth order diffraction pattern. The distance from the zeroth order spot to the first order spot represents the amount of displacement for the moving object and the line connecting of the first order spot and the zeroth order spot shows the direction of the movement of the object.

The timing charts corresponding to the driving circuits for FLC-SLM1 and FLC-SLM2, and that for extraction of signals from PS-PMT are shown in Fig.4. The first speckle pattern (reference) is written on FLC-SLM1 during the period of W1 and the second speckle pattern displaced relative to the reference pattern is written during the period of W2, where W1 and W2 were set at $150 \mu\text{s}$. The interval for the double-writing-in process T_i were chosen to be either 1.0 or 0.5 ms depending upon experimental conditions, to be explained later. The Joint transform correlation signals were extracted every 5 ms from PS-PMT in the case of $T_i=1.0$ ms.

4. Results and discussion

Figures 5(a)-(c) and (e) show the position signal outputs of the PS-PMT. The dots in Fig. 5 are the experimental results whereas the solid lines show the profile and trends of experimental results.

Fig. 5(a) shows the result for four velocities of $v=200, 300, 400$, and 500 mm/s. The ordinate represents the relative position of first order spot from PS-PMT, and the abscissa shows the time corresponding to the position signal output and the time elapsed. The output signals from PS-PMT represent the displacements of the object for 1.0 ms of double-write-in time and they are linearly proportional to the velocities as shown in Fig. 5(b).

Figure 5(c) shows the result for the case of four decelerations, $a=490, 980, 1960$, and 2940 mm/s². The slopes of the curves in the Fig. 5(c) are proportional to the decelerations as shown in Fig. 5(d). In Fig. 5(d), the ordinate represents slope which is the time rate of change of position signal output and the abscissa represents the absolute value of deceleration.

As is shown, the position signal outputs had a good linearities for both acceleration and the deceleration just as that for the constant velocity.

When the object for specklegram is moving fast enough, the displacement for the specklegram becomes larger. Meanwhile both the reference and the displaced speckle patterns will respectively spread out and appear in different shapes. That in turn will degrade the intensity of correlation peak and hence reduce the accuracy of position information.

Under this situation it is very difficult for the currently available devices, such as SLM and PSD,

to meet these requirements for real time processing. To circumvent these difficulties, we have proposed a technique to control the interval of double-write-in time for the FLC-SLM based on the output position signals of PSD. The feedback control for the interval of double-write-in time also serves to position the first order spot in the central part of the readout aperture for the PSD. The centralization of the first order spot not only contribute to minimize the position information errors but also enables one to reduce the size of PSD.

Figure 5(e) shows the experimental results of the spatial distribution of the first order spots at different time elapse for the double-write-in period. The left hand side of the figure shows the spot distribution without feedback control. As can be seen, when the movement of the object reaches at the relatively high velocity of 900 mm/s after acceleration at 980 mm/s², the spot distribution for time elapse become irregular and meaningless. These irregular and meaningless data for spot distribution can be converted into a more meaningful and useful ones by using feedback control and the results are shown in the right hand side of Fig. 5(e).

5. Summary

A new technique for real time optical displacement measurement based on the specklephotography using FLC-SLMs and PS-PMT has been proposed. An experimental system was constructed to demonstrate the proposed system.

By using this system, the displacements of specklegrams of a moving object occurring in less than duration of 1.0 ms, namely, the interval of double-write-in time, can be measured periodically, with period of several milliseconds (5 ms and 4.5 ms in the experiment).

It is experimentally shown that the range of measurement for the specklegram displacement can be improved by adjusting the interval of double-write-in time based on feedback technique (see Fig. 5(e)).

References

- 1) E.Archbold and A.E.Ennos, *Opt. Acta.* 19, 253 (1972)
- 2) T.Asakura and N.Takai, *Appl. Phys.* 25, 179 (1981)
- 3) D.W.Robinson, *Appl. Opt.* 22, 2169 (1983)
- 4) C.S.Weaver and J.W.Goodman, *Appl. Opt.* 5, 1248 (1966)
- 5) A.Ogawara, H.Sakai, and J.Ohtsubo, *Opt. Comm.* 78, 213 (1990)
- 6) S.Fukushima, T.Kurokawa, S.Matsuo, and H.Kozawaguchi, *Opt. Lett.* 15, 285 (1990)
- 7) N.A.Clark and S.G.Lagerwall, *Appl. Phys. Lett.* 36, 899 (1980)

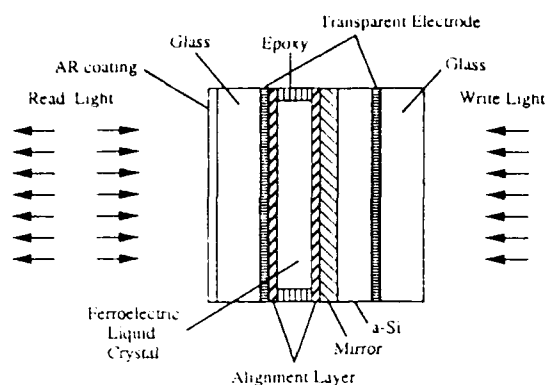
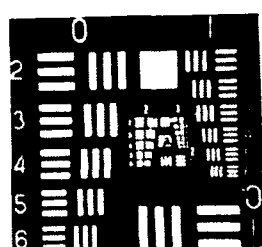


Fig.1 Structure of FLC-SLM.

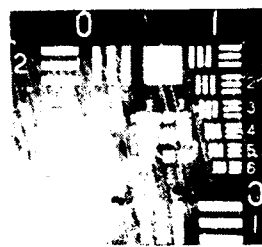
Active Area	20 X 20 [mm ²]
Response Time	$T_r=60, T_d=41$ [μ sec]
Resolution*	57 [lp/mm]
Sensitivity	100 [μ W/cm ²]
Contrast Ratio	100:1
Memory	Binary
Readout Wavelength	633 [nm]
Image Polarity	Bipolar

* Diffraction efficiency for the half intensity to the highest value.

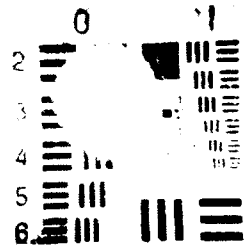
Table 1 Performance characteristics of FLC-SLM.



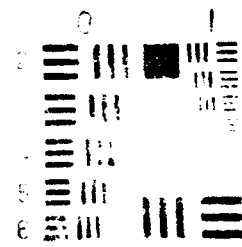
(a) Positive image in real time mode.



(b) Positive image in storage mode.



(c) Contrast reversed (negative) image in real time mode.



(d) Contrast reversed (negative) image in storage mode.

Fig.2 Readout images of FLC-SLM.

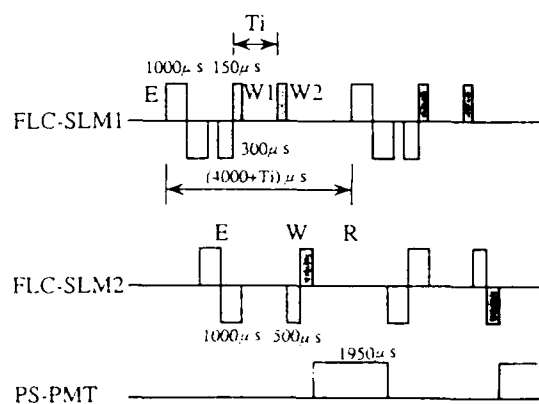
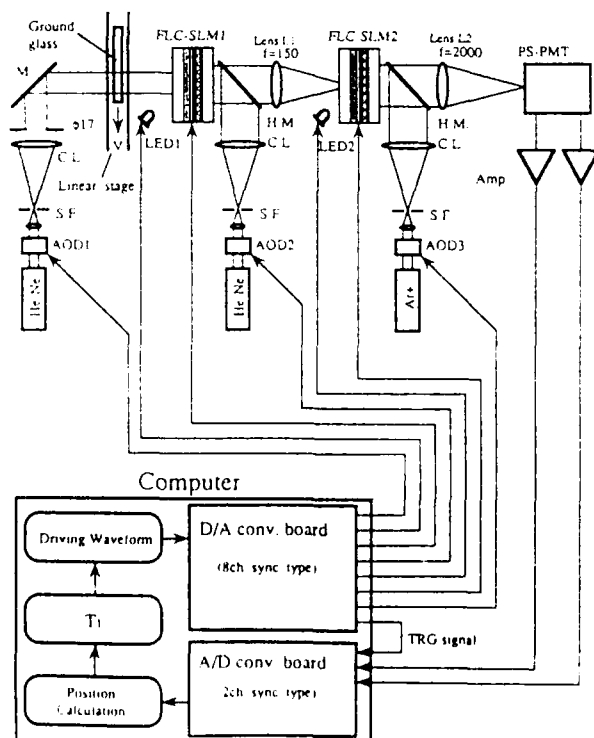
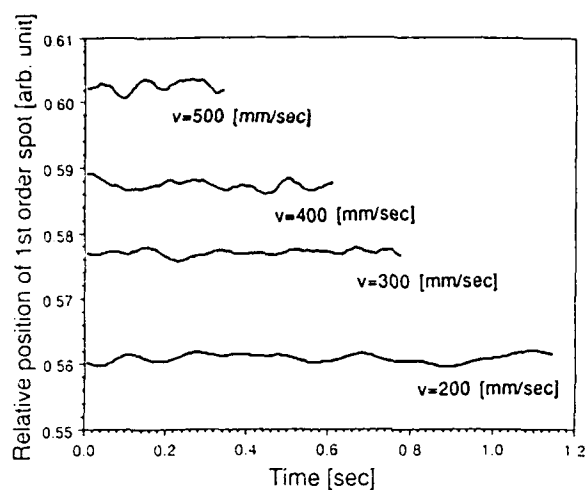
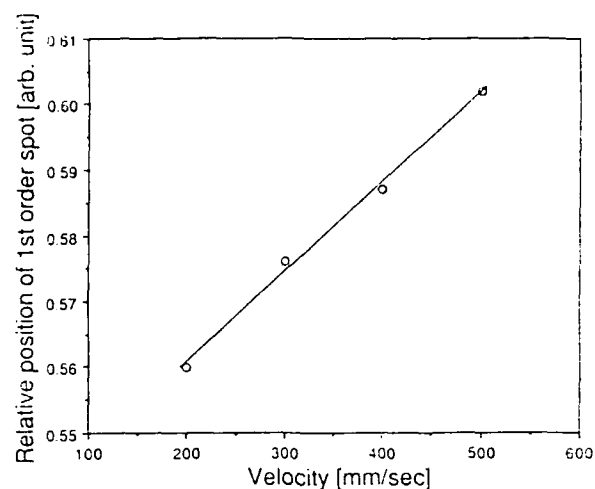


Fig. 4 Timing chart.

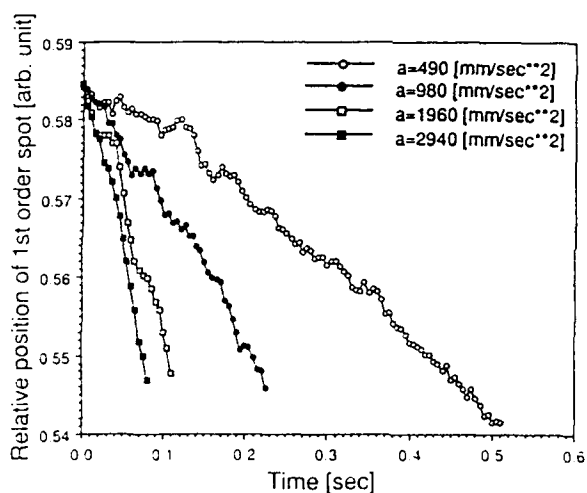
Fig. 3 Schematic diagram of the experimental setup.



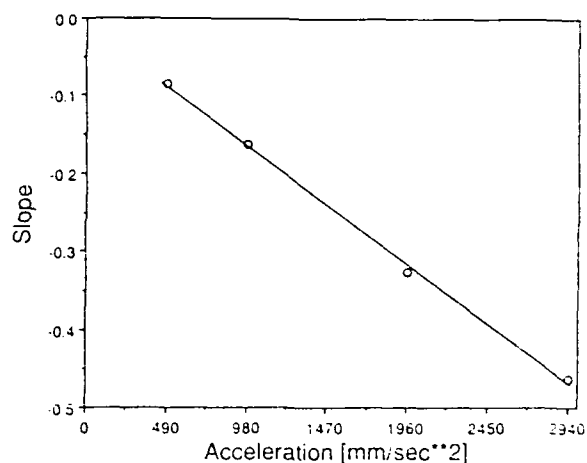
(a)



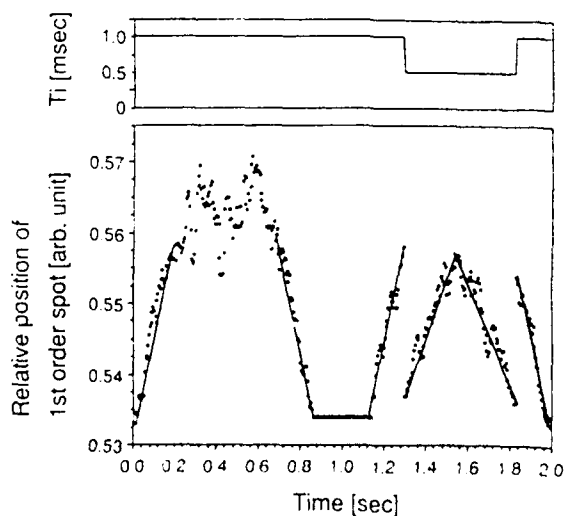
(b)



(c)



(d)



(e)

Fig. 5 Position signal output.

(a) Position signal outputs when $v=200, 300, 400$, and 500 mm/s.

(b) Position signal outputs corresponding to velocities.

(c) Position signal outputs when $a=490, 980, 1960$, and 2940 mm/s².

(d) Slopes of curves in Fig. 5(c) corresponding to accelerations.

(e) Position signal outputs with and without feedback control.

Monday, March 15, 1993

SLM Technologies: 2

SMC 1:40pm-3:00pm
Grand Ballroom West

Cardinal Warde, *Presider*
Optron Systems, Inc.

FABRICATION AND SWITCHING SENSITIVITY OF THE NEW MAGNETO OPTIC SPATIAL LIGHT MODULATOR

William E. Ross
Litton Data Systems
8000 Woodley Avenue
Van Nuys, CA 91409-7601
Tel. (818) 902-4136, Fax. (818) 901-2850

David N. Lambeth
Carnegie Mellon University
Dept. of Electrical and Computer Engineering
Pittsburgh, PA 15213-3890
Tel. (412) 268-3674, Fax. (412) 268-6978

A new reflected mode magneto-optic spatial light modulator (R-MOSLM) has been developed for production of Miniature Ruggedized Optical Correlators. A comparison with the transmission MOSLM is shown in Table 1. The smaller pixels and improved switching sensitivity permit an order of magnitude reduction in optical path length and increase in frame rate. Here we describe the progress that has been made in the design of the R-MOSLM, issues concerning its fabrication, and comparison of finite element analysis field modeling to experimentally determined current requirements to drive individual lines.

Table 1. Reflected MOSLM vs Old Transmission MOSLM

	Transmission T-MOSLM	Reflected R-MOSLM
Material	LLC	LLC
Resolution	128 x 128	128 x 128
Pixel Size	57 micron	22 micron
Pixel Spacing	76 micron	24 micron
Window Efficiency	54%	65%
Film Thickness	6 micron	2.5 micron
Y Drive Current	350 ma	70 ma
X Drive Current	450 ma	150 ma
Pulse Width	30 ns	10 ns
Power	1W @ 1 KHz	1W @ 10 KHz

Figure 1 is a schematic representation of the structure of a single pixel of the 128x128 R-MOSLM array. In operation, each individual pixel would be either magnetized up or down. As a polarized light ray enters from the non-magnetic substrate, transverses the magneto-optic film, reflects from the conductors and eventually again exits from the substrate, its polarization is rotated either clockwise or counter-clockwise depending upon the orientation of the magnetization direction of the pixel. This rotation then provides the correlator imaging state of the pixel. It is worth noting that it would be ideal if the film thickness were as large as possible in order to maximize the polarization rotation. However, the optical absorption of the film places this in direct conflict with keeping maximum light throughput to the correlator photodetectors. Likewise, each pixel must be magnetically separated from its neighboring pixels so as to prevent pixel-to-pixel cross talk.

This pixel separation is currently achieved by physically removing the film between the pixels using ion beam milling. The minimum spacing between the pixel mesas is directly related to the magneto-optic (MO) film thickness. From an imaging standpoint the smaller these mesas gaps are made compared to the mesa width the higher the optical efficiency. Currently, film thicknesses of 2.5 to 3.0 microns are being investigated. Figure 2 is a cross-sectional scanning electron micrograph (SEM) of a cleaved mesa gap. This clearly shows a high aspect ratio with a depth of approximately 3 microns and a mesa gap at the top surface of approximately 1.8 microns.

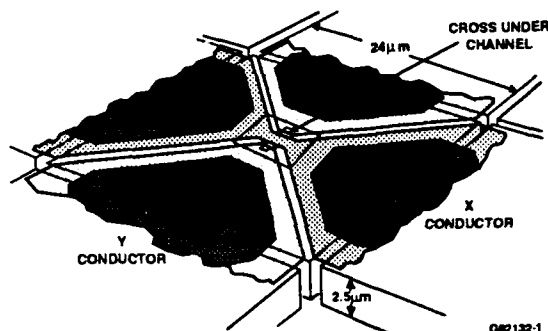


Figure 1. Ideal Pixel Representation



Figure 2. Mesa Gap

Figure 1 also demonstrates the two conductor concept of providing a localized, concentrated, magnetic field where the conductors cross for reversing the magnetization of the pixels. As shown the x and y conductor drive lines lie flat on the surface of the mesa forming the optical mirror. At the center of the mesa the y conductors cross under the x conductor and are physically separated by a 0.2 micron thick electrical SiO_2 insulator. At this central location the physical width of both the x and y conductors are approximately 1.6 microns. These values were chosen thick enough to provide good reflectivity and low drive impedance, while thin enough to maintain close proximity to MO film. Figure 3 is a cross-sectional SEM of a cleaved pixel across one of the cross under conductors. While the conductor does not appear to have a square cross-section, it is clear from the photo that the conductor is very close to being planar with the surface of the magnetic film. The magnetic field perpendicular to the film surface produced at the edge of this conductor would be slightly below the surface of the film.

The cross under conductor and the mirror-conductors are deposited prior to the mesa gap formation, hence a third metal layer is required to reconnect the x and y conductors and bridge across the mesa gaps. This fabrication sequence was necessitated by the inability to perform high resolution photo lithography at the mesa corners when the mesa gaps were cut prior to the conductor deposition. With the steep edges and desired high aspect ratio of the mesa gaps, good conductor step coverage with the reconnect metal is difficult, hence the mesa gaps are partially planarized using a non-magnetic photo-polymer prior to the reconnect metal deposition. The reconnect metal across the mesa gaps along with the corner structure of four pixels is shown in Figure 4. Likewise, Figure 5 shows the center of a pixel. Here, all three metal layers plus the insulator are clearly visible.

The magnetic fields in the vicinity of the crossing conductors have been modeled using three-dimensional finite element analysis programs by Ansoft Corporation. In addition, approximations to the structure have been modeled using only two dimensions. Figure 6 shows the field perpendicular (Hz) to the mesa surface produced by a conductor of rectangular cross-section (0.2 micron thickness by 1.6 micron width) carrying 100 MA current. The three line plots are taken starting at the edge of the conductor and at a height that would go through the center of the conductor ($z = 0$), at the bottom surface of the conductor ($z = -0.1$) and at 0.2

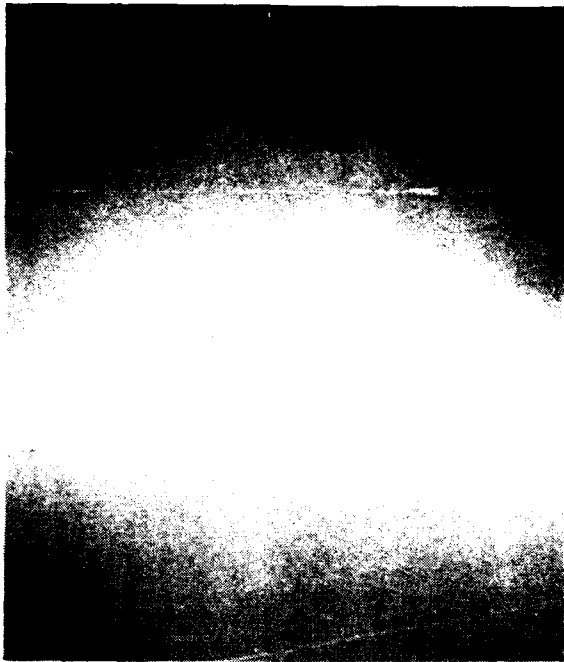


Figure 3. Channel Cross-Section

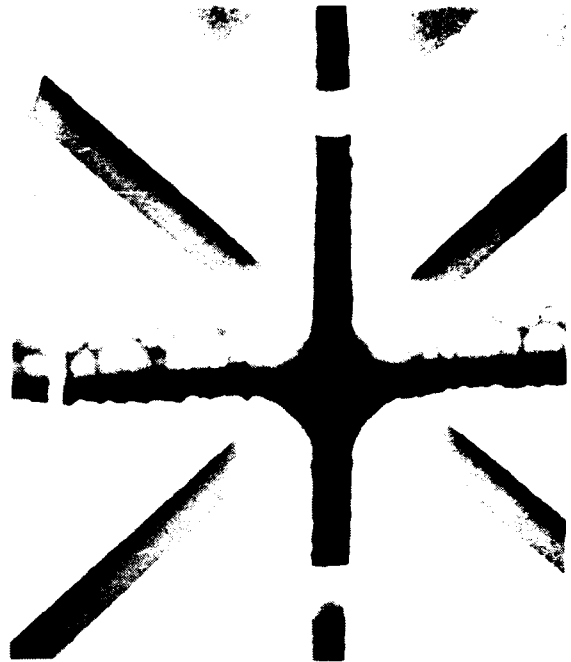


Figure 4. Pixel Corners

microns below the conductor ($z = -0.3$). Two observations should be made. First, the useful perpendicular field component (H_z) falls off very rapidly as a function of distance away from the edge of the conductor. At only 0.4 microns the magnitude is down by almost a factor of 2. Secondly, the peak at the center edge of the conductor is almost a factor of 2 times higher than the peak below the conductor. While not shown, a similar conductor of 0.4 micron thickness was modeled. The maximum H_z field produced at 0.1 micron below the bottom of this conductor was almost a factor of 2 down from the centerline maximum of the 0.2 micron thickness conductor. Assuming that the magnetic switching occurs just below the surface of the magnetic film, this clearly demonstrates the value of burying the conductor into the magnetic film to provide maximum switching sensitivity.

A test structure device was fabricated in which a single conductor was placed on several pixels. On some of these pixels the conductor was equivalent to the micro conductor and sat right on the surface of the magnetic film. On the rest of these pixels the conductor was buried into the magnetic film as a cross under structure. The use of a single drive line allows accurate comparisons of the switching sensitivity of the two structures. The drive current necessary to switch the pixel was found to be a factor of 2 greater for the conductor on top of the pixel as opposed to the buried conductor.

Figure 7 demonstrates a switched line of the 128x128 R-MOSLM array. Here a 30 nanosecond, 140 MA pulse was used to nucleate and demagnetize a row of pixels. Note the pixels are demagnetized, approximately half on and half off. Figure 7B shows a row of pixels which was saturated with a bias field in conjunction with the driveline pulse.

We have achieved a factor of 4 improvement in drive current reduction by use of narrower drive lines, and burying the channel conductor in the MO film. Further improvement is anticipated as we optimize the structure and modify the MO film magnetic characteristics.

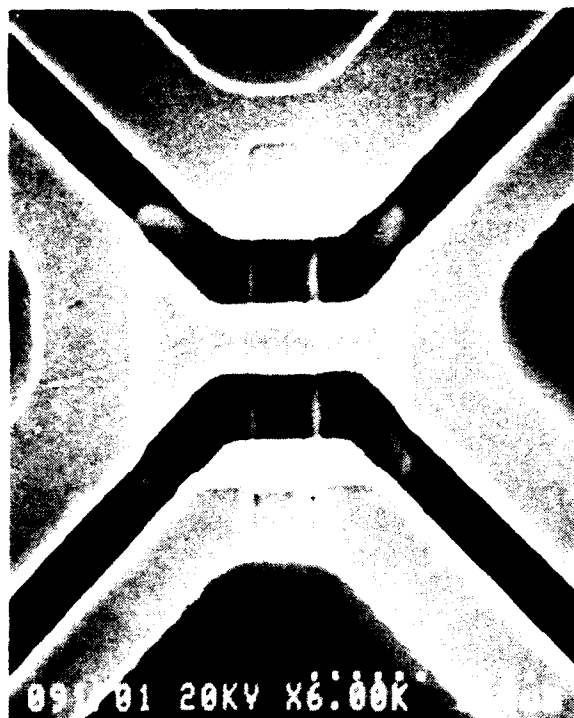


Figure 5. Channel Conductor Cross-Under at Pixel Center with SiO_2 Insulator Pad

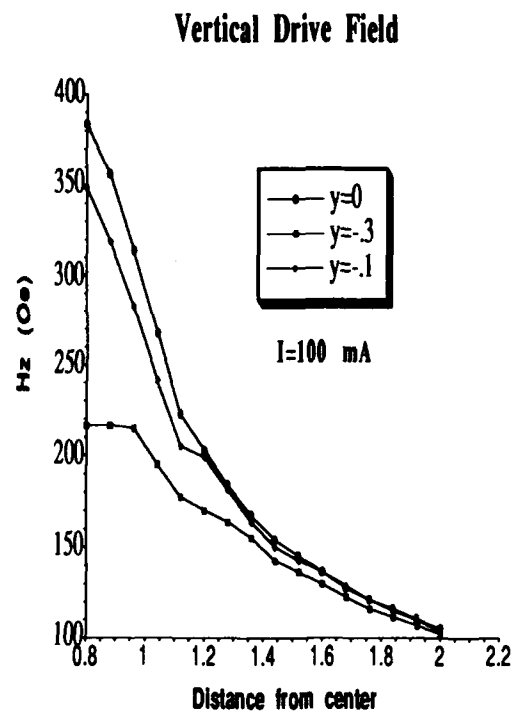
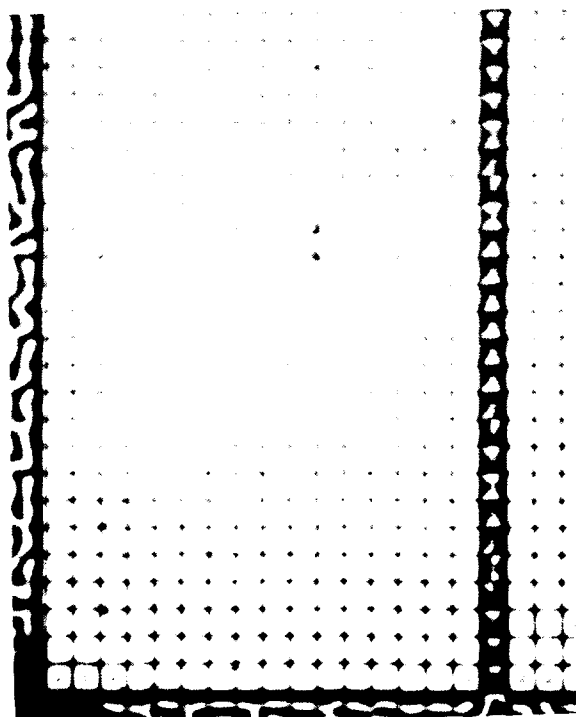
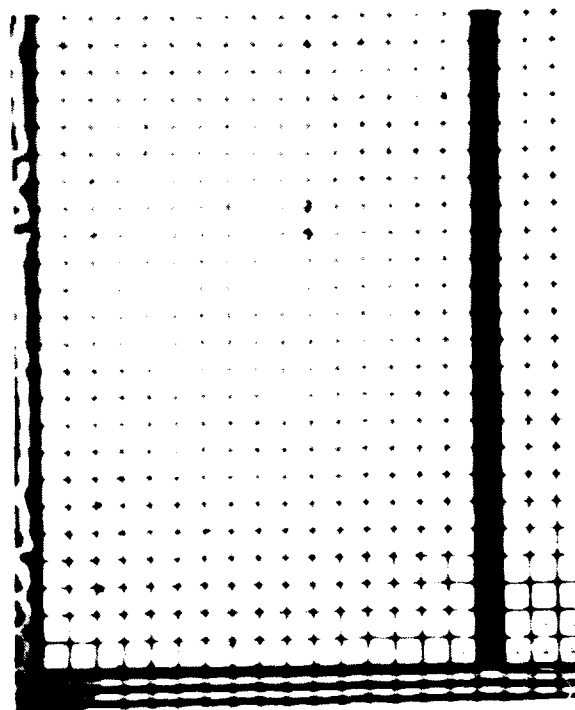


Figure 6. Plot of H_z Carrying 100 MA Current



A. Demagnetized



B. Magnetized

Figure 7. Switched Line of the 128x128 R-MOSLM Array

A New Type of Spatial Light Modulator with Binary Phase Gratings

L. Buydens and P. Demeester

University of Gent - IMEC,
Laboratory of Electromagnetism and Acoustics
Sint-Pietersnieuwstraat 41, B-9000, Gent, Belgium
Tel. : + 32 91 64 33 16

1. Introduction

During the last decade a lot of designs have been proposed for the fabrication in different material systems of optical free space modulators for use in optical processing systems^{1,2}. A large number of these use some kind of Fabry-Perot cavity. A serious drawback of this type of devices is the temperature dependence and the difficulty to make large arrays because stringent requirements are imposed on the thickness of the different layers in the cavity³. Another disadvantage is that generally these devices are only useful in reflection. Transmission devices reported in literature often have a too low contrast ratio and/or a too high insertion loss for use in a real optical system.

Here we want to propose a new structure which combines materials with a variable absorption with a binary phase grating to obtain modulators with high contrast ratios. The structure can be configured both for a reflection and a transmission type of device.

2. Basic principle

In figure 1 a general structure of the modulator is shown, consisting of a binary phase grating, made by selectively etching of material, and underneath it a layer of material with variable absorption. In this layer different regions must be defined which all can be addressed separately to change the absorption. The variable regions are all located underneath areas of the binary phase grating with the same phase. Similar to an asymmetric Fabry-Perot modulator, modulation is based on the total destructive interference between two beams with π phase difference and the variation of the amplitude of one of those beams by varying the absorption in the active layer.

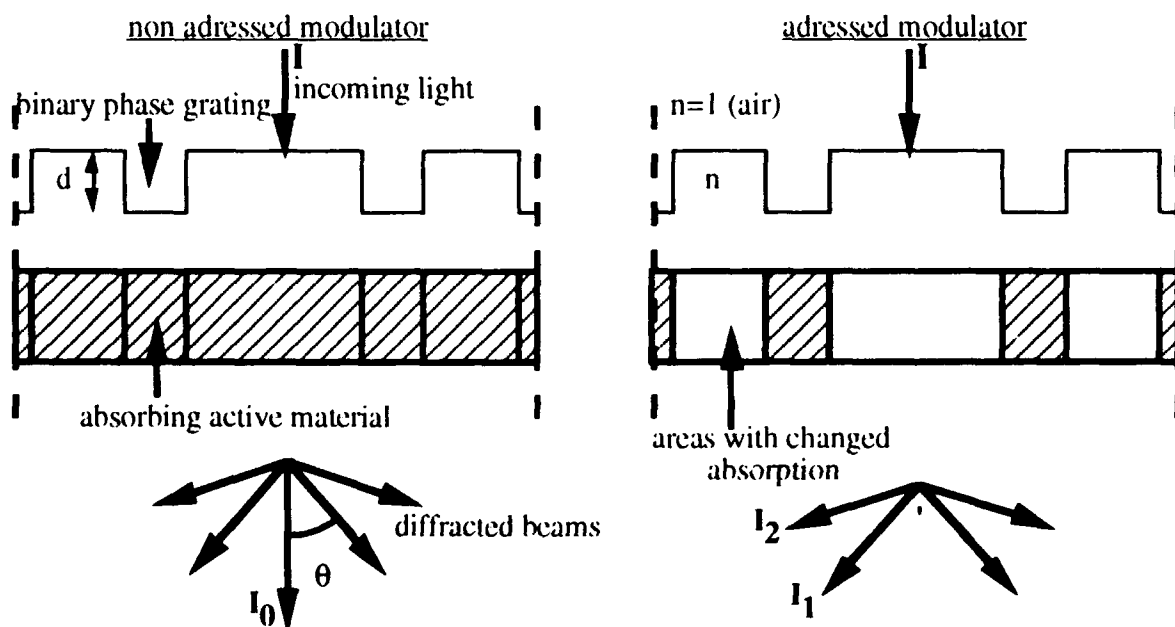


figure 1 : principle of the high contrast active binary phase grating modulator.

The phase difference between the two beams is obtained by the difference in light path between the two beams in the binary phase grating on top of the absorbing material. In this way the path difference can be kept to a minimum and still the needed phase difference is obtained. This minimal light path difference makes the device less sensitive to fabrication and temperature variations compared to other devices like an AFPM which also uses a phase difference to obtain a high contrast ratio but with a much longer optical path difference between the two interfering beams. Total extinction of the zero order diffraction beam of the grating is obtained when both interfering beams have the same amplitude. If the absorption for one of the phases is changed, the amplitude of both beams will no longer be the same and the zero order diffraction beam will no longer be zero. As one of the states of the modulator has a theoretically zero intensity, the contrast ratio of the modulator will be higher than the value obtained with the absorbing material on its own. In this design no mirrors are used, so the device can be used as a transmission modulator. However, one can also obtain a reflection modulator by incorporating a mirror underneath the active layer

3. Modulation characteristics

Using Fraunhofer diffraction theory⁴, we will now examine the modulation characteristics of these active binary phase gratings. The zero order diffraction peak of the active grating is influenced by several different factors which have to be controlled. In a general case the intensity of the zero order diffraction peak is given by formula 1. In this formula, λ is the wavelength, d the height difference between the two surfaces of the binary phase grating, n the refractive index of the grating material, S_0 and S_π the areas of these two surfaces with phase 0 and π respectively, and a_0 and a_π the absorption in the active layer underneath each of these surfaces.

$$\left| \sqrt{1-a_0} S_0 e^{\frac{2\pi i d}{\lambda}} + \sqrt{1-a_\pi} S_\pi e^{\frac{2\pi i d}{\lambda}} \right|^2 \quad (1)$$

The amplitudes of both interfering beams are equal when $\sqrt{1-a_0} S_0 = \sqrt{1-a_\pi} S_\pi$. In this case, the intensity of the zero order peak can become zero if both beams have a phase difference of π . If no absorption is present in both phase region of the active grating, both regions have to have the same area to obtain total destructive interference and the previous formula becomes :

$$\frac{\left| e^{\frac{2\pi i d}{\lambda}} + e^{\frac{2\pi i d}{\lambda}} \right|^2}{4} \quad (2)$$

The height difference d between the two levels of the binary phase grating needed to obtain a phase difference π can be easily deduced from formula 2 and is given in formula 3.

$$d_m = \frac{(2m + 1) \lambda}{2(n-1)} \quad m = 0, 1, 2, \dots \quad (3)$$

During the fabrication of the grating some error on the value of this height can be introduced. This causes the transmission at maximum destructive interference no longer to be zero as both beams are now slightly out of phase. Using formula 2, figure 2 shows the influence of this error on the peak intensity of the zero order peak at the demanded wavelength of $1 \mu\text{m}$ in areas of $\pm 5\%$ around different central d_m values. As one can see the variation of the intensity is still relatively limited for $m = 0$. If the error is only a few percent, a restriction which can be met by current fabrication technologies. One also sees that this is no longer true for higher m values. Small deviations from zero of this intensity cause large changes in the contrast ratio of the modulator. As a device as the AFPM has to use a cavity with a high m value to be able to incorporate the absorbing material, such devices are very sensitive to fabrication variations, a fact which is also observed in practice. From this one can also conclude that the grating

modulator will be much less sensitive to temperature variations. These variations cause a change in refractive index of the material Δn and a thickness variation of the layers in the cavity Δd , resulting in a variation equal to $2\pi(\Delta n d + n \Delta d)/\lambda$ of the phase difference between the two beams.

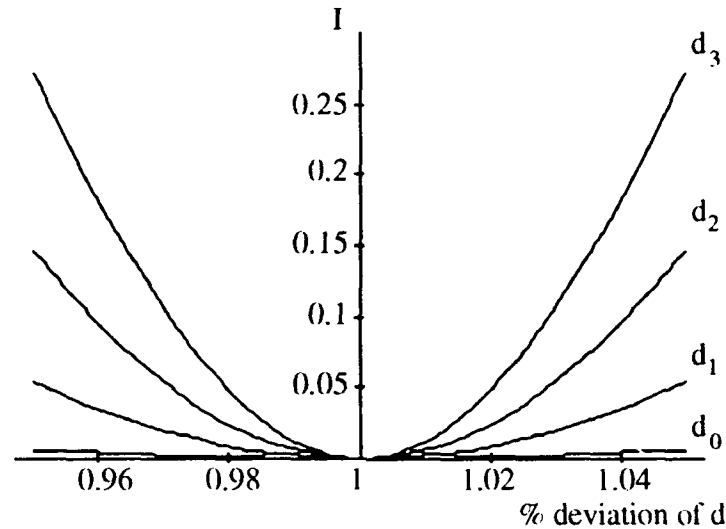


figure 2 : influence of the error on the height d on the intensity of the modulation minimum for different d_m values

In figure 3 the zero order diffraction intensity is shown as a function of the wavelength around a design wavelength of $1 \mu\text{m}$ for different values of d_m . As one can see the intensity of the zero order beams does not increase very fast for the lowest d value. This is an indication that it would be possible to obtain a large contrast ratio over a wide wavelength region with the active grating modulator. For this, one has to use a material with variable absorption which is not very sensitive to the wavelength. For higher d values however, the intensity increases much faster and a high contrast ratio is only obtained in a narrow wavelength region around the central wavelength.

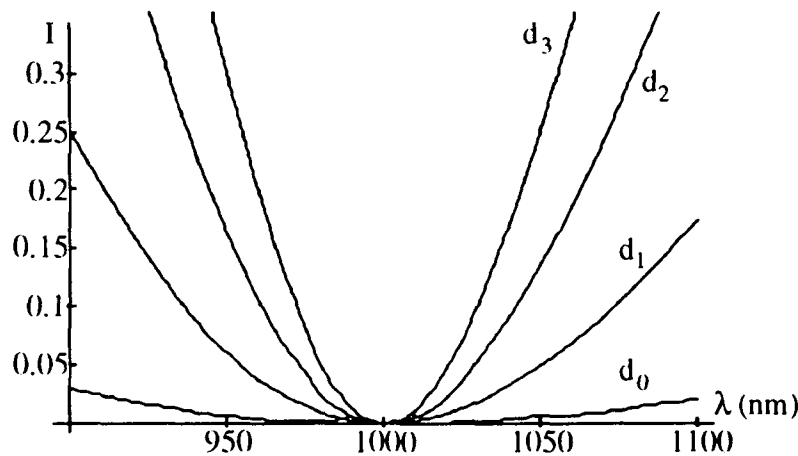


figure 3 : intensity of the zero order diffraction peak as a function of the wavelength for different d_m values;

The active grating modulator can be operated in two different modes. In the first one, the zero order diffraction peak is zero when there is no external influence on the device and the absorbing layer is uniform. So, in this case we obtain a normally off device. For the second mode of operation however, the zero order diffraction peak is zero only when an external influence is applied on the device and the absorption is no longer uniform underneath the phase grating. When the external influence is removed the absorption is uniform again, the two sets

of beams are no longer in equilibrium and the intensity of the zero order diffraction will no longer be zero. So, in this case a normally on device is created. Using simple diffraction theory it is possible to calculate the intensity of the diffraction peaks. In figure 4 the maximal intensity of the zero order peak is shown as a function of the maximal available absorption for both cases. As one can see the intensity is low for both types of modulators if the absorption variation is limited. An attractive device with a low insertion loss will only be obtained when large absorption variations (>0.8) are used. As the thickness of the absorbing layer does not interfere with the action of the grating, a large absorption variation can be obtained by using a thick absorbing layer underneath the binary grating. The absorption is also increased for a reflection modulator when one introduces a mirror underneath the absorption layer. The total light path through the absorbing layer will be doubled in this case.

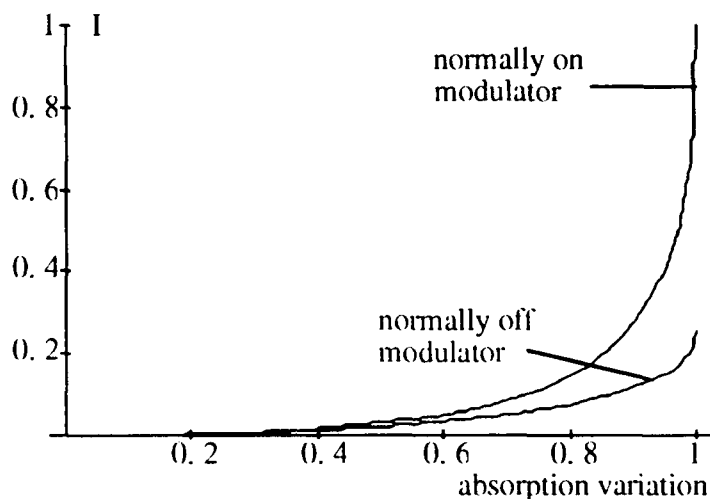


figure 4 : maximum intensity of the zero order diffraction peak as a function of the maximum absorption for the normally on and the normally off modulator.

4. Conclusions

Using simple diffraction theory we have shown theoretically that by integrating a binary phase grating and material with a variable absorption it is possible to obtain a modulation of the zero order diffraction peak with a high contrast ratio. It is shown theoretically that the device should be less sensitive to fabrication variations and temperature fluctuations compared to fabry-perot cavity modulators. To obtain a low insertion loss, active layers providing a large change in absorption are needed. The design can be used for a reflection or a transmission device.

5. References

1. M. Whitehead, and G. Parry, 'high-contrast reflection modulation at normal incidence in asymmetric multiple quantum well Fabry-Perot structure', *Electron. Lett.* 25 9 (1989) 566-567;
2. L. Buydens, P. Demeester, and P. Van Daele, 'asymmetric Fabry-Perot modulators with an InGaAs/AlGaAs active region', *Opt. and Quant. Electr.* 24 2 (1992) S167-S175;
3. R. H. Yan and L. A. Coldren, 'effect of temperature on the operating characteristics of asymmetric Fabry-Perot reflection modulators', *Appl. Phys. Lett.* 57 3 (1990) 267-269
4. M. Born and E. Wolf, 'principles of optics', sixth edition, Chap. 8.3.3 and 8.6.1, Pergamon Press, Oxford, England (1987);

Optical Memory Elements Based on Hetero-nipi Superlattice Asymmetric Cavity Spatial Light Modulators

M.K. Hibbs-Brenner, S.D. Mukherjee, and J. Lehman
Honeywell Systems and Research Center
10701 Lyndale Avenue South, Bloomington, MN 55420
(612) 887-6466

P.P. Ruden and J.J. Liu
Dept. of Electrical Engineering and Computer Science
University of Minnesota, Minneapolis, MN 55455
(612) 624-6350

A.A. Sawchuk and W.-F. Hsu
Signal and Image Processing Institute
University of Southern California, Los Angeles, CA 90089-2564
(213) 740-4622

Hetero-nipi superlattices are semiconductor structures in which both the composition and doping are varied in the direction of epitaxial growth in a periodic fashion. Figure 1 illustrates the band structure of one version of a hetero-nipi superlattice denoted as a Type II superlattice. Undoped layers of a smaller bandgap material (GaAs) are located between n- and p- doped layers of a higher bandgap material (AlGaAs). The alternately p- and n-doped layers produce strong internal electric fields. The hetero-nipi structures have two unique characteristics valuable for application to optical memory elements: 1) large optical non-linearities due to the internal electric fields; and 2) long carrier lifetimes due to the spatial separation of the electrons and holes. In particular, the absorption of light at energies just below the bandgap can be modulated by a pump beam of light with energy at or above that of the bandedge. This occurs because the pump beam creates free charge carriers which modify the internal electric fields of the hetero-nipi superlattice, thereby changing the absorption coefficient and index of refraction of the material (see excited state of Figure 1). Due to spatial separation of injected charge carriers, the carrier lifetimes are long, which causes the change in absorption characteristics to persist for microseconds to milliseconds, which is orders of magnitude longer than in standard quantum well material. Changes in absorption coefficient of up to 9100 cm^{-1} (normalized to the GaAs quantum well layer thicknesses) or 1300 cm^{-1} (normalized to the entire hetero-nipi structure thickness) at approximately 880nm have been demonstrated in the AlGaAs/GaAs semiconductor system which is in agreement with theoretical calculations.¹ This is approximately equal to the change in absorption (9000 cm^{-1}) observed in InGaAs/GaAs hetero-nipi structures at 1000nm.²

This work evaluates the use of a hetero-nipi superlattice for an optically written and optically read short term memory element. The device structure is illustrated in Figure 2. The superlattice is incorporated into an asymmetric cavity structure³ in order to increase contrast and consists of an epitaxially grown AlGaAs/AIAs quarterwave semiconductor reflector stack below an AlGaAs/GaAs hetero-nipi superlattice consisting of four layers per period; an undoped GaAs layer, and n-AlGaAs layer, an undoped GaAs layer and a p-AlGaAs layer. The AlGaAs-air interface at the top surface of the structure forms the low reflectivity (about 30%) reflector. Although the device is optically modulated and optically read, requiring no bias voltage, electrical contacts are required to remove optically injected charge carriers to rapidly erase the memory element or to provide electrical modulation, if desired. For this purpose selective n- and p- electrical contacts are made by ion implantation into side of the mesa.

The long carrier lifetimes in the material result in the excited or reflecting state persisting after the write beam has been removed. Thus the device can be considered to be a short term memory element. In many ways it is similar to the electronic DRAM, which consists of thin film capacitors with limited memory time, requiring periodic refreshing. Similarly, the element described here can be considered as an optically charged capacitor, with a memory time of the same order of magnitude as the optically excited carrier lifetimes.

It has been identified that a fast, low power, dense optical memory is critical for the development of general purpose optical computing.⁴ In the shorter term, we also see potential for an optical memory that would speed up processor-memory communication, by allowing data transfer to take place in a two-dimensional arrays, or that could be used as a buffer memory in packet-switched optical networks.

In evaluating the material and device as an optical memory element we have measured the change in absorption coefficient which can be achieved in a hetero-nipi superlattice as a function of the structure, have demonstrated a high, optically modulated contrast ratio when the structure is placed in a Fabry-Perot cavity, and have measured the lifetime of the carriers. Electrically contacted pixels have also been fabricated, electrical modulation has been demonstrated, and lifetime as a function of pixel size has been measured.

Figure 3 contains experimental results from a hetero-nipi superlattice asymmetric cavity structure with a 99% reflective bottom mirror, a 30% reflective top mirror, and a 4.2 μ m thick superlattice cavity layer. A contrast ratio of 16 dB and insertion loss of 6.5 dB was achieved with a pump power of 12 mW. By comparing to a theoretical calculation of reflectivity vs. absorption coefficient, it can be estimated that a change in absorption coefficient of 800 cm⁻¹ was achieved. The lifetime is defined as the time after removal of the pump beam at which the initial contrast ratio has been reduced by a factor of two. The lifetime depends strongly on the particular structure and the pump power. In an attempt to characterize the overall performance of the device, we have proposed a figure of merit which takes into account the contrast ratio, insertion loss, lifetime and optical pump power required to induce the reflectivity change. This figure of merit is defined as: (contrast ratio x lifetime (usec) x reflectivity in the on state)/(switching energy (nJ)). The switching energy is calculated by multiplying the dc pump power by the carrier lifetime. Figure 4 illustrates the experimentally measured contrast ratio, lifetime and figure of merit as a function of optical pump power for an asymmetric structure with 4.2 μ m thick hetero-nipi cavity layer. The figure of merit peaked at a contrast ratio of 53:1, a lifetime of 25 usec, an 8.5 dB insertion loss and a pump power of 3.8 mW. The associated figure of merit is \sim 95 usec/nJ.

An array of electrically contacted pixels is shown in Figure 5. Reflectivity as a function of applied voltage is illustrated in Figure 6. Although the contrast ratio is low (2:1), the significant result is that nearly all of the contrast change occurs within a range of 2V applied bias. Unlike modulators based on multiple quantum well structures, the required voltage is independent of the cavity layer thickness and is mostly due to contact resistance.

This work is supported by AFOSR and DARPA under contract # F49620-90-C-0075.

References.

1. J.J. Liu and P.P. Ruden, Superlattices and Microstructures **11** (1992).
2. A.G. Larsson and J. Maserjian, Optical Engineering **31** (1992) 1576.
3. M. Whitehead and G. Parry, Electron. Lett. **25** (1989) 566.
4. A. Guha and M. Derstine, Applied Optics **29** (1990) 287.

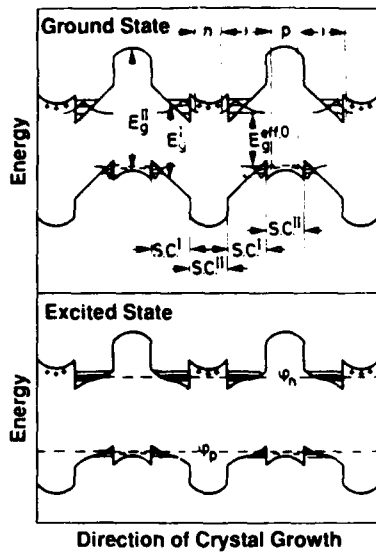


Figure 1. Schematic band structure of a Type II hetero-nipl superlattice in the ground state and after injection of carriers by optical or electrical excitation.

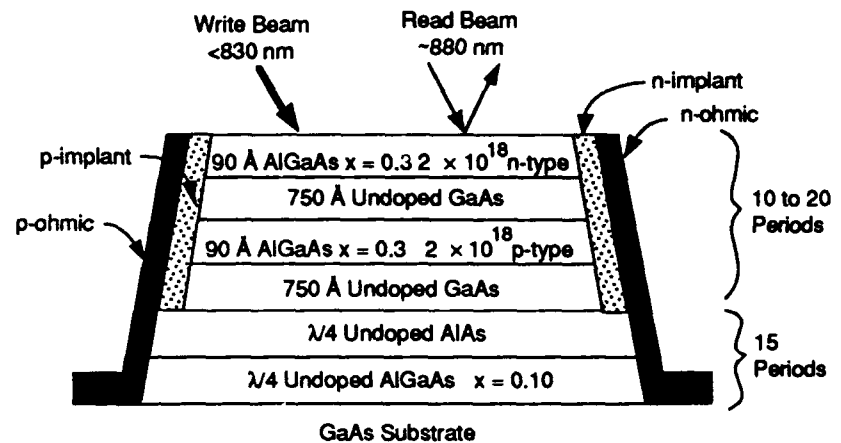


Figure 2. Cross-sectional diagram of a hetero-nipl asymmetric cavity spatial light modulator memory element with selective n- and p-ohmic contacts for electrical modulation or reset.

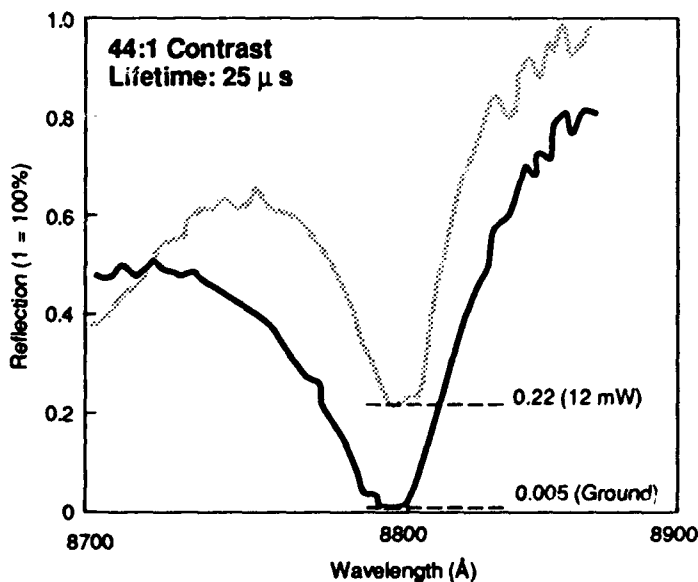


Figure 3. Reflectivity versus wavelength for an asymmetric cavity spatial light modulator with a 4.2 μm hetero-nipl active layer in the ground state and with 12 mW optical excitation.

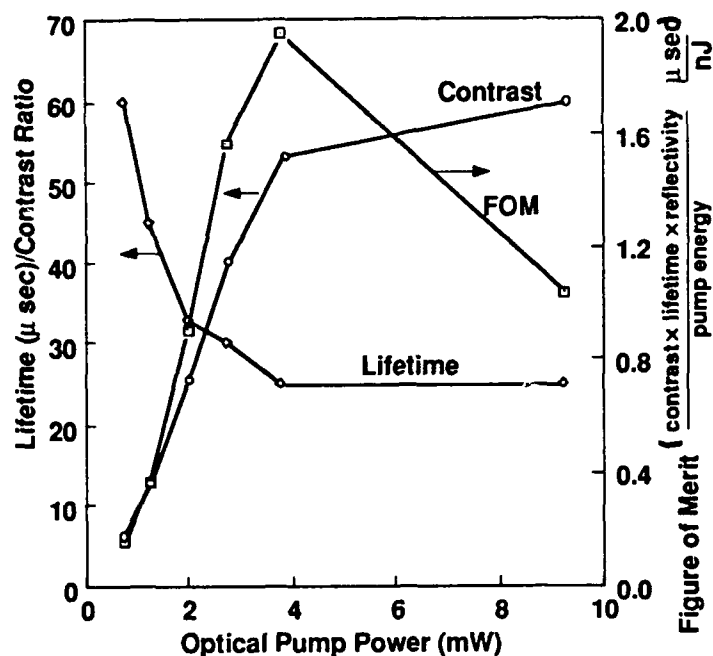


Figure 4. Contrast, lifetime and figure of merit versus optical pump power for a hetero-nipi spatial light modulator with a 4.2 μm active layer.

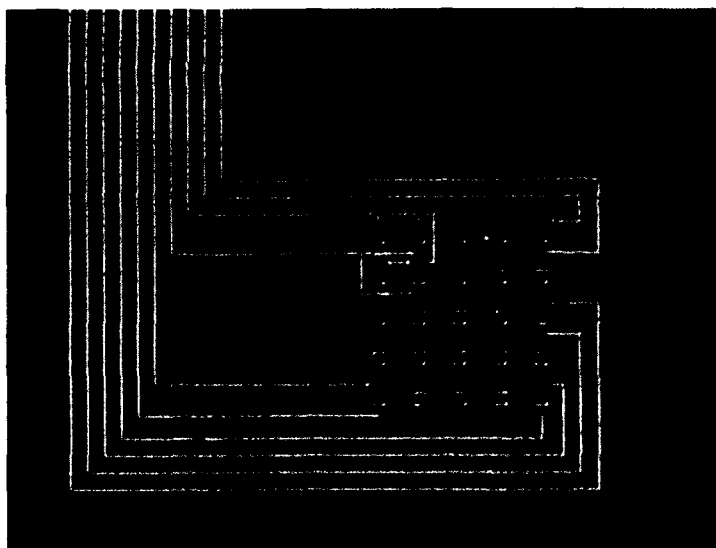


Figure 5. Photomicrograph of a processed memory element array.

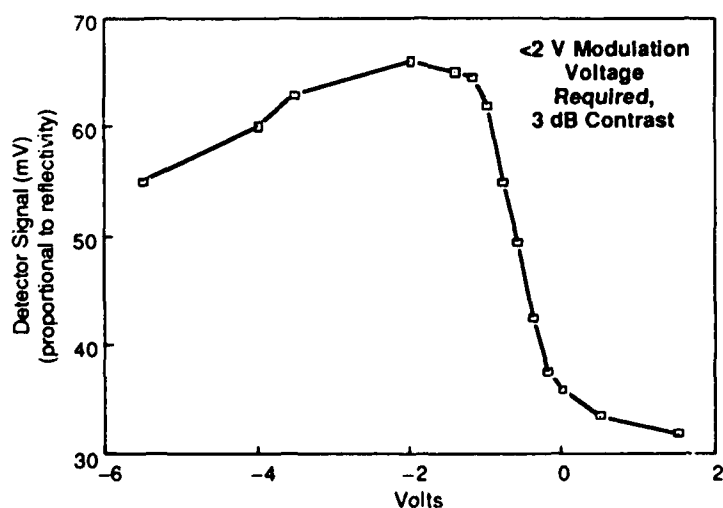


Figure 6. Reflectivity (arbitrary units) versus applied voltage for a hetero-nipi asymmetric cavity spatial light modulator. Although the contrast is low, the significant aspect is that most of the modulation occurs between 0V and -2V.

Amorphous Silicon Carbide Multilayer Modulators for Silicon Smart Pixels

Mark A. Neifeld

Department of Electrical and Computer Engineering
The Optical Sciences Center
University of Arizona
Tucson, AZ 85721
602-621-6102

I. Introduction

Smart spatial light modulators represent a class of device which combines optical detectors, simple processing electronics and optical modulators or sources to facilitate the high speed processing of 2-D arrays of optical data. Smart SLMs are extremely important to the next generation of optical computing and optical processing. This class of device is in many respects the enabling technology for the realization of optical interconnects, optical neural networks, parallel optical image processing and other forms of parallel optical computing. In the simplest such device the state of an optical modulator is determined by the intensity of the "write" light incident on an associated photodetector. The modulator in turn, can then affect the state of the reflected "reading" light. Utilizing a hard thresholding amplifier between detector and modulator, such an implementation can achieve optical logic through optical fan-in and will facilitate cascaded processing arrays. Utilizing a soft thresholding amplifier instead produces an array of optical neurons and would facilitate the realization of highly parallel optical neural network architectures. In more sophisticated smart SLM designs, neighboring pixels may be connected through simple processing electronics to produce optical modulation in response to local image characteristics such as gradients or averages. Through the use of locally connected electronics together with optical communications for broadcasting or global interconnections, an efficient usage is made of the resources available in each technology.

A large number of implementations have been proposed for the realization of smart SLMs (SEEDs, PLZT on Si, FLC on Si, VSELS, etc, ...).^[1-7] Several of these technologies are fully compatible with conventional silicon VLSI thereby providing the associated smart pixels with the full electronic functionality characteristic of this mature technology. Silicon compatibility is a motivating factor in the present work. In this paper we will discuss the use of a-Si:H/a-SiC:H multilayer modulators for the realization of smart pixels with sophisticated underlying functionality. This approach offers a number of attractive features including, compatibility with conventional Si VLSI, visible wavelength operation, high speed and fabrication simplicity.

II. Amorphous Silicon Carbide Multilayers

One mode of operation for the a-Si:H based modulators we discuss here parallels that of the GaAs MQW electroabsorption devices mentioned previously. In the case of GaAs MQWs the quantum confined stark effect is used to modulate the absorption of incident light whose photon energies are below the band gap. The wavelength of the incident light is tuned to correspond to the peak of the excitonic spectrum in the presence of a strong applied field. In the absence of any field, very low absorption results. When a field is applied however, the exciton spectrum is shifted to coincide with the incident wavelength and strong absorption is observed. The use of a quantum confined structure ensures that the strong applied field does not destroy the bound species whose spectrum is being probed. Similar confinement effects can be envisioned in a-Si:H/a-Si_xC_{1-x}:H; however, the effects of band tailing in these materials will require the use of narrower wells so that the effective band gap might be shifted away from the bulk band edge. Since the effective bulk bandgap of a-Si_xC_{1-x} can be tuned from 1.75eV to about 2.75eV by adjusting the carbon content from 0% to 35%, very large energy barriers can be engineered in these materials.^[8] For this reason, quantized states in the well layers can be tuned to reside away from the bulk band tails. Furthermore, due to the relatively slow deposition rate of a-Si:H compounds using RF glow discharge deposition (60Å- 7500Å per minute), a-Si:H/a-Si_xC_{1-x}:H multilayers have been produced with very thin well layers (2Å) and extremely good interface abruptness.^[9-13] A number of other researchers have characterized a-Si_xC_{1-x}:H and multilayers of a-Si:H/a-Si_xC_{1-x}:H as well as a-Si:H/a-Si_xN_{1-x}:H.^[14-17] Much of this characterization work however has involved the study of electroluminescence and photoluminescence spectra (toward the goal of producing high

efficiency silicon sources) and on the electronic properties of superlattices of these amorphous semiconductors (e.g., resonant tunneling). In the experiments reported here we have fabricated amorphous semiconductor multilayers which exhibit strong confinement effects. It is expected that large Stark shifts in the confined state energies can be observed in such structures. In addition, large NLO effects owing to band filling effects are also expected.

III. Experimental Results

In order to provide an initial characterization of the $a\text{-Si}_x\text{C}_{1-x}\text{:H}$ materials and growth facilities, preliminary depositions have been performed for a number of different carbon concentrations (0%–28%). For these trials, ethylene was used as the process gas for carbon incorporation. The resulting materials demonstrate the expected variation in band gap with carbon content as measured using room temperature VIS-IR spectroscopy (see figure 1) and the expected surface morphology (as indicated by atomic force microscopy). Earlier tests utilizing carbon fractions larger than $\approx 15\%$ resulted in a severe disruption of the material morphology which we suspect was due to graphitization within the $a\text{-Si}$. Careful adjustment of process parameters alleviated this problem.

Multilayers were fabricated using the constituent materials $a\text{-Si:H}$ and $a\text{-Si}_{0.86}\text{C}_{0.14}\text{:H}$ serving as well and barrier layers respectively. Conduction band and valence band quantum wells with barrier energies of 0.16eV and 0.29eV respectively were formed using a simple PCVD deposition system. 31 periods of 37.5Å wells and 112Å barriers were deposited. The TEM data shown in figure 2 indicates that these samples maintain good layer uniformity throughout deposition. The uniformity was quantified using X-ray diffraction to be $\pm 2\text{\AA}$ and the interface quality is seen to be moderately good also. Interface abruptness was measured at roughly 10Å which we believe can be drastically improved through the incorporation of additional hydrogen during the deposition process.

Using effective masses for particles in the conduction and valence bands of $m_c = 1.0m_0$ and $m_v = 0.6m_0$, we predict the existence of three quantized levels in each band. We can calculate the first excited state of the multilayer to reside at an energy of 1.88eV, 0.04eV above the bulk band edge corresponding to an excitation wavelength of 661nm. This prediction agrees well with Tauc plot data extracted from the multilayer spectra shown in figure 3 (measured band edge at 1.90eV). In figure 3 we show the transmission spectra for the multilayer sample both with and without an applied field of 10^5V/cm . We see that a large change in transmission occurs for the case of a field applied normal to the layer boundaries and corresponds to a roughly 20% change in absorption (i.e., $\Delta\alpha/\alpha = 0.2$). A time domain measurement has not yet been performed so that the thermal component of the observed modulation is not yet known. We do however, observe large conduction currents in these initial samples owing to the presence of defect states in the constituent materials. These defects arise as a result of insufficient hydrogen incorporation which is necessary for passivation of Si dangling bonds present in the amorphous materials. Lack of hydrogen in our samples was recently verified using FTIR and supports this conclusion. The existence of an abundance of such defects suggests that conduction current heating is playing a role in the observed modulation.

IV. Conclusions

We have demonstrated confinement effects in amorphous silicon multilayers. Although the optical modulation data is likely to have been influenced by thermal effects, the observed spectral data agrees well with simple quantum mechanical predictions based on a particle in a finite potential well model. Our samples were fabricated in a straightforward fashion using PCVD with silane and ethylene process gasses. The next step in this work will involve incorporation of additional hydrogen in our samples so as to reduce the number of defect states and improve interface quality. We also plan to fabricate a p-i-n diode structure incorporating an amorphous silicon carbide multilayer within the intrinsic region. Nonlinear optical measurements in our initial samples is difficult owing to the short interaction lengths involved ($< 1\mu\text{m}$); however, we intend to utilize a thin film waveguiding technique to improve the SNR in these NLO measurements in the future.

The potential benefits from realizing optical modulators in Si using a process compatible with conventional Si VLSI are very nearly uncountable. The long term results of this work and the integration of $a\text{-Si:H}$ modulators with CMOS VLSI processing electronics is extremely important for the realization of a number of critical optical technologies including optical neural networks, optical image processing and optical

interconnects. The capability to utilize a-Si:H processing which is compatible with silicon VLSI, will make this technology competitive with others such as flip-chip bonding, solder bump reflow and GaAs on silicon for the realization of high speed optical interconnects in silicon based computers. Furthermore, since the $a\text{-Si}_x\text{C}_{1-x}\text{:H}$ is tunable from IR to visible, these systems offer a degree of flexibility which is not present with other technologies.

V. References

- [1] D. A. B. Miller, "Quantum Wells for Optical Information Processing," *Optical Engineering*, Vol. 26, No. 5, 1987.
- [2] T. K. Woodward, T. Sizer, D. L. Sivco, and A. Y. Cho, "InGaAs/GaAs Multiple Quantum Well Optical Modulators for the 1.02-1.07 μm Wavelength Range," *Applied Physics Letters*, Vol. 57, No. 6, 1990.
- [3] D. S. Chemla, et. al., "Electroabsorption by Stark Effect on Room Temperature Excitons in GaAs/GaAlAs Multiple Quantum Well Structures," *Applied Physics Letters*, Vol. 42, No. 10, 1983.
- [4] M. J. Goodwin, C. J. G. Kirby, A. D. Parsons, I. Bennion and W. J. Stewart, "8X8 Hybridized PLZT/Silicon Spatial Light Modulator Array," *Electronics Letters*, Vol. 25, No. 18, 1989.
- [5] D. A. Jared, et. al., "Optically Addressed Spatial Light Modulator for Early Vision Processing," *Proceedings of SPIE*, Vol. 1359, pp.15-16, 1990.
- [6] S. H. Lee, S. C. Esener, C. Sakik, M. A. Title and T. J. Drabik, "Two Dimensional Silicon/PLZT Spatial Light Modulators: Design Considerations and Technology," *Optical Engineering*, Vol. 25, No. 2, 1986.
- [7] D. G. Ast, "a-Si:H FET Addressed LCD Panel," in *Semiconductors and Semimetals*, ed. by J.I. Pankove, Vol. 21, Part D, Academic Press, 1984.
- [8] D. Kuhman, S. Grammatica and F. Jansen, "Properties of Hydrogenated Amorphous Silicon Carbide Films Prepared by Plasma Enhanced Chemical Vapor Deposition," *Thin Solid Films*, Vol 177, pp.253-262, 1989.
- [9] G. W. Wills, A. S. Harrus and M. J. Thoms, "Plasma Assisted Deposition and Device Technology: Interlevel Dielectric Considerations," *Proceedings of SPIE*, Vol. 1185, pp.98-109, 1989.
- [10] Shin-Ichiro Ishihara, Masatoshi Kitagawa and Takashi Hirao, "Anomalous Deposition Rate Dependence of Hydrogenated Amorphous Silicon on Substrate Temperature," *Journal of Applied Physics*, Vol. 62, No. 7, 1987.
- [11] M. M. Rahman, et. al., "Properties and Device Applications of Hydrogenated Amorphous Silicon Carbide Films," *Journal of Applied Physics*, Vol. 67, No. 11, 1990.
- [12] K. Guanglin, Zhang Quing and Chen Shiming, "Some Results for a New a-Si:H/a-SiC:H Superlattice," *Proceedings of the 1987 International Workshop on Amorphous Semiconductors*, pp.251-255, 1987.
- [13] H. Ohta and K. Morigaki, "Photo Induced Absorption in a-Si:H/a-Si₃N₄:H Superlattices,"
- [14] K. C. Hsu, C. S. Hong, Y. L. Jiang and H. L. Hwang, "On the Stability of Amorphous Silicon Superlattices," *Solid State Communications*, Vol. 72, No. 7, 1989.
- [15] I. Pereyra, et. al., a-Si:H/a-SiC:H Multilayers," *Journal of Noncrystalline Solids*, pp.871-874, 1987.
- [16] Masataka Hirose and Seiichi Miyazaki, "Superlattices and Multilayers in Hydrogenated Amorphous Silicon Devices," *IEEE Transactions on Electron Devices*, Vol. 36, No. 12, 1989.
- [17] Yeu-Long Jiang and Huey-Liang Hwang, "Field Drifting Resonant Tunneling Through a-Si:H/a-Si_{1-x}C_x:H Quantum Wells at Different Locations of the i-Layer of a pin Structure," *IEEE Transactions on Electron Devices*, Vol. 36, No. 12, 1989.

VI. Acknowledgements

The author would like to acknowledge the assistance of the Arizona Materials Laboratory and Michael Jacobson for providing the PCVD facility in which the multilayer materials were fabricated. Acknowledgements should also be made for characterization facilities made available by Charles Falco and Dror Sarid of the University of Arizona Optical Sciences Center.

VII. Figures

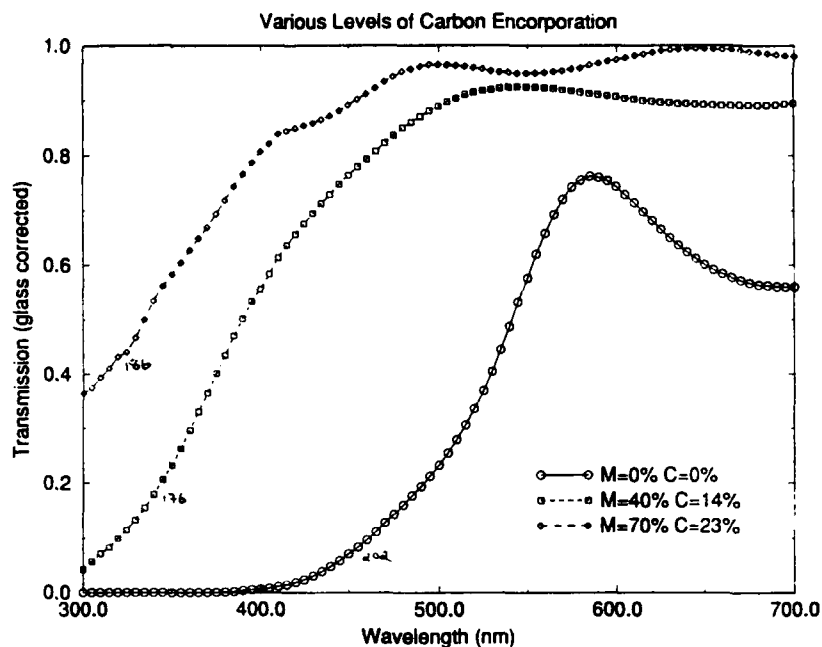


Figure 1: Transmission spectra for multilayer constituents depicting variation in band gap with carbon content.

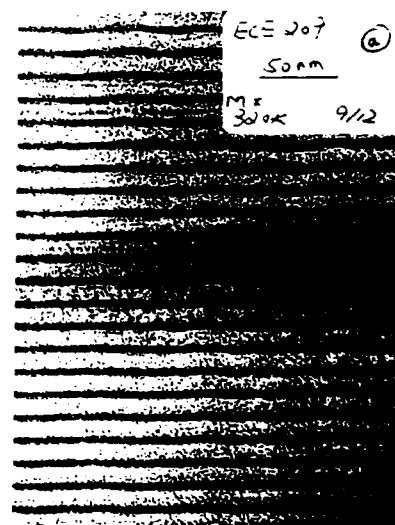


Figure 2: Transmission electron micrograph of multilayer sample with 37.5Å wells (dark layers) and 112Å barriers.

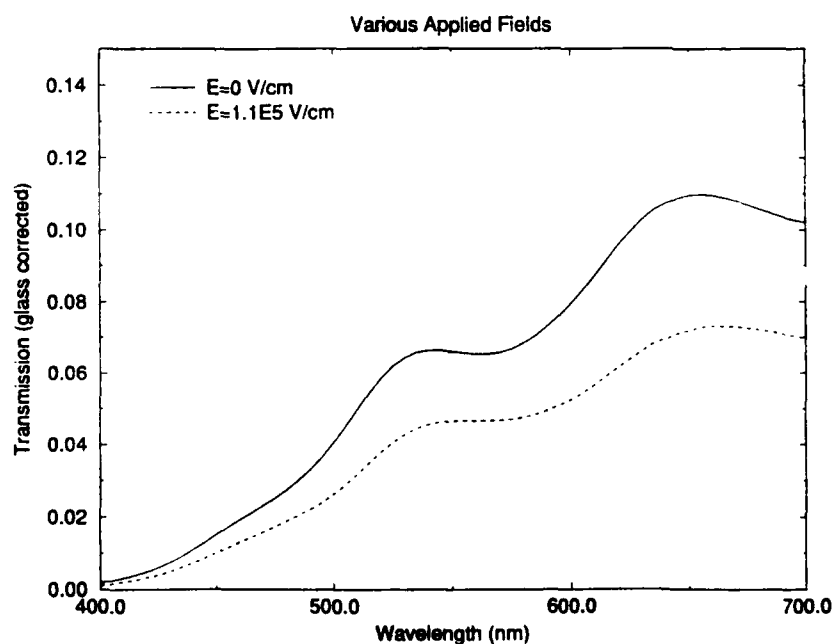


Figure 3: Transmission spectra for multilayer sample with (solid curve) and without (dashed curve) an applied field.

Monday, March 15, 1993

Smart Pixel SLMs

SMD 3:30pm-5:40pm
Grand Ballroom West

William Miceli, *Presider*
Office of Naval Research

Smart and Advanced Spatial Light Modulators

J R Brocklehurst, CRL, Dawley Rd, Hayes, Middlesex, UB3 1HH, UK
Telephone: +44 81 848 6488

N Collings, Institute de Microtechnique, Breguet 2, CH-2000 Neuchâtel, Switzerland

W A Crossland, BNR Europe Limited, London Road, Harlow, Essex, CM17 9NA, UK¹

R J Mears, Dept of Engineering, University of Cambridge, Cambridge, CB1 2PZ, UK

D G Vass, Dept of Physics, University of Edinburgh, Edinburgh, EH9 3JL, UK

M R Worboys, GEC Marconi Research Centre, Gt Baddow, Essex, CM2 8HN, UK

Introduction

This paper reports the work of a collaboration which has sought to design smart ferroelectric liquid crystal spatial light modulators (Smart SLMs) by starting with potential systems applications and asking what functions are required of the smart SLM for it to perform a useful task in the system. Three system areas have been studied: interconnections for telecommunication systems, neural networks and image processing systems. In each case a set of ideal parameters has been drawn up, and possible common ground between the devices has been sought. None was found so devices have been designed which will function in two of the three systems. A brief description of each of the application studies will be given, followed by the outline device designs, and first experimental results.

System Studies

Interconnections

There has been a great deal of interest in recent years in the possibilities of building optical interconnection systems to take advantage of the connectivity and low cross-talk of free-space optics². However, what we have sought to do is examine the potential of hybrid optical/electronic systems using each aspect in the most efficient way. The concept of smart pixels is that these are electronic islands³ whose size is such that within the pixel electronics is always the most efficient means of communication. The interconnection between pixels is optical and hence has very high connectivity. As such the smart pixel can have a variety of functions, and switches composed of arrays of them have very large bandwidth, switch at the message rate, and can switch optical signals of any format.

Recent advances in the design of matrix vector multiplier type single stage cross-bar switches⁴ have opened up a number of possible advantages for the use of smart SLMs. Some aspects of switch control and arbitration can be integrated into the backplane, and such devices could be used in route protection or optical distribution frames in emerging networks. However, a key application of smart pixel devices is serial to parallel and parallel to serial data conversion.

Image processing

The concept of pooling the values of a neighbourhood of data points before performing a logical operation was first proposed by von Neumann⁶, and is now central to digital optics processing. Optical implementation of local neighbourhood operations by a smart SLM has no requirement for scanning since all pixels are processed in parallel. Possible operations range from numerical and morphological filtering operations to edge detection and noise reduction. Applications occur wherever there is a need to manipulate 2D images, from matte processing in TV and cinematography to image recognition and correlation. We have considered a number of smart SLM designs, in particular an isophotic contour detector and a distributed optical array processor. Although the latter would have produced a very powerful general purpose optical processor it was felt that the complexity (300 transistors per pixel) was too high to tackle with the programme's limited resources. Consequently the isophote design is being carried forward to silicon. The performance has been simulated and is shown in Figure 2, together with a conventional edge detection rendering of the same image. A 64 x 64 pixel grey scale image of a Toucan has been processed for Laplacian edge detection, and isophote contour mapping at a number of threshold levels. Those shown are for the lowest (edge of the darkest regions) and highest (edge of the brightest regions) thresholds.

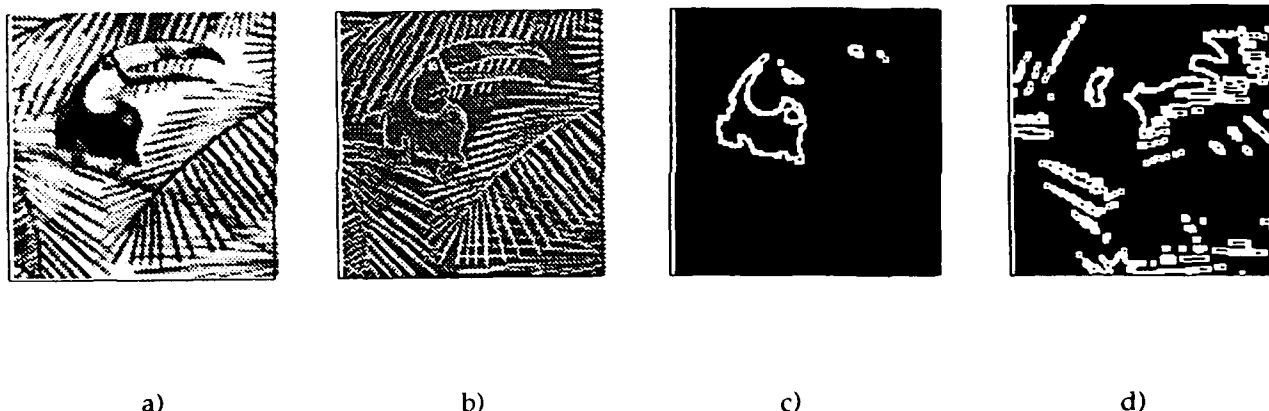


Figure 2: Simulation results for isophote backplane. a) Original image, b) Laplacian edge detected, c) Lowest threshold isophote, d) Highest threshold isophote.

Silicon design

Three silicon fabrication runs are planned on the programme. The design for the first of these contains the building blocks (modulator pads, detectors, threshold circuitry) for the two smart SLM designs, together with two simple arrays. The first of these has in each pixel a photo-detector with variable threshold, an electrically configurable logic element, and an optical modulator. The 8x4 array will perform nearest neighbour cellular logic with neighbours along a row. Despite this limitation it will be able to model cellular automata, slice images and multiplex images together. The second array has 8x8 smart pixels each with a phototransistor, modulator and logic capable of shifting on data so as to isolate the modulator pad. The results of experiments with these simple arrays will be presented.

This opens up the possibility, in future networks, of building wavelength crossconnects and optical backplanes. In the former the input fan-out can be made wavelength selective so as to place different optical channels onto different pixels. In the latter free space optics offer greatly improved spatial connectivity.

A novel approach to fast packet switching has been developed, involving free space optics and smart SLMs. It uses optics and electronics in the most appropriate manner, does not require optical memory, and minimises bit rate switching. Fast serial data is formatted in such a way that it can be switched *en bloc* through the optical interconnect using image replicating optics. The implications of such image replicating switching systems in telecommunication systems are being considered. It has been decided not to proceed to designing a smart SLM for this application until more detailed modelling of system performance has been carried out.

Neural Networks

A range of possible neural network architectures has been studied. The emphasis has been on treating the components of the network as sub-systems which are then organized in an appropriate fashion to give an independent neural system. The basic classes of smart pixel configuration examined have been: individual (detection, decision(thresholding), amplification, delay, output), laterally connected (with additional inputs from neighbouring pixels) and complex (assemblies of sub-cells). The mode of interconnection, especially how best to introduce weighting, has also received a great deal of attention. Two architectures have been examined in great detail, and the decision on which to progress to silicon fabrication has been based on the group's confidence to build functional devices within a restricted resource budget, rather than pursuit of the most technically challenging route.

The first scheme was for a smart pixel capable of supervised error back-propagation learning with analogue weight. However, this would have been a quite complex device which would have needed one-off test systems to prove itself. The second scheme will yield a device which can be tested in existing rigs. This design has on-chip learning in the incremental weight iterative learning model. It will allow the incremental delta rule to be implemented with moderate complexity. Considerable modelling of unipolar delta rule learning has been undertaken in order to determine which device parameters are crucial to good system performance.⁵ Figure 1, taken from reference 5, shows a simulation of the unipolar binary bidirectional associative memory (UBBAM).

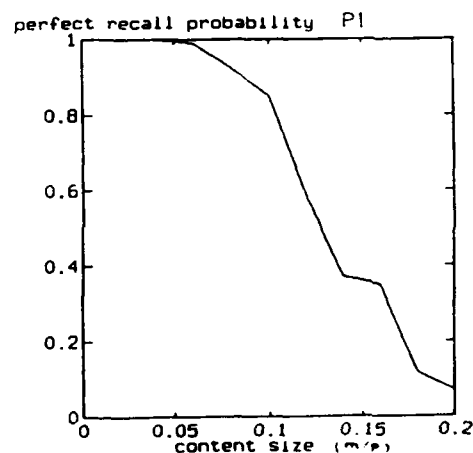


Figure 1: Recall performance of UBBAM as a function of order of memory

The second design is the neural network one. In this case each pixel will comprise two phototransistors and an analogue liquid crystal modulator plus a local processing circuit. The array size will be 64x64. The third (isophote) design is based on the photodetector signals from nine nearest neighbour pixels being combined logically. Signals from opposing detectors are logically XORed, and the resulting four terms are ORed to determine whether or not the modulator is switched. The function of the modulator is to signal the presence of an edge passing through the location. More detailed discussion of these two designs will be presented.

References

1. Northern Telecomm Research Professor of Photonics in the Cambridge University Engineering Department.
2. Hinton H S, "Photonic Switching Fabrics", IEE Comms Mag. 71-89, April 1990.
3. Esner S, Wang J, Title M & Lee S H, Optical Engineering, 26(5), 406-413, (1987).
Midwinter J E, "Photonic Switching Technology: Component Characteristics versus Network Requirements", J Lightwave Technology, 6, 1412-1419, (1988).
4. Kirk A G, Crossland W A & Hall T J, "A Compact and Scalable Free-space Optical Crossbar", Proc SPIE vol 1574, (1991).
5. Yu T C B & Mears R J, "Design and Implementation of a Unipolar Binary Bidirectional Associative Memory with a Smart Advanced Spatial Light Modulator", in Intelligent Engineering Systems through Artificial Neural Networks Vol II, Eds Dagli, Burke & Shin, ASME Press (1992).
6. Preston K & Duff M J, "Modern Cellular Automata, theory and application", Plenum Press (1984).

**Electrically addressed field effect transistor self electro-optic effect device (FET-SEED)
amplified differential modulator array.**

A. L. Lentine

AT&T Bell Laboratories, Naperville IL 60566

L. M. F. Chirovsky, L. A. D'Asaro, E. J. Laskowski, and S. S. Pei

AT&T Bell Laboratories, Murray Hill NJ 07974

M. W. Focht, J. M. Freund, G. D. Guth, R. E. Leibenguth, and L. E. Smith

AT&T Bell Laboratories, Breinigsville PA 18031

T. K. Woodward

AT&T Bell Laboratories, Holmdel NJ 07733

The integration of Gallium Arsenide field effect transistors (GaAs - FETs) and multiple quantum well modulators is an exciting advancement in the area of optical interconnections [1-3]. While most of our efforts on quantum well self electro-optic effect devices (SEEDs) have been concentrated on devices with optical inputs and optical outputs [4], some applications, such as connections between circuit boards or multi-chip modules (MCMs), require electrically addressed optical modulators. Arrays of electrically addressed multiple quantum well electro-absorption modulators with as many as 128 elements have been made[5]. Although operation of devices within the arrays has been demonstrated beyond 1 GHz, generally voltages above 5V are needed to achieve a reasonable output contrast with low loss in the "on" state. Low voltage (2-3volts) modulators have been made using Fabry-Perot cavities [6] and ultra-shallow barriers [7], although even this voltage may be considered too high for some applications.

In this paper, we describe a monolithic integrated 6 by 6 array of electrically addressed amplified differential modulators. Each element in the array contains a two transistor amplifier so that the input voltage swing can be as small as a few hundred millivolts yet the voltage across the multiple quantum well modulators can be as high as 10 volts. Such a low input swing would allow (provided the threshold was correctly designed) an array such as this to be used with standard silicon bipolar emitter-coupled logic (ECL) or GaAs FET electronic logic families that have typical voltage swings of less than 1 volt.

A schematic diagram and photograph of the array are shown in Fig. 1. A detailed description of the FET-SEED structure and fabrication are given in Ref. 3. The reflection-type electro-absorption modulator had 71 pairs of GaAs/AlGaAs quantum wells. The devices that we report on here were anti-reflection coated. The optical modulators had $10\mu\text{m} \times 10\mu\text{m}$ optical windows with center to center spacing of the two modulators within a cell of $40\mu\text{m}$. The unit cell size was $80\mu\text{m} \times 80\mu\text{m}$ in both directions for a total array size of $480\mu\text{m} \times 480\mu\text{m}$. The excitonic peak in absorption at 0 volts bias was at 853 nm.

The field effect transistors had a $1\mu\text{m}$ gate length, with the load transistor having a $25\mu\text{m}$ gate width and the input transistor having a $50\mu\text{m}$ gate width. The measured DC currents of the transistors at $V_{gs} \sim 0\text{V}$ were 45 mA/mm at $V_{ds} \sim 2\text{V}$, and the measured transconductance at $V_{gs} \sim 0\text{V}$ was $\sim 70\text{ mS/mm}$. The measured threshold voltages of the transistors were $\sim -1\text{V}$, and the drain-source breakdown voltages were greater than 10 V.

Roughly 2/3 of the elements in the 6 x 6 array that we tested were operational. A whole row

was inoperable, presumably due to a short circuit, and four others were "blown" during the few months of testing. While we have not yet tested a fully operational array, we recently built and tested several good arrays of optical switching nodes with 400 transistors per array [8]. Because of this, we feel confident that a fully operational electrically addressed amplified modulator array could be made.

In Fig. 2, we show the output reflectivities of the modulators as a function of the electrical input voltage for all of the devices except those in the "bad" row superimposed. The modulator bias was set to 6.5 V and the wavelength was 860 nm, 7 nm above the wavelength of the exciton peak at zero volts, λ_0 . The individual modulators are said to be "normally on" modulators when operated at a wavelength longer than the exciton peak (λ_1) because they have their highest reflectivity at zero volts bias across them. The switching transition varied by only ± 0.070 volt from device to device but the threshold appears different for each diode in the differential pair. This is simply because of the non-linear absorption versus voltage relationship of the modulators. That is, when the voltage across each of the modulators is $V_0/2$ or 3.25 V, the reflectivity of the devices is not much different from its reflectivity at zero volts. If the reflectivity at this voltage was equal to the average of the minimum and maximum reflectivities then the switching transitions might appear symmetric. The switching transition was at a higher voltage than the threshold voltage, because of the voltage drop in the power lead feeding the source of the input transistor. The voltage drop could be reduced by re-designing the array with wider and thicker power leads. Individual elements that were not part of the array had their switching transition at -1 V as expected.

From Fig. 2, you can see that an input voltage swing less than ± 0.1 volt is required to change the state of the output modulators. However, with a voltage swing this small, the output current difference between the load transistor and the input transistor will also be small. The switching time is inversely proportional to this current difference (more current - shorter time). Thus we would expect that the switching time would depend on the input voltage swing. We have measured risetimes of the amplified modulator array by monitoring the optical output with a fast photodiode. The electrical input was a 200 MHz square wave with a risetime of ~ 250 ps with peak to peak voltage swings between 0.6 volt and 2 volts. For a voltage swing of 0.6 V, the slowest of the rise and falltimes was 730 ps, decreasing to 530 ps for a 1 V input and 370 ps for 2 V input. In Fig. 3, we show the output reflectivity for one of the modulators with a 2Gb/s data stream with a 2 V peak to peak input voltage applied to the input.

Using a spectrum analyzer, we measured the modulation of the output reflectivity with a 500 MHz square wave to applied to the electrical input of the device and with a 500 MHz square wave applied only to the electrical input of an adjacent device. The ratio of these two measurements gives some indication of crosstalk. We chose adjacent devices that also had long electrical leads in proximity to each other. The ratios of the two measurements were 57 dB at 500 MHz, 53 dB at the third harmonic (1.5 GHz), and > 31 dB at the fifth harmonic (2.5 GHz). In the 5th harmonic measurement, the noise of the spectrum analyzer obscured the "crosstalk signal" so it may have been much better.

We also measured the reflectivities of the modulators versus input voltage at a variety of optical powers. We see some increased voltage swing required at high powers, and this is because the FET currents must overcome the photocurrents generated in the modulators. We see very little degradation in contrast ratio at the higher powers at this wavelength, although measurements taken at the exciton peak, λ_0 , do show severe degradation in contrast ratio at high powers. The fact that there is less degradation in contrast ratio for "normally on" modulators been previously reported in "unamplified" quantum well modulators [9].

In conclusion, we have built and tested a 6 x 6 array of differential quantum well modulators, each with a voltage amplifier using the FET-SEED technology. The voltage input swing required is only a few hundred millivolts to achieve an output voltage swing at the modulators up to 10V. We showed that the speed of operation is limited by the currents in the FETs, and that for input voltage swings up to 2 V, operation beyond 2Gb/s is possible. We found that the devices are capable of modulating optical inputs with powers up to 1 mW for "normally on" operation. Lastly, we measured crosstalk in the arrays and found it to be better than 30 dB below 2.5GHz.

1. D. A. B. Miller, M. D. Feuer, T. Y. Chang, S. C. Shunk, J. E. Henry, D. J. Burrows, D. S. Chemla, "Field-effect transistor self-electro-optic effect device: integrated photodiode, quantum well modulator and transistor", *IEEE Photon. Technol. Lett.*, 1, 61-64, (1989).
2. T. K. Woodward, L. M. F. Chirovsky, A. L. Lentine, L. A. D'Asaro, E. J. Laskowski, M. W. Focht, G. D. Guth, S. S. Pei, F. Ren, R. E. Leibenguth, M. T. Asom, R. Kopf, J. M. Kuo and M. D. Feuer, "Operation of a fully integrated GaAs/AlGaAs FET-SEED: A basic optically addressed integrated circuit," *IEEE Photonics Technology Lett.* 4 614-617 (1992)
3. L. A. D'Asaro, L. M. F. Chirovsky, E. J. Laskowski, S. S. Pei, T. K. Woodward, A. L. Lentine, R. E. Leibenguth, M. W. Focht, J. M. Freund, G. D. Guth, and L. E. Smith, "Batch fabrication and operation of GaAs-AlGaAs field effect transistor self electro-optic effect device (FET-SEEDs) smart pixel arrays," *IEEE J. Quantum Electron.* (to be published, special issue on smart pixels, 1992)
4. see e. g. D. A. B. Miller "Quantum-well self-electro-optic effect devices", *Optical and Quantum Electronics*, 22, S61-S98, (1990)
5. L. M. F. Chirovsky, M. W. Focht, J. M. Freund, G. D. Guth, R. E. Leibenguth, G. J. Przybylek, L. E. Smith, L. A. D'Asaro, A. L. Lentine, R. A. Novotny, and D. B. Buchholz, "Large arrays of symmetric self electro-optic effect devices," in Technical digest, Topical meeting on Photonics switching, Optical Society of America, Washington D. C. paper ThB2 (1991)
6. R. H. Yan, R. J. Simes, L. A. Coldren, and A. C. Gossard, "Transverse modulators with a record reflection change of > 20 percent / volt using asymmetric Fabry-Perot structures," *Appl. Phys. Lett.* 56 1126-1128 (1990)
7. K. W. Goossen, J. E. Cunningham, and W. Y. Jan, "Excitonic electroabsorption in extremely shallow quantum wells," *Appl. Phys. Lett.* 57 pp. 2582-2584 (1990)
8. A. L. Lentine, T. J. Cloonan, H. S. Hinton, L. M. F. Chirovsky, L. A. D'Asaro, E. J. Laskowski, S. S. Pei, M. W. Focht, J. M. Freund, G. D. Guth, R. E. Leibenguth, L. E. Smith, G. D. Boyd and T. K. Woodward, "4 x 4 arrays of FET-SEED embedded control 2 x 1 switching nodes," *IEEE Topical meeting on Smart Pixels*, post-deadline paper 1 August, 1992
9. R. A. Morgan, L. M. F. Chirovsky, M. W. Focht, and R. E. Leibenguth, "High power multiple quantum well modulators exploiting resonant tunneling," *Appl. Phys. Lett.*, 59 pp. 3524-3526 (1991)

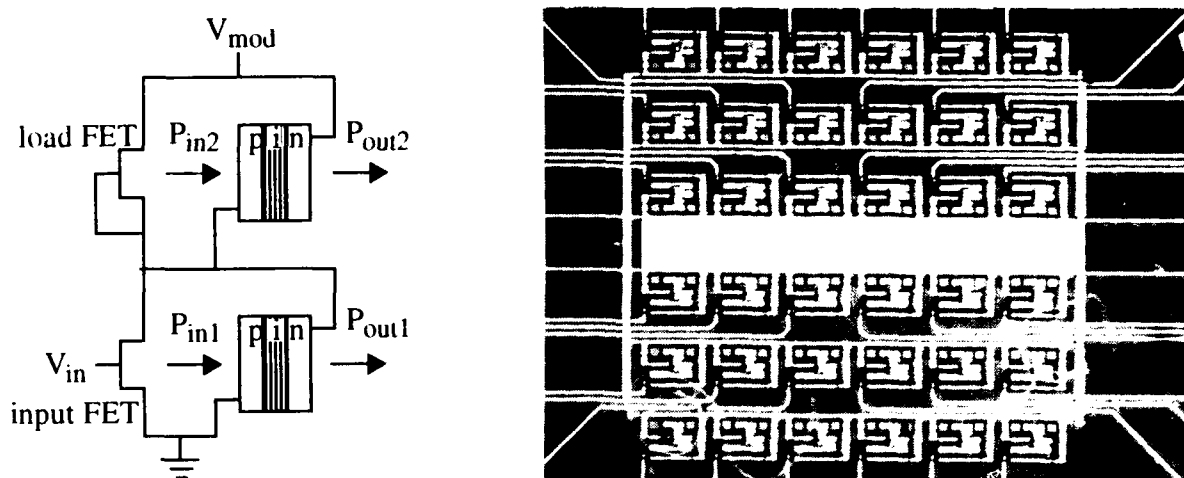


Fig. 1. Schematic diagram, layer structure and photograph of the 6 x 6 array of amplified differential modulators. a) Schematic diagram, b) photograph of the array

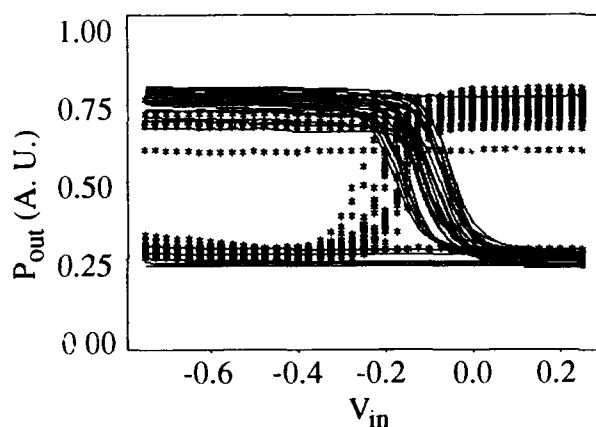


Fig. 2. Superposition of reflectivity versus input voltage for 30 of the devices in the array. Solid curves are for the top modulators and "stared" curves are for the bottom. $V_{ds} = 6.5$ V, $\lambda = 860$ nm, and $P_{optical} = 50 \mu W$.

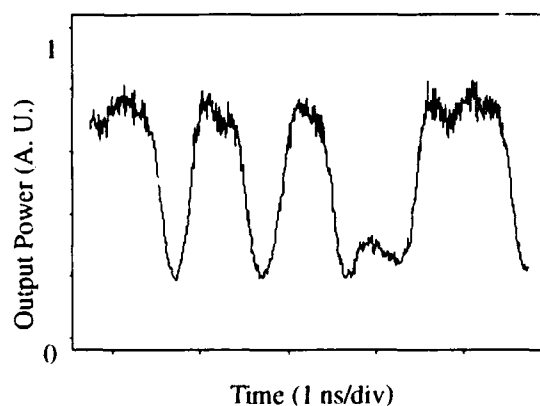


Fig. 3. Output reflectivity for one of the modulators for a 2 Gb/s NRZ input with an input voltage swing of 2 V. Slightly reduced performance can be achieved with < 1 volt swings.

VLSI/Liquid Crystal Winner-Take-All Modulators for Optical Competitive Learning

Timothy M. Slagle and Kelvin Wagner

Optoelectronic Computing Systems Center, Campus Box 525
University of Colorado, Boulder, CO 80309-0525

Introduction

An optical winner-take-all (WTA) device which chooses the largest of an array of optical intensities would be useful for a variety of applications. For example, a two-dimensional WTA array placed at the output plane of an optical correlator would find the pixel at which the correlation peak is a maximum, thereby locating the target in a background of clutter. An electronic 2-D WTA output could go to circuitry which reports the location of the peak, or an optical output could be used by further stages of optical processing. Another use for an optical WTA would be in an optical associative memory. The WTA device would select the largest of the optically computed inner products between an input and an array of stored vectors. The optical output from the winning unit could then illuminate the stored vector array to read out the undistorted target vector. A third use for an optical WTA is in self organizing optical neural network implementations. Essentially all unsupervised learning systems require some form of WTA neuron activation function. Examples of these systems include competitive learning [1] and adaptive resonance [2] network models.

VLSI/Liquid Crystal WTA Devices

Figure 1 shows a schematic cross section of two units in a one-dimensional VLSI/Liquid Crystal WTA array. The VLSI/LC devices are made by flowing a layer of liquid crystals between an integrated circuit (IC) die and a cover glass which is coated with a transparent conductor and an alignment layer. Polarized light passes through the

glass and liquid crystal layers and strikes the second-level metal electrode mirror on the surface of the IC. Light which is not reflected by the metallic electrode is absorbed by a photodetector under the electrode and is converted to a current. This current is the input to the two-transistor competitive circuit [3], which selects the largest of the inputs to all of the units through non-specific global inhibition. The output of the competition circuit is then thresholded and buffered to drive the modulator electrode. The molecules in the liquid crystal layer orient themselves according to the electric field between the chip and cover glass electrodes. The reflected light, which makes two passes through the LC material, has its polarization altered according to the liquid crystal alignment. The LC alignments and electrode voltage levels are chosen so that light reflected from the winning pixel is passed by an analyzer, while light from the losing pixels is blocked.

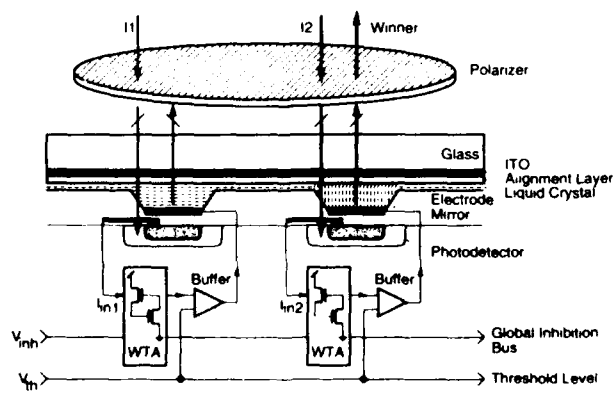


Figure 1: Cross-sectional diagram of two units of a VLSI/LC winner-take-all device.

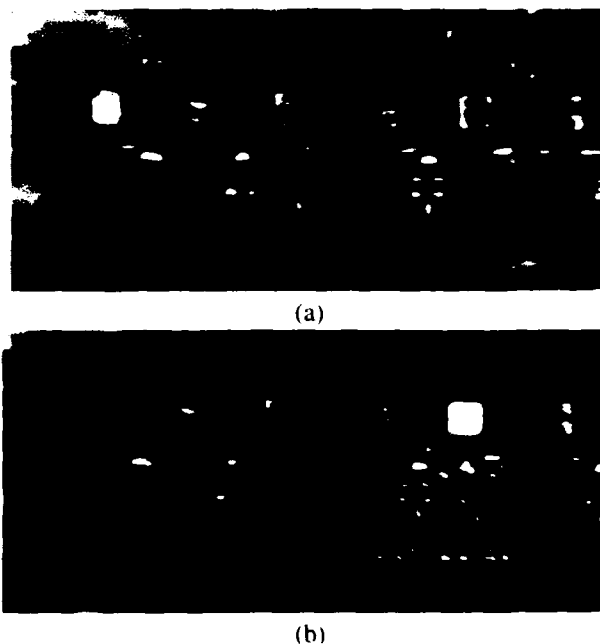


Figure 2: Photomicrographs of a one-dimensional WTA array: (a) Uniform illumination. (b) Additional illumination on fifth unit.

Figures 2(a) and 2(b) are polarizing microscope photographs of a one-dimensional array demonstrating winner-take-all behavior. In Fig. 2(a), the array is illuminated with uniform light from the microscope's incandescent il-

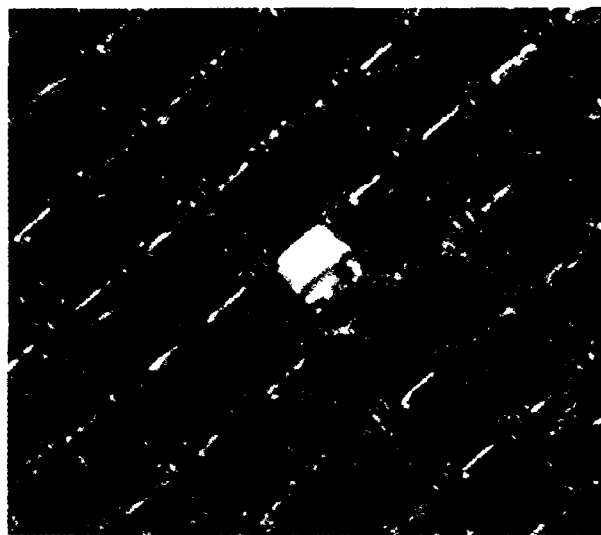


Figure 3: Photomicrograph of a two-dimensional WTA device.

luminator. The leftmost unit in the array "wins" in this case because end units receive more photocurrent from the surrounding substrate (which is not shielded in this design). Fig. 2(b) shows the result of illuminating the array with an additional stripe of light about one pixel ($50\mu\text{m}$) wide. The unit that is illuminated by the stripe switches on, and the unit on the left side is switched off by the electronic competitive circuitry. This demonstrates the non-local WTA operation, since the light level on the leftmost pixel has not changed, yet the pixel's output has changed.

Figure 3 shows a two-dimensional winner-take-all array of 32×32 units on a different region of the same chip. The WTA units in this array are $75\mu\text{m}$ square, with a LC modulator electrode that covers the unit's detector and circuitry. Figure 3 shows that a single unit has won the competition and is active. The two-dimensional array exhibited a hysteresis or latching effect which caused the winning pixel to stay activated after it no longer received the largest input. This effect was also present to a smaller extent in the one-dimensional arrays of the first-generation device.

A new circuit was designed based on the results of tests of the first chip, and was used in one- and two-dimensional WTA arrays. Figure 4 shows a schematic diagram of the new circuit, and Fig. 5 shows a photomicrograph of the fabricated chip. The output of each WTA node is now taken to be the current that each unit supplies to the inhibition bus through transistor Q5 instead of the voltage level V_{in} at the current input node. This resulted in an exponential increase in the sensitivity of the circuit. Improvements were also made in the circuit layout. A second-level metal layer now covers the WTA arrays and

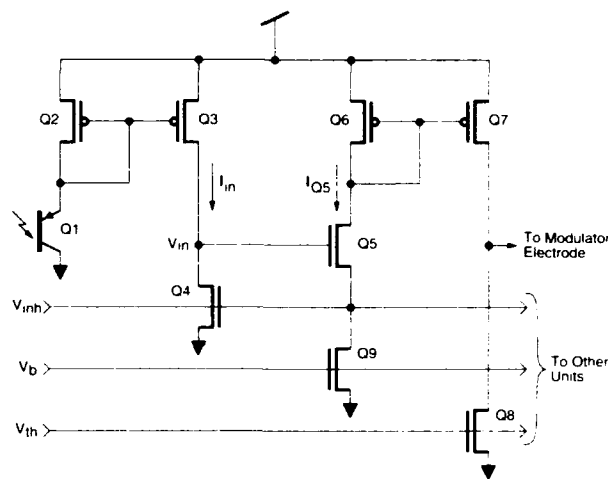


Figure 4: Schematic of the new WTA circuit.

the spaces in between the rows to prevent incident light from generating carriers in the substrate or affecting circuit operation. The holes in the light shield around the LC modulator pads and the detectors have been enlarged to expose more of the detector's sensitive area to light that falls outside of the modulator. Guard rings were put around the detectors in each unit to reduce crosstalk between units in the array, and wide guard rings were put around the entire block of 1-D arrays to prevent light hitting the chip outside of the arrays from contributing to the inputs of units around the edges.

Fig 6 shows the electrical response of the circuit in Fig. 4. The light from a Hewlett-Packard Q100 LED array is demagnified onto the chip so that each LED in the array is imaged onto a single WTA unit. The LED drive currents are generated and the modulator pad voltages are measured under computer control. To produce the data in Fig. 6, units 3-8 received an intensity of $3.7\mu\text{W}/\text{cm}^2$, unit 2 was set to $11.4\mu\text{W}/\text{cm}^2$, and unit 1 was varied around unit 2's input value. The control voltages V_b and V_{th} were both set to 1.0V. These settings gave the correct circuit operation over a wide range of input intensities. The outputs of units 3-8 in the array are not shown on Fig. 6, but were less than 0.01 V over the entire range of inputs. As Fig. 6 shows, the overlap between rising and falling unit outputs around the point of equality can be controlled by introducing small offsets between the V_{th} threshold and V_b bias voltage inputs. This may be useful as a kind of "vigilance" parameter in an optic 1 competitive learning system. [2]

Competitive Learning System

Figure 7 shows a block diagram of an optical competitive learning system that uses a VLSI/liquid crystal winner-take-all modulator. [4] A set of input patterns are applied one at a time to the input SLM. Some of the in-



Figure 5: Photomicrograph of the WTA unit fabricated in $2\mu\text{m}$ CMOS.

put light is diffracted by the volume hologram towards the array of VLSI/LC reflective modulators. The modulators are positioned in a sparse grid pattern which prevents crosstalk through the volume hologram by eliminating Bragg degeneracy. The winner-take-all competition circuit causes the pixel in each competitive patch which is receiving the largest input to switch the liquid crystal above that pixel to reflect the light back through the polarizer, which also blocks light from the losing units. Meanwhile, the undiffracted light that has passed through the volume hologram is retroreflected by the phase conjugate mirror. The phase conjugate beam interferes with the reflections from the winning pixels in the volume of the photorefractive crystal, strengthening the interconnections between the input pattern and each of the winning pixels. Thus, the optical system implements the competitive learning algorithm, with individual units in the competitive arrays becoming tuned to different statistical clusters of inputs.

In order to study the dynamics of the competitive learning system and the effects of device non-idealities, we have developed a computer simulation that uses the beam propagation algorithm. [4, 5] Figure 8 shows the fields that result as light from an array of 16 input modulators propagates through the system after learning has converged. The light from the modulators is collimated into a plane wave by a holographic lens, and enters a volume hologram, which learns to diffract light towards the WTA array. The diffracted light is focussed by another lens onto the detectors of a 2- and 5-unit WTA array. The unit in each array which receives the most optical power "wins" the competition and is activated for

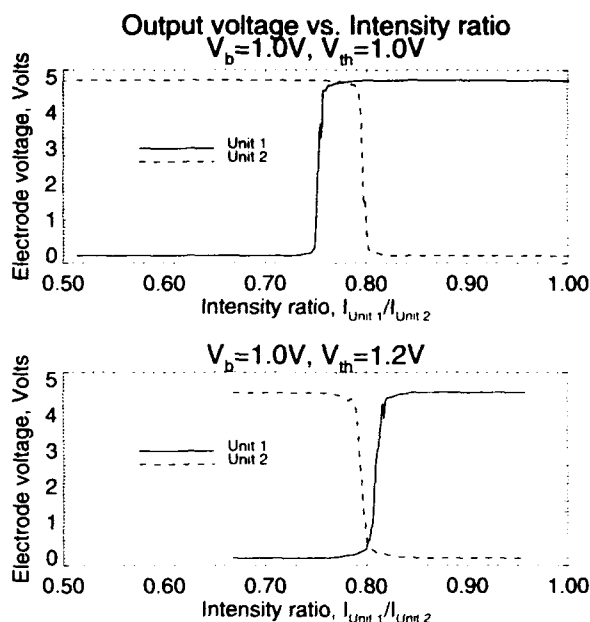


Figure 6: Modulator electrode voltage as input intensity ratio is varied, for two values of V_{th} .

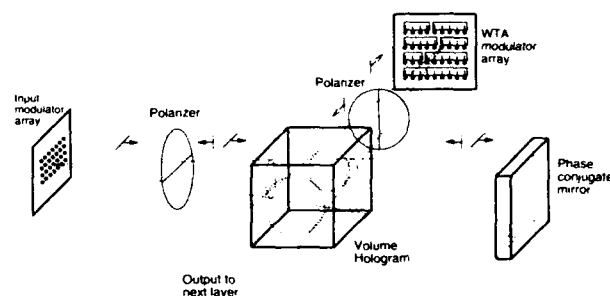


Figure 7: Optical competitive learning system architecture.

the backward pass of light through the system. In the backward pass, light from the WTA modulators interferes with a phase-conjugated version of the input beam in the volume hologram. The index of refraction at each point in the material is perturbed by an amount proportional to the intensity at that point minus an erasure term.

The cycle of input propagation, diffraction, winner-take-all, reverse propagation, interference, and index perturbation is repeated many times with inputs that are noisy versions of three binary patterns. The winning WTA units in each array become tuned to one or more of the input patterns by gratings that diffract light in a given pattern to that unit. Figure 9 shows the Fourier transform of the hologram index grating after 400 training cycles. The collimated input and WTA beams interfere to form planar gratings which transform to spots in Fourier space. In the

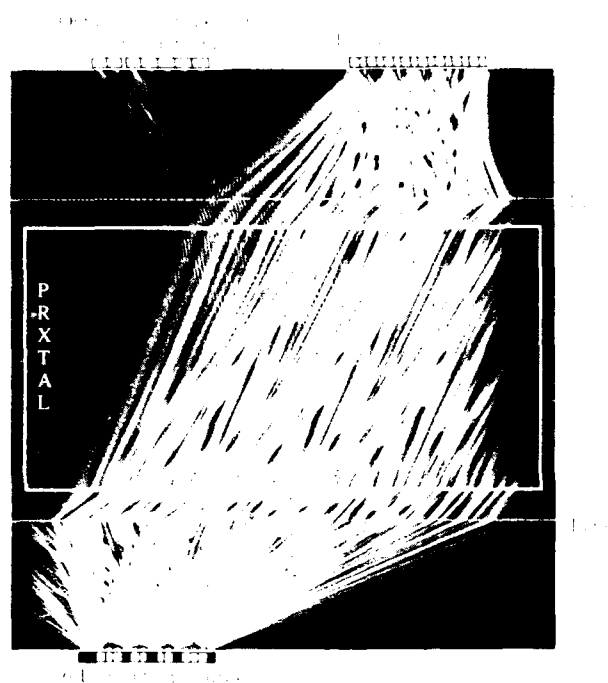


Figure 8: Simulation of optical field propagation in the competitive learning system

expanded section of the transform it is possible to identify the unique gratings that link each input pixel with an active WFA modulator. The ability to directly visualize the interconnection gratings, as well as the freedom to select device and system parameters such as contrast ratios, noise levels and recording rates make the beamprop simulations a useful tool for analyzing system behavior and guiding optoelectronic neuron development.

Summary

We have developed a new kind of spatial light modulator which uses the potential for nonlocal nonlinearities that "smart" modulators can offer. We will provide quantitative measurements of the optical properties of the improved one- and two-dimensional WFA devices. Simulations of the WFA devices in an optical competitive learning system are encouraging and provide a useful tool for determining system and device performance requirements.

We thank David Jared for useful discussions and Mark Handschy of Displaytech for filling chips. This work was supported by NSF Engineering Research Center grant number ECD-9018128 and by the Colorado Advanced Technology Institute (CATI), an agency of the State of Colorado.

References

- [1] D. Rumelhart and D. Zipser, "Feature discovery by competitive learning," vol. 9, pp. 75-112, 1988.

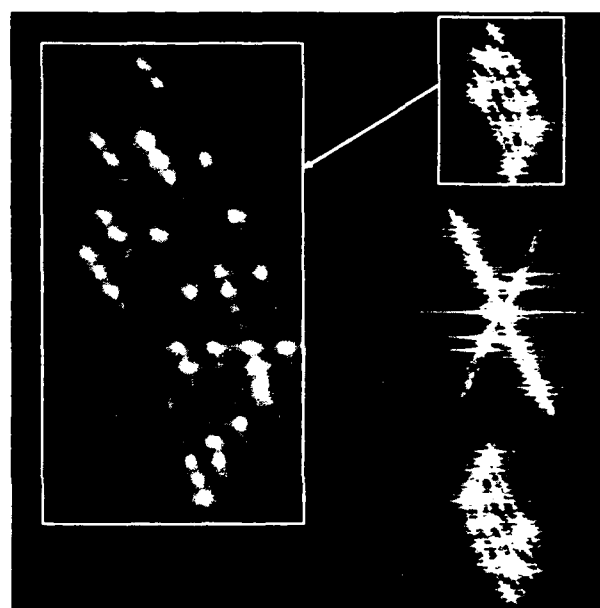


Figure 9: Fourier transform of the learned index gratings

- [2] S. Grossberg, "Competitive learning: From interactive activation to adaptive resonance," vol. 11, pp. 23-63, 1987.
- [3] J. Tazdaro, S. Ryckebusch, M. A. Mahowald, and C. A. Mead, "Winner take all networks of O/N complexity," in D. Touretzky, ed., *Advances in Neural Information Processing Systems 1*, Morgan Kaufmann, 1989, p. 703.
- [4] K. Wagner and L. M. Slagle, "Optical competitive learning with VLSI-liquid crystal winner take all modulators," *Applied Optics*, 1993. Submitted for Publication.
- [5] J. A. Fleck Jr., J. R. Morris, and M. D. Feit, "Time-dependent propagation of high-energy laser beams through the atmosphere," *Applied Physics*, vol. 10, pp. 129-160, 1976.

Multipurpose Spatial Light Modulator

Mark A. Handschy, David B. Banas

Displaytech, Inc., 2200 Central Avenue, Boulder, Colorado 80301
(303) 449-8933

Stephen D. Gaalema

Black Forest Engineering, Colorado Springs, Colorado 80962-2083
(719) 495-0735

Spatial light modulators (SLMs) with sophisticated pixel functions promise to enhance the performance of optical processing systems. A technique immediately at hand for making such SLMs uses a hybrid optoelectronic technology of ferroelectric liquid crystal (FLC) light modulating layers directly atop silicon integrated circuits. Silicon VLSI (very large scale integration) already offers an unmatched repertoire of electronic functions with unmatched miniaturization. FLCs permit the integration with silicon circuitry of fast ($100\ \mu\text{s}$) light modulators. We demonstrate the potential of this technology here with an SLM integrating photodetectors, light modulators, and intra-pixel processing to implement a "universal" function. Our device functions as an electrically addressed SLM, an optically addressed SLM, and as a camera. In its optically addressed mode it can programmably threshold, subtract, or invert images. Our design realizes these functions with a 14-transistor pixel that occupies $50 \times 50\ \mu\text{m}$ in $1.2\ \mu\text{m}$ CMOS design rules. We have verified our design with a 26×26 prototype implemented on a "TinyChip."

VLSI design. Figure 1 schematically shows the circuit of our pixel. Each pixel receives optical input through phototransistor Q1. Optical output is provided by the FLC modulator shown as capacitor C3. Offset nulling, image

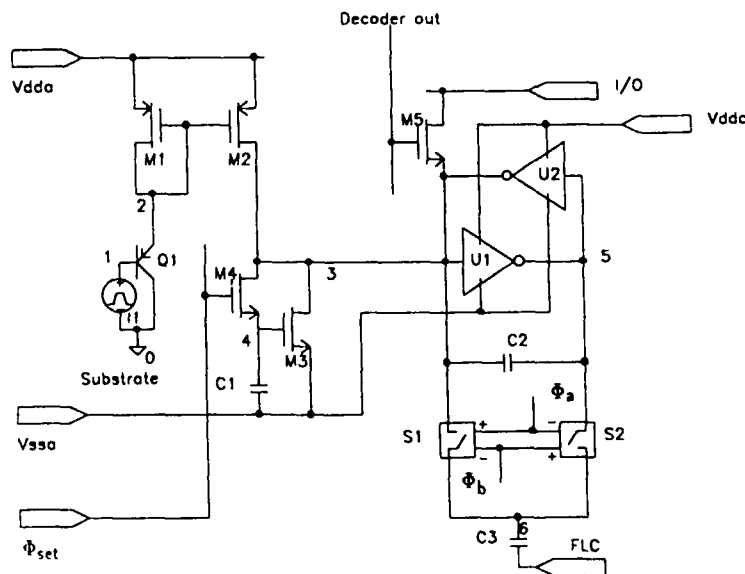


Figure 1: Pixel schematic.

subtraction, thresholding, and image memory are provided by the remaining circuitry. The phototransistor converts light intensity to a linearly proportional current which is mirrored by M1 and M2 onto the drain of M3. M3 provides a constant current load, which is set proportional to a REFERENCE intensity incident during a period when a high value of Φ_{set} causes M4 to conduct. C1 then charges up, increasing the gate voltage of M3 until its drain current just balances the mirrored photocurrent. After Φ_{set} falls C1 is isolated, and M3's drain current remains constant at the REFERENCE level. The REFERENCE image is then replaced by an INPUT image, and a current proportional to the images' intensity difference flows at node 3.

This difference current drives the input to the single-bit latch comprising coupled inverters U1 and U2. U2's transistors are made to have a higher threshold than U1's, so that at intermediate values of V_{ddc} U1 is on and U2 is off. In this intermediate state, the input difference current quickly charges or discharges, depending on its sign, the input of inverter U1, forcing its output to V_{ss} or V_{ddc} . Raising V_{ddc} to 5 V then closes the latch. This latch now stores the state of a sharply thresholded REFERENCE – INPUT image subtraction operation. The state of the FLC modulator can reflect either the stored bit or its complement, depending on which of S1 or S2 is closed. The stored state can be read out electrically by activating M5 and monitoring the state of the I/O line. This same line can alternately be used to write the state of the latch electrically.

The SLM element operation as described above has several desirable features. The high gain of the inverters provides a sharp thresholding action. The threshold level is adjustable, being set by the intensity of the optical reference image. The use of the same optical detector for both the reference and input images removes element-to-element variation in detector sensitivity. The use of uniform, featureless REFERENCE image provides simple globally-uniform thresholding, although the true capability is for image subtraction since the reference image can equally well contain data. The provision for memory in the static latch permits the modulator to be read out with high intensity light without corruption coming from the adjacent detector, simply by separating the read and write operations in time. By connecting together all the M5 gates in each column of pixels, and connecting together all the I/O lines in a row of pixels, the states of all the pixels in an SLM array can be written and read electrically in a column-sequential fashion identical to that in a conventional SRAM (static random access memory). This writing function permits the array to operate as an electrically-addressed SLM. The reading function, which can be either binary or analog, permits the array to operate as a camera.

We laid out this pixel circuit of Figure 1 in a $50\text{ }\mu\text{m}$ square using Orbit Semiconductor's $1.2\text{ }\mu\text{m}$ CMOS design rules. The pixel had a $475\text{ }\mu\text{m}^2$ phototransistor, and had a $47\text{ }\mu\text{m} \times 39\text{ }\mu\text{m}$ metal2 pixel mirror lying over the remainder of the circuitry. We fabricated a 26×26 array of pixels on a 2.25 mm square TinyChip.

Results. We assembled the TinyChips with small ITO-coated windows to make SLMs. The windows were first cleaned and coated with a rubbed nylon alignment layer. The windows were contacted to the chip, and glued in place. The thickness of the passivation overglass on the chip brought the window to within about $1.1\text{ }\mu\text{m}$ of the highest metal points in the pixel mirrors. The SLM was then vacuum filled with Merck ZLI-3654 at $100\text{ }^{\circ}\text{C}$, and cooled to room temperature.

Initial testing showed that test phototransistors identical to those in the pixels had a current gain of $\beta = 78$ and a response time of under $3\text{ }\mu\text{s}$ at modest illuminations. The complete photodetector circuit, including the current mirror with its gain of four, had a photosensitivity of $0.78\text{ }\mu\text{A}/(\text{mW}/\text{cm}^2)$. We optically addressed the SLM by illuminating it with a pair of LEDs. The first LED provided a spatially uniform REFERENCE image. The second LED was placed behind a simple mask imaged onto the SLM to provide the INPUT image. The two LEDs were activated at appropriate times while a simple clock circuit cycled the SLM's control lines. After the difference image was latched, the SLM was removed from the writing setup and transferred to a conventional polarizing microscope, where the photograph shown in Figure 2(a) was taken. Once written, the pattern could be inverted simply by reversing the levels on Φ_a and Φ_b . Performing this image inversion provided the simplest way to measure the modulator response times, which were less than $525\text{ }\mu\text{s}$. We were also able to electrically write the SLM, with the results shown in Figure 2(b). The structure within each pixel results from the mirror bumpiness, the imperfect OFF state being caused by FLC alignment nonuniformity, and the unsaturated ON state resulting from thickness-modulated retardance variation.

Conclusion. We have demonstrated the utility of FLC/VLSI hybrid optoelectronic technology in the form of a prototype SLM with pixels having a "universal" capability. The $50\text{ }\mu\text{m}$ pixel design and current foundry capabilities for 14 mm square silicon chips would enable a fully engineered device as large as 256×256 in the same $1.2\text{ }\mu\text{m}$ design rules used for the prototype. With a $65\text{ }\mu\text{s}$ FLC response time this device would yield a 1 Gb/s data rate. It could be used in iterative image processing systems where, for example, morphological processing steps were performed in sequence by transferring an image from one SLM to another through programmable transform optics in a "ping-pong" fashion. System input and output would proceed through the electrical I/O provisions of the SLM. Before such systems can be practical the SLMs must be planarized, as the current VLSI topography causes the mirrors to diffract strongly, with no single diffraction order having more than 1% of the incident light. We believe that adoption of current industry processes should achieve this goal in the near term.

This work was supported by the NASA Ames Research Center.

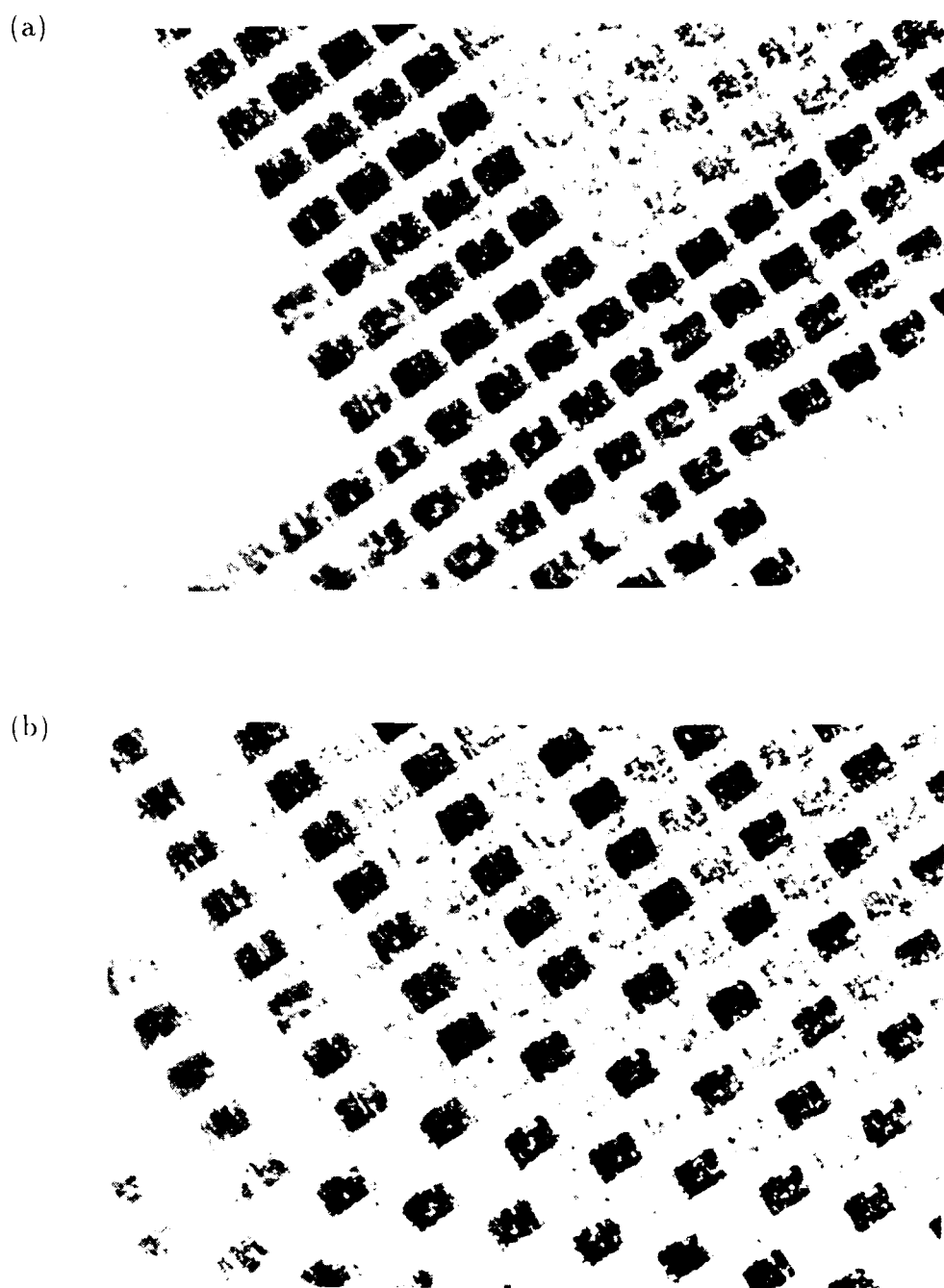


Figure 2: Photomicrograph of the prototype SLM showing (a) optically and (b) electrically written patterns. The pixels are on $50\text{ }\mu\text{m}$ square centers.

Optically addressed zero-crossing edge detection spatial light modulator

David A. Jared
Kristina M. Johnson

University of Colorado
Department of Electrical and Computer Engineering
Optoelectronic Computing Systems Center
Boulder, CO 80309-0525
jared@boulder.colorado.edu
kris@boulder.colorado.edu

1. Introduction.

This paper describes an optoelectronic system that performs zero-crossing edge detection using an VLSI, ferroelectric liquid crystal (FLC) spatial light modulator (SLM). The SLM consists of a VLSI CMOS backplane and FLC modulator. The FLC is sandwiched between the CMOS backplane and a sheet of glass coated with a transparent conductor.

In 1980, Marr and Hildreth [1] proposed a method of edge detection based upon locating the zero-crossings in an image convolved with the Laplacian operator and a Gaussian: $\nabla^2 g(x, y) * i(x, y)$. Abrupt changes in the spatial intensity of an image will produce a sign change when convolved with the Laplacian operator and a Gaussian. By examining the zero-crossings resulting from convolving the input image with Gaussians of different widths, a condensed sketch of the image can be compiled that reflects the information in the image.

Bair and Koch [2] demonstrated a one-dimensional, 64 pixel, analog CMOS chip that performed the "Gaussian" convolutions, and the zero-crossing detection. Two parallel resistive networks were used to perform the "Gaussian" convolutions. A differential amplifier followed by a exclusive-or circuit was used to identify the zero-crossings. The chip was successful, but the design does not readily scale to two-dimensions.

2. Optical System Design.

The optical system used to determine the zero-crossings is shown in Fig. (1). A defocused imaging system is used to performed the Gaussian convolutions. However, because only intensities can be detected, it is difficult to represent negative values. To be able to locate sign changes, a method of representing negative number had to be developed. Neg-

ative values are represented by performing the positive and negative parts of the Laplacian of a Gaussian kernel separately and subtracting the resulting convolutions on the CMOS SLM. The two convolutions are temporally separated. The two FLC polarization switches shown in Fig. (1) sequentially switch between two different optical paths to perform a convolution with two different Gaussian kernels.

The function of the zero-crossing section of the optical system is to combine the write-beam and read-beam so they can be imaged onto the CMOS SLM. A chrome-on-glass mask is used to combine the two beams. The chrome-on-glass mask consists of an array of micro-mirrors on 100 micron centers. The geometry of the mask matches the geometry of the CMOS SLM. The two temporally multiplexed images are reflected by the micro-mirrors and imaged only onto the phototransistors on the CMOS SLM. The read-beam is transmitted through the mask and imaged onto the liquid crystal modulating pads. The output of the CMOS SLM is imaged back through the polarizing beamsplitter. The output of the system is an image of the zero-crossing of the input image.

3. Zero-Crossing SLM.

A micrograph of the SLM is shown in Fig. (2). The SLM consists of an array of 32×32 pixels on 100 micron centers. The chip was fabricated using the n-well, low noise analog CMOS process provided by Orbit Semiconductor, Inc. and MOSIS.

The circuitry at each pixel consisted of a phototransistor, a transconductance amplifier with an hysteretical feedback element, a zero-crossing detection circuit, and a modulating pad as shown in the Fig. (3). The layout of the pixel is show in Fig. (4).

The transconductance amplifier with the hys-

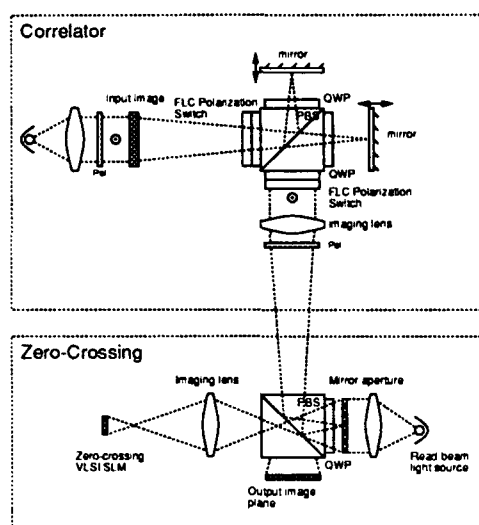


Figure 1: Schematic of the optical system that performs zero-crossing edge detection.

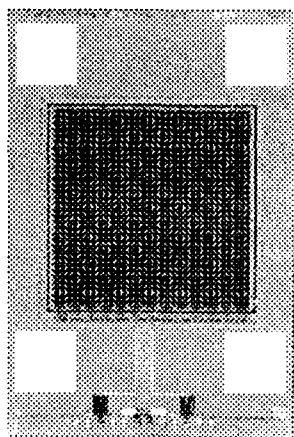


Figure 2: Micrograph of the zero-crossing SLM.

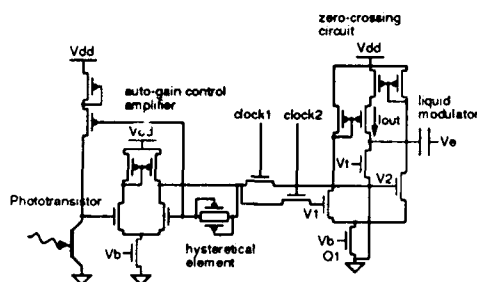


Figure 3: Schematic of the circuitry at a pixel.

teretical feedback element is an auto-gain control amplifier. This can be understood by examining the IV characteristics of the hysteretical elements. As can be seen in Fig. (5), the hysteretical elements behaviors like a large resistor when a small voltage is placed across it. This provides the amplifier with a high gain. However, when the voltage across the hysteretical element is larger than ± 1 V, the element has a small resistance. Thus, the amplifier will function as a source follower with low gain. These two operating regimes, coupled with the temporal response of the circuit, allows the circuit to adjust to the input light intensity and have the circuit operate over a larger input dynamic range.

The zero-crossing circuit consists of a differential pair with the currents mirrored together down a common path. The IV characteristics of this circuit are given by

$$I_{out} = \frac{I_b}{4} \sinh^2 \left(\frac{V_2 - V_1}{2V_0} \right) \quad (1)$$

Where V_1 and V_2 are signals from the two Gaussian convolved images, I_b is the current in the circuit set by transistor Q_1 , and $V_0 = \frac{kT}{e}$. Essentially, when V_1 and V_2 are near the same voltage, the circuit generates a current, and when V_1 and V_2 are not the same, the circuit generates no current. This is the essences of identifying a zero crossings: a zero-crossing corresponds to when V_1 and V_2 are near the same voltage.

4. Experimental Results.

The electrical characteristics of the auto-gain control amplifier and zero-crossing circuit have been tested. Figure (6) shows the response of the zero-crossing section of the pixel. As can be seen, when V_1 and V_2 are near the same voltage (i.e., a zero-crossing), the output of the circuit is 5 volts, and when V_1 and V_2 are not near the same voltage, the output of the circuit is 0 volts.

The response of the entire pixel was tested by illuminating the phototransistor with a light from an LED. A square wave current was applied to the LED to simulate temporally convolving an image with two different Gaussians. By varying the amplitude and offset of the square wave current, it was possible to examine how the pixel responds to zero-crossings (i.e., similar intensity) and to non-zero-crossings (i.e., different intensities). Figure (7) shows the output of the pixel as a function of ratio of the applied light intensities. As can be seen, when the ratio of the applied light intensities is near 1.0, the output of the circuit is 5 volts, but when

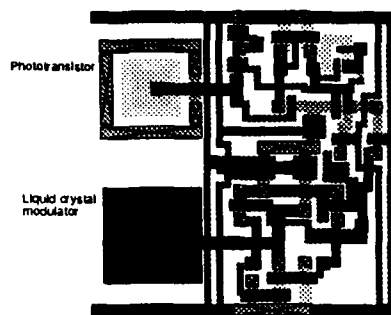


Figure 4: Layout of a pixel.

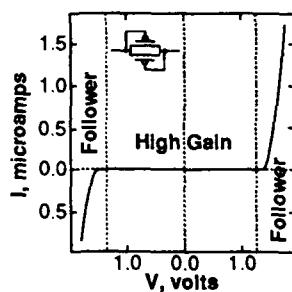


Figure 5: IV characteristics of hysteretical element in the auto-gain control amplifier.

the intensities differ, the output of the circuit is 0 volts. This indicated that circuit is functioning as expected.

References.

1. D. Marr and E. Hildreth, "Theory of edge detection", *Proceedings of the Royal Society of London, B*, 207, 187-217, 1980.
2. W. Bair and C. Koch, "An analog VLSI chip for finding edges from zero-crossings", *Advances in Neural Information Processing Systems 3*, 399-405, 1991.

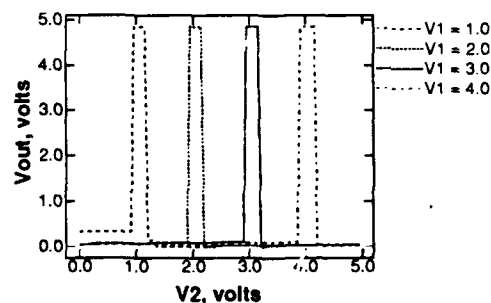
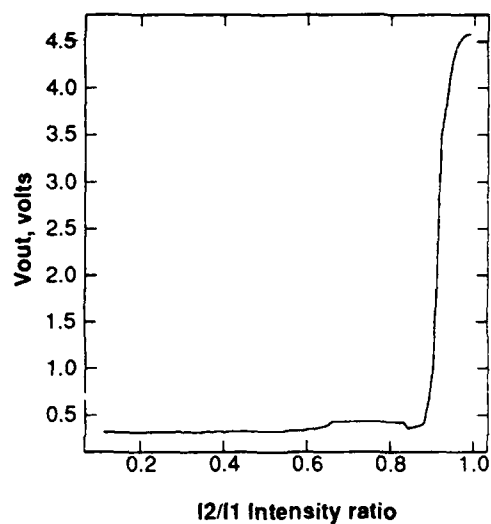
Figure 6: Experimental data from the zero-crossing section of the pixel. The output of the circuit is 5 volts when V_1 and V_2 is near the same voltage.

Figure 7: The output voltage of the pixel as a function of the ratio of temporally applied intensities.

DANE Switching Arrays for High Performance Computing (HPC) Modules

Peter S. Guilfoyle,
OptiComp Corporation, PO Box 10779, Zephyr Cove, NV 89448

David E. Grider
Honeywell Inc., 10701 Lyndal Avenue South, Bloomington, MN 55420

Bart Van Zeghbroeck
University of Colorado at Boulder, Optoelectronic Computing Systems Center,
Campus Box 525, Boulder, CO 80309

Introduction

High performance computing (HPC) modules are being developed which incorporate a 2-D GaAs, high speed, spatial light modulator called a DANE array (Figure 1).

DANE: Detection, Amplification, Negation, Emission

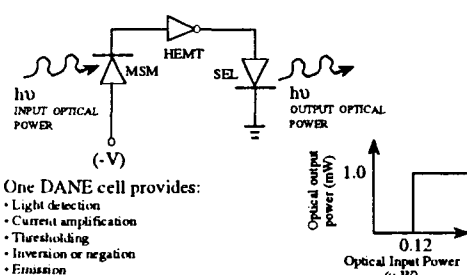


Figure 1: Simple example of a DANE cell

"DANE" is an acronym that refers to an array which [1] detects light, [2] amplifies the result, [3] negates the result (inversion) and [4] emits the Boolean value through the output laser. DANE is focused towards augmenting GaAs technology through free space "smart" optical interconnects.

This technology allows an all-GaAs implementation utilizing processes compatible with E/D MESFET (metal semiconductor field effect transistor) or CHFET (complimentary heterostructure field effect transistor) fabrication. This enhanced interconnect capability will maintain system level balance so that the faster processing capability can be fully utilized, which allows for a reduction in pipeline delays. The inherent benefits of integrating GaAs DANE technology with free space "smart" optical interconnects include:

- High FAN-IN and FAN-OUT
- Low power consumption
- High algorithmic efficiency by implementing wide word primitives (64 bit addition and multiplication)

- High noise margin
- Free space leverage of GIBP (gate interconnect bandwidth product)

Single Channel DANE Circuit

Figure 2 is a single channel DANE circuit. Figure 3 is a photograph of a single channel circuit. This initial prototype

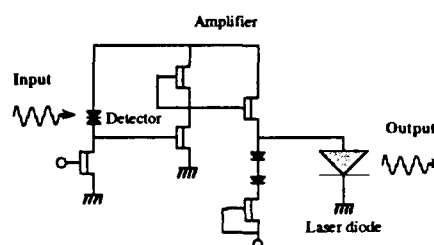


Figure 2: Layout of a single channel DANE circuit

of the GaAs DANE cell utilizes MSM detector technology and a two stage integrating current amplifier capable of driving 30 ma to the output laser. Ultimately, a transimpedance 3 stage amplifier will be utilized to achieve the specified system parameters.

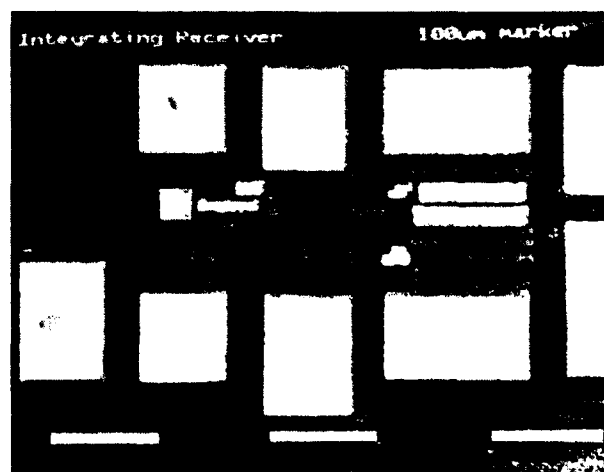


Figure 3: Photograph of a single channel DANE cell

the silicon carrier. Light focussed on the photodetectors as well as light emitted from the VCSELs is designed to pass through the GaAs [2].

Sub Nanosecond Potential and Balance of Power

Clock speeds may approach that of GaAs propagation delays (i.e., a few hundred picoseconds). Power consumption per gate can be reduced from 0.3 - 1 picoJoules (pJs) to a few femtoJoules (fJs) because of the ability to operate at the KT limit (i.e., logic level "zero" is the no light condition, and logic level "one" is shot noise limited to a few thousand photons).

Through the integration of GaAs with "smart" optical interconnect technology, signal extents will be on the order of a few millivolts and BERs (bit error rates) consistently may approach 10^{-18} . In order to obtain more accurate BERs, an on-off ratio for the laser diode of greater than 600 must be obtained which is why the laser must be initially biased below threshold (Figure 6). A large pulse may be applied to decrease delay in order to obtain this contrast. In contrast, the signal extents of conventional logic families range from one volt to several volts with BERs on the order of 10^{-15} . Thus, algorithmic flexibility is increased due to the ability to increase FAN-IN capabilities without the capacitive loading effects. This provides high speed at low power consumption levels.

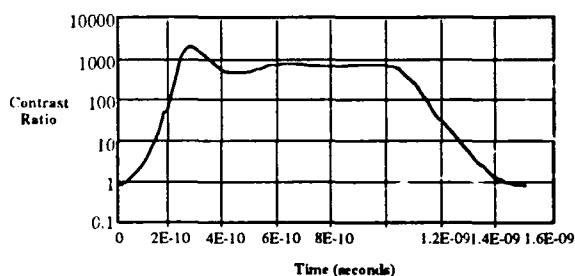


Figure 6: Contrast ratio for on-off pulsed operation

"Smart" Pixels

The "smart" pixel configuration emulates the binary multiplication of N-bits where N may approach 100 (Figure 7). The current architecture detects a large FAN-IN in an OR fashion (i.e. 0, 1 threshold, inverts the result and re-emits the result). The re-emission represents the Boolean multiplication of the input bits when the inputs are represented in inverted form by DeMorgan's theorem [3]. Consequently, "free space computation" of wide AND products are formed. Fixed and/or reconfigurable inter-

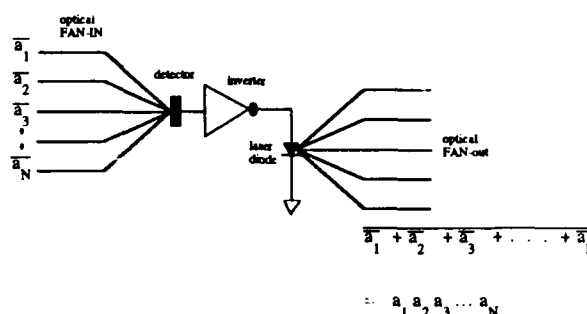


Figure 7: Simple example of "smart" interconnect which demonstrates DeMorgan's theorem on free space optical interconnects to achieve a wide input AND function

connects allow the introduction of control logic which ultimately allows specific AND/OR reprogrammable microcode control operation between stages of the GaAs structure.

Holographic optical interconnect elements (HOIEs) selectively image, in free space, each laser diode element on the DANE's surface emitting laser diode array to predetermined positions in the detector plane of the next DANE. This process occurs in accordance with the minterms and/or switching function(s) to be calculated (Figure 8).

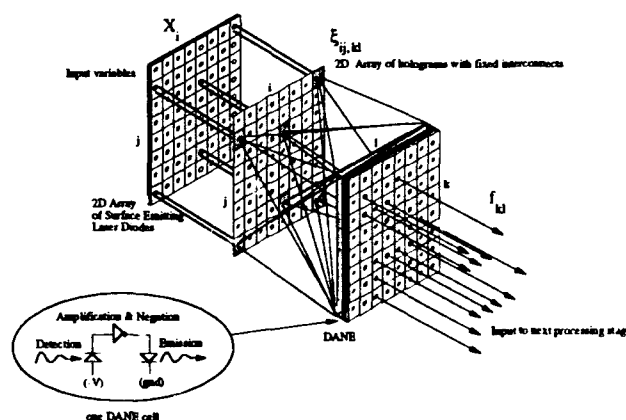


Figure 8: Single stage global free space "smart" interconnect module utilizing a 2-D DANE optoelectronic computing device forming arbitrary minterms

10^{14} Interconnects / Second

The number of bit operations per second per DANE / DBR, global interconnect module approaches N^4 times the clock rate. For 32×32 arrays of DANE cells, the total interconnect density may approach 32^4 or 10^6 . A 64×64 element array configuration provides over 16 million interconnect availability. In the 32 bit case, at a 100 MHz clock rate (which is considered to be slow for GaAs technology), the total sustained bit operations per second approaches 10^{14} .

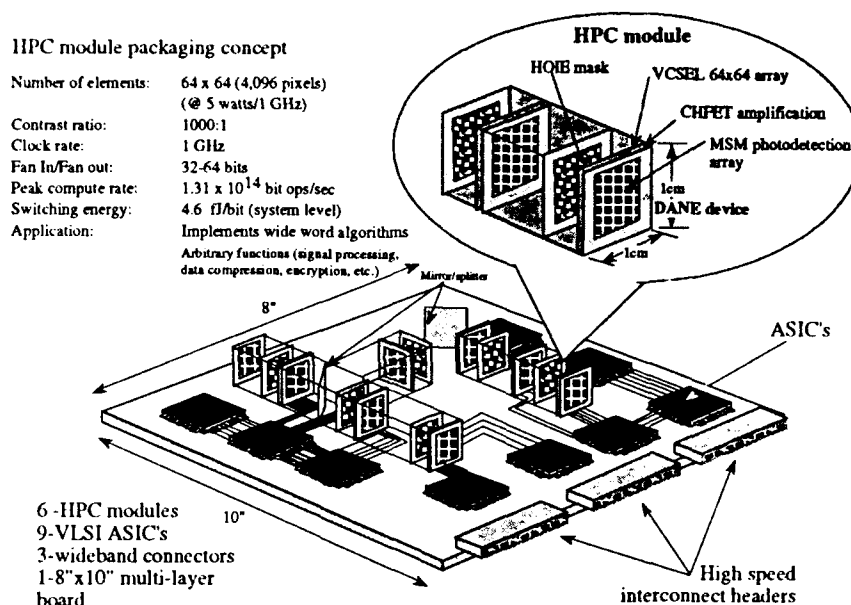


Figure 9: Layout of high performance computing (HPC) modules

HPC Modules

Each high performance computing (HPC) module consists of a DANE array, an HOIE mask and a global optical interconnect stage(Figure 8). The use of optical interconnect technology will allow 1 fJ per gate energy consumption. Thus, each module will dissipate at 10E14 bit operations per second at approximately 1 to 5 watts of power. This compares favorably with the kilowatt equivalent levels in current GaAs and tens of kilowatt levels in ECL. The reduced power consumption will allow for an increased density of modules.

It is anticipated that several HPC modules can be integrated onto a single "board". The proposed design also provides for HPC module feedback, thus increasing generic algorithmic computational capabilities. Several parallel and pipeline configurations of HPC modules are anticipated. HPC modules may be easily integrated into current and new electronic and optoelectronic architectures. Ultimately, large arrays of of "smart" pixel DANE arrays will be integrated on a single chip.

Conclusions

High speed, low power, HPC modules are being developed which integrate 2-D GaAs DANE switching devices with free space "smart" optical interconnects. The advantages of combining both technologies include: FAN-INS and FAN-OUTs approaching 128, speeds up to 10E14

bit operations per second, power consumption per gate on the order of few femtoJoules and BERs approaching 10^{-18} .

Acknowledgements

OptiComp's research has been sponsored by the Innovative Science and Technology Directorate at the Strategic Defense Initiative Organization through the Office of Naval Research.

References

- [1.] D.E. Grider, A.I. Akinwande, R. Mactaggart, P.P. Ruden, J.C. Nohava, T.E. Nohava, J.E. Breezley, P. Joslyn, and D.E. Tetzlaff, "Development of Static Random Access Memories Using Complementary Heterostructure Insulated Gate Field Effect Transistor Technology", 1990 IEEE GaAs IC Symposium Technical Digest 90CH22889-4, 143 (1990).
- [2.] J.L. Jewell, J.P. Harbison, A. Scherer, Y.H. Lee, L.T. Florez, "Vertical Cavity Surface Emitting Lasers: Design, Growth, Fabrication, Characterization," IEEE J. Quantum Electron., Vol. 27, pp. 1332-1348, (1991)
- [3.] P. S. Guilfoyle, "Motivation for DOC III: 64 bit digital Optical Computer", Proceedings of the SPIE, International Congress on Optical Science and Engineering, The Hague, Netherlands, Vol 1505, March 1991, PL04 (Plenary, invited).

Monday, March 15, 1993

Poster Session

SME 8:30pm-10:00pm
Grand Ballroom Center

The requirements for spatial light modulators for optical interconnection

Hiroyuki Ichikawa, Neil McArdle and Mohammad R. Taghizadeh

Department of Physics, Heriot-Watt University, Edinburgh EH14 4AS, UK

Tel: +44-31-449-5111

Fax: +44-31-451-3136

1 Introduction

The spatial light modulator (SLM) is an instrument for real-time wavefront transformation. Although one of the most attractive applications of SLM appears to be dynamic optical interconnection in computing and communications, existing SLMs are not capable enough to replace electronic counterparts. In this article, we discuss the required performance of SLMs for optical interconnections and state some problems arising.

2 Modelling

We limit our interconnection model to the one where both input and output beam arrays are in parallel to optical axis. This implies the system with two electronically addressed SLMs (Fig. 1(a)). The whole active area of the SLM is divided into $L \times L$ facets, each of which is illuminated by a Gaussian beam. Each facet consists of $M \times M$ pixels of width a (Fig. 1(b)). We also assume that the SLM is a multiple-phase-only modulator, and that the structure of the SLM is the same in both x - and y -directions. In order to achieve arbitrary (space-variant) interconnection, each facet should ideally be a saw-tooth grating, which deflects the input beam to the direction of the first diffraction order. Owing to pixellated SLM structure, the saw-tooth grating profile must be approximated by a quantised multilevel profile.

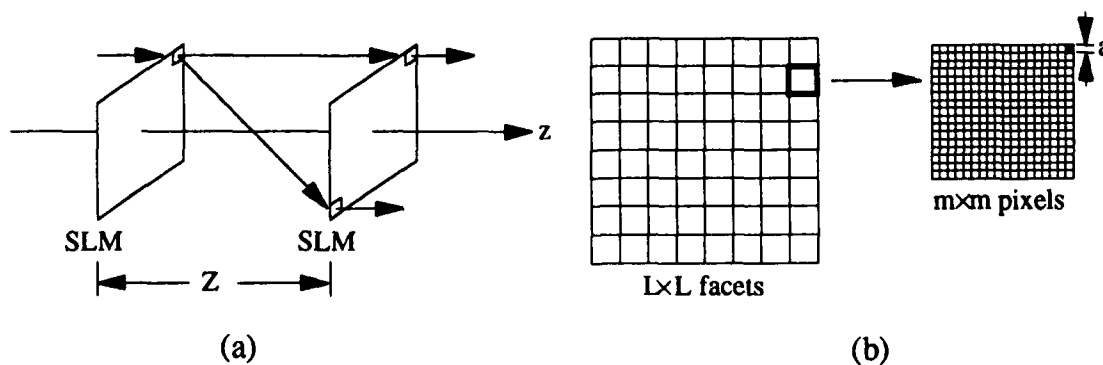


Fig. 1 Interconnection model with two SLMs.

The performance of the whole system is determined by the severest interconnection path, i.e. the largest deflection angle, which is realised with the smallest grating period. We denote by N the minimum number of pixels per grating period, by J the number of facets to be crossed in interconnection, by λ the wavelength in vacuum, and by p a fraction of the modulated area of a pixel. Then, the figures of merit for this interconnection system are written as follows:

$$\text{Interconnection distance: } Z = \frac{JMN a^2}{\lambda}, \quad (1)$$

$$\text{Diffraction efficiency: } \eta_N = \frac{\sin^4(\pi/N)}{(\pi/N)^4} \cdot p^2, \quad (2)$$

$$\text{Uniformity error: } U = \frac{1 - \eta_N^2}{1 + \eta_N^2}, \quad (3)$$

$$\text{Compression ratio: } C = \frac{1}{2} \left(\frac{\pi M}{JN} \right)^{1/2}. \quad (4)$$

Equation (1) for the minimum interconnection distance follows from the grating formula and simple geometrical considerations. Equation (2) represents the combined efficiency of two N -level phase gratings, while Eq. (3) is the worst-case uniformity error, obtained by assuming that both the severest interconnection path and an undiffracted path are present simultaneously. Finally, Eq. (4) for the beam compression ratio (the full $1/e^2$ width of the Gaussian beam/facet size) at both the input and output SLMs follows from Gaussian beam propagation laws, assuming that positive lenses of focal length equal to Z are also overwritten on the facets in order to rectify the beam-spreading owing to Fresnel diffraction.

The ultimate (ideal) target of the figures above and the effect of each parameter, i.e. whether increasing the value is a positive effect for the particular figure of merit or not, is given in Table 1. It is obvious that fine saw-tooth grating structure (large N) improves both η_N and U , but this leads to a long interconnection distance and poor beam compression ratio.

Table 1 The effect of SLM parameters on the figures of merit. + and - denote positive and negative effects towards the targets, respectively.

	Target	a	J	M	N
Z	≈ 0	-	-	-	-
η	≈ 1				+
U	≈ 0				+
C	$\gg 1$		-	+	-

3 Examples

As an example, we consider 8-facet SLMs with $50\mu\text{m}$ pixel size for fully arbitrary interconnection ($J=7$) and perfect shuffle ($J=3$). This is the pixel size of most advanced electronically addressed nematic liquid crystal SLMs. The number of pixels in one dimension of the whole SLM and free-space interconnection distance are shown in Table 2. To suppress the twin image, N needs to be at least 4, but as η_4 is merely 0.66 even when $p=1$, $N=8$ is preferred. Also $C > 1.5$ is needed to reduce crosstalk between neighbouring facets.

Table 2 The number of pixels and free-space interconnection distance.

C	N	Fully arbitrary		Perfect shuffle	
		Number of pixels	Z (m)	Number of pixels	Z (m)
1	4	288	4.0	120	0.71
1	8	568	15	248	2.9
1.5	4	640	8.9	272	1.6
1.5	8	1280	35	552	6.5

As seen, the free-space interconnection distance is too long even for perfect shuffle in a practical experiment. One of the techniques to reduce the distance is using the symmetrical combination of two afocal systems [1]. This achieves a reduction factor of approximately 10.

4 Concluding remarks

We showed some of the difficulties when SLMs are implemented in optical interconnections in computing and communications. These difficulties are mainly due to the poor resolution of currently available SLMs. The inactive area of each pixel also deteriorates the efficiency of the system significantly. In order to find a realistic role for SLMs, a small pixel size, i.e. even less than $10\mu\text{m}$, with high aperture ratio is required. This has to wait for a new fabrication technology.

References

- [1] H. Ichikawa, T. H. Barnes, M. R. Taghizadeh, J. Turunen, T. Eiju, and K. Matsuda, "Dynamic space-variant optical interconnections using liquid crystal spatial light modulators", *Opt. Commun.* **93**, 145-150 (1992).

Enhanced Performance of AlGaAs/GaAs Asymmetric Fabry-Perot Reflection Modulators

M. A. Gross

Electro-Optics and Physical Sciences Laboratory
Georgia Tech Research Institute
Georgia Institute of Technology
Atlanta, GA 30332
Tel. No. 404-894-3420

R. P. Kenan

School of Electrical Engineering
Georgia Institute of Technology
Atlanta, GA 30332

T. K. Tran and C. J. Summers

Electro-Optics and Physical Sciences Laboratory
Georgia Tech Research Institute
Georgia Institute of Technology
Atlanta, GA 30332

Optical bandwidth and contrast are key to the performance of all-optical asymmetric Fabry-Perot (ASFP) reflection modulators. Once a device has been grown and fabricated, these properties are completely determined by the absorptive and dispersive changes that occur with the nonlinearity, and how well impedance matched the device is initially. The question arises as to how bandwidth and contrast may be extended over a limited range of wavelength without much change in insertion loss for the existing device which usually is addressed with surface-normal light. This possibility is achievable without having to incur the expense of designing, growing, and fabricating a new device by considering operation of the device with off-axis, i. e., non-surface normal incident TE and TM light. This talk will focus on calculations that predict enhanced contrast and extended passband in such a situation and under what conditions reasonable increases in these parameters can be produced, and how they may be optimized by structural and

materials properties. The nonlinear cavity media studied are AlGaAs/GaAs multiple quantum wells and hetero-nipi structures.

Figure 1 shows the reflectivity of an all-optical ASFP reflection modulator designed to be addressed normally with TE light. All the reflectivity curves are calculated using a transfer matrix approach involving unimodular matrices and Chebyshev polynomials. The structure of the modulator consists of a Bragg reflector comprised of 15 periods of alternating AlAs and $\text{Al}_{.1}\text{Ga}_{.9}\text{As}$ $\frac{1}{4}$ -wave stacks on top of a GaAs base, followed by a 61 period 100 Å well and barrier width $\text{Al}_{.32}\text{Ga}_{.68}\text{As}$ /GaAs multiple quantum well structure, and a capping layer of $\text{Al}_{.32}\text{Ga}_{.68}\text{As}$ of sufficient thickness to place the Fabry-Perot resonance mode where desired. The linear and saturated absorption data for the calculation used to make Figure 1 was obtained from the literature.¹ The three lower curves in Figure 1 are for the linear absorption profile as a function of wavelength for 0, 5, and 7.5 degrees incidence, while the upper three curves are for the saturated profile at the same angles. Both absorptive changes and dispersive changes were used in the calculations. It should be noted that it is assumed that a pump write beam is used to produce saturation while the off-axis beam is the read beam.

Figure 2 exhibits the contrast ratios for the two sets of three curves of Figure 1 for each respective angle. The Fabry-Perot near-impedance matched resonance is located at approximately 852.5 nm. As can be seen from Figure 2, the contrast for normally incident operation is quite high, but there is a region to the left of the high peak where the contrast for the same device is higher at 5 and 7.5 degrees incidence than at 0 degrees. This higher contrast region effectively increases the passband of the device towards shorter wavelength without increasing the insertion loss.

The physical basis for these results is that at nonnormal incidence the effective optical cavity length $L\cos\theta$ is slightly decreased, shifting phase and thereby moving the reflectivity minimum slightly towards shorter wavelength. For this small shift in minimum, which is on the order of 1-2 Å, the structure still operates nearly impedance matched and the change in the absorptive and dispersive properties that occur when the absorption is saturated is compounded by the effective optical path length change for the upper off-axis curves of Figure 1.

The curves shown in Figure 3 are the ratios of the 5 and 7.5 degree incidence contrasts relative to the contrast at 0 degrees demonstrating the wavelength regions where the contrast is higher at these off-axis angles. The region where the ratio of contrasts is greater than 1 is where enhanced contrast and passband occurs.

The calculated results of Figures 1-3 are not representative of an optimized structure, but they nevertheless demonstrate the concept. The talk will address optimization and the use of other nonlinear cavity materials, such as hetero-nipi structures.

1. H-C. Lee, A. Kost, M. Kawase, A. Hariz, P. D. Dapkus, and E. M. Garmire, "Nonlinear Absorption Properties of AlGaAs/GaAs Multiple Quantum Wells Grown by Metalorganic Chemical Vapor Deposition," IEEE J. Quantum Electron., 24, 1581-1592 (1988).

Figure 1-Reflectivity vs Wavelength for ASFP Reflection Modulator

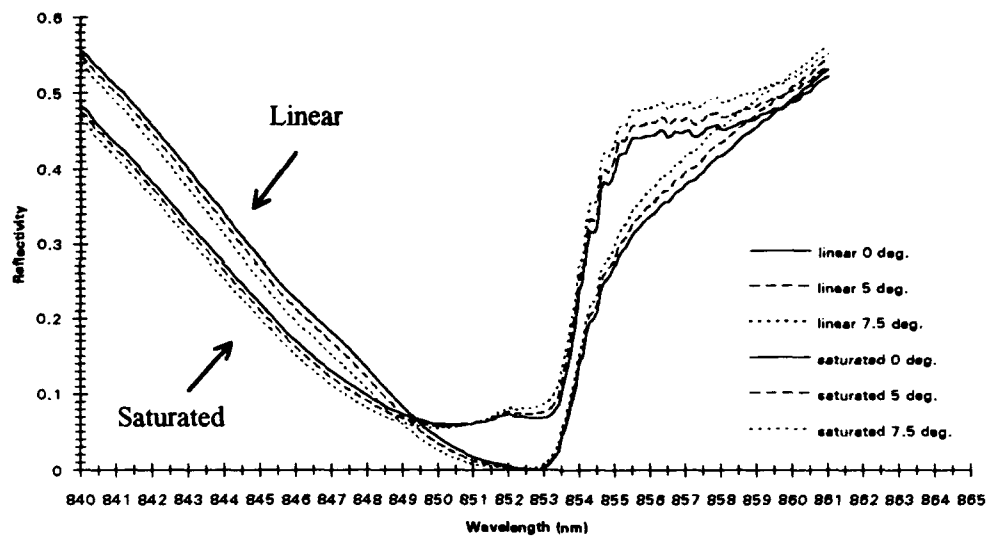


Figure 2-Contrast for ASFP Reflection Modulator

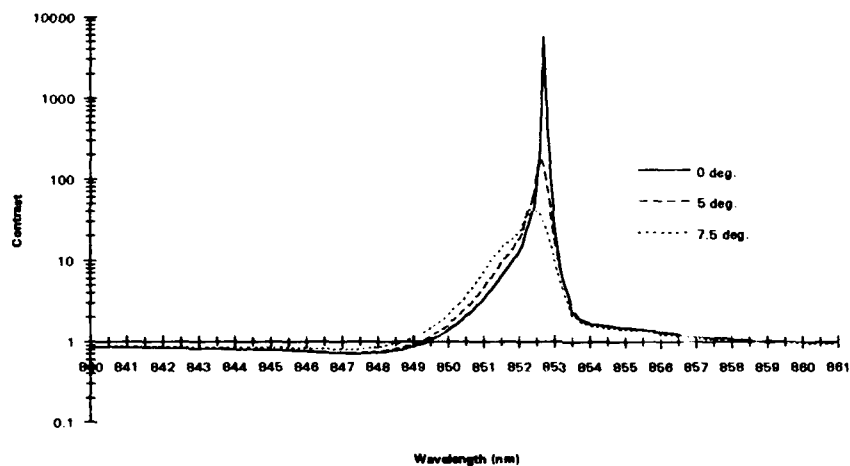
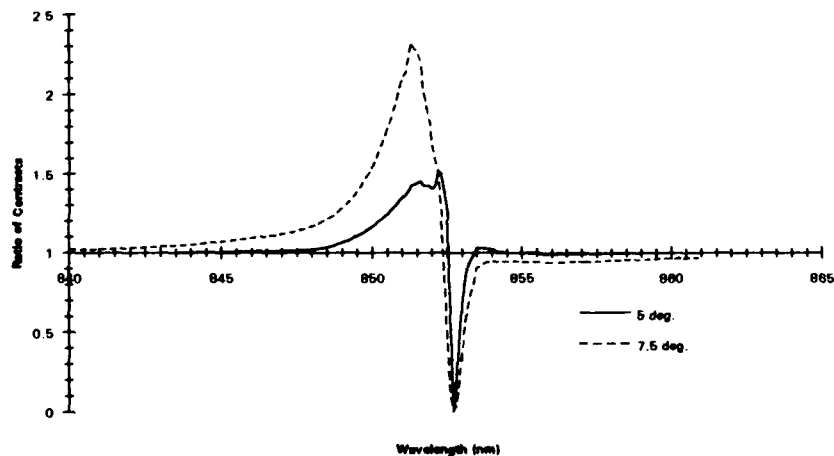


Figure 3-Ratio of Contrasts vs Wavelength for ASFP Reflection Modulator



**OPTICAL DATA SELF-ROUTING SYSTEM
BASED ON MULTIPLE QUANTUM WELL
MODULATOR AND OPTICAL BISTABLE MATRICES**

P. Chavel, P. Koppa, J. Taboury

Institut d'Optique Théorique et Appliquée

Bât. 503 - Centre Universitaire d'Orsay

BP 147 - 91403 Orsay Cedex (France)

Tel. : 33 1 69 41 68 41

J-L. Oudar, R. Kuszelewicz

FRANCE TELECOM - CNET

Laboratoire de Bagneux

BP 107 - 92225 Bagneux Cedex (France)

Tel. : 33 1 42 31 72 58

J-P. Schnell, J. Raffy, J-P. Pocholle, M. Papuchon

Thomson-CSF, Laboratoire Central de Recherches

Domaine de Corbeville, 91404 Orsay (France)

Tel. : 33 1 60 19 70 00

This work, currently in progress, is motivated by a general need to develop systems for optical information processing.

The system is an optical serial demultiplexor, which, through its address identification and channel switching functions, takes benefit of the ability of optics to deal with parallel processing and logic operations.

This self-routing system is schematically represented in figure 1 and involves 8x8 electrically addressed multiple quantum well SLM (figure 2) and bistable reflector (figure 3) matrices, optically conjugated.

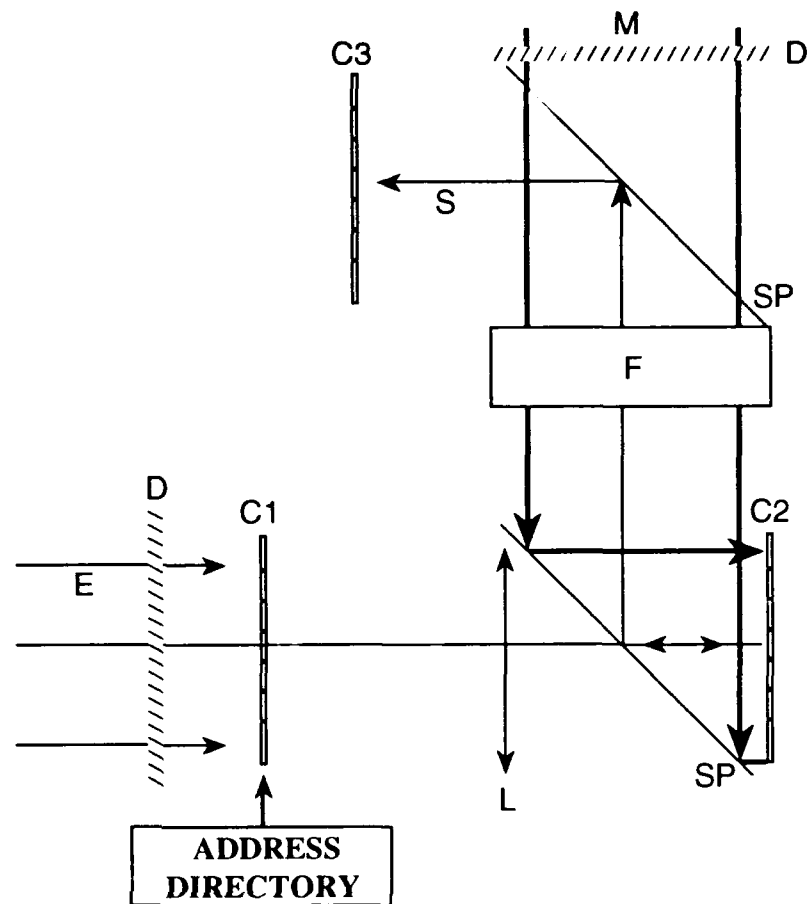
Briefly, it works as follows :

The bistable elements are initialized in their high reflectivity state by Damman grating generated 8x8 holding beams. The incident optical beam divided into 8x8 beamlets illuminates the whole SLM matrix. This beam carries a binary sequence in a temporal dual rail coding (01 for bit 0, 10 for bit 1) : the address of the channel to be selected, followed by the data to be transferred through it. A synchronizing pulse precedes the address and its arrival on the modulator matrix triggers each modulator pixel to deliver its own address in inverse dual rail code. By this way, only the selected channel transmits optical levels that never reach the bistable switching threshold. Consequently the corresponding bistable element keeps its high reflectivity state while all others switch to their low reflectivity state. The data that follow are thus transmitted through the selected channel only.

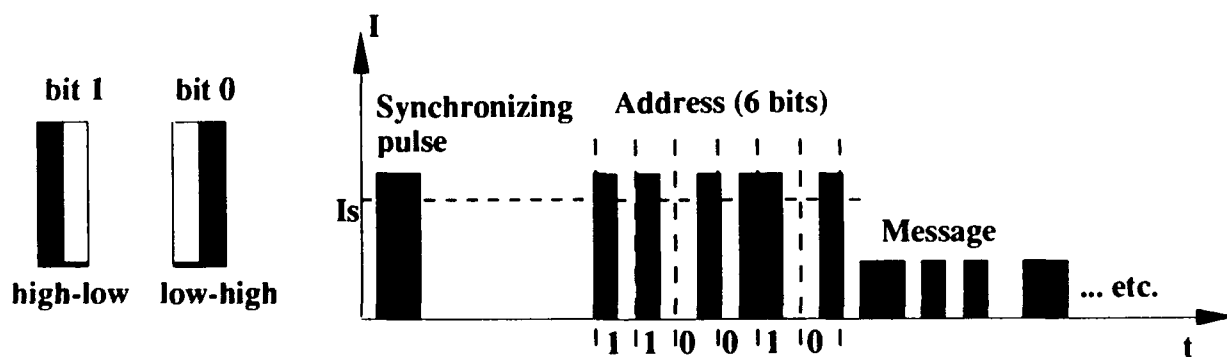
A detailed presentation of the components of this optical data self-routing system and of its working mode will be made.

This study has received a financial support from the French Ministry for Research and Space (MRE) within the project MOTS/OSTI 91.

- C1. Electrically addressed
MQW SLM 8x8 matrix
- C2. Optical bistable matrix
- C3. Photodetector matrix
- D. Dammann grating
- E. Input Optical beam
carrying the signal
- F. Faraday rotator
- L. Lens
- M. Holding beam
- S. Output signal
- SP. Polarizing beam splitter



1-a- Demultiplexor scheme



1-b- Signal coding, an example of input signal

Figure 1

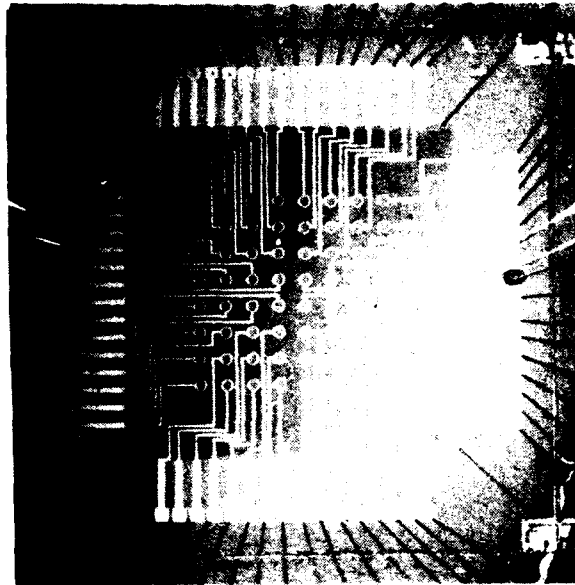


Figure 2 : 8 x 8 MQW SLM matrix

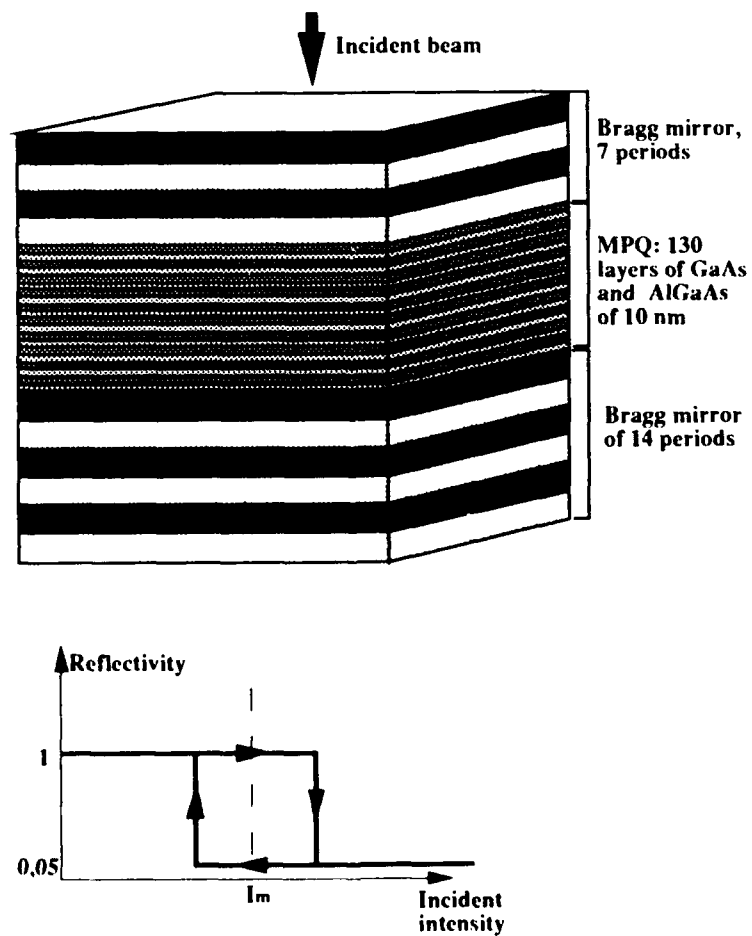


Figure 3 : Bistable device and its response curve

A Space-Modulating Ferroelectric Liquid-Crystal Light Valve and its Application to Multi-Valued Logic Gates

Shigeto Kohda, Yasushi Inaba, Noriyoshi Yamauchi
NTT Interdisciplinary Research Laboratories
Masakatsu Hirai
NTT Communication Switching Laboratories

3-9-11 Midori-cho, Musashino-shi, Tokyo, 180, JAPAN

I. Introduction

Electro-optical logic gates using liquid-crystal light valves (LCLV) have been studied for a wide range of applications including digital optical computing, optical communications and optical neural networks(1)(2). The large parallelism of LCLVs is a most attractive feature for innovations of computing algorithms but their processing speed may not be fast enough. To improve the performance of LCLVs, multi-valued or analog-valued computing algorithms have been proposed(3)(4). However, few actual devices have appeared on the stage due to the complex processing and subtle accuracy required. In this paper, we propose and demonstrate a high-speed multi-valued electro-optical modulator using a ferroelectric liquid-crystal light valve (FLCLV) and a space-modulation method based on spatially divided polarized light controlled by electronic binary signals. We also describe very simple multi-valued or analog logic gates by employing various configurations of FLCLVs and polarizers.

II. Binary Space-modulating FLCLV

Since FLCLVs have a fast switching speed and a memory effect, many efforts have been made to apply them to spatial light modulators and display devices. However, it is difficult to get a stable and accurate intermediate value only by controlling the voltage level because the switching mechanism of ferroelectric liquid-crystal molecules is virtually bistable with respect to the applied electric field (5). Instead of the voltage level control, we have developed a binary space modulation (BSM) method, which is controlled by digital signals and which utilizes the bistability of the molecule motion which is determined by applying either plus or minus voltage.

The structure of the space-modulating FLCLV cell is shown in Fig. 1. A cell is divided into stripe shaped subcells, each of which acts as an electrically controlled half-waveplate. Each subcell has a width in the ratio of 2^0 , 2^1 , 2^2 , ..., and is supplied with a voltage corresponding to a data bit "1" or "0" of a BCD coded digital signal that represents multiple values. When a voltage representing bit "1" is applied to subcells, the directors of the liquid-crystal molecule in the subcells are oriented 45 degrees towards the vertical direction, while applying a "0" voltage, the directors are oriented parallel to the vertical direction. Therefore, for a vertically polarized beam incident on the subcells of "1", the output beam irradiates with a polarization rotation of 90 degrees through the binary space-modulating (BSM) FLCLV. On the other hand, vertically polarized light passing through the subcells of "0" retains its polarization direction. Attaching a horizontal polarizer on the exit side of the cell, a stripe pattern shaped horizontally polarized beam is obtained. The total sum power of the stripe beam can be modulated with an accuracy according to the number of input bits. This modulation method not only can convert electrical signals to optical ones but also digital signals to

multi-valued or analog signals simultaneously.

To confirm the operation and to evaluate the accuracy of D/A conversion, a 4-bit space-modulating FLCLV has been fabricated. The cell size is 1-mm square and the subcells consist of a folded structure with a minimum width of $20\mu\text{m}$ to make the spatial distribution of light power in the cross section of the transmitted beams uniform. The response time of the FLCLV was about $80\mu\text{s}$ and the extinction ratio between the orthogonally polarized lights was more than 20 dB under DC voltage and for a wavelength of 633 nm.

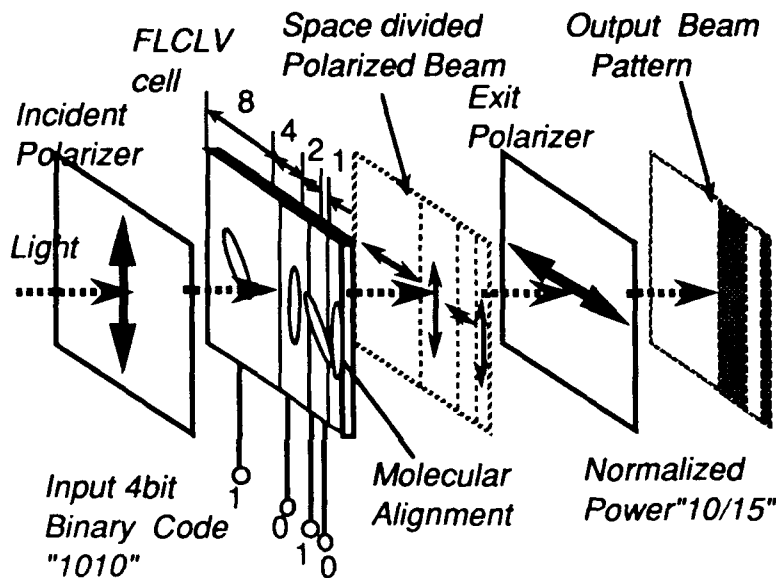


Fig. 1 Structure of the FLCLV cell and the principle of binary space-modulation (BSM) method.

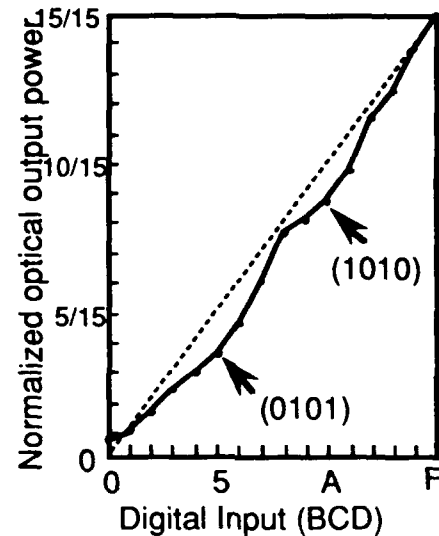


Fig. 2 Multiple-value of optical output power as a function of digital input.

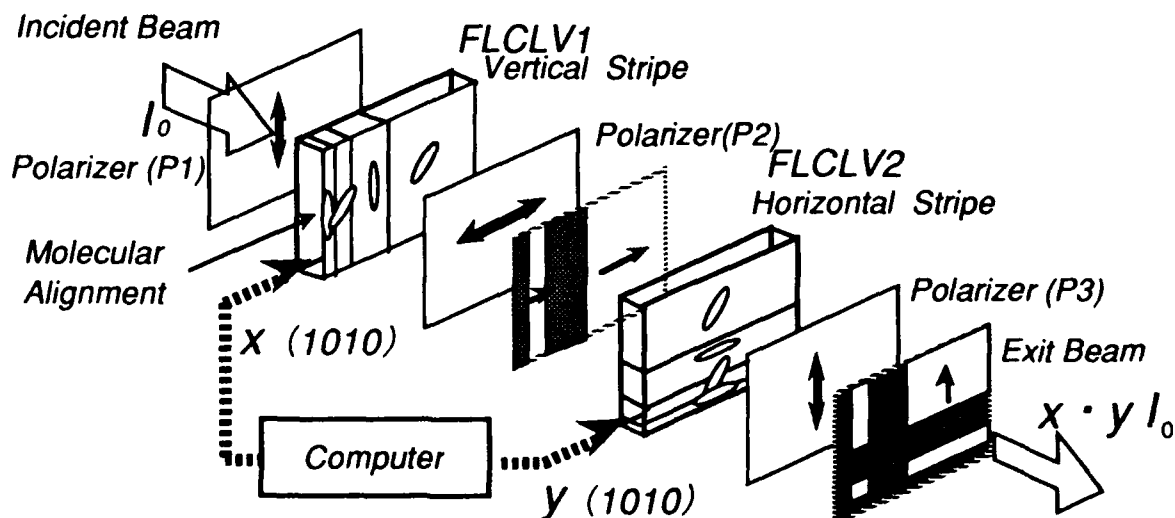


Fig. 3 Example of the configuration of multi-valued logic gate using two BSM FLCLVs.

When BCD-coded increment signals "0000" to "1111" are supplied to the FLCLV set up between the crossnichol polarizers, the sum of the transmitted light power measured by a Si-photodiode is shown in Fig. 3 as normalized optical power. The linearity of the modulated optical power is fairly good compared with other LCLVs. Large deviations from the expected value (dotted line) occurred at the input of "1010" and "0101", meaning that the error is mainly caused by diffraction of the stripe pattern of subcells.

III. Multi-Valued Logic Gates (MVLG)

Liquid-crystal optical logic gates for two independent binary variables have previously been investigated to implement Boolean logic using nematic LCLVs (1)(2). In this paper, we extend the binary data processing to the multi-valued or analog data processing by using newly developed space-modulating FLCLVs.

The implementation example of the MVLG which executes multi-valued multiplication is shown in Fig. 3. Two FLCLVs modulated by BCD-coded inputs x and y and three polarizers are stacked sequentially. The two FLCLVs are arranged to make the subcell stripe orthogonal to each other to provide the correlations between two FLCLVs. Various logic functions can be achieved by different combinations of polarizer directions. When the collimated beam passes through the MVLG, output light power represents the operation results. To clarify the states of polarization components in the MVLG, each implementation is expressed as a transfer function (6) of the input polarization vector (V_i, H_i) and the output one (V_o, H_o), where V and H denote the component of vertically and horizontally polarized light power.

$$\begin{bmatrix} V_o \\ H_o \end{bmatrix} = \begin{bmatrix} A & B \\ C & D \end{bmatrix} \begin{bmatrix} V_i \\ H_i \end{bmatrix}$$

The vertical and horizontal polarizer are expressed by

$$[P_V] = \begin{bmatrix} 1 & 0 \\ 0 & 0 \end{bmatrix}, \quad [P_H] = \begin{bmatrix} 0 & 0 \\ 0 & 1 \end{bmatrix}$$

The FLCLV spatially modulated by a multiple or analog value x is expressed by

$$[M(x)] = \begin{bmatrix} 1-x & x \\ x & 1-x \end{bmatrix},$$

where x corresponds to the horizontal polarization component. Hence, the general expressions of MVLG using two or three polarizers are

$$\begin{bmatrix} V_o \\ H_o \end{bmatrix} = [P_3][M(y)][P_2][M(x)][P_1] \begin{bmatrix} V_i \\ H_i \end{bmatrix}$$

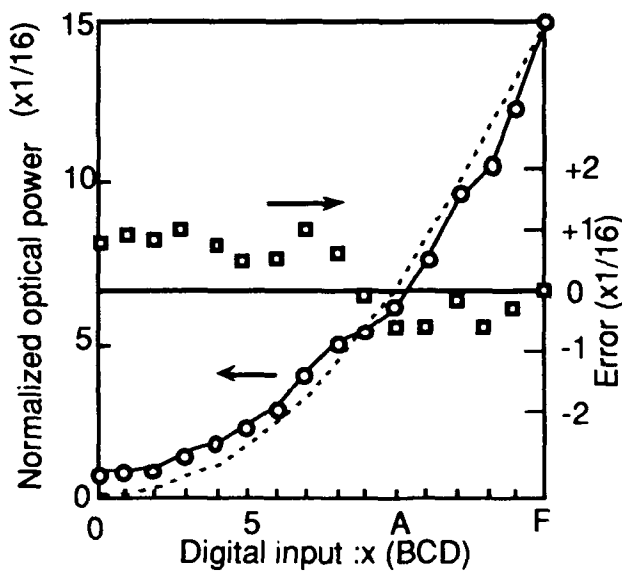
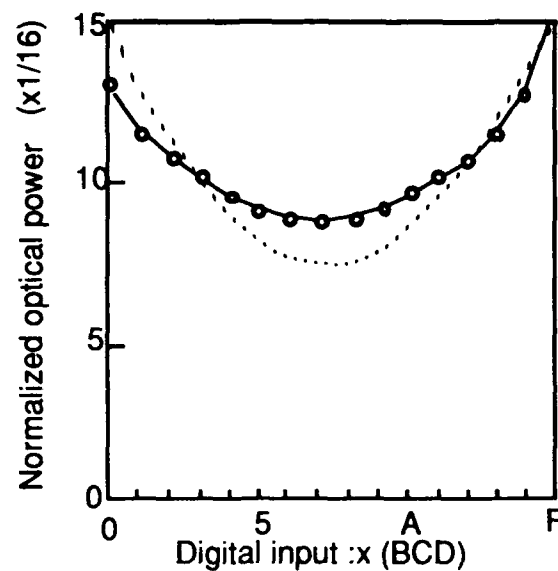
$$\begin{bmatrix} V_o \\ H_o \end{bmatrix} = [P_3][M(y)][M(x)][P_1] \begin{bmatrix} V_i \\ H_i \end{bmatrix}$$

Defining $\bar{x} = 1 - x$ and $x \cdot \bar{y} + \bar{x} \cdot y = x \oplus y$, six MVLGs can be derived from the above formulas as shown in table 1 with the similar expression to binary logic gates.

To confirm the operation of multi-valued algebra, some configurations were implemented and appreciated. Figure 4 and Fig. 5 show the normalized optical power of x^2 and $x \oplus y$ operations respectively as digital signal input is incremented from $x=y="0000"$ to "1111". The measured data (circles) agrees well with the expected value (dotted line). In Fig. 4 the deviation errors of the operation are also shown by a square. The deviations from expected values are in the range of $\pm 1/16$, that indicate a 3-bit accurate operation. These deviations are due to the degradation of the extinction ratio as well as the diffraction of the output beam of the FLCLV as mentioned above.

Table 1. MVLG functions obtained for various polarizer directions

Transparent direction of polarization			Multi-valued logic
P1	P2	P3	
Pv	Pv	Pv	$\bar{x} \cdot \bar{y} = \overline{x+y}$
Pv	Pv	PH	$x \cdot \bar{y} = x \subset y$
Pv	PH	Pv	$x \cdot y$
Pv	PH	PH	$\bar{x} \cdot y = x \supset y$
Pv	--	Pv	$\overline{x \oplus y}$
Pv	--	PH	$x \oplus y$

Fig. 4 Optical output power as a function of digital input showing accuracy of x^2 operationFig. 5 Optical output power as a function of digital input showing accuracy of $\overline{x \oplus y}$ operation

IV. Conclusion

A binary space-modulation (BSM) method to achieve multi-valued or analog optical processing has been proposed. The optical multiple values are controlled by electronic binary signals which are suitable for switching ferroelectric LCLVs, which are bistable and more than two-order faster than nematic LCLVs. We also proposed very simple optical multi-valued logic gates using these light valves. In addition, the operation of the BSM FLCLV and the MVLG were successfully demonstrated with experimental devices. The speed and accuracy of operations for electro-optical computing are significantly better than those of previous devices.

References

- (1) A. H. Khan and U. R. Nejjib: Appl. Opt. **26**, 270 (1987).
- (2) Y. Hanazawa and T. Uchida: Jap. J. Appl. Phys. **31**, L349 (1992).
- (3) T. T. Dao and D. M. Cambell: Opt. Eng. **25**, 14 (1986).
- (4) H. Mada, Y. Nakajima and T. Ozawa: Jap. J. Appl. Phys. **26**, L139 (1987).
- (5) N. A. Clark and S. T. Lagerwall: Appl. Phys. Lett. **36**, 899 (1980).
- (6) H. Hamano and T. Uchida: Trans. IEICE Jpn. **J73-C-II**, 703 (1990), (in Japanese).

Retina-like Adaptive Thresholding in a Nonlinear Joint Transform Correlator

K. L. Schehrer, L. Schirber, M. Handschy*, and M. G. Roe

Rockwell International, 6633 Canoga Avenue, Canoga Park, CA 91303

*Displaytech Inc., 2200 Central Avenue, Boulder, CO 80301

I. Introduction

Joint transform correlators, now made practical by the availability of many electrically- and optically- addressed spatial light modulators (SLM) and convenient coherent light sources, have been shown to be effective at both optical pattern recognition (OPR) [1] and tracking [2].

In this paper we present a novel retina-like adaptive thresholding (RAT) technique that greatly enhances the recognition and tracking performance of a nonlinear joint transform correlator (NLJTC). This technique can be readily implemented with a specific optically addressed integrated circuit spatial light modulator (ICSLM). In section II we introduce joint transform correlation and discuss the basis for the RAT. In section III, algorithm specifics and quantitative simulation results are presented. We summarize in section IV.

II. Retina-like Adaptive Thresholding Concept

Figure 1 shows a simplified schematic of a joint transform correlator. For illustrative purposes, consider two grey-scale SLMs at the input plane, and an optically addressed grey-scale SLM at the first Fourier transform (FT) plane. The reference and input functions are $r(x,y)$ and $f(x,y)$, respectively, with x in the plane and y out of the plane of the figure. The inputs are each a distance a from the optic axis, hence the input is $r(x+a,y)+f(x-a,y)$. Letting $R(\alpha,\beta)$ be the FT of $r(x,y)$, and assuming the FT-SLM to be linear in its response to the writing intensity, the read out of the FT-SLM is

$$\left[\|R(\alpha,\beta)\|^2 + \|F(\alpha,\beta)\|^2 \right] + \left[R(\alpha,\beta)F^*(\alpha,\beta)e^{+i2ka} \right] + \left[R^*(\alpha,\beta)F(\alpha,\beta)e^{-i2ka} \right] \quad (1)$$

This quantity is optically Fourier transformed and the resulting intensity at the second FT plane is captured with a detector array. The FT of the second and third terms gives the intensity of the correlation between $r(x,y)$ and $f(x,y)$, one correlation appearing $2a$ above axis and the other, its conjugate, appear $2a$ below the axis. When r and f are the same the correlation peak is large, and when r is a subset of f a correlation peak also appears, but can be surrounded by significant noise peaks. Thus, the appearance of a large peak intensity in the correlation indicates recognition of something that is similar to $r(x,y)$ in $f(x,y)$.

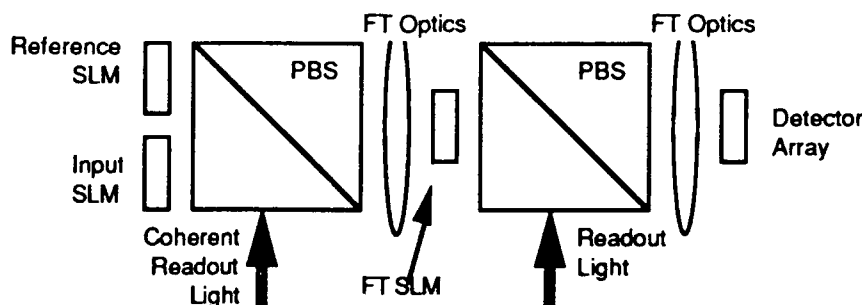


Fig. 1. Joint transform correlator.

The correlation terms in Eq. (1) give rise to an amplitude modulated grating of period $(\lambda/2\pi)(2ka)$. The correlation peak can be thought of as the diffraction peak from this grating. To make this even more apparent, consider a "special" FT-SLM that divides

the write light intensity by $|RF|$ before modulating the medium on the read out side of the FT-SLM, in this case a pure grating would be formed.

The *nonlinear* joint transform correlator (NLJTC) has been shown to have numerous advantages over linear JTCs and Vanderlugt architecture correlators. Namely, higher correlation peak values, higher peak to sidelobe ratios, and better discrimination [1]. A highly nonlinear, approximately binary, NLJTC can be implemented by placing a ferroelectric liquid crystal (FLC) optically addressed SLM (OASLM) [3] at the joint transform plane. By adjusting the voltage applied to the FLC-OASLM and the light intensity incident upon it, a spatially homogeneous binarization threshold is selected. However, since the FT of either of the input functions varies by orders of magnitude, the number of fringes that are written on the FLC-OASLM (FT-SLM) can be relatively few.

Hahn and Flannery [4] recognized that adaptive thresholding at the FT plane could substantially increase the number of fringes contributing to the correlation peak and thereby improve the performance of a correlator. Their technique uses the local *uniformly* weighted average intensity (over an $n \times n$ pixel window) at each pixel as a spatially varying threshold for the binarization process. While this technique works quite well, we are unaware of any SLM that can implement this algorithm intrinsically. Thus, such a scheme requires detection and computations prior to modification of the transform plane intensity and this increases both system complexity and processing time.

In contrast, the retina like adaptive thresholding (RAT) method we present here is implementable using an optically addressed integrated circuit spatial light modulator (ICSLM) with interconnected pixels. This device is a silicon retina, like that of Mead [5], coupled to ferroelectric liquid crystal as the light modulating medium [6]. Such a device has been constructed and tested at Displaytech Inc. The retina (animal or silicon) distinguishes local changes in intensity in a scene where the global intensity levels vary by several orders of magnitude. A thresholding scheme that follows its processing steps picks out variations in intensity that are large on a local scale but small on a global scale. The *amplitude modulation of the grating* discussed following Eq. (1) is thus made unimportant and a larger number of fringes result. (Retinas also enhance changes in time and this function was included in the device of Ref. [5]; however, this function is not exploited in the RAT.)

In the results presented below, we show that significantly more fringes are produced using this retina-like adaptive thresholding (RAT) as compared to the simple binarization and that the correlation peak intensity was therefore much higher.

III. Simulation Description and Results

The silicon retina ICSLM consists of an array of photoreceptors, each connected to a node in a resistor network that connects every node with its nearest neighbors. Each photoreceptor circuit produces an output voltage that is proportional to the natural logarithm of the incident intensity at its photodetector. The resistor network produces an exponentially weighted average of the logarithm input image, centered at the pixel in question. The weighting function has a maximum at the node connected to the corresponding photoreceptor and drops off exponentially in all directions. The output current of each retinal element is proportional to the difference between the voltage and the computed spatially averaged voltage. When this current exceeds a threshold, the corresponding FLC pixel is turned ON, else it remains OFF.

To simulate the silicon retina, an incident intensity $A_{i,j}$ is considered, and from it $B_{i,j}$, which is an exponentially weighted average of $\ln(A_{i,j})$ is computed; i.e.,

$$B_{i,j} = \frac{1}{V} \sum_{k=-r}^r \sum_{l=-r}^r w_{k,l} \ln(A_{i+k,j+l}) \quad (2)$$

$$w_{k,l} \equiv \exp\left[-\frac{\sqrt{l^2 + k^2}}{\sigma}\right], \quad V \equiv \sum_{k=-r}^r \sum_{l=-r}^r w_{k,l}$$

The weighting factor $w_{k,l}$ determines the contribution of neighboring $A_{i+k,j+l}$ to the value of $B_{i,j}$ at point (i,j) , and V approximates the integrated volume under the exponential. In an actual hardware implementation of the silicon retina the smart pixel interconnections include a resistor network that effects the averaging over an r [Eq. (2)] that extends over the pixel array. In the simulation, we chose to limit r to some finite value much smaller than the size of the pixel array. The relative contributions of neighboring $A_{l,m}$ to $B_{i,j}$ are set by choice of σ , which is not necessarily an integer.

In an ICSLM implementation of the retina, $B_{i,j}$ are compared by the circuitry to the values $\ln(A_{i,j})$, and when that difference exceeds some threshold, T , that pixel is turned ON. In other words, the read out of the FT-SLM at the (i,j) pixel is given by $O_{i,j}$, following Eq. (3):

$$O_{i,j} = \begin{cases} 1, & B_{i,j} - \ln(A_{i,j}) > T \\ 0, & B_{i,j} - \ln(A_{i,j}) \leq T \end{cases} \quad (3)$$

In this way, the only pixels that are turned ON are those at points in the pixel array where the intensity changes appreciably relative to its neighbors.

The images used in the simulation are shown in Figure 1, they are nominally 256×256 eight bit images. Image 1 was captured by imaging a model of a T-72 tank onto a CID detector array with the CID camera elevated to a 17° aspect angle and the range adjusted to capture approximately one hundred pixels across the body of the tank. Image 2 is a binarized version of image 1. Image 3 is the result of an exclusive OR of image 1 with a photograph of some woods at the edge of a pond. The edges of the background were made jagged to disrupt the $(\sin(X)/X)^2$ modulation due to the square aperture. The fourth image was formed by adding uniformly random noise from zero to 255 with mean spatial period of eight pixels.

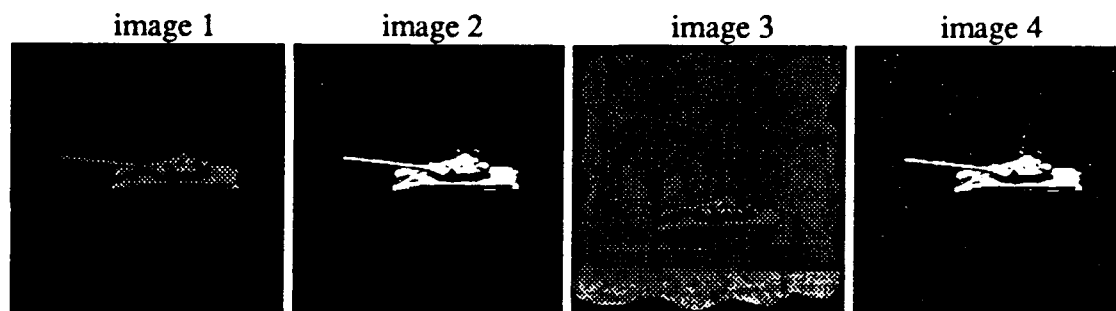


Fig. 2. Images used in JTC simulation

To illustrate the effect of using RAT we correlated Image 1 with Image 2 and computed the intensity of the joint transform. Figure 3a shows this intensity over a relatively small (21×21) region in the transform plane. The amplitude modulated fringes discussed following Eq. (2) are apparent in this figure. For a simple binarization as is performed by a homogeneous optically addressed SLM such as that of Ref. [3] the binarization is not effective in extracting the fringes as seen in Fig. 3b. To obtain Figs. 3c and 3d, we applied Eqs. (2) and (3) and set $(r,\sigma)=(2,0.5)$ and $(12,3)$, respectively. It is clear in these figures that RAT can be very effective in extracting the fringes that contribute to the correlation peak. Note that r is large with respect to σ in the sense that, at $r/\sigma=4$ the weighting function is $\exp[-4]=0.018$ its maximum value.

The simple binarization resulted in a correlation peak of $1.14\text{e-}4$, while that for $(r,\sigma)=(2,0.5)$ gave $22.04\text{e-}4$, that for $(r,\sigma)=(12,3)$ gave $15.71\text{e-}4$. It is straightforward to see the reason that the cases $(r,\sigma)=(2,0.5)$ and $(12,3)$ result in nonnegligible differences in correlation peak value. The separation of the input images leads to a sinusoidal modulation with period of order four pixels in the transform plane; hence, a weighting function with a diameter of this order is most effective in isolating the peaks from the troughs in the sinusoidal modulation; i.e., forming the highest efficiency diffraction grating.

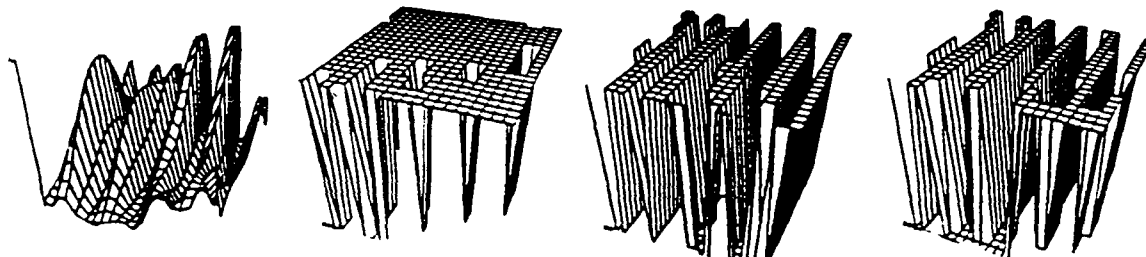


Fig. 3 Incident transform plane intensity, a), simple binarization, b), RAT with $(r,\sigma)=(2,0.5)$, c), and RAT with $(r,\sigma)=(12,3)$, d).

While Fig. 3 illustrates qualitatively that RAT should produce better correlations than a simple binarization, the table below quantifies RAT performance over a broader range of r and σ , and includes the cluttered and noisy images of Fig. 2.

r,σ (pixels)	1 vs 2	2 vs 3	1 vs 4	3 vs 4
simple binarization	1.14 / 0.13	1.06 / 0.14	0.39 / 0.05	0.25 / 0.04
2.0,0.5	22.04 / 1.05	3.54 / 0.33	3.03 / 0.11	0.87 / 0.13
4.0,1.0	21.92 / 0.90	4.56 / 0.30	2.99 / 0.11	0.95 / 0.11
6.0,1.5	21.30 / 0.83	4.68 / 0.29	2.80 / 0.08	1.02 / 0.08
8.0,2.0	19.45 / 0.70	4.70 / 0.27	2.59 / 0.07	0.99 / 0.08
12.0,3.0	15.71 / 0.58	4.41 / 0.23	2.23 / 0.06	0.88 / 0.08

Table: Computed values, $\times 10^{-4}$, of the correlation peak divided by the largest noise peak

IV. Conclusion

We have shown that, compared to a simple binarization, the retina-like adaptive thresholding (RAT) technique improves correlation performance by more than an order of magnitude for an image versus a matched binarized filter. The presence of noise in the matched filter or the addition of clutter to the image reduces the performance improvement factor but still produces a substantial fourfold increase in correlation peak intensity. We suspect that in our further exploration of the (T, r, σ) parameter space, we will find regions of that space that are more effective for noisy and cluttered images.

References

1. B. Javidi, C. J. Kuo, Appl. Opt. **27**, (1988).
2. E. C. Tam, F. T. S. Yu, D. A. Gregory, and R. D. Juday, Opt. Eng. **29**, (1990).
3. W. Li, R. A. Rice, G. Model, L. A. Pagano-Stauffer, and M. A. Handschy, IEEE Trans. Electron. Devices, **36**, (1989)
4. W. Hahn, D. Flannery, Opt. Eng. **31**, (1992).
5. C. Mead, *Analog VLSI and Neural systems*, (Addison-Wesley, Reading, MA, (1989).
6. M. Handschy, T. J Drabik, OSA Technical Digest, V-15 pp 259 (1990).

Polarization Behavior of a Ferroelectric Liquid Crystal Light Valve

W. Xue and N. Collings

Institute of Microtechnology, University of Neuchâtel,

CH-2000 NEUCHÂTEL, Switzerland.

Tel: +41 38 20 52 75

Fax: +41 38 25 42 76

Introduction

Surface stabilized ferroelectric liquid crystal spatial light modulators (FLCSLM's) might be used in both neural network and optical interconnect applications^{1,2}. In such applications, it is required that the FLCSLM rotates the polarization vector of the light field through 90°. Moreover, if the read-in light is linearly polarized, then the read-out light should also be linear. However, a linearly polarized read-out beam is only obtained when the liquid crystal cell satisfies the half-wave condition. The retardation of the cell depends on the thickness and the birefringence of the liquid crystal layer at a given wavelength. We assume that in a surface stabilized FLC the birefringence does not change with electric field. Therefore it is the manufacturing tolerances associated with engineering the correct thickness which are of concern. An incorrect thickness will result in an elliptical polarization. Of equal concern is the correct choice of liquid crystal material in order to assure the 90° rotation. Our purpose, here, is to elucidate the basic theory and to present some experimental results on a ferroelectric liquid crystal light valve (FLCLV) so that the manufacturers of such devices understand where improvements should be made. It is also hoped that the theory will allow the experimental arrangement to be optimized when imperfect devices are used.

The configuration and operating principles of the FLCLV

The FLCLV (fabricated at BNR Europe) consists of three main parts between two transparent electrodes: the hydrogenated amorphous silicon (a-Si:H) photosensor; the smectic C ferroelectric liquid crystal layer; and the metal mirror assembly. The mirror is pixellated with 20µm repeat spacing in order to maintain good resolution. The basic characterization of this device is reported in ref. 3.

Because of its inherent bistable states, a FLCLV must be driven by using a bipolar waveform. A pulse of one polarity SETS the spatial distribution of director orientation according to the image incident on the write side, and a pulse of opposite polarity ERASES that distribution. In our experiment, the positive pulse in the drive waveform corresponds to the ERASE pulse, which switches the valve off, and the negative pulse corresponds to the SET pulse, which enables the write light to switch the valve on.

The polarization characteristic of the FLCLV

A. Theoretical analysis.

In the general case, the polarization behavior of a surface stabilized FLCLV can be described by two Jones matrices, one each for the OFF- and ON-states:

$$J_{\text{off}} = \begin{bmatrix} \cos \frac{\Delta}{2} - i \sin \frac{\Delta}{2} & 0 \\ 0 & \cos \frac{\Delta}{2} + i \sin \frac{\Delta}{2} \end{bmatrix}; J_{\text{on}} = \begin{bmatrix} \cos \frac{\Delta}{2} - i \sin \frac{\Delta}{2} \cdot \cos 2\gamma & -i \sin \frac{\Delta}{2} \cdot \sin 2\gamma \\ -i \sin \frac{\Delta}{2} \cdot \sin 2\gamma & \cos \frac{\Delta}{2} + i \sin \frac{\Delta}{2} \cdot \cos 2\gamma \end{bmatrix}$$

where $\Delta = 4\pi \delta n d / \lambda$ is the retardation of the cell, and γ is the rotation angle of the liquid crystal director between OFF- and ON-states. (The birefringence and thickness of the cell are δn and d , and the wavelength of light is λ .)

Provided the read-in light is linearly polarized and the polarization is parallel to the LC director, the read-out light in the ON-state can be described by the following equations, which relate the parameters describing the polarization state of the read-out light to the parameters describing the state of the liquid crystal⁴:

$$\sin 2\varepsilon = \sin 2\gamma \sin \Delta \quad (1)$$

$$\tan 2\theta = \tan 2\gamma \cos \Delta \quad (2)$$

where $\tan \varepsilon = b/a$ and b, a, θ are as illustrated in Fig.1.

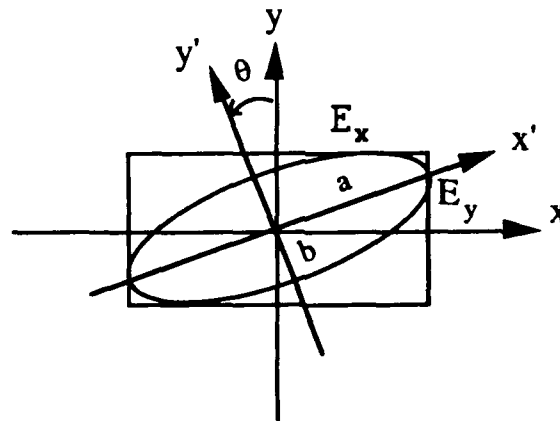


Fig. 1 The elliptical polarization state of the read-out light in the ON-state.

The ellipticity ε and orientation θ of the read-out polarization depend on the director rotation γ and the retardation Δ as shown in Figs. 2 and 3, respectively. From Fig.2 it can be seen that the ellipticity is more strongly dependent on the retardation Δ than on the director rotation γ . In contrast, Fig.3 shows that the orientation θ is only weakly dependent on the retardation Δ . One consequence of this is, for example, that when the director rotates 45° and the ellipse has an orientation of 90° , then we can have crosstalk in the vertical polarization channel. This crosstalk is rarely observed because a polarizer is oriented with the major axis of the ellipse.

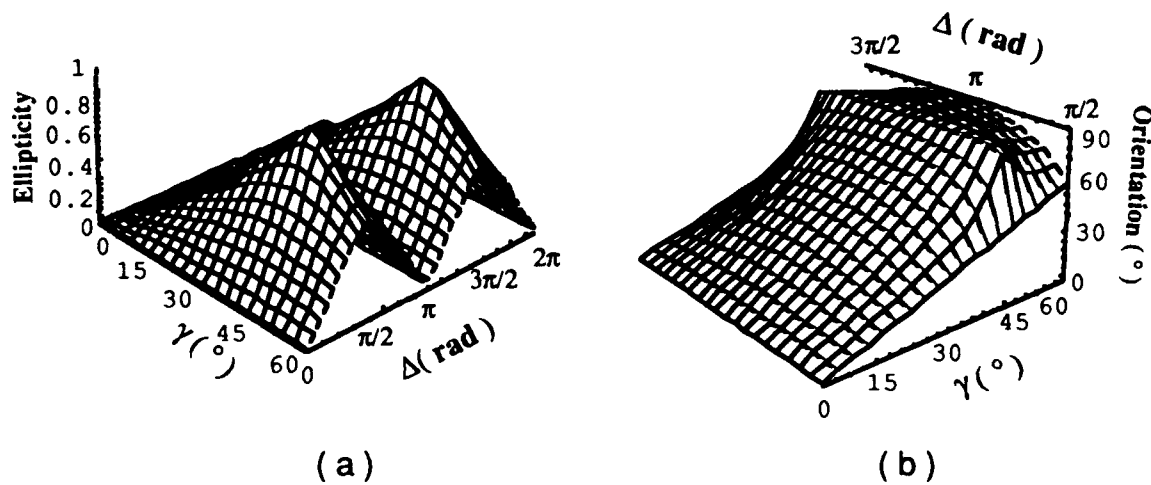


Fig. 2 The ellipticity (a) and the angular orientation (b) of the output polarization vs γ and Δ .

B. Experimental results.

For the measurements reported here we used an Argon ion laser at 514 nm. We measured the director rotation $\gamma = 49^\circ$ by crossing the polarizer and analyzer and finding the two null positions for the ON- and OFF-state. Then we measured the maximum rotation of the ellipse $\theta + \gamma = 82^\circ$, by rotating the analyzer in the ON-state to find a minimum. We can use Eq.(2) to evaluate that the optical path difference $\delta n \cdot 2d = (m+1)\lambda/2 \pm \lambda/5$, with m integer. For example, if we use $m = 2$ and the negative deviation, then we get a path difference of $0.67 \mu\text{m}$. This could be accounted for by a birefringence $\delta n = 0.18$ and a cell thickness $d = 1.86 \mu\text{m}$. The cell thickness should be increased by 13% to $2.11 \mu\text{m}$ in order for the cell to function efficiently as a half wave plate. Moreover, from Eq.(1) the ellipticity is $\epsilon = 0.61$. We also converted the elliptical light into linear light by use of a Soleil-Babinet compensator. The compensated path difference is about 0.21λ , which confirms the independent measurement above.

Conclusion

It appears to be difficult to operate the FLCLV in polarization output unless the thickness of the FLC layer can be precisely controlled in the fabrication. This is a further demand on the manufacturer in addition to the more important request for higher gain devices, which is consequent on the prior characterization reported in ref.3, and briefly summarized here with reference to Figs.3 and 4.

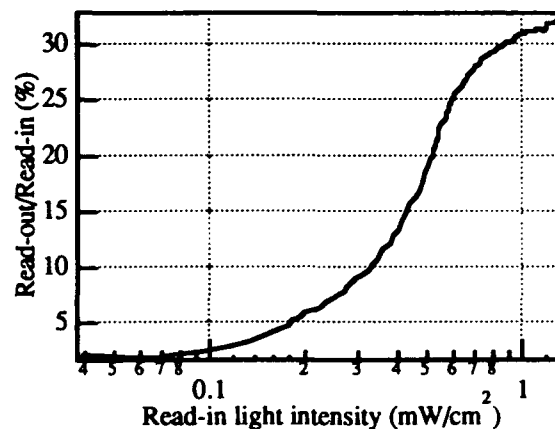
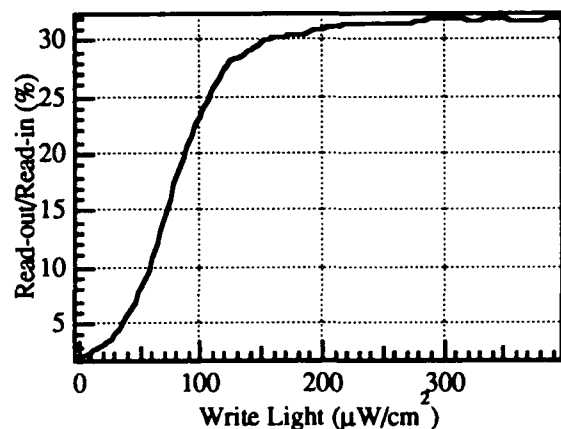


Fig.3 Read-out efficiency vs. write intensity

Fig.4 Read-out efficiency vs. read-in intensity

We see that the maximum read-out efficiency of the valve is only 32% (Fig.3). When we account for absorption in the analyzer, the maximum usable intensity in the orthogonal polarization falls below 20%. This imperfection is due to a number of factors which are detailed in ref.3. Of importance here is the reduction due to pixellation and the use of aluminum. A high quality dielectric mirror and light blocking layer would be preferable. The imperfect isolation between the read and write sides of the valve is more directly illustrated in Fig.4, where we see that a read-in intensity of 1 mW/cm² will almost switch the valve fully ON! In the absence of an alternative device, we are trying to avoid the consequences of the pixellation on collimated illumination by using structured illumination.

References

1. K. M. Johnson and G. Moddel, "Motivations for using ferroelectric liquid-crystal spatial light modulators in neurocomputing," *Appl. Opt.* **28**, 4888-4899 (1989).
2. K. M. Johnson, M.R. Surette, and J. Shamir, "Optical interconnection network using polarization-based ferroelectric liquid crystal gates," *Appl. Opt.* **27**, 1727-1733 (1988).
3. W. Xue, N. Collings and K. J. Weible, "The performance characteristics of a ferroelectric liquid crystal light valve with pixellated metal reflector," *Optical Computing & Processing.* **2**, 107-114 (1992)
4. R. M. A. Azzam and N. M. Bashara, *Ellipsometry and polarized light*, (North-Holland Physics Publishing, 1987).

Optically addressed liquid crystal phase only modulating spatial light modulator

N.Yoshida, N.Mukohzaka, T.Hori, H.Toyoda, Y.Kobayashi, and T.Hara
Central Research Laboratory, Hamamatsu Photonics K.K.
Hamakita-city, 434 Japan, +81-53-586-7111

1.Introduction

In the optical information processing such as remote sensing, optical communication and optical computing, numerous optical systems such as adaptive optics have been studied to retrieve the phase information associated with the information transmission. The phase filters have also been studied to control the optical phase term in the Fourier transform domain, in which the optical phase is controlled in a two dimensional (2-D) fashion. Attempts have been made to use the spatial light modulators (SLMs) as a 2-D phase modulator in such a system^{1),2)}.

Various types of SLMs have been developed^{3),4)}. However most of them make use of the intensity modulation of light such as scattering, beam deflection and change of polarization. Few are especially developed for use as a 2-D phase modulator^{2),5),6),7)}.

In this paper, an optically addressed liquid crystal spatial light modulator for 2-D phase modulation will be presented. This SLM can modulate phase of reading light due to parallel aligned nematic liquid crystal.

2.Structure of the device

The structure of the phase modulating spatial light modulator is shown in Fig.1. The device has a sandwich structure consisting of a undoped hydrogenated amorphous silicon (a-Si:H) photo-conducting layer for addressing material, a dielectric mirror (multilayer of SiO₂ and TiO₂), alignment layers (SiO) and a parallel aligned nematic liquid crystal layer for modulating material between the two transparent electrodes (ITO).

3.Performance of the device

When writing or addressing light is illuminating on the a-Si:H layer, the resistivity of a-Si:H is reduced, then voltage applied across the two ITO layers is mainly supplied to the liquid crystal layer. Therefore the orientation of the molecules changes in such a way that polarization of reading light passing through the layer is unaffected. Consequently the refractive index of the liquid crystal layer changes, then reading light is modulated in phase in the layer.

Transfer characteristics (the relationship between writing light intensity and phase shift of reading light) are measured with the optical arrangement shown in Fig.2. The Michaelson interferometer consisting of the dielectric mirror in the device and the external mirror is used in the reading optical system. The interference pattern of this system is analyzed with the image analyzing system. The experimental results are shown in Fig.3. The phase shift of 2π radians can be accomplished with writing light intensity of $200 \mu\text{W}/\text{cm}^2$ when the applied voltage is 3.2 V, in the case of reading laser polarized parallel to the molecule axis of the liquid crystal. On the other hand if laser light is polarized perpendicular to the molecule axis, no phase shift is observed. Moreover the characteristics can be controlled by changing the applied voltage as shown in same figure. Figure 4 is photographs of interference patterns which indicate the phase shift of 0, π and 2π radians. Rise and decay times are 70 msec and 40 msec respectively, when the phase shift is 2π radians.

Diffraction efficiency of the device is also measured. Figure 5 shows the experimental setup to measure the diffraction efficiency. The interference fringe pattern is

written on the device, and it is read out by a collimated He-Ne laser beam in the far field. Diffraction efficiency η is defined as $\eta = I_1/I_2$, where I_1 is the intensity of the +1st order diffraction and I_2 is the intensity of effective readout beam. Diffraction efficiency is shown in Fig.6. The maximum diffraction efficiency has been obtained as over 30 %.

4. Conclusion

The optically addressed liquid crystal spatial light modulator to be used as a 2-D phase modulation device has been developed. The performance parameters and the transfer characteristics of the device were measured. The experimental results show that such SLM exhibits excellent phase modulation characteristics and should be very useful as a 2-D interface device, for the system where 2-D phase information processing is essential. As dealing with phase information becomes more widespread, various application for such devices are expected.

References

- 1) A.D.Fisher and C.Warde, Opt. Lett., 4, pp.131-133 (1979).
- 2) T.H.Barnes et al., J. Modern Opt. , 37, pp.1849-1863 (1990).
- 3) A.D.Fisher and J.N.Lee, Proc. SPIE, 634, pp.352-371 (1986).
- 4) J.A.Neff et al., Proc. IEEE, 78, pp.826-855 (1990).
- 5) T.Hara, Electron. and Comm. in Japan, Part2, 74, pp.40-45(1991).
- 6) D.A.Yocky et al., Optik, 84, pp.140-144 (1990).
- 7) P.Joffe et al., Proc. SPIE, 1126, pp.13-20 (1989).

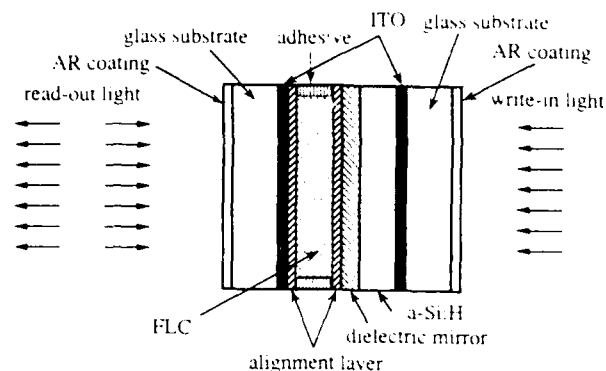


Fig.1 Structure of LC-SLM.

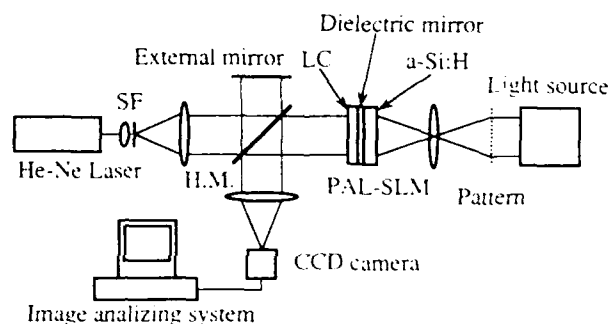


Fig.2 Experimental arrangement for transfer characteristics measurements.

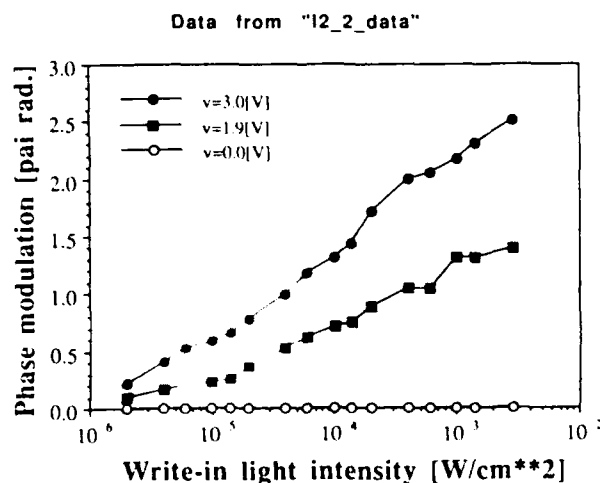
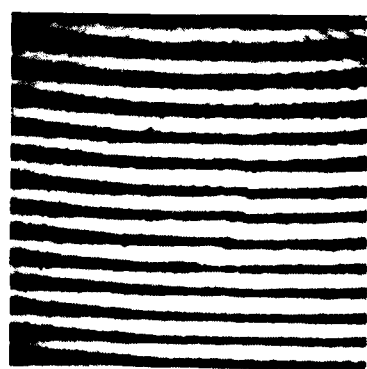
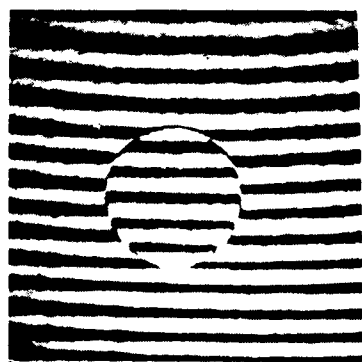


Fig.3 Transfer characteristics of the device.



(a)



(b)



(c)

Fig.4 Interference patterns showing phase change at various addressing intensity level.

- (a) 0 radians. ($0 \mu\text{W}/\text{cm}^2$)
- (b) π radians. ($30 \mu\text{W}/\text{cm}^2$)
- (c) 2π radians. ($200 \mu\text{W}/\text{cm}^2$)

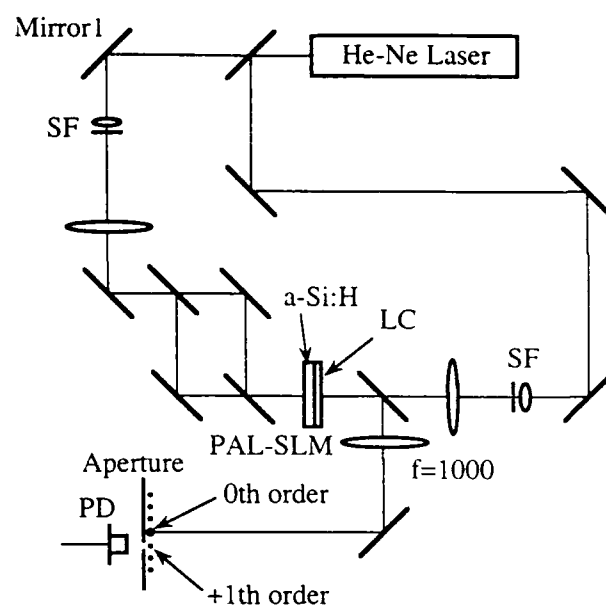


Fig.5 Experimental setup for diffraction efficiency measurement.

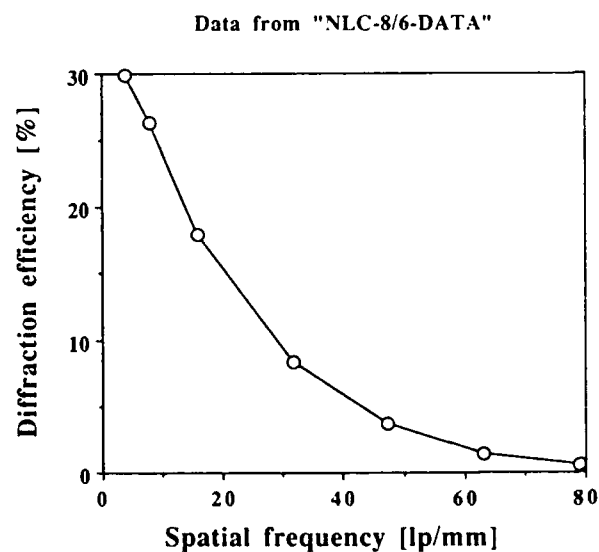


Fig.6 Diffraction efficiency at various spatial frequency.

Hadamard Transforms with Ferroelectric-Liquid-Crystal-over-Silicon Spatial Light Modulators

J.Gourlay and P.McOwan,

D.G. Vass, I.Underwood†, M.Worboys‡.

Applied Optics Group, Department of Physics, University of Edinburgh,
Edinburgh, U.K. EH9 3JZ, Tel. (+44) 031-650-1000

† Department of Electrical Engineering, University of Edinburgh,
Edinburgh, U.K. EH9 3JL Tel. (+44) 031-650-1000

‡ GEC-Marconi Research Centre, Great Baddow,
Chelmsford, U.K. CM2 8HM Tel. (+44) 0245-73331

Introduction

The ability to perform image processing tasks requires computationally intensive two dimensional matrix handling with particular emphasis on transformations¹. Optical systems utilising Spatial Light Modulators (SLMs) have been shown to perform simple matrix algebra operations effectively and efficiently.² A logical progression is to use similar systems to perform image transform operations, so that the advantages of such transform representations of real-time images can then be exploited for a variety of image processing requirements. The Hadamard transform is produced from an orthogonal set of binary basis functions³ which in an optical implementation, is readily displayed on a Ferroelectric-Liquid-Crystal-over-Silicon (FLCS) SLM. The basis function update can be extremely fast, and the accuracy of the transform may be made insensitive to optical contrast of the SLM device. A simple prototype real-time system is described with examples of Hadamard transformation. The specific advantages of the Hadamard transformation implemented with SLM devices, are discussed.

Image Representation in Orthogonal Bases

Many of the models used for image processing are based on analytical techniques which assume that the transformations are linear. Also in many practical applications the images are inherently pixelated and are therefore described in terms of discrete parameters. In such cases, image processing can be reduced to manipulation of large dimensional matrices according to the rules of linear matrix algebra. Consider an image matrix $[G]$ has dimensions N^2 (assumed a square matrix for simplicity). A general separable linear transformation on an image matrix $[G]$ may be written in the form: $[a] = [U]^t [G] [V]$, where $[a]$ is termed the unitary transform domain of the image, $[U]$ and $[V]$ are unitary operators, and the superscript t denotes the matrix transpose. Due to the unitary nature of $[U]$ and $[V]$, the inverse transform may be written in the form $[G] = [U][a][V]^t$. This can be represented in another way as $[G] = \sum_{i=1}^N \sum_{j=1}^N a_{ij} u_i v_j^t$, where u and v are the vectors made up from the columns of $[U]$ and $[V]$ respectively and a_{ij} is the value at the i^{th} row and j^{th} column of $[a]$. The outer product $u_i v_j^t$ may be interpreted as an image so that a sum over all the combinations of outer products, weighted appropriately by the a_{ij} regenerates the original image $[G]$. The image $[G]$ is decomposed into a sum of N^2 matrices each weighted by the appropriate coefficient a_{ij} . The set of outer products form basis images, which can be chosen to generate Fourier, Walsh, Haar, Hadamard, Karhunen-Loève, singular value decomposition and even identity expansions that can decompose image $[G]$ into transform coefficients to permit certain image processing operations. Selection of the transforms represented by matrix quantities

$[U]$ and $[V]$ is essentially arbitrary. The selection of the set of orthogonal bases functions is highly dependent on application and device characteristics. The Hadamard/Walsh transform and the Haar transform have binary basis functions with 1's and -1's (additionally zero's for the Haar) which can easily be implemented by fast switching Ferroelectric Liquid Crystal modulator arrays⁴.

Application to SLMs

Optical systems have previously been designed around such ideas but have been limited to using mechanical moving masks and sliding slits to perform the transform.³ These systems use a single high bandwidth detector, where the light representing the transform coefficient is gathered to convert the optical data to electronic. High performance electronically addressed SLMs are ideal devices to display the required basis images required for direct transformation and inverse transformation. A schematic of a simple transformation system used in the experiments is shown in figure 1. An analogue input scene is decomposed into serial transform coefficients by repeated optical multiplication with binary basis patterns displayed sequentially on the SLM and summation at the photo-detector. The input scene can be a real incoherently illuminated object. The vectors u_i and v_j^t may be stored in shift registers at the side of the modulator array on a Smart⁴ VLSI backplane FLCSSLM device. The k, l^{th} element of the outer product $u_i v_j^t$ is then obtained at the k, l^{th} modulator element and as the vectors changed at the shift register so the required set of images is displayed. Only power supply connections need be made to such SLMs as the shift registers would be designed to generate the required vectors sequentially. Thus in only one shift register clock cycle the next pattern is generated on the SLM. Such a device could have considerable speed advantages over digital electronic systems.

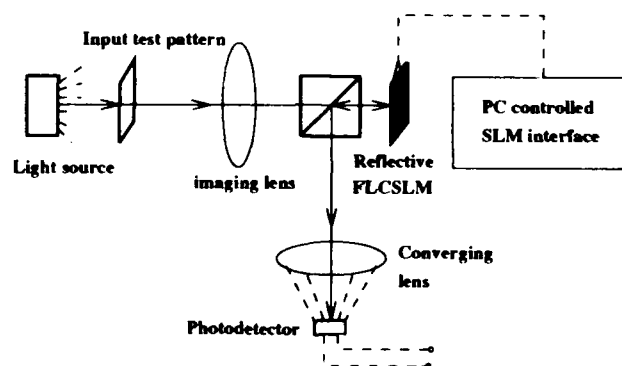


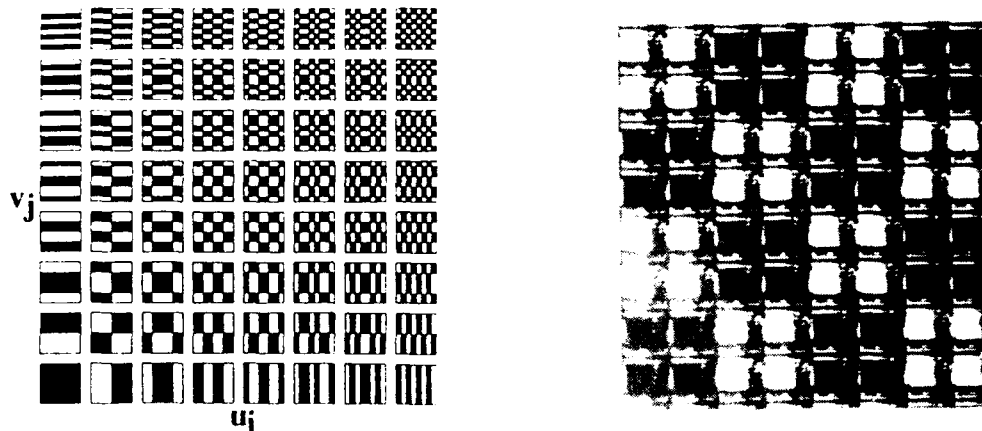
Figure 1, An example of an SLM implementation of image transformation.

Hadamard/Walsh Implementation

In a Hadamard transform the corresponding row and column vectors are the same i.e. $[U] = [V]$. Figure 2 shows the set of outer product expansion images for display on a SLM. The Hadamard transform requires positive and negative weights. Incoherent optical systems deal only with positive intensities. One way of overcoming this and retaining good signal-to-noise ratio is by implementing a two channel system: firstly calculating the positive contribution (white areas) and then subtracting electronically the negative contribution (black areas). This time-multiplexed transform implementation is insensitive to device contrast due to the background subtracted out at detector. Positive only versions of Hadamard bases images (called S-matrices) are available² and would be useful for all optical decomposition and reconstruction, but would be more sensitive to device non-uniformities.

SLM Device

The SLM device used in the experiments is a FLC device with $6\mu\text{m}$ NMOS SRAM backplane⁶ with SCE13 (Merck-BDH) Ferroelectric Liquid Crystal over the electrically addressed modulation mirrors. The SmecticC* liquid crystal is in the chevron structure, contrast ratio of 5:1 and the switching speed of $50\mu\text{s}$ with a 5V power supply⁷. The device is controlled by a PC through a custom interface. Zero overall d.c. voltage bias across the LC modulator is achieved, to avoid electrochemical degradation, with a 50 percent duty cycle. Due to the orthogonal nature of the bases functions, each SLM pixel, after displaying all the bases, has been 50 percent in the ON state and 50 percent in the OFF state so aiding future addressing schemes. Also the requirement in this implementation to generate both positive and negative frames, is usually what is generated in a device addressing scheme to retain zero d.c. balance for a bistable FLC device. An example of an 8X8 Hadamard transform bases function displayed on the SLM is shown in figure 3.



Figures 2 and 3, Hadamard/Walsh outer product expansion (black=+1,white=-1), and a bases function displayed on the SLM.



Figures 4 and 5, the simple input test pattern and its reconstruction (inverted) after optical decomposition and electronic reconstruction.

Preliminary Results

A simple 8X8 test pattern (figure 4) was decomposed optically and reconstructed electronically. It was imaged onto an 8X8 section of a Ferroelectric-Liquid-Crystal-over-Silicon SLM device. The 64 positive and 64 negative basis functions for an 8X8 Hadamard transform were displayed on the SLM device. The

light reflected from the SLM was summed onto a photodetector where electronic subtraction of negative basis function signal from positive basis function signal, gave a scaled Hadamard transform coefficient value i.e. the Hadamard transform of the image in figure 4. This set of 64 positive or negative numbers was input to a computer and an inverse transformation operation performed by computer simulation (figure 5). Experimental measurement error on the coefficients was significant in this simple system due to low light levels incident upon the detector. The effects of this error can be observed as noise in the reconstruction. Greater accuracy in the measurements will reduce the noise level and allow analogue scenes to be processed. Improvements include reducing the insertion losses in the SLM device and improving the sensitivity of the detector.

Discussion

A simple implementation of the Hadamard transform using a prototype system based on a FLC SLM has been described. The Hadamard transform can bring advantages of fast implementation and improved signal-to-noise ratio. Current feasibility studies are investigating improved and increased resolution transforms, other implementations of the Hadamard, and other types of transforms, all with particular regard to the performance of FLC SLM device technology. As this specific implementation is device contrast invariant, it should be possible to use much faster but low contrast liquid crystal material. With sub-microsecond liquid crystal switching times and on chip bases generation, high resolution Hadamard transformation should be possible in excess of T.V. frame rates.

References

1. HUANG T.S.(ed.): *Picture Processing and Digital Filtering*, Springer-Verlag (1979), pp 21-67
2. O'BRIEN D.C., CROSSLAND W.A. and MEARS R.J.: *A Holographically Routed Optical Crossbar: Theory and Simulation*, Opt. Comp. and Pro., 1991, Vol. 1, No. 3, pp 233-243
3. HARWIT M. and SLOANE N.J.: *Hadamard Transform Optics*, Academic Press Inc., New York (1979)
4. CROSSLAND W.A., BIRCH M.J., VASS D.G., UNDERWOOD I., REID S.A. and LATHAM S.G.: *Silicon active backplane spatial light modulators using ferroelectric liquid crystals*, Proc. OSA, 1990, Lake Tahoe, Technical digest 14
5. VASS D.G., BRADFORD G. and UNDERWOOD I.: *The design of Smart SLMs and applications in optical systems*, IOP, Proc. Conf. Appl. Opt. and Opto-electronic, 1990, Nottingham, U.K.
6. UNDERWOOD I., VASS D.G. and SILLITTO R.M.: *Evaluation of an NMOS VLSI array for an adaptive liquid-crystal spatial light modulator*, IEE Proc., Vol.133, Pt.J, No.1, Feb. 1986
7. GOURLAY J., McOWAN P., VASS D.G., UNDERWOOD I. and WORBOYS M.: *Optical Engineering Aspects of Ferroelectric-Liquid-Crystal-over-Silicon Spatial Light Modulators*, IOP Proc. Conf. Appl. Opt. and Opto-electronic, 1992, Leeds, U.K.

Tuesday, March 16, 1993

International Perspective on Liquid Crystal SLMs

STuA 8:30am-10:00am
Grand Ballroom West

Kristina M. Johnson, *Presider*
University of Colorado

Computer Generated Hologram Reconstruction using Liquid Crystal Spatial Light Modulators

Tomio Sonehara, Jun Amako and Hirotsuna Miura

Seiko Epson Corporation R&D Division

Owa 3-3-5, Suwa, Nagano 392 JAPAN

Introduction

Liquid Crystal Devices (LCDs) have been widely used for Spatial Light modulators (SLMs) because of its easy operating characteristics. Almost all application is still for display devices using 2-dimensional amplitude modulation characteristic. Another potential of phase modulating becomes noticeable and has been studied recently. We also have been researching the possibility of spatial wavefront modulation using the features, and trying Computer Generated Hologram (CGH) reconstruction.

Hologram using Liquid Crystal-SLMs (LC-SLMs)

Holograms using LC-SLMs are distinguished between CGH and interference hologram¹⁾ as shown in Table 1. And the CGH is classified to amplitude modulation (AM), phase modulation (PM) and complex amplitude modulation (APM) which can be modulate amplitude and phase independently. The CGH may be called the direct wavefront generation, which seems to be Gabor type in-line hologram, without reference light. In the same way, the interference hologram can be separated to AM and PM. As for the light efficiency, APM is the best because of the elimination of 0th-order and conjugate image. For pixel utilization, AM is the worst.

We will describe here the experimental results for the all CGH type by employing Thin Film Transistor (TFT) driven LC-SLMs, which show the good linearity of optical response for applied voltage and the capability of multi-level representation. (Fig. 1).

Amplitude Modulation

Figure 3 shows the reconstructed image of a Lee type CGH²⁾ with a pattern shown in Fig. 2. In this experiment the LC-SLM incorporated a Twisted Nematic (TN) mode. The noisy image is caused by residual phase change in amplitude modulation.

Phase only Modulation

Since PM neglects the amplitude term of light, it cannot generate complete wavefront. Accordingly, we tried Kinoforms³⁾ which decide the phase distribution by iterative calculations. The LC-SLM for PM incorporate an Electrically Controlled Birefringence (ECB) mode of which LC is aligned homogeneously. The thickness and birefringence of the LC layer are designed to obtain more than 2π phase modulation (Fig. 1). The device has the same specifications of EPSON LC projector and the appearance is shown in Fig. 4.

Figure 5 are the examples of reconstruction images. (a) is an array

illumination with uniform intensity. The illumination shows the capability of real-time beam steering and optical interconnections. In the case of (b), we summed a lens function into original phase distribution, so that the good image quality of 0th-order free is obtained.

Spatial Wavefront Modulation

To generate exact wavefront, we have developed a new device, which is optically coupled an AM and a PM LC-SLM, which incorporate the TN and the ECB mode respectively. In experiments, we tried two systems of the optical coupling shown in Fig. 6. One is an afocal system⁴⁾, shown in (a), and another is a directly coupled system⁵⁾ in (b) and (c). Although the both system show almost the same results, the direct system has a potential to design the optical system with less space.

AM and PM data are generated by Fast Fourier Transform (FFT) and the both data are input to the two LC-SLMs as NTSC video signals. The residual phase change, above mentioned, is compensated by subtracting it from the phase data.

Using the directly coupled system, we tried 3-dimensional real image reconstruction. Fig. 7 is an example of a "Rubic Cube", which is accumulated 41 sections along depth direction. Although the experimental LC-SLMs are too small to observe its depth by eyes, we can observe the clear image of the each section in turn by moving a CCD detector along depth direction.

The system has the possibility of complete 2-dimensional wavefront control in real time, and enables moving 3-dimensional CGH by applying AM and PM video signals. At our presentation, we will show the example of moving CGH by using a VCR.

Conclusion

Comparing three ways of CGH using LC-SLMs, we show the new device and the experimental results of the complete wavefront modulation in real time. According to the recent activities of LCD developments for high definition TVs, the LCD of about 2000×2000 pixels would be in an actual range. And LCDs will keep fascinating in the field of SLM.

References

- [1] N.Hashimoto, S.Morokawa, and K.Kitamura: "Real-time Holography using the high-resolution LCTV-SLM", Proc. SPIE 1461, p.291 (1991)
- [2] J. Amako and T.Sonehara: "CGH using TFT Active Matrix Liquid Crystal Spatial Light Modulator", Japan Journal of Applied Physics, vol.29, p.L1533 (1990)
- [3] J.Amako and T.Sonehara: "Kinoform using Electrically controlled Birefringence Liquid Crystal Spatial Light Modulator", Applied Optics, vol.30, p.4622 (1991)
- [4] J.Amako, H.Miura, and T.Sonehara: Submitted to Applied Optics
- [5] T.Sonehara, H.Miura, and J.Amako: "Moving 3D-CGH Reconstruction using a Liquid Crystal Wavefront Modulator", Proceedings of the 12th International Display Research Conference, p.315 (1992)

Table 1 Comparison of Holograms using LC-SLM

	LC-SLM	Recording	pixel/cell	Light efficiency	
CGH	AM	binary	area & position	$n \times n \geq 2$	10%
		multi-level	transmittance & position	3×3	10%
	PM	binary	refractive index	1	50%
		multi-level	refractive index	1	100%
	APM	transmittance & refractive index	1	100%	
Fringe hologram	AM	transmittance	$\geq 2/\text{fringe}$	10%	
	PM	refractive index	$\geq 2/\text{fringe}$	40%	

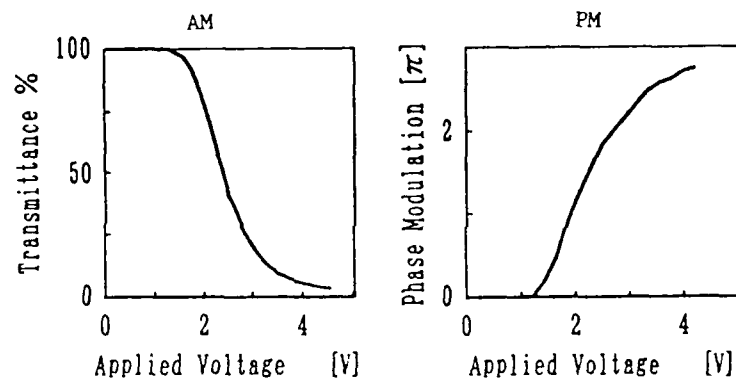


Fig.1 Modulation characteristics

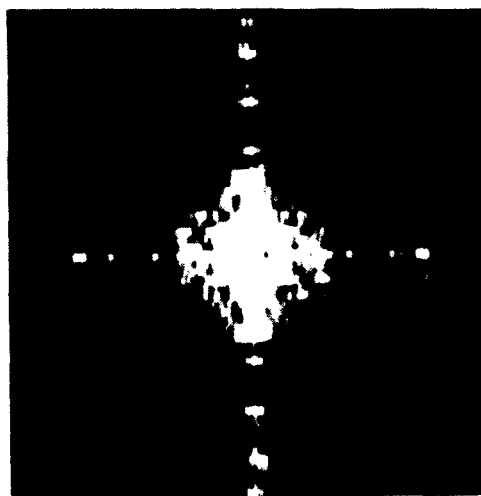


Fig.2 CGH pattern of Lee type

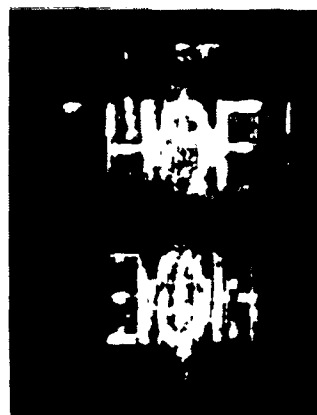
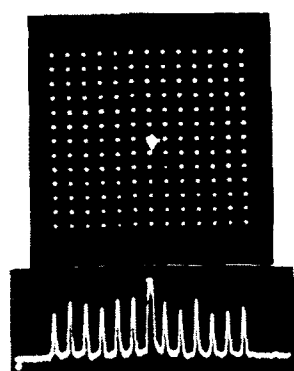
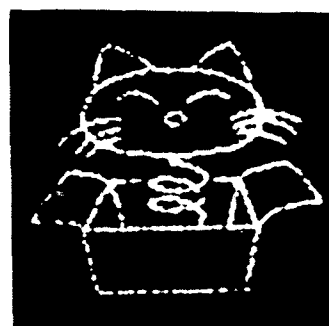


Fig.3 CGH image of Lee type

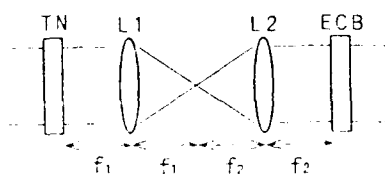


(a) Array illumination

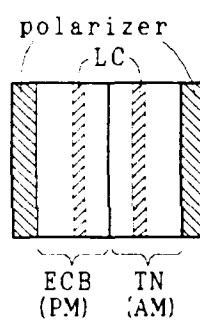


(b) 0th-order free image

Fig.5 Kinoform images



(a) Afocal system



(b) Directly coupled system

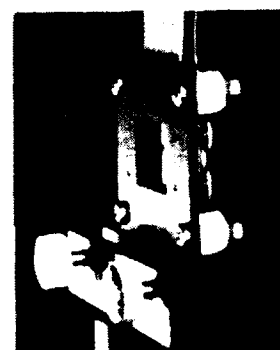


Fig.6 Spatial wavefront modulating system

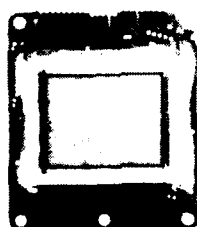


Fig.4 Appearance of LC-SLM

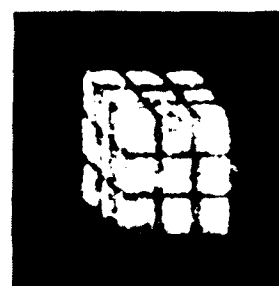


Fig.7 3D reconstruction by wavefront modulator

Issues in Improving the Performance of Liquid-Crystal-over-Silicon Spatial Light Modulators

I. Underwood, D.G. Vass[†], A. O'Hara[†] and D.C. Burns

Edinburgh Microfabrication Facility
Department of Electrical Engineering
([†] Applied Optics Group
Department of Physics)
The University of Edinburgh
The King Buildings
Mayfield Road
Edinburgh EH9 3AF

1. Introduction

The marriage of the two technologies of Very Large Scale Integrated (VLSI) silicon backplane active drive and Ferroelectric Liquid Crystal (FLC) light modulating layers has attracted much attention as a promising means of implementing compact high performance, smart and advanced Spatial Light Modulators (SLMs)^[1]. Two of the attractions of the hybrid technology are (i) that the two component technologies show a significant degree of compatibility, and (ii) that vast resources are being poured into these component technologies so that the performance of VLSI/FLC SLMs can be expected to continue to improve at a useful rate simply as a consequence of improvements in the component technologies^[2].

The ready availability of both user friendly Computer Aided Design (CAD) tools for VLSI design and relatively cheap silicon fabrication for prototype quantities of devices have combined to make the technology accessible to a wide range of potential users so that, to date, many new devices have been reported^[3]. In fact, most reports concentrate on the description of either larger/faster arrays of simple pixels or new (smart) pixel designs; progress in these areas has been rapid while, in the authors' opinion, the rate of improvement in the quality of the SLMs as measured by factors such as contrast ratio and uniformity has failed to keep pace.

Some of the issues which must be addressed in order to maximise the optical quality of VLSI/FLC SLMs include (i) optimisation of the optical properties of the silicon backplane, (ii) consistent repeatable production of a high quality Surface Stabilised Ferroelectric Liquid Crystal (SSFLC) layer, (iii) optimal electronic addressing of the SSFLC by the backplane, and (iv) the production of grey scale from the inherently binary SSFLC effect. In this paper we discuss the initial approach we have taken, at The University of Edinburgh, to tackling these issues.

2. Custom Processing of the Silicon Backplane

Here, we present a brief description of two of the primary deficiencies of "standard" silicon when applied to driving an overlying FLC layer; we discuss the consequences of the deficiencies and present results of our efforts, within the Scottish Collaborative Initiative in Optoelectronic Science (SCIOS), to overcome them.

1. The surface profile of the layers making up a pixel circuit typically shows layer boundary step heights of up to the order of $1\mu\text{m}$. This leads to intra-pixel variations in the amplitude and phase of light reflected from a metal pad covering the whole pixel and to variations in the thickness of the FLC layer. The alternative approach of sharing the pixel real estate between un-flat circuit and flat pad leads to a lower optical fill factor. The preferred solution is planarisation of the dielectric layer underlying the metal pad. Three options have been explored - spin on polyimide, Electron Cyclotron Resonance (ECR) oxide deposition and chemical-mechanical polishing. The last of these techniques has been tried successfully^[4] on an electrically defective SLM wafer. An optical interferogram of part of a polished wafer is shown in Figure 1(B). Operational SLM wafers are currently being polished; it is anticipated that these will produce "optically flat" working pixel arrays with a high pixel fill factor ($>90\%$).

2. The granular nature of the thick metal layer gives rise to light scattering and leads to poor FLC alignment and bistability. "Hillocks" which are present in the metal layer also scatter light and can be high enough to span the FLC layer causing short-circuits between the pad and the ITO counter electrode; furthermore they may be the cause of uneven LC layer thickness. The electrically necessary step of sintering the aluminium is largely responsible for the poor optical quality of the metal. We have explored the use of dielectric over-layers during sintering which have resulted in a significant improvement in the smoothness of the final sintered metal surface as shown in Figure 2. Recent results also indicate an improvement in LC alignment and layer thickness uniformity as a result of the high quality metal finish.

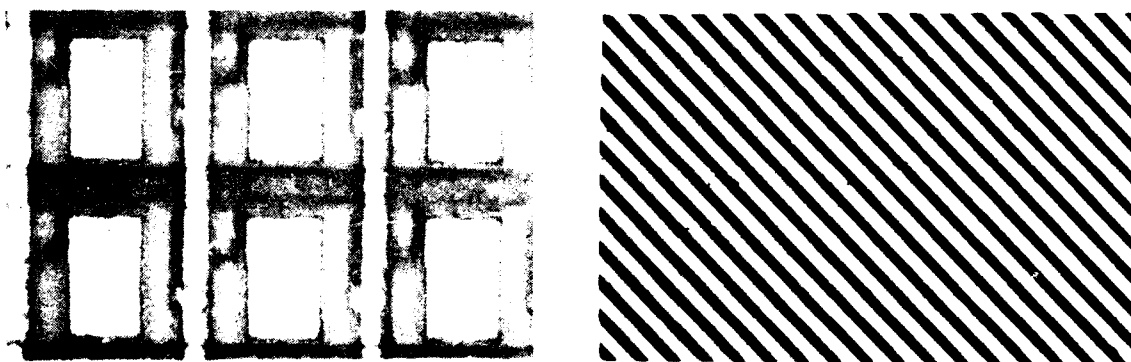


Figure 1. Left - photograph of a portion of a 176^2 pixel array ($30\mu\text{m}$ pixel pitch).
Right - optical interferogram ($\lambda = 564\text{nm}$) of portion of the array after planarisation

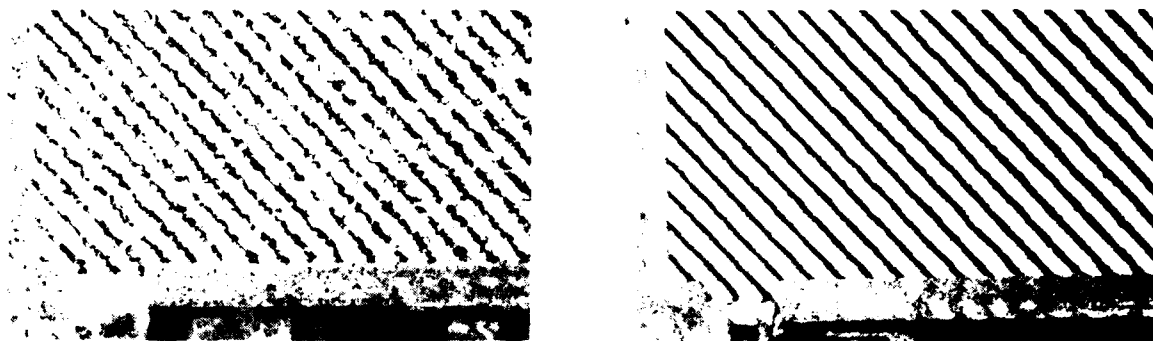


Figure 2. Left - Optical interferogram ($\lambda=564\text{nm}$) of part of a metal pad (approx $74 \times 50 \mu\text{m}^2$) following standard sintering. Right - Optical interferogram of similar metal pad after modified sintering operation. An ECR oxide layer of thickness $0.3 \mu\text{m}$ was present during sintering.

3. Electronic Addressing of the SSFLC layer

It is generally accepted that LC longevity requires that no net long term DC field is allowed across the layer. This leads to complications in addressing the bistable SSFLC based SLMs. The High Performance (HP)SLM 176^2 device^[5] solves this problem by building each frame from two sequential complementary sub-frames in a system where a pulsed light source illuminates only the positive sub frame. We have devised (in collaboration with BNR Europe) a 2 transistor pixel^[6] which is capable of both DC balancing and a high (approaching 100%) duty cycle. We have also developed drive schemes^[7] which allow a modified-SRAM pixel to supply a very stable drive signal to a SSFLC layer as demonstrated in §4 below.

4. Grey scale in SSFLCs

Although inherently binary in nature, the switching speed of SSFLCs is such that effective grey scale can be achieved by temporal multiplexing of sequential bit planes while maintaining a significant speed advantage over the older analogue nematic LCs. Several options exist, including

1. Equal weight subframes
2. Binary weighted sub-frame duration with constant illumination intensity
3. Binary weighted illumination intensity with constant sub-frame length
4. A combination of 2 and 3 (for increased dynamic range).

We are currently active in investigating the first three and present here, in Figure 3, preliminary results from the first of these^[8]. The microdensitometer trace shows a fairly linear range of grey scale on part of a 16×16 pixel SLM. (It also shows significant non uniformity in transmitted intensity across individual pixels - an example of the problem we are tackling as described in §3 above.

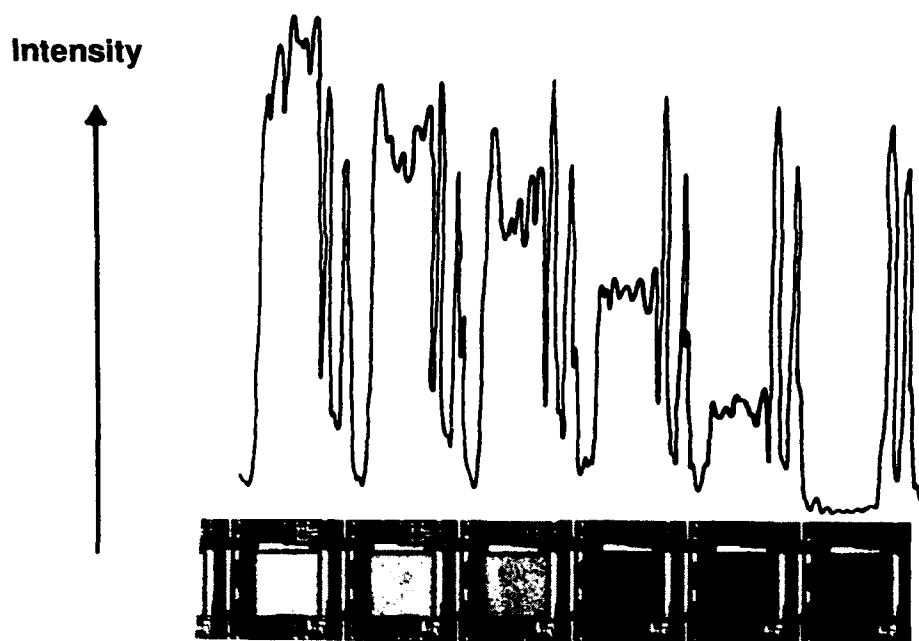


Figure 3. Top - Photograph of a line of pixels (pitch $200\mu\text{m}$) showing grey scale achieved by time multiplexing **Bottom** - corresponding microdensitometer trace.

5. Conclusions

We have presented an analysis of some issues which must be addressed in order to maximise the potential of the VLSI/FLC SLM technology. Preliminary results are very encouraging and indicate the potential for significant performance improvements.

6. References

1. N Collings, WA Crossland, PJ Ayliffe, DG Vass and I Underwood, *Evolutionary Development of Advanced Spatial Light Modulators*, Appl Opt, Vol 28, 1989, pp4740-7.
2. KM Johnson, DJ McKnight and I Underwood, *Smart Spatial Light Modulators Using Liquid Crystal on Silicon*, JQE 1993, to be published.
3. See for example Optical Society of America Conference on Spatial Light Modulators, Lake Tahoe, Nevada, September 1990, OSA Technical Digest Series 14.
4. A O'Hara, RJ Hannah, RJ Holwill, I Underwood and DG Vass, *Improvements in the Mirror Quality of Reflective Spatial Light Modulators using Dielectric Coatings and Mechanical Polishing*, in Optical Interference Coatings Technical Digest 1992, (Optical Society of America, Washington DC, 1992) Vol 15, pp274-6.
5. I Underwood, DG Vass, RM Sillitto, G Bradford, NE Fancey, AO Al Chalabi, MJ Birch, WA Crossland, AP Sparks and SG Latham, *A high performance Spatial Light Modulator*, in Devices for Optical Processing, DM Gookin, Ed, Proc SPIE 1562, pp107-15.
6. WA Crossland, MJ Birch, AB Davey and DG Vass, *Active Backplane Spatial Light Modulators using Chiral Smectic Liquid Crystals*, Proc SPIE/IS&T Symp on Electronic Imaging Science and Technology, San Jose, CA, February 1992, paper 1665-36, p143.
7. I Underwood and G Bradford, *Driving FLC SLMs using SRAM backplanes*, Edinburgh University Internal Report, January 1990 (available from authors).
8. DC Burns and I Underwood, *Real Time Grey Level Generation using a Binary Mode Spatial Light Modulator*, In Applied Optics and Optoelectronics Technical Digest 1992, Leeds, England, September 1992, paper OE P6, pp14-15.

"Smectic A and C* liquid crystal light valves: application to parallel information processing"

J.L. de Bougrenet de la Tocnaye

Groupe Optique et Systèmes de Communication
ENST de Bretagne
BP 832, 29285 Brest Cédex, France

I. Introduction:

Optically addressable imaging devices, often referred to as light valves, have played a crucial role in adaptive optics and optical processing during the two last decades [1]. The development of light valves for applications in the domain of imaging and information display has benefited from simultaneous advances in liquid crystal materials. We will focus here on recent developments involving the use of smectic A and C* liquid crystals. We will briefly discuss the current trends in these materials, as well as their various addressing modes and their applications in the field of information processing and optical computing.

II. Smectic A and C* liquid crystal light valves (LCLV):

A LCLV is an optical-to-optical image transducer capable of accepting a low intensity, white or monochromatic light input image and converting it, in real time, into an output image by modulating light from another source. Generally, the device is designed in such a way that the input and output light beams do not interact. This gives the device great flexibility in its operating modes. Different layer combinations are possible. As previously mentioned, we will only consider here the use of smectic A and C* liquid crystals as modulating element.

The smectic phase is characterized by a layered structure appearing when decreasing the temperature (phase transition from the nematic to the smectic phase) [2]. The first smectic phase that appears is the smectic A phase. In this phase, the long axis of the rod-shaped molecules is oriented perpendicular to the layers. In the soft-mode, a tilt angle θ can be induced by an applied field E . The existence of this mode is due to the coupling between θ , P (the induced electroclinic polarization) and E according to a linear relation which is at the basis of grey scale formation. Operating behaviour close to that of nematic materials is observed, but with switching speeds largely superior. Switching times of 1-10 μ s can be measured, making the smectic A the fastest liquid crystal phase.

Lowering the temperature further can cause the molecules to tilt at an angle θ with respect to the layer normal, forming the smectic C phase, the most ordered and least symmetric liquid crystal phase. R.B. Meyer et al. recognized that making the liquid crystal chiral removes the liquid crystal mirror plane symmetry thus producing microscopic ferroelectricity. Therefore, chiral smectic C (smectic C*) liquid crystal could have spontaneous polarization. However, the liquid crystal molecules form a spontaneous helix along the layer normal, thereby averaging out the spontaneous polarization on a macroscopic scale. An observation of a macroscopic spontaneous polarization supposes to unwind the helix. This has been performed by N. Clark and S. Lagerwall by confining between two electrodes a very thin layer of liquid crystal, leading to the Surface Stabilized Ferroelectric Liquid Crystal (SSFLC) structure. The latter is a twofold degenerated system, which means that only two orientations of the molecules are possible depending on the direction of the applied electric field. This is the cause of the bistability and the resulting possibility to memorize two stable states. Switching times of 100-10 μ s can be measured and contrast ratio of 20-500:1 can be expected with standard FLC OASLMs. Contrast ratio that exceed 1000:1 have been measured for individual optical shutter.

Although SSFLCs are basically bistable devices, it is possible to obtain grey levels under certain driving conditions. Under these conditions, the cell does not switch uniformly, but shows a grainy structure due to the appearance of small black and white domains. Averaging the optical response over a given area results in a grey level. One advantage of creating grey levels with bistable devices instead of other materials like nematics or smectic A is the memory of the device. The grey level can be stored, and in the case of an optically addressed SLM, optically read and modified. This is a very powerful property for a large number of applications in optical computing and display. The grey level phenomenon is due to multi-domain switching, as described in [3]. Switching by wall propagation is less energy consuming than uniform switching. The spatial distribution of switched domains is determined by the more or less random distribution of defects in the smectic layer structure which act as nucleation sites for the domains. It has been shown that grey level process can be either charge or voltage controlled, as when used with photoconductor addressing.

III. The main addressing modes:

A LCLV is a combination of two elements: the addressing layer and the light modulator. Basically, there are two main addressing modes. The massive one (using the bulk crystal) and the pixelated one. The latter can be divided into three categories: electrical addressing, optical addressing and smart addressing, the last two belonging properly to the light valve category.

In an optically addressed SLM (OASLM), a write beam carrying spatially varying information, is absorbed by the photosensor. The spatially varying properties of the photosensor translate into spatially varying electric field across the liquid crystal and a variation of the optical properties of the liquid crystal. The SLM modulates either the phase, polarization, intensity or wavelength of a read-beam. Several groups have produced OASLMs coupling a-Si:H, GaAs or silenite photosensors with smectic A and C* modulators. As a photosensor, the a-Si:H has been shown to have many advantages over crystalline photosensors, e.g., a high spatial resolution and the possibility to be deposited at a low temperature, in a thin and uniform layer.

Due to its bistability, a FLC OASLM can be operated either in a reflective or in a transmissive mode. In the transmissive mode, a compromise between the quantum efficiency and the transparency of the photosensor obliges to deposit only thin semiconductor layers. The device speed is limited by the photoconductor. This can be seen as a real limitation, when using FLC materials. Such a consideration has given rise to original contributions concerning the design of fast speed light valves based on the association of a bistable FLC and an amorphous silicon p-i-n structure [4].

The smart addressed SLM can still be considered as a proper light valve, due to the optical to optical conversion, although this conversion is performed separately of each pixel. This means that each pixel operates independently as a small light valve. Furthermore, in this case, the conversion operation is more complex because intermediate electronic processing can be included as well as the interaction with the neighbours. Smart OASLMs have been fabricated using silicon VLSI backplanes [5]. Switching energies of FLC materials are typically a few fJ/mm², and switching speeds in tens of microseconds can be contemplated for binary FLC modulators driven from a silicon VLSI die. Analog operation at comparable switching energies and speeds is expected from smectic A materials. Although CMOS logic speeds are much higher than FLC switching rates, the low static power dissipation of silicon CMOS logic permits a sub-picoJoule speed-power product to prevail at low clock rates. This reciprocity allows CMOS circuitry to operate at clock rates matching liquid crystal switching times (10³-10⁵ Hz) without suffering an increase in switching energy.

IV. Recent domains of applications:

A large number of applications, based on the use of FLC light valves [6], have been proposed. We decided to focus on two major applications. The first concerns the domain of information processing, more precisely, the implementation of Joint Transform Correlators (JTC). The principle of such a correlator is not new. However, a recrudescence of attention has been paid to such an architecture, during the last two years, due to device

improvements, resulting from the supply of fast FLC light valves and EASLMs [7]. The use of fast switching elements allows time multiplexing of the references with respect to the video rate. Taking into account a reasonable device development, time multiplexing of 50-100 different references for each video scene can be expected, when using, for instance, a silicon backplane EASLM for inputting the references. The second improvement is due to the use of a FLC bistable OASLM (BOASLM) in the Fourier plane. Although the dynamic range of the nonlinear response is limited, experimental results have shown that this feature can be adjusted. Increasing the severity of the nonlinearity is well known to improve the discrimination capability. Such devices have been successfully used to enhance the correlation peak and therefore to improve the detection performance of standard correlators.

The second kind of very promising applications concerns the domain of complex systems and neural computing [8]. Requirements for optical neurocomputing are similar to those of digital optical computing, except that a high frame rate are not essential. Therefore, FLC light valves can be used in neurocomputing as input-output display, storage medium for the synaptic weights as well as nonlinear elements for decision making. The critical step of optical implementations of neural nets is the learning process and more precisely the weight encoding and updating. To encode weights, grey levels are needed. Although the FLC devices are binary devices, grey levels can be achieved by temporal, and/or spatial multiplexing. A supervised learning algorithm has been implemented by storing the connection weights as pixels in a EASLM [8]. The trade-off is, in this case, between encoding capacity and control.

All optical alternatives exist. Smectic A materials are very promising in this domain. Because they provide a linear modulation of light in response to an applied field and permit a high switching speed, smectic A OASLMs potentially have all the operating characteristics necessary to build large size, fully interconnected neural network architectures with grey level capability. Recent improvements of the contrast ratio of smectic A materials make them very credible. Another solution, using smectic C* and aiming at taking advantage of the multi-domain switching of BOASLMs to implement the weight encoding and updating has been proposed [10]. In this manner, the value of the grey level may be stored, increased or decreased. The spatial accumulation capability of the device, together with possible thresholding of the image bearing light beam, allows the memorization, accumulation, and erasure of pictures. The device performs basically a logic OR between successive picture exposures. Data can therefore be successively recorded with varying gains. The value of the gain depends on the apparent sensitivity of the device and can be influenced by varying the electrical driving parameters of the BOASLM.

To be complete, we may mention that FLC light valves can also be used to implement decision steps in neural architectures. A good example can be given by the implementation of the Winner Takes All (WTA) algorithm. Nevertheless, a proper WTA function is well known to be difficult to implement with conventional massive nonlinear-optical devices like BOASLMs, due to the need of a nonlocal nonlinearity. Therefore the emerging very-large-scale integrated circuit/liquid crystal (VLSI/LC) device technology enables the design of devices with optical inputs and outputs that can be coupled with almost any desired electronic functionality. A noteworthy illustration of such an implementation, coupling FLC material with photoaddressable silicon VLSI array of two units in a one-dimensional VLSI/FLC WTA array, has been recently proposed [11].

V. Discussion and material trends:

Liquid crystal light valves still remain certainly the crucial element for many optical information processing, communication, and display systems. Progress in the development of light valves, in particular for optical processing applications, has accelerated in the last few years. We are also observing the penetration of such SLM technologies into new applications, namely, those of phase conjugation, adaptive optics, and neural network systems. The implementation of real time correlators using fast light valves and SLMs is now a reality. This is due to the arrival of new devices on the market, with better performances and reliability. Therefore, the implementations have overcome the level of the bench prototype and concern now the domain of industrial applications. Advances in the field of optical light

valve design have been decisive and contribute directly to the elaboration of a new kind of optical hardware.

We believe that the real challenge lies in our ability to design complex versatile devices such as smart light valves and, more generally, devices coupling electronic and optical functions on a large interconnectable array. It is expected that smart light valves will be the key components of future data processing systems because they can blend the functional flexibility of electronics and the communications and interconnections capabilities of optics. Therefore, we can foresee applications of silicon VLSI / smectic A or C* optoelectronic devices in areas where massive parallelism and low power operation at moderate speeds may be suitable, such as special purpose image processing systems, realization of early vision models and optoelectronic neural network. Silicon VLSI / FLC light valves have the great advantage of simplicity of design and fabrication, simplicity of integration with standard electronics, low power requirements, relatively inexpensive fabrication, high frame rates, and the possibility of fabricating large two-dimensional arrays. In this prospect, new generations of light valves based on this principle will bring considerable changes in the field of image processing in the next few years, if we are able to design devices with a satisfying optical quality.

Furthermore, SLMs have suffered both a moderate speed and contrast reduction due to alignment defaults (particularly true with FLC materials). Developments of new materials such as fast smectic A and antiferroelectric liquid crystals (AFLC) [11], with better optical quality than FLCs, (i.e. high contrast, no zig-zag defects etc.) will considerably improve the performances of smectic A and C* LCLVs. Particularly, the use of AFLC will reduce considerably the technological constraints, and therefore will militate in favour of strong developments of smart light valves involving low power and high contrast liquid crystal material in the near future.

References:

- [1] D. Casasent, "Coherent light valves", *Applied Optics and Optical Engineering*, R. Kingslake Ed. New York: Academic, 1979, Vol. 6, pp. 143-200.
- [2] J.S. Patel and J.W. Goodby, "Properties and applications of FLC", *Optical Engineering*, Vol. 26, 1987, pp. 373-384.
- [3] M. Killinger, J.L. de Bougrenet, R.C. Chittick and B. Crossland, "Bistability and nonlinearity in FLC OASLMs: application to neurocomputing", *Applied Optics*, Vol. 31, N°22, 1992, pp. 3930-3936.
- [4] G. Moddel, K.M. Johnson, W. Li and R.A. Rice, "High-speed binary optically addressed SLM", *Applied Physics Letters*, Vol. 55, N°6, pp. 537-539.
- [5] T. Drabik, M. A. Handschy, "Silicon VLSI/ FLC technology for micropower optoelectronic computing devices" *Applied Optics*, Vol. 29, N°35, 1990, pp. 5220-5223.
- [6] K.M. Johnson, M.A. Handschy and L.A. Pagano-Stauffer, "Optical computing and image processing with ferroelectric liquid crystal", *Optical Engineering*, Vol. 26, N°5, 1987, pp. 385-391.
- [7] D. Jared, K.M. Johnson and G. Moddel, "Joint Transform Correlation using an amorphous silicon FLC SLM", *Optics Communications*, Vol. 76, 1990, pp. 97-102.
- [8] K.M. Johnson and G. Moddel, "Motivations for using FLC SLMs in neurocomputing" *Applied Optics*, Vol.28, N°22, 1989, pp. 4888-4899.
- [9] K. Yao, J. Duvillier, M. Killinger and J.L. de Bougrenet de la Tocnaye, "All-optical implementation of a Kohonen-like Map Neural Net: a preliminary approach" special issue of *Applied Optics on Neural Networks*, 1993.
- [10] T.M. Slag and K. Wagner, "Winner-take-all SLM", *Optics Letters*, Vol. 17, N°16, pp. 1164-1166, 1992.
- [11] Y. Yamada et al., "Ferroelectric liquid crystal display using tristable switching" *Japanese Journal of Applied Physics*, Vol. 29, N° 9, pp. 1757-1764, september 1990.

LIQUID CRYSTAL SPATIAL LIGHT MODULATORS FOR OPTICAL IMAGE PREPROCESSING

A. V. Parfenov

Optoelectronics Division
P.N.Lebedev Physics Institute
Academy of Sciences
Leninsky Pr., 53
117924 Moscow B-333, Russia
Tel. (095) 132-6664
FAX (095) 135-7880
Internet: 72360.2260@compuserve.com

J. C. Buchholz

Micro-Optics Technologies, Inc.
8608 University Green #5
Middleton, WI 53562
Tel. (608) 831-0655
FAX (608) 831-0655
Internet: 71665.1551@compuserve.com

Spatial light modulators (SLM) are considered as the main elements of optical data processing systems. Liquid crystal SLMs (LCSLM) having high performance parameters are normally used in optical systems as image transducers and optical filters. The value of LCSLM for optical data processing is increased by combining image transducing and image preprocessing functions in the same sample. Such a combination improves the flexibility and productivity of optical data processing methods, and simplifies optical setup. Among realized preprocessing functions of LCSLM are the edge enhancement, the selection of nonstationary objects, the optical analog of lock-in-amplifier, image subtraction, and spatial selection of the image details corresponding to their intensity. Most of mentioned preprocessing functions and new features like IR-sensitivity, IR-modulation are primarily realized in LC SLM at P.N.Lebedev Institute. The physical mechanisms for these opportunities are discussed together with possible improvements in parameters and features. Recently observed new electro-optical effects in ferroelectric liquid crystals are reported as ones giving new opportunity to combine image preprocessing and fast response.

Image preprocessing functions can be implemented in LCSLM not only through engineering of the electro-optic response of the liquid crystal material, the subject of the first part of this paper, but also through solid state engineering of the semiconductor receptor layer in optically addressed LCSLM. We will also describe work at Micro-Optics Technologies in implementing preprocessing functions in the photosensor layer. Local interconnects in a pixelated layer are implemented through the use of silicon micromachining techniques. A device implementation is described that provides a convolution preprocessing function.

Tuesday, March 16, 1993

Silicon-Addressed Hybrid SLMs

STuB 10:30am-12:10pm
Grand Ballroom West

Sing H. Lee, *Presider*
University of California, San Diego

Title to be announced

J. Fan
Kopin Corporation
695 Miles Standish Blvd.
Taunton, MA 02067

Summary not available at time of printing.

Bonding of Si thin films to PLZT Substrates for Smart Spatial Light Modulator Applications

M.S. Jin, J. H. Wang, V. H. Ozguz and S. H. Lee
Univ. California-San Diego, Electrical and Computer Engineering Dept.
La Jolla, CA 92093-0407
Tel: 619 534 7891

In order to realize smart spatial light modulators (S-SLMs), electronic processing materials (e.g. Si, GaAs) and light modulation materials (e.g. Ferroelectric ceramics or liquid crystals, III-V semiconductors, Si) need to be combined. One of the most promising combination consists of Si for its mature electronic processing capabilities and PLZT (a ferroelectric ceramic, Lead Lanthanum Zirconate Titanate) for its fast light modulation with high contrast ratio. In the past, several approaches have been identified for joining Si with PLZT [1]. However, in the approach where PLZT film is deposited on the windows of Si on SOS, the light modulation is not effective because the PLZT film is too thin. In the approach where amorphous Si is deposited on bulk PLZT and then recrystallized, the quality of Si is not high enough to implement large number of transistors and efficient light detectors. In the flip-chip bonding approach where bulk quality Si is combined with bulk PLZT, there is a compatibility problem between the driver circuit for PLZT modulators (requiring 30-50 V) and the remaining logic circuits (operating at 5 V).

To overcome this voltage compatibility problem, we are studying two approaches to bond Si thin films onto bulk PLZT for the modulator driver circuits. The logic circuits and detectors are still implemented in bulk, foundry processed Si wafers with excellent lifetime and minimum defect densities, and light modulators in bulk PLZT. Flip-chip bonding is applied to connect electrically the outputs from logic signal processing circuits in bulk Si to the driver circuits on the Si thin film that is bonded on bulk PLZT. The cross section of one unit cell of Si/PLZT S-SLM is illustrated in Figure 1.

The two approaches for bonding Si thin films onto bulk PLZT are as follows: (i) a commercially available thin (2-4 μm) Si film of very high quality is bonded onto bulk PLZT with an interface layer (e.g. Al_2O_3); driver circuits are fabricated after bonding; (ii) driver circuits are implemented in a commercially available SOI wafer with 0.6 - 2.0 μm thick Si film on 1.0 μm thick SiO_2 on Si substrate; a back-etch technique is next used to etch away the Si substrate and to obtain thin Si film (containing circuits) on SiO_2 which is then bonded onto bulk PLZT. The bonding between Si film and bulk PLZT in the first approach must be very strong because it has to withstand subsequent processing steps for the driver circuits, especially the high temperature oxidation step at 850°C. The second approach alleviates this requirement on bonding since only limited amount of processing takes place after bonding. However, the difficulty is shifted to the techniques used to obtain and handle thin Si films containing circuits.

Photomicrograph of MOS test circuits fabricated on 4 μm Si films obtained from Virginia Semiconductors, bonded to PLZT using a 20 nm thick sputtered Al_2O_3 layer as an interface is shown in Figure 2. Si islands were formed using dry etching. A PECVD deposited SiO_2 film is used for isolation/passivation as well as for additional clamping of the Si islands. We have used an NMOS process with one 850°C pyrogenic oxidation step. The bonding of Si films withstood this high temperature step indicating the quality of the bonding. The device characteristics are presented in Figure 3. The electrical performance of the devices is similar to that of devices fabricated in bulk Si. This bonding technique seems also suitable for SOI technologies, especially for obtaining a bulk quality thin film Si on sapphire (Al_2O_3).

As an alternative, we have used wafers provided by KOPIN Corp with 0.6 - 2 μm Si film on top of 1 μm thick SiO_2 layer. We have applied conventional NMOS process to fabricate test structures. A back-etch technique was used to obtain thin Si films containing

circuits. The SiO_2 layer provides self-termination of the etching process. These films were subsequently bonded to PLZT using epoxy, SiO_2 and polyimide as interface layers. Photomicrographs of devices before etching (Figure 4a) and after etching (Figure 4b) show that $0.6\text{ }\mu\text{m}$ Si films containing circuits can be obtained and transferred successfully. Approximately $10 \times 10\text{ mm}$ Si area containing transistors has been transferred. The electrical characteristics of the devices before and after etching is compared in Figures 5a and 5b, confirming that the etching/transfer/bonding does not degrade the device performance. Approximately 0.5 V shift in threshold voltage along with increased transconductance have been observed in some of the characterized devices. The change in interface charge at the bonding interface is most likely the cause of the observed variations. Experiments are under way to identify the specific mechanism responsible for the slight changes.

The circuit yield and performance of PLZT modulators driven by Si transistors fabricated by the techniques presented here are being characterized as part of an ongoing study. In either approach, the quality of the Si film used is very close to the bulk and logic circuits of any complexity and transistor count can be implemented in the thin Si layer. Both techniques also allow for the possibility of implementing much larger Si areas onto PLZT substrates without introducing further complications into the processing steps. The thin film bonding techniques will allow an efficient implementation of S-SLMs.

1. A. Ersen, et al., Appl Opt., V31 (20), 3950-3965, 1992.

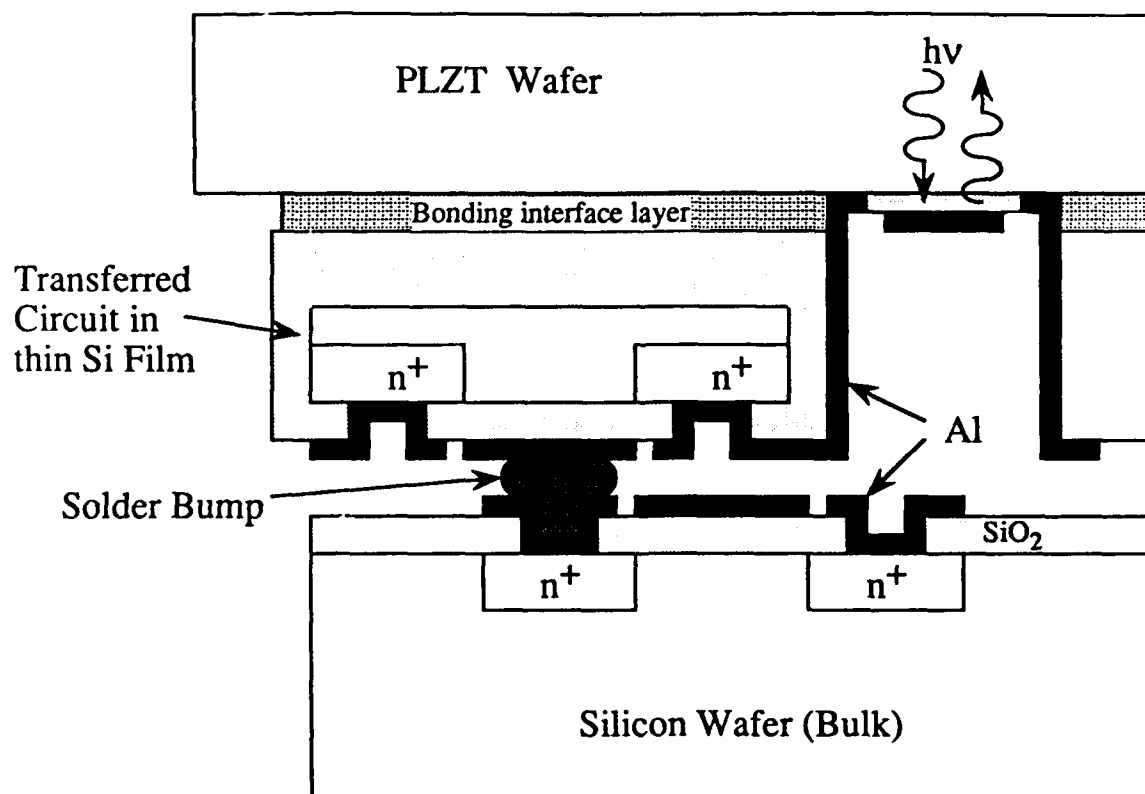


Figure 1. The cross section of one unit cell of Si/PLZT S-SLM implemented by using combination of thin Si film bonding to PLZT along with flip-chip bonding.



Figure 2. Photomicrograph of MOS transistors fabricated on 4 μm Si film bonded to PLZT substrate. The Si islands have been etched by dry etching and clamped by a SiO_2 overlayer. The bonding resisted 850°C processing temperature.

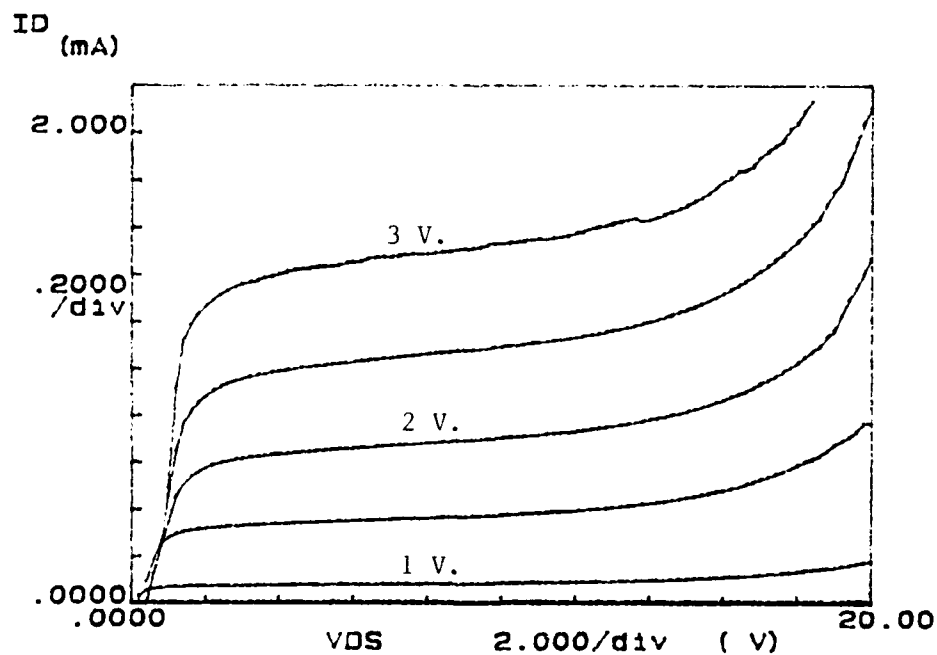


Figure 3. The output characteristics of NMOS transistor fabricated in 4 μm thin Si film bonded to PLZT.

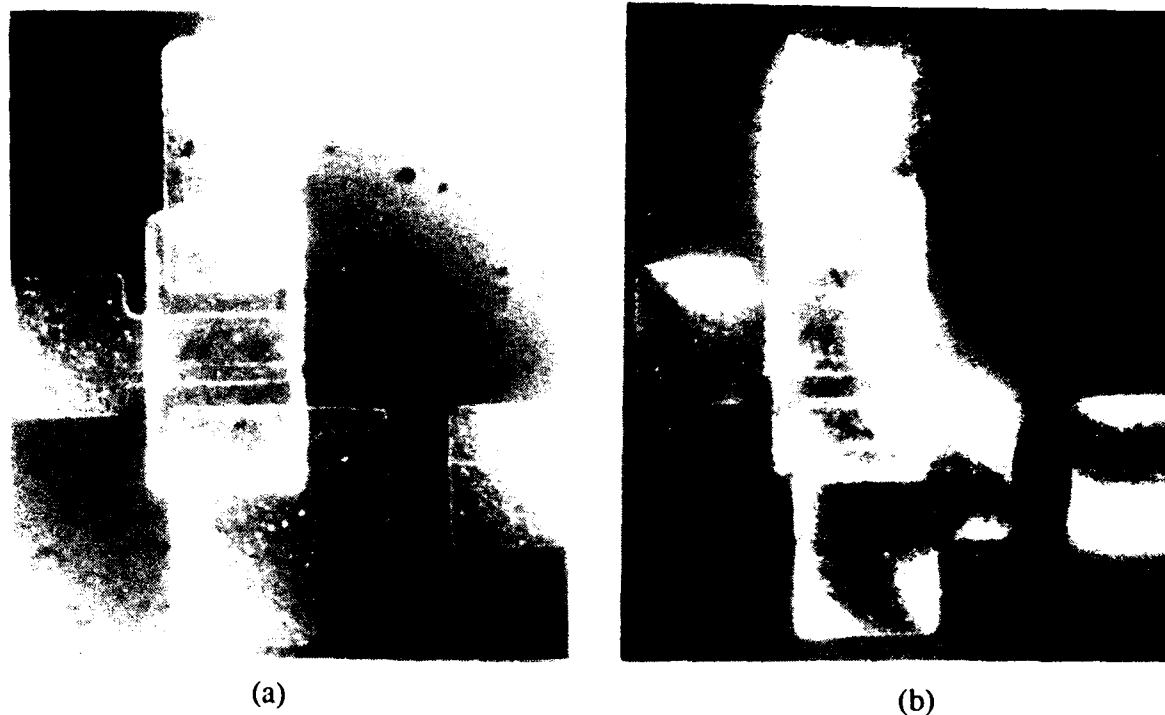


Figure 4. Photomicrographs of MOS transistors (a) before etching on Si/SiO₂/bulk Si Kopin SOI wafer and (b) after etching on 0.6μm Si film back etched from previous wafer. The results indicate no visible damage to the devices during etching and transfer.

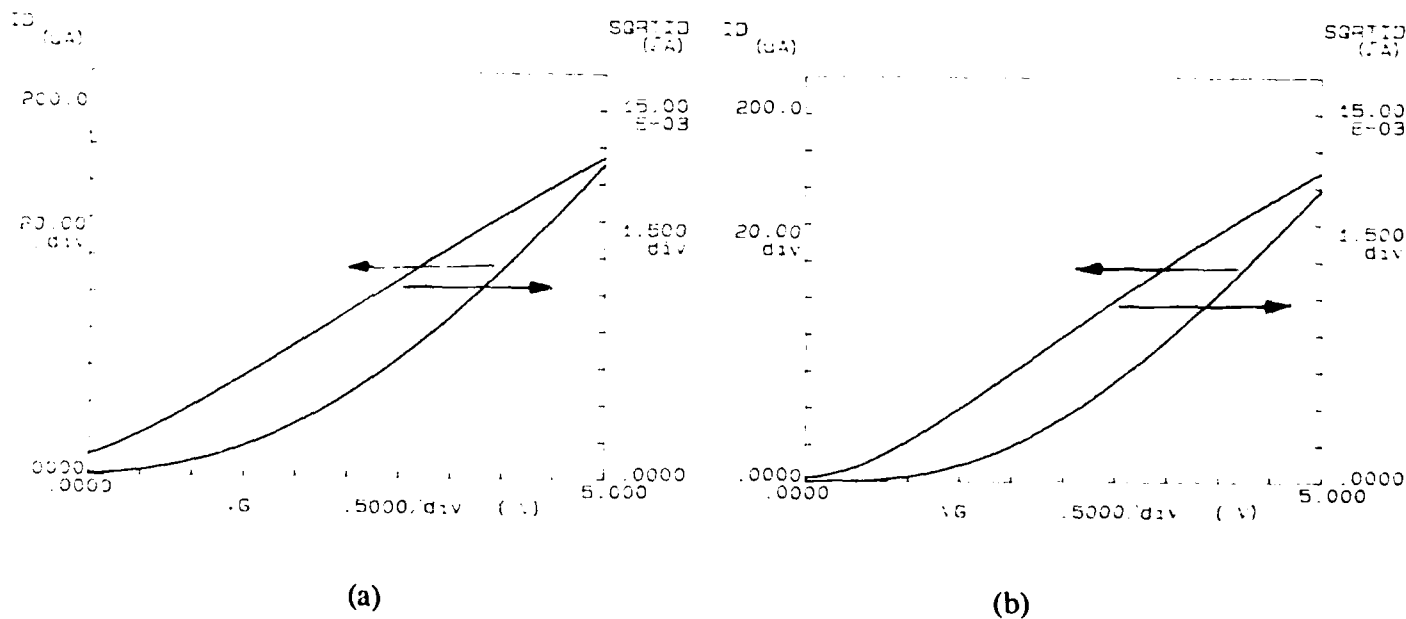


Figure 5. I_D vs. V_G curves of NMOS transistors (a) before etching on Si/SiO₂/bulk Si Kopin SOI wafer and (b) after etching on 0.6μm Si film back etched from previous wafer. Only a slight shift in threshold voltage is observed.

Hybrid Silicon/gallium Arsenide Inverted Fabry-Perot Cavity
MQW Spatial Light Modulators

Armand R. Tanguay, Jr., Anupam Madhukar, B. Keith Jenkins
University of Southern California
520 Seaver Science Center
MC0483, University Park
Los Angeles, CA 90089-0483

High bandwidth (>10 MHz) smart pixel SLMs based on the hybrid integration of silicon-based detection and control electronics with gallium-arsenide-based MQW modulators by flip chip bonding are described. The use of an inverted asymmetric cavity design obviates the need for through-substrate vias, and allows for the incorporation of high reflectivity ex situ-deposited dielectric mirrors.

Characterization of a Free-Space Opto-Electronic Interconnect System based on Si/PLZT Smart Pixels.

B. Mansoorian, G. Marsden, V. Ozguz, C. Fan, S. Esener
University of California, San Diego
Department of Electrical and Computer Engineering
Mail Code 0407
La Jolla CA, 92093
(619) 534-1743

The characteristics of Si/PLZT smart pixels suggests that they are suited for use in opto-electronic systems requiring moderate speeds and a large dynamic range due to noise and fan-out considerations^{1,2}. However, as the complexity and density of smart pixel-based systems are increased, secondary factors such as electrical and optical cross-talk between channels, device uniformity, insertion loss and scattering in modulator material, diffraction efficiency and aberration in the optical interconnection etc. are likely to dominate the performance of the interconnect. Before large scale systems can be implemented, the effects of device characteristics on system performance need to be quantified.

The best approach for this quantification is small prototype systems. These systems need to reflect the key aspects of larger systems, such as integrated modulator drivers and detectors based on typical VLSI processes. At UCSD, we are implementing a test bed for the characterization of integrated opto-electronic interconnection systems for various transmitter and detector technologies.

In order to have arrays of integrated transmitters for this system, we have designed and implemented Si/PLZT smart pixels based on a flip-chip bonding process. Figure 1 shows the cross-section of a processing element in a hybrid silicon/PLZT smart pixel array. Silicon chips are placed on a PLZT wafer that is used both as a support substrate and for light modulation (Figure 2.). The driver circuitry is placed on the silicon chips and connected to the PLZT modulator using metal bumps. The flip-chip process aligns the silicon chips to the modulators on the PLZT wafer. Since all chips use the same PLZT substrate, a chip aligned to the substrate is also aligned to all other chips on the substrate.

Integrated modulator drivers are a key part of our prototype system. This has been a problem in the past since PLZT requires a voltage of 20-40 volts to modulate light with a large dynamic range (Figure 3.). High voltage bipolar and MOS processes are presently incapable of supporting VLSI circuit densities. On the other hand, transistor breakdown voltages in VLSI chips are too low to provide high voltage outputs directly. We have designed an amplifier circuit based on series connected transistors to drive PLZT with a 35 volts swing. When flip-chip bonded, the combination of driver and reflective PLZT modulator produces light modulation with a dynamic range of 600:1. Studies of the speed response show a rise time of 250ns and a fall time of 50ns, limited by the drive circuitry (Figure. 4)^{3,4}. Figure 5 shows a microphotograph of 100 μ m diameter gold bumps connecting the silicon circuits to pads on the PLZT surface.

At the highest level, a computer system is evaluated by its functionality, reliability and speed. In the case of opto-electronic computing, we have identified bit-error rate, data transfer rate, and optical fan-out (the number of detectors receiving the signal of a single transmitter) as critical parameters. We measure the physical parameters of Si/PLZT smart pixels to the system parameters of bit error rate, frequency and optical fan-out. In particular, we perform bit error rate measurements for various combinations of frequency and fan-out.

Within the experimental phase of the characterization, two types of measurements are carried out. Eye diagram measurements are made to obtain a rough estimate of the bit error rate. The eye diagrams are also used to guarantee the optimal optical alignment for each configuration. In addition, the eye diagrams provide qualitative information as to the

main sources of error limiting the performance of the link. Once the link is optimized, the experimental setup shown in Figure 6 is used to accurately measure the bit error rate. A 64K pseudo random bit sequence (PRBS), generated by a Tektronix HFS 9003, is repetitively passed through the link. The detected signal is compared to the original signal to detect bit errors. Counts are made of both the number of bit errors and the total number of bits transmitted, with their ratio yielding the bit error rate. This system is used to study the effects of various binary coding schemes such as RZ, NRZ, Manchester, etc. on the performance of the link. Our measurement results will be reported during our conference presentation.

In summary we have designed and implemented small arrays of Si/PLZT smart pixels to be used in a prototype opto-electronic interconnect test bed. The performance of the link is currently under study.

References

- ¹S. Esener et al, "One-dimensional silicon/PLZT spatial light modulators", Optical Engineering, May 1987, vol. 26, no.5, 406-413.
- ²C.J. Kirby et al. "PLZT/silicon hybridised spatial light modulator array design, fabrication and characteristics", International Journal of Optoelectronics, 1990, vol.5, no.2, 169-178.
- ³S. Esener, G. Marsden, B. Mansoorian, "Opto-electronic free-space Interconnection system", OTC Review Meeting, Ithaca (1991)
- ⁴B. Mansoorian et al, "Design and implementation of flip-chip bonded Si/PLZT smart pixels", LEOS Summer Topical Meeting on Smart Pixels, Aug 10-12, 1992, 22-23.

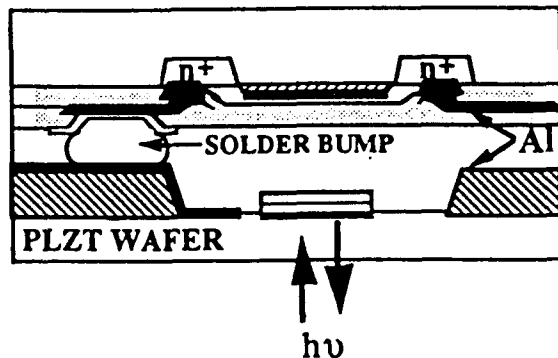


Fig. 1

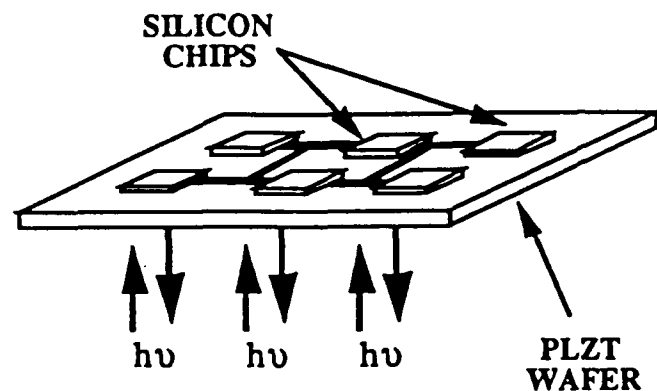


Fig. 2

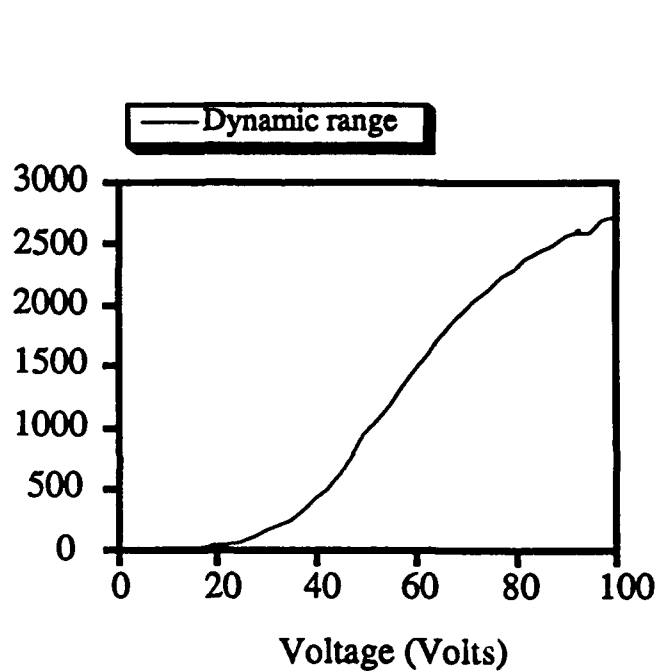


Fig. 3

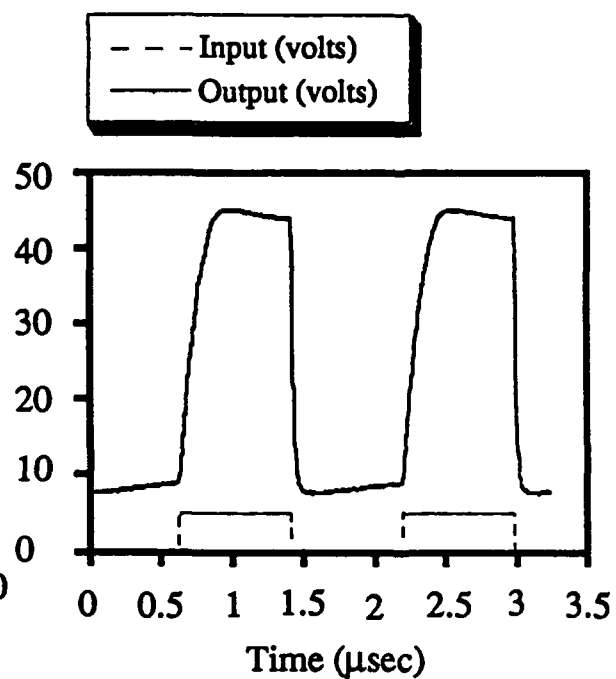
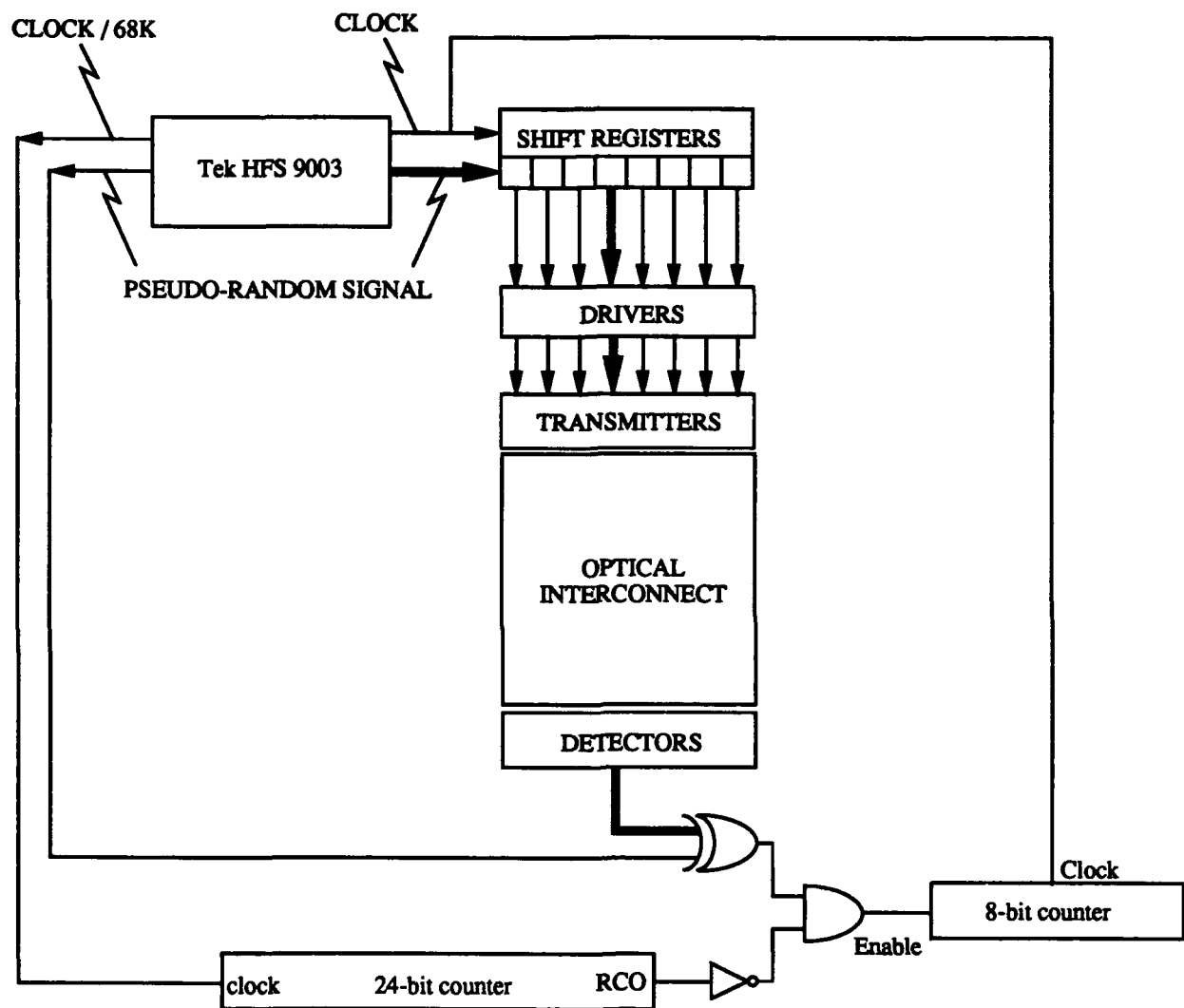


Fig. 4



Fig. 5

**Fig. 6**

Tuesday, March 16, 1993

Joint Optical Computing/ Photonics in Switching/ Spatial Light Modulators Plenary Session

JTuC 2:00pm-5:30pm
Grand Ballroom East

B. Keith Jenkins, *Presider*
University of Southern California

Joseph W. Goodman, *Presider*
Stanford University

Extended Generalized Shuffle Networks

G. W. Richards

AT&T Bell Laboratories
Room 2E-252
263 Shuman Blvd.
Naperville, IL 60566-7050

Tel. (708) 713-5425
Fax. (708) 713-7951

1.0 Introduction

A successful network architecture generally must consider the technology being proposed for implementation. A design suitable for an electronic application may prove to be unwieldy or even impossible to implement in the photonic domain. Basically this is due to the limitations and constraints imposed by the optical technology at hand.

The talk provides an overview of a new class of networks called Extended Generalized Shuffle (EGS) networks^{[1],[2]} and considers how various attributes of these networks can address some photonic switching constraints. From a purely mathematical and topological viewpoint EGS networks are technology independent and they will be handled as such in subsequent more detailed papers^{[3],[4]}. However, our current focus is on photonic switching and we will thus limit most of our discussion to those aspects of EGS networks that primarily impact the implementation of photonic switching networks. The talk is primarily intended to bridge some of the gap between photonic switching technology and switching network theory.

The following two sections catalog some constraints imposed by free-space and guided-wave photonics, respectively. The fourth section briefly summarizes how EGS networks can deal with such constraints.

2.0 Some Free-Space Photonic Switching Constraints

Free-space photonic network implementation assumes the use of symmetric self electro-optic devices (S-SEEDs)^[5] as logic gates in the switching modules of the network.

2.1 Switching Module Fan-Out/Fan-In Limitations

There are several reasons for preferring small values of fan-out and fan-in when dealing with free-space optics^[6]. If the fan-out in a particular system is large, then the optical power that is emitted from a single S-SEED must be divided before being routed to the many detecting S-SEEDs, and the optical power arriving at any one of the detecting S-SEEDs will be relatively low. Since the maximum switching speed of an S-SEED is directly proportional to the amount of optical power that sets the device, smaller fan-outs will yield faster switching speeds.

Smaller values of fan-in are also desirable within a system because the signal-to-noise ratio at the input of any S-SEED will increase as more signals are fanned into the device. The bit error rate of the system will also increase. In addition, larger values of fan-out and fan-in will typically require more complicated beam-steering optics which tend to increase the overall system cost.

Reference [6] reports a lossless beam splitting and recombination technique that suggests advantages for limiting fan-out and fan-in to values of two between stages of logic. This in turn suggests the use of switching modules having no more than two inputs and two outputs. Such modules may or may not be conventional crossbar switches; an issue we consider next.

2.2 Switching Module Functionality

The functionality provided in switching modules should consider overall network implementation complexity and efficiency. For example, consider two switching modules A and B and suppose that more B modules than A modules are required to construct a non-blocking $N \times N$ network. We next consider the implementation complexity (no. of S-

SEEDs, no. of stages, no. of control beams, etc.) of the two module types. If the complexity of module B is less than that of module A, we may find that a network using B modules has less overall complexity than one using A modules (in spite of the fact that more B modules than A modules are required to construct the network).

2.3 Switching Stage Uniformity

One important advantage in having uniform or identical switching stages is that only one type of switching stage needs to be fabricated. However, such uniformity requires that each switching stage has equal numbers of inputs and outputs (because to fully interconnect all of the outputs of a given stage with all of the inputs of the next stage requires that these numbers of inputs and outputs are equal and hence, via uniformity, that the numbers of inputs and outputs on all stages are equal). Thus, switching stage uniformity implies that the number of interconnections between stages is the same throughout the network. We consider this further in the next section.

Efficient, high performance EGS networks can be designed with uniform switching stages. In fact this constraint carries with it almost no disadvantages.

2.4 Interstage Interconnection

The "free-space" descriptor for photonic switching networks refers to the means of interconnecting successive stages of switching modules. It is advantageous for this technique to have constant numbers of interconnections between stages (as mentioned above). Two additional interconnection attributes, which have been found to be particularly convenient when employing free-space optics, are symmetry and stage-to-stage pattern invariance.

The so called "crossover"^[7] interconnection pattern has constant numbers of interconnections between stages and exhibits symmetry, but does not result in stage-to-stage invariance. However, the stage dependent variations are such that they can be achieved by selecting an appropriate prismatic mirror array for each stage. We are willing to accept these stage-to-stage variations because the crossover interconnection pattern can be shown to yield EGS networks.

2.5 Switching Stage Size and Number of Stages

There are usually advantages in keeping both the switching stage size and the number of stages small. These advantages relate to such aspects as efficiency, reliability, and power. For example, as the switching stage size is increased, the size of the S-SEED array that implements the logic of the switching stage must also increase. As a result, the optical components (lenses, beam-splitters, etc.) within a stage must be capable of providing diffraction-limited imaging over larger fields of view. In addition, system lasers must provide more optical power if larger S-SEED arrays are used. Both of these requirements will increase the cost of a single stage within the system.

If, on the other hand, the number of stages is increased, then the overall system cost will begin to increase. Also, the expected availability of the system will decrease as the number of stages is increased, because the components within the multiple stages have non-zero failure rates. Unfortunately, it is usually not possible to have small values simultaneously for both switching stage size and number of stages. What sort of compromises are possible?

S-SEED photonic EGS switching networks generally exhibit the following helpful attribute. For a given number of input and output terminals and for a given probability of blocking (including zero), as the S-SEED array size increases (decreases), the required number of stages of S-SEED arrays tends to decrease (increase). Thus, these networks give the designer the capability to trade-off between switching-stage size and number of stages.

3.0 Some Guided-Wave Photonic Switching Constraints

Guided-wave photonic network implementation assumes the use of lithium niobate couplers^[8] as the switching modules of the network.

3.1 2x2 Basic Element

The lithium niobate coupler is inherently a 2x2 device. Thus, we assume the use of switching modules having no more than two inputs and two outputs. As with free-space photonics, such modules may or may not be viewed as conventional crossbar switches.

3.2 Switching Module Functionality

Crosstalk due to imperfect lithium niobate couplers can grow to an undesirable level in a large network. One solution to this problem is to allow no more than one active signal in any coupler^[9]. This means that a coupler may be

unavailable for use even though the desired input and output of the coupler are both idle. EGS networks are able to deal directly with this constraint in network design.

3.3 Interstage Interconnection

To keep losses at a minimum, the waveguide bends between stages of couplers have relatively large radii of curvature. Additionally, the couplers themselves are relatively large in comparison to the substrate wafer used in the fabrication process. The result is that there is low coupler density and therefore limited switching functionality per substrate module. The challenge for EGS networks is to be able to utilize such low functionality modules in the design of efficient high functionality networks.

3.4 Switching Stage Size and Number of Stages

As with free-space networks, there are usually advantages in keeping both the switching stage size and the number of stages small. Overall crosstalk and loss are two items of consideration. EGS networks allow trade-offs between switching stage size and the number of stages. As one increases (decreases) the other decreases (increases). Furthermore, in the most efficient configurations, the number of stages increases slowly ($\log N$) in comparison to N (the number of inlets and outlets).

4.0 EGS Network Attributes

The following subsections catalog a few of the EGS network attributes that are helpful in dealing with photonic switching constraints.

4.1 Global Generalized Conditions for Non-Blocking Operation

It is possible to establish conditions for non-blocking EGS networks in very general terms. These conditions do not impose any constraints on the number of inlets or outlets in a network or any relationship between these two values. There is no symmetry required in the network. There are no constraints on the number of stages in the network. There is no relationship required between the size of the switching modules in one stage and any other stage. Also, the size of the switching modules in any particular stage are not generally constrained.

The major impact here is that for the most part switching networks can be designed with arbitrarily sized modules and an arbitrary number of stages. Thus, 2×2 modules can be utilized easily and switching stage uniformity becomes a natural outgrowth.

4.2 Multiple Stage Modularity

Under certain easily met conditions EGS networks exhibit the following attribute. For specific (not necessarily consecutive) stages i and j , there exist subsets of switches in both of these stages such that every switch in the stage- i subset has a path to every switch in the stage- j subset and paths to no other switches in stage j . This allows networks to be constructed via multi-stage modules, each of which is entirely unconnected from other modules in the corresponding stages.

4.3 Different Types of Switching Module Functionality

The analysis of EGS networks allows switching modules to have functionalities less than that of conventional crossbar switches. Such reduced functionality usually relates to the sizes of specified subsets of inlets and outlets on the module that can be individually connected to each other. For example, one type of module may only be able to connect all inlets to all outlets or no inlets to no outlets. Efficient EGS networks can be constructed from such modules.

4.4 Network Isomorphisms

Two networks may have the same connectivity, differing only in the way their switching modules and links are labeled or in the way they are drawn. Any two such networks are said to be isomorphic. This relationship divides the collection of all networks into isomorphic classes. It is the fortunate case that many isomorphic classes of EGS networks have members that are amenable to photonic implementation. Formal mapping functions provide the ability to similarly analyze and control many of the members of a given isomorphism class, thereby allowing technology considerations to dictate the particular member chosen for implementation.

4.5 Network Shape Trade-Offs

The generality inherent in EGS networks allows a network with a given number of inlet and outlets to have many dif-

ferent "shapes". More specifically, one can typically trade-off the number of modules per stage with the number of stages. Thus network designs can be tailored to accommodate the needs of various technologies.

4.6 Other Attributes

The theory of EGS networks encompasses other dimensions of switching applications such as routing and control. These items and others have also found value in the implementation of photonic networks. Unfortunately, the limited scope of this summary does not allow further elaboration of such topics.

5.0 References

- [1] G. W. Richards, *U.S. Patent Numbers: 4,993,016 and 4,991,168*.
- [2] T. J. Cloonan, G. W. Richards, A. L. Lentine, F. B. McCormick, and J. R. Erickson, "Free-space photonic switching architectures based on extended generalized shuffle networks", *Appl. Opt.* 31, pp. 7471-7492 (1992).
- [3] G. W. Richards and F. K. Hwang, "Extended generalized shuffle networks: sufficient conditions for strictly nonblocking operation", in preparation.
- [4] G. W. Richards and F. K. Hwang, "Extended generalized shuffle networks and switching module functionality", in preparation.
- [5] A. L. Lentine, H. S. Hinton, D. A. B. Miller, J. E. Henry, J. E. Cunningham, and L. M. F. Chirovsky, "Symmetric self-electrooptic effect device: optical set-reset latch, differential logic gate, and differential modulator/detector", *IEEE Journ. of Quant. Elect.* 25, pp. 1928 - 1936 (1989).
- [6] F. B. McCormick and M. E. Prise, "Optical circuitry for free-space interconnections", *Appl. Opt.* 29, pp. 2013-2018 (1990).
- [7] J. Jahns and M. J. Murdocca, "Crossover networks and their optical implementation", *Appl. Opt.* 27, pp. 3155-3160 (1988).
- [8] H. S. Hinton, "Photonic switching using directional couplers", *IEEE Communications Magazine*, Vol. 25, No. 5, May 1985, pp. 16-26.
- [9] K. Padmanabhan and A. N. Netravali, "Dilated networks for photonic switching", *IEEE Transactions on Communications*, Vol. COM-35, No. 12, pp. 1357-1365, December 1987.

ATM Objectives and Requirements For Next-Generation Networks

Kai Y. Eng
AT&T Bell Laboratories
Room 4F525
101 Crawfords Corner Road
Holmdel, NJ 07733-3030
Phone: (908) 949-2201 Fax: (908) 949-9118
Email: kye@boole.att.com

1. Introduction

Worldwide activities on ATM (Asynchronous Transfer Mode) have been intensifying with rapidly evolving standards (CCITT and ATM Forum) [1,2]. Applications include multimedia services, high-speed LAN's, central-office switches and high-speed digital crossconnects. Potential large-scale network conversion into ATM is being considered and debated within various research and development communities. The push for deploying ATM to upgrade the existing network infrastructure has sometimes been compared to the "analog-to-digital revolution". The primary incentive to do so stems almost entirely from its service flexibility. Here, we discuss various aspects of ATM networking, emphasizing the transport objectives and requirements for next-generation networks. We will begin with the basic notions of ATM networking and then shift to a specific example of a VP (Virtual Path) transport network using an integrated ATM Crossconnect as a key network element.

2. Basics of ATM Networking

In ATM networking, all user-generated information (voice, video and data) is converted into standard fixed-size packets called "cells" for switching and transport. This process of converting the original data into ATM cells is called "adaptation". An ATM cell has a fixed size of 53 octets consisting of a 5-octet header followed by a 48-octet payload (Fig. 1). The header contains primarily the routing information for the cell (VCI and VPI values). Unlike traditional synchronous TDM transmission systems where data are sent via preassigned time slots, ATM traffic is transported by cell multiplexing without dedicated slots, and cells from a given source would appear to the network as asynchronous traffic. A simplified depiction of an ATM network connecting two users, A and B, is illustrated in Fig. 2. In order to initiate a communication connection between A and B, a call set-up procedure has to be invoked, e.g., a call request from A to B via ATM Switch I (signaling and control not shown in Fig. 2). As part of the call set-up process, ATM Switch I needs to inform A's ATM adapter proper VCI and VPI values to use and also to assure that these header parameters are recognized by various network elements along the assigned route for routing. Let us focus on the routing function first.

An ATM end-to-end connection from A to B is designated as a Virtual Circuit and hence a VCI in the cell header. A specific path from ATM Switch I to ATM Switch II, however, is called a Virtual Path which may contain many Virtual Circuits between various source-destination pairs connected to ATM Switches I and II. Along a specific VP, there may be multiple ATM Crossconnects (XC's) which are VP switches. Therefore, a VP is essentially a specific routing path from an originating ATM Switch to a destinating ATM Switch through a series of ATM XC's. All cells from a given source in the same connection traverse the same Virtual Path, and

their original sequence is thus maintained. The VPI value in the header designates the VP, but its use requires a translation process explained later in the next section.

The transmission line standard between ATM network elements (Switches and XC's) is assumed to be SDH (or SDH), e.g., 155 Mb/s OC-3c, 622 Mb/s OC-12c or 1.4 Gb/s OC-48. As specified in the standards, ATM cells are mapped into the payload of the SDH envelope. Since the VPI value has 12 bits, each transmission link can carry up to 4096 unique VP's. The processing of the SDH overhead and ATM cells in the payload is an important part of the line interface at each ATM XC (often called "line cards"). The delivery of cells according their VP, namely VP transport, plays an important role in ATM networking because of its flexible service and fast restoration capabilities [3]. We will focus on the operation of VP transport by describing an overview of an integrated ATM XC.

3. ATM Crossconnect Functions and Requirements

When ATM cells are carried as payload in the SDH envelope for optical transmission, they have to be recovered before switching can take place at each ATM XC. The function of receiving the optical signal, terminating its SDH overhead and recovery of its payload (i.e., ATM cells) is usually called the LTE (lightwave terminal) function. The VP switching of cells is of course the main goal of the XC. VP switching here means the routing of the incoming cells to the appropriate output ports according to their VPI values on a cell-by-cell basis. Although not required, today's technology permits an integrated design whereby both the LTE and the VP switching functions are combined in a single machine. The LTE part is implemented mostly in the line cards, and the VP switching in the "XC fabric". For subsequent discussions, we only consider an integrated ATM XC.

Various essential functions required in an integrated ATM XC are summarized in Fig. 3. After optical detection, the received SDH signal is descrambled and frame synchronized so that the overhead bytes can be retrieved. Processing of these overhead bytes is required to provide several maintenance functions such as line integrity, line protection switching, inter-XC data communications, etc. Furthermore, pointer processing has to be performed to establish synchronization for recovering the "floating" frames (called virtual containers) of ATM cells in the payload. The beginning of each cell has then to be identified within the virtual container. After the cells are extracted, they have to be properly processed before the actual switching, and this part may either be implemented in the line card or as part of the XC fabric.

In ATM cell processing, OA&M (operation, administration and maintenance) cells are separated from data cells. OA&M cells may be destined for the local system controller or for further transport. The data cells are first processed with HEC (header error correction). Cell headers with 1-bit errors can be corrected, and those with more than 1-bit errors are discarded immediately. The VPI value is then examined in a table look-up for validation and also to identify the output port for the routing of each cell. Cell routing is implemented in the XC fabric which is functionally identical to a conventional ATM switch fabric. As such, cell buffering is required because multiple cells may destined for the same output port at the same time. This aspect has been well understood in ATM switching. In addition to the routing, the most important processing is perhaps the translation of the incoming VPI value in each cell to a new value (preassigned by network control). That is, for each cell transit through the ATM XC, there is a unique mapping of its incoming VPI value to its outgoing value. Consequently, a VP can be characterized by a unique series of VPI values along the various physical links in its route. Doing so allows for maximum utilization of the VPI values (limited to 12 bits) in each physical link.

At an output port of the XC fabric, cells from different inputs are multiplexed together to form a stream. They have to be individually checked for errors and to verify proper routing (plus internal diagnostics) before passed on as input to a SDH processor. In this SDH processor (output line card), the ATM cells are inserted into the payload envelopes, and new pointer and other overhead bytes are included in the final assembly of the whole SDH signal for optical transmission.

The capability of electronics is advancing rapidly to meet the requirements of high-performance ATM network elements. An integrated prototype ATM XC recently demonstrated includes an 8x8 ATM fabric operating at 2.5 Gb/s and with multiple-rate line cards (OC-3c to OC-48) [4]. This is equivalent to a total system capacity of 20 Gb/s, supporting up to 128 bidirectional OC-3c (155 Mb/s) interfaces or up to eight bidirectional OC-48 (2.4 Gb/s) interfaces. Expansion to much larger fabric sizes is possible and is being researched.

4. Conclusions

VP transport is a fundamental aspect of ATM networking. It provides flexible service and fast restoration capabilities in next-generation networks. An ATM XC capable of cell-by-cell routing is a key network element to support VP transport. In addition, extensive SDH and ATM cell processing is required in implementing the ATM XC, today's VLSI technology is adequate to meet these challenges efficiently and economically.

REFERENCES

- [1] Martin de Prycker, *Asynchronous Transfer Mode*, Ellis Horwood, 1992.
- [2] *CCITT Recommendations*, I.113, I.121, I.150, I.211, I.311, I.321, I.327, I.361, I.362, I.363, I.413, I.432 and I.610.
- [3] K. Sato, H. Ueda, and N. Yoshikai, "The Role of Virtual Path Crossconnection," *IEEE LTS Magazine*, August 1991, pp. 44-54.
- [4] K. Y. Eng, M. A. Pashan, R. A. Spanke, M. J. Karol and G. D. Martin, "A High-Performance Prototype 2.5 Gb/s ATM Switch For Broadband Applications," *IEEE Globecom '92 Conference Record*, Vol. 1, Dec. 6-9, 1992, pp. 111-117.

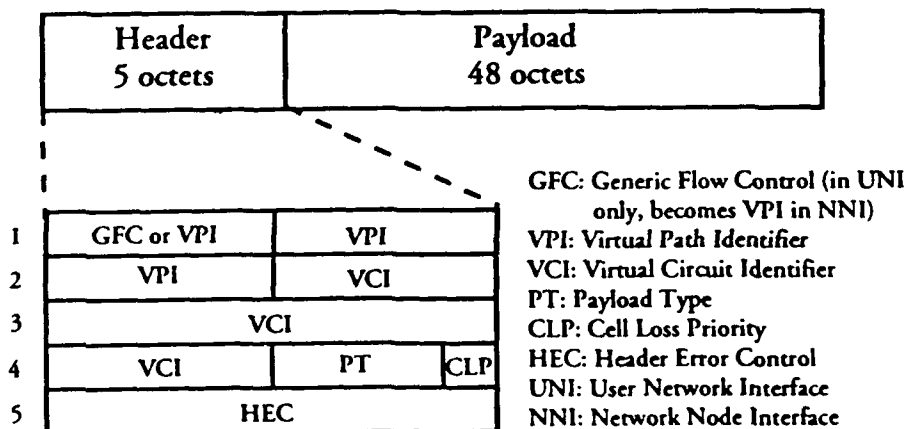


Fig. 1 ATM Cell

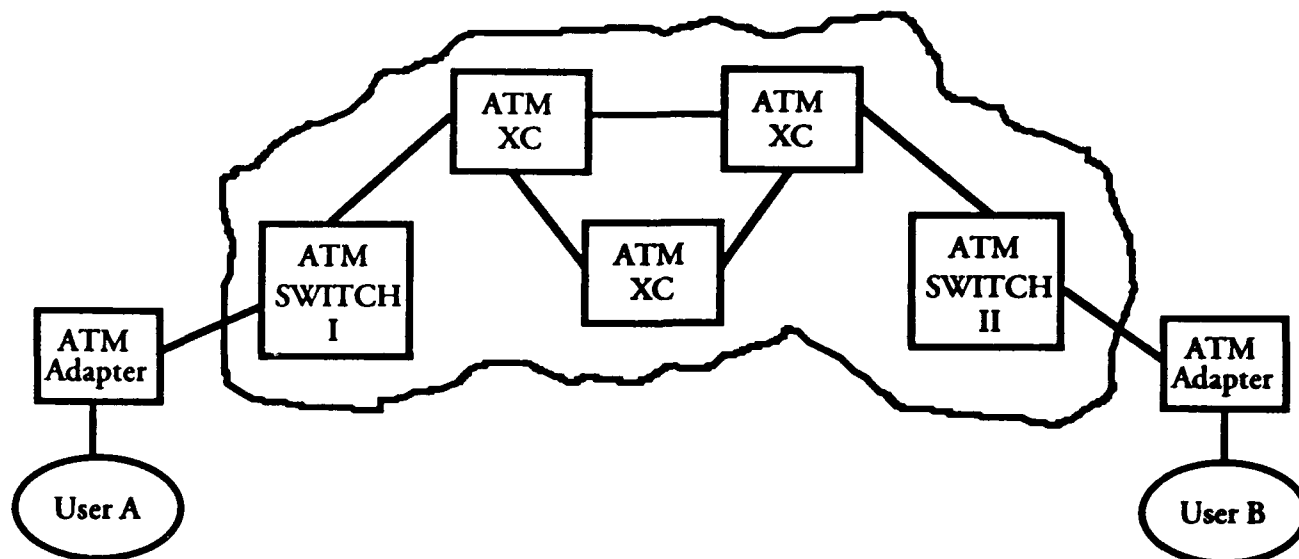


Fig. 2 An ATM Network Example

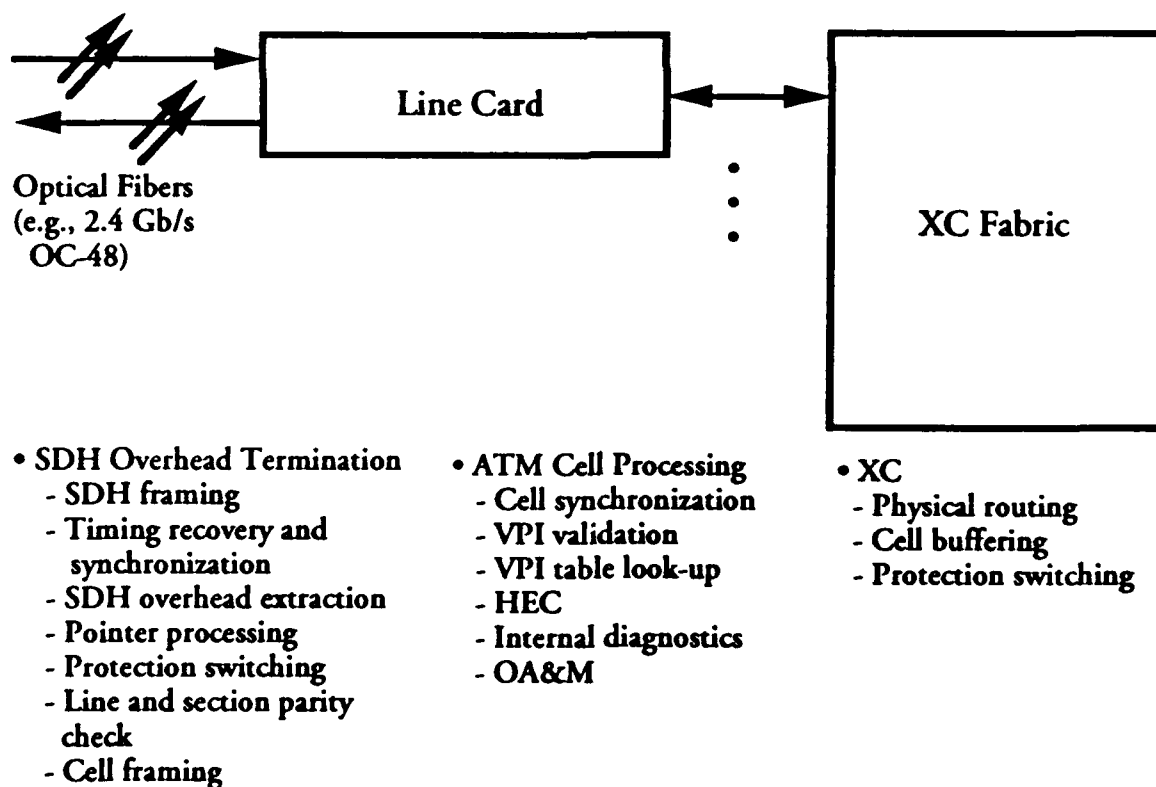


Fig. 3 Essential Functions of An Integrated ATM XC

Photonics in switching: European systems demonstrators and the long term perspective

Lars Thylén *

Dep of Microwave Engineering
Royal Institute of Technology
S-100 44 Stockholm Sweden

January 13, 1993

Status in the area of photonics in switching in Europe, highlighted by systems demonstrators, is reviewed, and the long term perspective for photonics in switching is discussed.

1 INTRODUCTION

It is widely recognized that the progress and role of photonic switching have not paralleled that of fiber optics point to point communications, where new avenues for fiber optics keep opening, most recently in the shape of *fiber to the home* and the associated introduction of broadband services. The discussions concerning fiber to the home, and the corresponding systems issues, seem to have been only marginally influenced by the possibilities offered by photonic switching. Part of the explanation for this state of affairs is the competition from electronics, and the uncertainty of the actual bandwidths required by different services and subscriber categories, but mostly the lack of clear and verifiable systems solutions where photonic switching offers significant and unique advantages. In addition, we have the comparative immaturity of the device technology required as well as the lack of a practical and reasonably standardized way of assembling optical systems. This situation is reflected in the comparatively small number of systems demonstrators and the virtually nonexistent field trials to date. Ref [1], [2] are exceptions here, but they can not be described as fully fledged field trials.

This paper discusses development over the last few years concentrating on the European scene, where several European research programs (COST as well as RACE) have included projects (especially the RACE OSCAR R1033) more or less devoted to photonic switching. Some current representative systems demonstrators are described. Comments on the relationship between electronic and optical switching, based on switching energy, pertinent for ATM switching, are finally made.

This paper concentrates on *guided wave switching systems and devices*, there are strong proponents of *free space 3D systems and technology*, [3], [4]. However, the situation here is even less mature as far as technology is concerned, and systems proposals and technology demonstrated so far are no more convincing than the guided wave concepts. The rationale and motivation for *integrated photonics* in photonic switching is the same as those underlying the unparalleled success of *integrated electronics*.

2 DEVELOPMENTS IN PHOTONICS IN SWITCHING

The rationale for photonic switching is the uncontested bandwidth and loss of the optical guided wave transmission as well as the speed allowed by optical interactions. Different attempts have been made to

*Also with Fiber Optics Research Center, Ericsson Telecom AB, S-126 25 Stockholm, Sweden

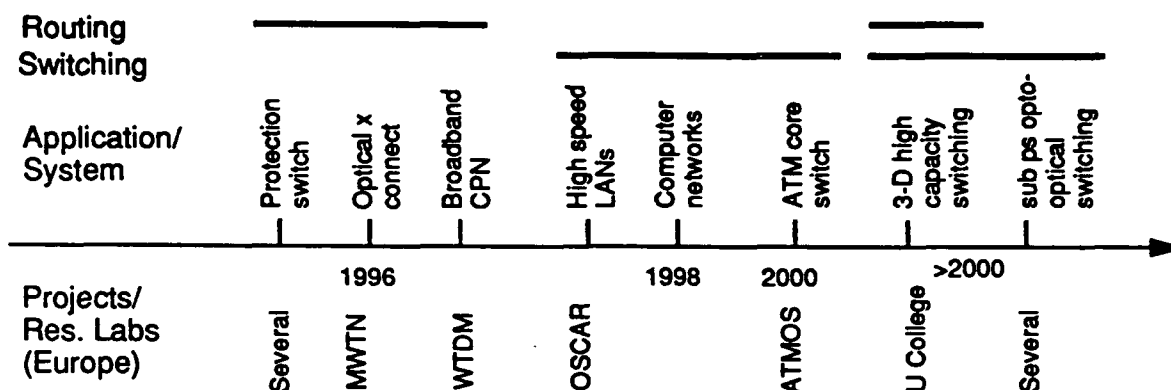


Figure 1: Evolution scenario of photonic switching. Years indicate possible time of field trial. MWTN, WTDM, ATMOS and OSCAR are RACE projects, mentioned in the text

shape this into new systems architectures, ("optical ether"). Broadly speaking, this has led to a number of schools:

- Circuit type low speed switching, involving switching in space and wavelength
- STM, ATM and PTM type switching, where optical temporal switching is involved, in some cases in conjunction with wavelength and space division switching.
- 3D optical interconnects in combination with OEICs, where the processing is (mainly) electronic and the transmission optic.
- Whereas the above approaches can in essence be classified as *optical interconnect under electronic control*, there also is the possibility for *opto-optical switching*, e.g. via soliton interactions [5]

Crucial in all attempts to apply temporal switching is the lack of an optical RAM type memory, comparable in integration and performance to electronic ones, since various degrees of synchronization and storage are required. It appears that only wavelength and space division switching make use of the bandwidth in a way commensurate with the bandwidth of the transmission medium, thus creating a novel fiber optic "network" that is to a degree bitrate and coding independent ("transparency"). It should be borne in mind that we are dealing with an *analog, nonlinear* network. However, time division switching type network structures have been suggested and partly demonstrated, where optical switching functions are simple and in some cases memoryless ([6], [7]), again taking advantages of the basic features of the optical transmission medium. See also [8]. One could attempt to structure the development in photonic switching according to Fig 1.

3 SYSTEMS DEMONSTRATORS

The systems demonstrators, which in some sense can be labeled as photonic switching ones, currently developed within the RACE program, are part of the following projects: Wavelength and time division multiplexing (WTDM) broadband CPN network, Multiwavelength transport network (MWTN) and ATM optical switch (ATMOS). The first two are essentially in category A) in section 2, the third in category B). All these projects are based on RACE I projects. In addition there is a German program, which addresses ATM type switching. The talk will discuss these projects, two of which are described below. Fig 2 shows the basic structure of the R2039 ATMOS demonstrator [9]. This utilizes synchronized ATM cells at the input (for all practical purposes of electronic origin). The cell encoder wavelength encodes the packets utilizing wavelength converters (e.g. in the shape of bistable DBR lasers). Contention is resolved by a cell buffer block with K fiber optic delay lines (K=16 in a suggested system; with no contention, this entire block can of course be deleted). Power splitters and optical gates (semiconductor laser amplifiers) route the packets to the pertinent delay line. The packets (still of course synchronized), enter a space switch in the shape of a star coupler, with optical filtering at the output. Four layers of this type, each comprising a Clos net with 3 stages of 16×16 switches will have a total throughput of 10 Tb/s, with a 10^{-9} cell loss rate for 16 cell buffers (fig 2), with $10\mu s$ delay. The line rate is 2.6 Gb/s. A rigorous comparison with an all electronic system still remains to be done and is a challenging research topic. It

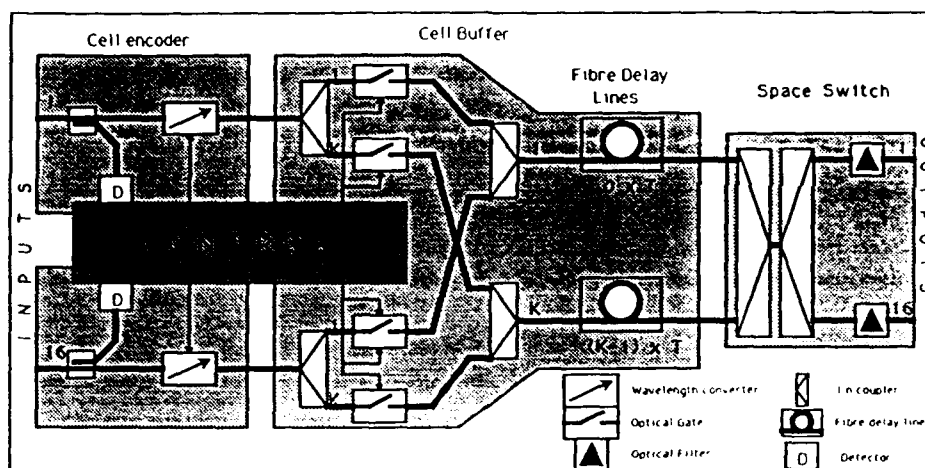


Figure 2: ATM optical switch (ATMOS) system demonstrator

should be noted that impressive results have been reported recently on fiber optic delay lines, applicable to this concept [10]. The ATMOS system presents a number of very challenging device requirements, notably wavelength converters and optical storage. Fig 3, on the other hand, represents an example of a *routing system* [11], see also [12]. The structure in fig 3 performs routing in the space and wavelength domains. Hence, we are not concerned with a reconfiguration of the network, more rapid than that called for by eg protection switching ($> \mu s$). The core of the network is formed by tunable lasers in the transmission system, tunable filters and space switches in the switching system and fiber amplifiers in a line system. Also important (but historically given little attention in systems like this) is the control system. Since the signals are not immediately available in electronic form (with a few exceptions, such as laser amplifiers [13]), the control system has to be structured accordingly, and the devices provided with control interfaces, the need of which is not superficially obvious. Two issues of prime importance are wavelength referencing and power equalization. The system in fig 3 constitutes a logical extension to the existing transport network concepts, adding flexibility, reliability as well as resilience, by performing routing in a frequency and code transparent way. The systems claims made here (the underlying systems rationale is about the same in WDM) are maybe not as far reaching as for ATMOS, but the application appears reasonably near term. In fact, in view of the continued development of the transport network with electronic cross connects, the optical cross connect appears to be a good candidate for a fairly imminent application, being uncontested by electronics.

4 HIGH SPEED SWITCHING: PHOTONICS OR ELECTRONICS OR BOTH?

A view often advocated in the optics community is to justify photonic switching by extreme speed and superior bandwidth. However, MODFET transistors have been reported with speeds up to 500 GHz, and several roads into the THz realm exist: Superconductors, quantum interference, single electron transfer, and brute force scaling of dimensions. The last exercise has given uninterrupted *exponential* performance growth since the 40s! "Fundamental" limits appear to be no hindrance to continued development for the next few decades. This means that electronic integration levels, switch energy as well as speed will continue to improve. Concerning integration and switch energy, it appears that basic considerations prevents photonics from presenting a viable alternative to electronics [14]. Hence, the combination of photonics and electronics has to be given serious consideration. One example could be low level of photonic integration (where dissipation is less of a concern) for extremely high speed (sub ps) multiplexing and demultiplexing, with the slower and complex (more integration intensive) tasks carried out by electronics.

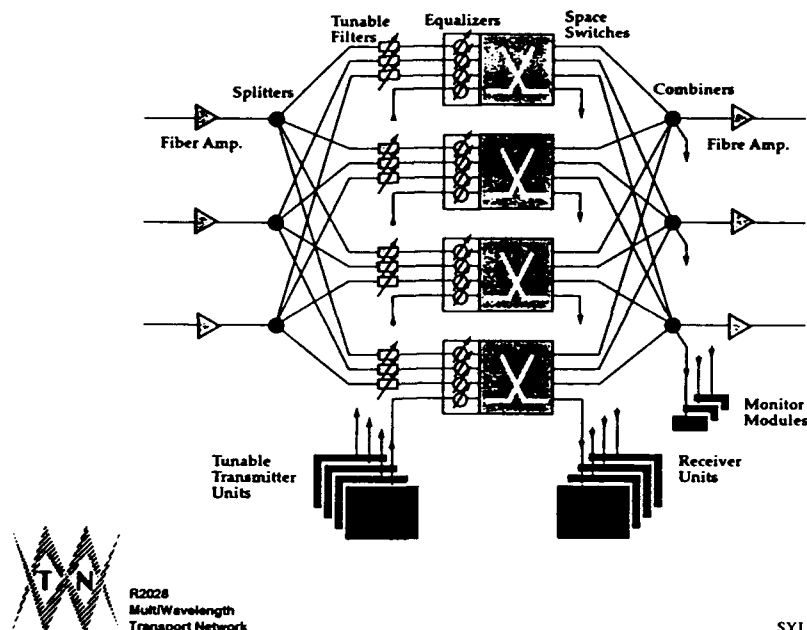


Figure 3: MWTN system demonstrator

5 CONCLUSIONS

This paper has described two representative examples of photonic switching demonstrators, showing different approaches, differing device requirements and addressing different time perspectives. It should be emphasized that photonic switching can not be seen in isolation but only from a total systems perspective. Some research items of photonic switching can be identified: Rigorous research on electronic vs photonic switching, including systems considerations; the potential of extremely high speed, low integration switching using nonlinear optical interactions, such as solitons; 3D reconfigurable interconnect, combined with OEICs. While these are certainly worthwhile to pursue, it appears that the span to the present needs to be bridged by more applied research; thus field trials are highly desired in the next few years, unless photonic switching is to share the fate of at least part of the field of optical computing.

References

- [1] D Edinger, P Duthie, G R Prabhakara, "A new answer to fiber protection", Telephony, (1990), p 53
- [2] T G Lynch et al, "Experimental field demonstration of a managed multinoded reconfigurable wavelength routed optical network", Proc 18th European Conf on Optical Communications, Berlin, Germany, (1992), p 609
- [3] J E Midwinter, "Photonics in Switching: The next 25 years of optical communications?", IEE Proceedings-J, vol 139, (1992), p 1
- [4] H S Hinton, "Overview of freespace photonic switching", Proc Int Top Meeting Photonic Switching, Kobe, Japan, (1990), paper 12 D1
- [5] M N Islam, C J Chen, C E Soccolich, "Ultrafast all-optical fiber soliton logic gates", Proc Top Meeting Photonic Switching, Salt Lake City, USA, (1991), paper WD2
- [6] D J Blumenthal, K Y Chen, J Ma, R J Feuerstein, J R Sauer, "Demonstration of a deflection routing 2×2 photonic switch for computer interconnects", IEEE Phot Techn Lett, vol 4, (1992), p 169
- [7] P Prucnal, P Perrier, "Self routing photonic switching with optically processed control", Optical Engineering, vol 29, (1990), p 170

- [8] T. M. Martinson, "Synchronization of passive access nodes in very high speed optical packet networks", Proceedings of ECOC '90, Amsterdam, The Netherlands, p 473, (1990)
- [9] J M Gabriagues, "Exploitation of the wavelength domain for photonic switching in the IBCN", Proc 17th European Conf on Optical Communications, Paris, France (1992), p 59
- [10] M Eiselt et al, "One million pulse circulations in a fiber ring using a slalom for pulse shaping and noise reduction", Proc 18th European Conf on Optical Communications, Berlin, Germany, (1992), p 875
- [11] S Johansson, M. Lindblom, P. Granstrand, B. Lagerström, L. Thylén, "Optical Cross-Connect Systems in Broadband Networks: System Concept and Demonstrators Description."; G. R. Hill, et. al. "A Transport Network Layer Based on Optical Network Elements.", to be published in J Lightwave Techn.
- [12] T Shiragaki et al, "An experimental optical digital crossconnect system using $LiNbO_3$ photonic switch matrices and optical amplifiers", Proc 18th European Conf on Optical Communications, Berlin, Germany, (1992), p 605
- [13] M. Gustavsson, L. Thylén, A. Djupsjöbacka, *Electron.Lett.*, **25**: 1375, (1989)
- [14] L. Thylén, T Palm, to be published

Transition from Optical Interconnections to Optical Computing

**Richard C. Williamson
Massachusetts Institute of Technology
Lincoln Laboratory
Room C317, 244 Wood St.
P.O. Box 73
Lexington MA 02173-6479**

Optical interconnections will be a foot in the door to the next generation of computer systems and provide an evolutionary path toward the use of optics in finer scales.

Wednesday, March 17, 1993

Multiple-Quantum Well SLM Technology

SWA 8:30am-10:00am
Grand Ballroom West

Anthony L. Lentine, *Presider*
AT&T Bell Laboratories

Applications and Technology of Quantum Well Self-Electrooptic-Effect Device Arrays

David A. B. Miller

*AT&T Bell Laboratories, Rm. 4B401
101 Crawfords Corner Road
Holmdel, NJ 07733-3030*

Self-electrooptic-effect devices (SEEDs) [1] are combinations of quantum well modulators and photodetectors, possibly with other circuitry, that allow devices with optical inputs and outputs. Quantum well modulators are based on strong electroabsorptive effects in quantum wells [2]. These effects are so large that useful absorption changes (e.g. $\times 2$) are possible in a single pass through only a micron of material. This strength means that two-dimensional arrays of devices can be made for light beams propagating perpendicular to the surface of a semiconductor wafer. Such arrays can be used for optically bistable switching and logic [3], for both optically [4] and electrically [5] addressed spatial light modulators, and for novel analog optical processing functions [6]. This technology can also be extended to make various kinds of digital [7] and analog [6] "smart pixels", including integration with GaAs electronics (FET-SEEDs) [8], and possibly Si electronics [9]. We will summarize here the current status of some of this work and the future directions.

One very important feature of these devices is that they can be made with high yields and they can be integrated. When made in arrays [10], the yields on individual devices are about 999 out of 1000, allowing arrays of many thousands of devices with good total yields of fully functional arrays. Unlike lasers, they are not threshold devices, and no sophisticated lateral processing is required to make them work. This processing simplicity makes integration of the quantum well devices with other devices, such as transistors, relatively straightforward. This relative simplicity has led to the successful demonstration of complex integrations of field effect transistors and quantum well modulators and detectors (FET-SEEDs) [8]. The quantum well devices are also intrinsically very fast, and have low energy consumption. These various properties make these integrated quantum well device arrays an interesting technology for high performance smart arrays.

This device technology also has been tested in various large digital systems experiments, which have significantly influenced the evolution of the devices. Recent work [11, 12] has concentrated on switching systems. Recent large systems use devices that can be viewed as smart electrically and optically addressed spatial light modulators. The needs of working digital systems first forced the use of pairs of light beams, rather than single beams, to improve system tolerances. More recently, the requirement of high performance from a large system have created a need for even lower optical input energies and smarter functionality between the optical inputs and outputs. Such needs can be satisfied by integrating with electronics, using transistors to give energy gain at the optical inputs and to give increased smartness. The current FET-SEED technology [8] can operate at hundreds of megahertz. Current circuits have about 20 transistors per smart pixel, and optical input energies can be less than 100 fJ.

Although most attention in SEEDs has focussed on digital applications, they also have various analog modes. Recent work [6] has proposed a variety of analog functions that could be

performed in parallel in arrays of devices based on the existing SEED array technologies. Functions proposed include addition, subtraction, uniform amplification, replication, spatial differentiation, convolution, cross-correlation, and optically controllable weights for matrix-vector processors or neural nets. Many of the devices can operate with differential pairs of light beams, allowing full bipolar analog processing. Such functions could be useful for image processing applications.

In conclusion, SEED technology continues to evolve towards a flexible, integrated, optoelectronic array technology that could allow us to take best advantage of both electronic and optical domains for a variety of analog and digital processing tasks.

- [1] For a review of SEEDs, see D. A. B. Miller, "Quantum well self-electrooptic-effect devices", *Optical and Quantum Electron.*, **22**, S61-S98 (1990)
- [2] For a review of quantum-well electroabsorption and devices, see D. A. B. Miller, "Quantum well optoelectronic switching devices", *Int. J. High Speed Electronics*, **1**, 19-46 (1990)
- [3] For a review of recent progress in SEEDs, see A. L. Lentine and D. A. B. Miller, "Evolution of the SEED technology: Bistable logic gates to optoelectronic smart pixels", to be published, *IEEE J. Quantum Electron.* (Special Issue on Smart Pixels, February 1993)
- [4] G. Livescu, D. A. B. Miller, J. E. Henry, A. C. Gossard, and J. H. English, "Spatial light modulator and optical dynamic memory using integrated self-electrooptic-effect devices", *Optics Lett.* **13**, 297-299 (1988)
- [5] A. L. Lentine, L. M. F. Chirovsky, L. A. D'Asaro, R. F. Kopf, and J. M. Kuo, "High-speed 2x4 array of differential quantum well modulators", *IEEE Photonics Tech. Lett.*, **2**, 477-80 (1990)
- [6] D. A. B. Miller, "Novel analog self-electrooptic-effect devices", to be published, *IEEE J. Quantum Electron.* (Special Issue on Smart Pixels, February 1993)
- [7] A. L. Lentine, F. A. P. Tooley, S. L. Walker, F. B. McCormick, R. L. Morrison, L. M. F. Chirovsky, M. W. Focht, J. M. Freund, G. D. Guth, R. E. Leibenguth, G. J. Przybylek, L. E. Smith, L. A. D'Asaro, and D. A. B. Miller, "Logic self electrooptic effect devices: Optoelectronic multiport logic gates, multiplexers, demultiplexers and shift registers", *IEEE J. Quantum Electron.* **28**, 1539-1553 (1992)
- [8] L. A. D'Asaro, L. M. F. Chirovsky, E. J. Laskowski, S. S. Pei, T. K. Woodward, A. L. Lentine, R. E. Leibenguth, M. W. Focht, J. M. Freund, G. D. Guth, and L. E. Smith, "Batch fabrication and testing of GaAs-AlGaAs field effect transistor self-electrooptic-effect device (FET-SEED) smart pixel arrays", to be published, *IEEE J. Quantum Electron.* (Special Issue on Smart Pixels, February 1993)
- [9] K. W. Goossen, G. D. Boyd, J. E. Cunningham, W. Y. Jan, D. A. B. Miller, D. S. Chemla, and R. M. Lum, "GaAs-AlGaAs Multiquantum well reflection modulators grown on GaAs and silicon substrates", *IEEE Photonics Tech. Lett.*, **1**, 304-6 (1989)
- [10] A. L. Lentine, F. B. McCormick, R. A. Novotny, L. M. F. Chirovsky, L. A. D'Asaro, R. F. Kopf, J. M. Kuo, and G. D. Boyd, "A 2kbit array of symmetric self-electrooptic-effect devices", *IEEE Photonics Tech. Lett.*, **2**, 51-53 (1990)
- [11] F. B. McCormick, F. A. P. Tooley, T. J. Cloonan, J. L. Brubaker, A. L. Lentine, R. L. Morrison, S. J. Hinterlong, M. J. Herron, S. L. Walker, and J. M. Sasian, "Experimental

investigation of a free-space optical switching network by using symmetric self-electrooptic-effect devices" Appl. Opt., **31**, 5431-46 (1992)

- [12] H. S. Hinton and D. A. B. Miller, "Free-space photonics in switching", AT&T Tech. J., **71**, No. 1 (Jan./Feb.), 84-92 (1992)

Spatial Light Modulator using Semi-Insulating Multiple Quantum Well Material

A. Partovi, A. M. Glass
AT&T Bell Laboratories, Murray Hill, New Jersey, 07974

T.H. Chiu
AT&T Bell Laboratories, Holmdel, New Jersey, 07733

In recent years, the large excitonic electroabsorptive nonlinearities of multiple quantum wells (MQWs) has been used for electrically as well as optically addressed two dimensional optical modulators. Most of the modulators so far place the MQW material in a p-i-n structure thereby necessitating the need for pixelation of the device. Multiple quantum well materials made semi-insulating either through proton implantation [1] or doping with a mid-gap level such as Cr [2] can provide electroabsorptive nonlinearities similar to undoped MQWs while alleviating the need for pixelation. Here we describe spatial light modulators based on Cr-doped GaAs/AlGaAs MQW material. The optically addressed device has been used as the holographic element in a joint Fourier transform correlator for pattern recognition and performs a correlation in 1 μ sec.

The optically addressed SI-MQW device consists of 155 periods of 10 nm GaAs wells and 3.5 nm $\text{Al}_{0.29}\text{Ga}_{0.71}\text{As}$ barriers grown by molecular beam epitaxy (MBE) and sandwiched between evaporated layers of 200 nm of phosphate silica glass (PSG) dielectric layer and cadmium tin oxide (CTO) transparent electrode. The entire MBE grown MQW is doped with $10^{16}/\text{cm}^3$ of Cr to provide semi-insulating behavior. Applying an ac voltage of 5-20 volts to the sample, large absorption changes ($\Delta\alpha \sim 6000 \text{ cm}^{-1}$ for 20 V applied) and refractive index changes ($\Delta n \sim 0.06$ for 20 V applied) are obtained near the exciton peak at 850 nm due to quantum confined stark effect (QCSE) [2]. Illumination of the device with photon energies larger than the band-gap produces photogenerated carriers that can drift to the MQW/dielectric interface and screen the applied electric field from the MQW. The absorption and refractive index of the MQW can in this way be optically modulated.

To characterize the device, we performed a wave mixing experiment with two single longitudinal mode diode lasers. The beam from an 830 nm diode laser was split into two equal beams and crossed at the SI-MQW device to produce a 20 μm period interference pattern. The beam from another diode laser at 850 nm (near heavy-hole exciton peak) was used to probe the grating. Applying an ac voltage of 20 V and 5.6 kHz frequency to the sample, diffraction of the 830 nm light from the grating was observed. To investigate the relation between the nonlinearity and the incident intensity, we varied the total intensity of the 830 nm beams incident on the

sample while keeping their ratio unity. Figure 1 shows the relative diffraction efficiency into the first order for the 850 nm beam as a function of the total 830 nm intensity. It can be seen that for the experimental conditions used, the diffraction efficiency $\eta \sim \Delta\alpha^2$ or $\Delta n^2 \sim I^2$. We can see that the nonlinearity is proportional to the incident intensity for the range studied. The SI-MQW device can therefore be used to record real-time holograms for image processing applications such as optical correlators.

We have used the optically addressed SI-MQW device in an optical correlator system as the real-time holographic medium. Using 150 mW diode lasers, the correlation is obtained in 1 μ s and the hologram can be erased in 2 μ s presenting the possibility of a system capable of 3×10^5 correlations/sec. However, in our initial implementation, the images are input to the system using a liquid crystal spatial light modulator (LCSLM) and the output is read-out by a CCD camera. Thus the throughput of the system is limited by the input SLM in this experimental arrangement. Using a 2-dimensional spatial light modulator based on semi-insulating MQW material as the input SLM, we expect to be able to take full advantage of the μ s response time of the optically addressed SI-MQW device.

The experimental setup for the correlator is shown in Fig. 2. The output of a 150 mW single longitudinal mode diode laser at 830 nm reads the input image on a 320x220 pixel Epson liquid crystal spatial light modulator (LCSLM). The two images to be correlated $f(x,y)$ and $g(x,y)$ are input side by side to the LCSLM. A doublet lens with $F=26$ cm is used to Fourier transform the images. The SI-MQW device is placed at the Fourier plane and records the interference pattern due to multiplication of the fourier transforms of the two images. A square-wave voltage of ~ 10 kHz and 15-20 V is used to drive the SI-MQW device. An 850 nm diode laser reads the recorded pattern. This laser is typically run at ~ 10 mW and its wavelength can be temperature tuned to the optimum value for high diffraction efficiency from the SI-MQW device. After passing through the SI-MQW and the Fourier transform lens, the correlation pattern is formed on the CCD camera placed at the back focal plane of the lens. The throughput of the system is limited by the input SLM in the present experimental arrangement. Real-time correlation of images using bulk photorefractive materials have been demonstrated in the past [3]. The advantages of the current system include: i) Higher speed due to the high sensitivity ($1 \mu\text{J cm}^{-2}$ incident energy density to write a grating) of the optically addressed SI-MQW device. ii) Lack of space-bandwidth limitations on the input image due to the Bragg condition at the holographic material [3]. The thin SI-MQW material operates in the Raman-Nath regime. iii) The wavelength compatibility with current high power diode lasers.

Figure 3a shows a surface plot of a portion of the output of the CCD camera in response to the hand-written input image shown in Fig. 3b. A strong peak corresponding to the auto correlation of the bottom "2" with the similar upper right "2" and a weaker cross-correlation peak

for the bottom "2" with the different upper left "2" is seen. As expected, no strong correlation peaks are observed for the digit "4". This example shows the high signal to noise ratio achievable with SI-MQW correlators. The lack of scatter noise is a major advantage of atomically flat MQW devices. In addition, it can be seen that a certain tolerance to image shape exists. By correlating two images of typed image "SI-MQW" and varying the size and shape of one of the images until the correlation peak falls to the average noise value, we find an angular tolerance of $\pm 20^\circ$ and size tolerance of $\pm 20\%$ for the correlator system.

REFERENCES

1. Y. Silberberg, P.W. Smith, D.A.B. Miller, B. Tell, A.C. Gossard, and W. Wiegmann, Appl. Phys. Lett. **46**, 701 (1985).
2. "Cr-doped GaAs/AlGaAs Semi-Insulating Multiple Quantum Well Photorefractive Devices", A. Partovi, A. M. Glass, D. H. Olson, G. J. Zydzik, H.M. O'Bryan, T.H. Chiu, and W.H. Knox, Submitted to Appl. Phys. Lett.
3. L. Pichon, and J.P. Huignard, Opt. Comm. **36**, 277 (1981).

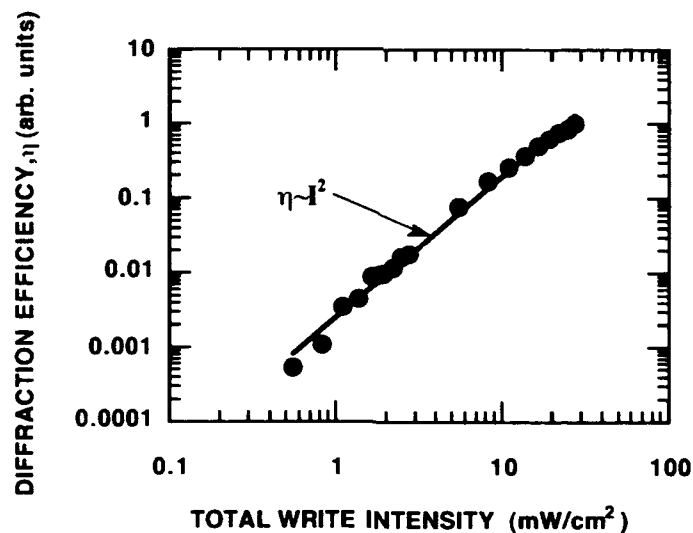


Fig. 1 Diffraction efficiency into the first order for the 10 mW cm^{-2} read beam at 850 nm as a function of the total intensity of the two equal write beams at 830 nm. The line is a best fit quadratic dependence.

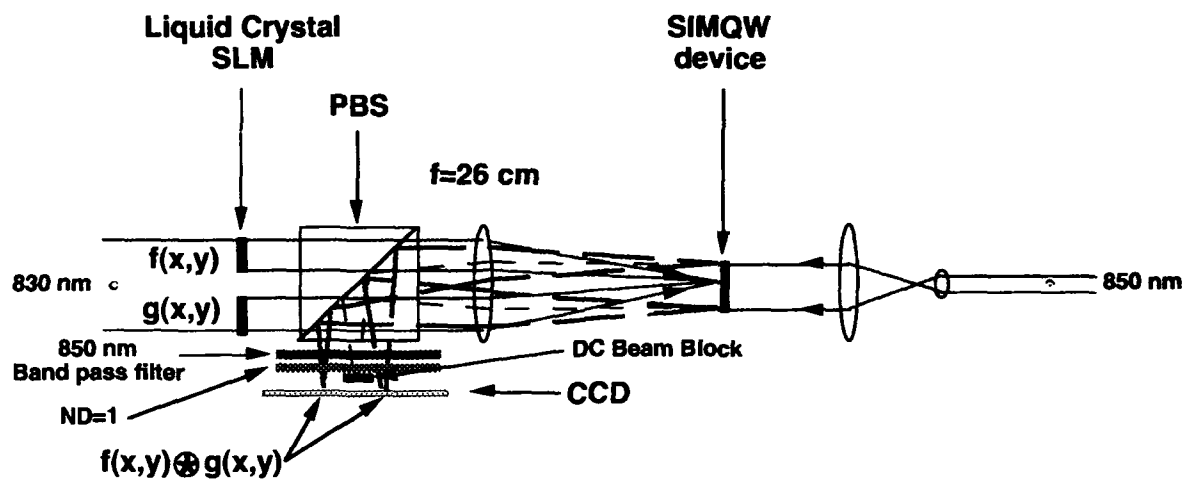


Figure 2. Schematic diagram of the experimental setup for the joint Fourier transform correlator. PBS: polarizing beam-splitter.

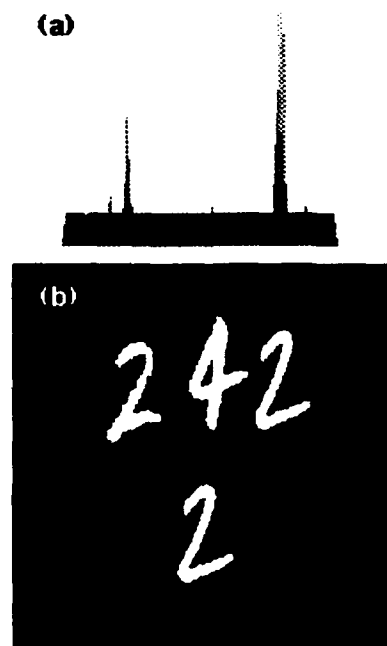


Figure 3. (a) Surface plot of a portion of the output of the CCD camera in response to an input image shown in (b) consisting of the hand-written number "242" to be correlated with "2".

High Contrast Spatial Light Modulator Using Stark Effect Tuning and Heterostructure Acoustic Charge Transport (HACT) Pixel Addressing

F. Jain, S.K. Cheung, and R. LaComb
Electrical and System Engineering Department
The University of Connecticut, Storrs, CT. 06269-3157

and
T. Grudkowski, R. Sacks, and D. Cullen
United Technologies Research Center, East Hartford, CT. 06108

The demonstration of optical modulation by Miller et. al.[1] using the Stark effect in multiple quantum wells (MQWs) has resulted in a variety of device structures[2] based upon changes in absorption, index of refraction, and polarization. In addition to modulation, important issues in the realization of spatial light modulators (SLMs) include adequate high on/off contrast ratio and methodology of addressing a large array of pixels ($> 10^6$). This paper describes a novel spatial light modulator structure which utilizes the high contrast ratio feature of a Fabry-Perot cavity along with Stark effect tuning, and pixel addressing by the heterostructure acoustic charge transport (HACT) scheme.

The transport of signal charge in a HACT structure, employing a modulation doped channel, to manipulate electronic functions has been reported in literature[3]. The presence of a charge packet in the channel adjacent to the MQW layers, hosting excitons created by an incident laser input, is shown to result in significant electric field[4,5] to affect optical modulation. The 3-D structure as well as the cross sectional view of a HACT SLM is schematically shown in Fig. 1. The signal charge packet, which is generated or injected by an optical or electronic modulating signal, induces an electric field E_{\perp} across the underlying InGaAs-GaAs multiple quantum well layers. The electric field in turn causes a Stark effect shift in optical parameters[6] such as absorption and index of refraction. Pixel-addressing is achieved by transporting the charge packet from one pixel to another by the surface acoustic wave generated by an interdigitated transducer. The modulated output is proportional to the signal charge transported in the HACT channel. This method of addressing the pixels is in contrast with other techniques which include the use of charge-coupled devices (CCDs)[7] and conventional row/column interconnects. Unlike other techniques, HACT addressing does not require elaborate electrodes and clocking circuits. It is also compatible with frame freeze analog memory mode of operation[8].

The basic HACT-SLM shown in Fig. 1(a), like other MQW modulators using excitonic Stark effect, offer modest (10--20 : 1) contrast ratios[9]. The contrast can be enhanced by the usage of a Fabry-Perot cavity. Fig. 2 shows an integrated SLM structure having a HACT structure realized on top of a Fabry-Perot cavity consisting of InGaAs/GaAs multiple quantum wells sandwiched between AlAs-GaAs mirrors. The results of simulations are shown in Fig. 3, which compares a Fabry-Perot cavity with and without the layers associated with the HACT structure. Here, M1 and M2 are the number of AlAs-GaAs periods in the top and

bottom mirrors, respectively, and C is the thickness of the InGaAs-GaAs MQW cavity. High contrast ratios in Fabry-Perot structures have been reported in the literature[10]. We believe that a variety of Fabry-Perot structures possessing high contrast ratios can be integrated with the HACT addressing scheme.

This work has been supported by a SDIO-ONR contract N00014-91-C-0090. Discussions with Dr. W. Miceli are gratefully acknowledged. Technical assistance of Messers G. Peterson, R. Carroll and G. Ball has been valuable to this project.

References:

- [1]. D.A. B. Miller, D.S. Chemla, T.C. Damen, A.C. Gossard, W. Wiegmann, T.H. Wood, and C.A. Burrus, "Electrical Field Dependence of Optical Absorption Near the band Gap of Quantum Well Structures," *Phys. Rev. B* 32, pp. 1043-1060, July 15, 1985.
- [2]. F. Jain, K. Bhattacharjee, and T. Grudkowski, "Recent Developments in Multiple Quantum Well Acousto-optic and Electro-optic Modulator Structures", *Proc. IEEE 1991 Ultrasonics Symposium*, Vol. 1, pp.529-536, December 1991 (Lake Buena Vista, FL).
- [3]. W. J. Tanski, S.W. Merritt, R.N. Sacks, D.E. Cullen, E.J. Branciforte, R.D. Carroll, and T.C. Eschrich, "Heterojunction Acoustic Charge Transport Devices on GaAs," *Appl. Phys. Lett.*, 52, pp. 18-20, January 1988.
- [4]. F.C. Jain and K.K. Bhattacharjee, "Two-Dimensional Spatial Light Modulators Utilizing HACT-Controlled Quantum Confined Stark Effect," *SPIE Proc.* 1347, pp. 614-622 (San Diego, CA.; July 8-10, 1990).
- [5]. K.K. Bhattacharjee, and F.C. Jain, "Spatial Light Modulators Using Acoustic Charge Transport Controlled Stark Effect in Multiple Quantum Well Structures," *Technical Digest*, 14, pp. 64-67, (OSA Topical Conference on Spatial Light Modulators, September 10-12, 1990).
- [6]. Y. Kan, H. Nagai, M. Yamanishi, and I. Suemune, "Field Effects on the Refractive Index and Absorption Coefficient in AlGaAs Quantum Well Structures and their Feasibility for Electrooptic Device Applications", *IEEE J. of QE*, QE-23, pp. 2167-2179, 1987.
- [7]. W.D. Goodhue, E.E. Burke, K.B. Nichols, G.M. Metz, and G.D. Johnson, "Quantum Well Charge-coupled Devices for Charge-coupled Device Addressed Multiple Quantum Well Spatial Light Modulators," *J. Vac. Sci. Tech.*, B4, pp.769-772, 1986.
- [8]. D. Cullen and M. Miller "First HACT Analog Memory Devices Demonstrated" *Proc. IEEE 1991 Ultrasonics Symposium*, Vol. 1, pp.529-536, December 1991 (Lake Buena Vista, FL).
- [9]. A. Harwit, R. Fernandez, and W.D. Fades, "High Contrast Ratio InGaAs/GaAs Multiple Quantum Well Spatial Light Modulators," *SPIE Proc.* 1541 [San Diego, CA.; July 24, 1991].
- [10] R. Jin, G. Khitrova, H.M. Gibbs, C. Lowry, and N. Peyghambarian, " High Contrast, Submilliwatt power InGaAs/GaAs Strained-Layer Multiple -Quantum Asymmetric Reflection Modulator" *Appl. Phys. Lett.* 59, 3216-3218(1991).

Amplitude / phase modulation • Up to 10 μs delays • Bandwidth up to 500 MHz

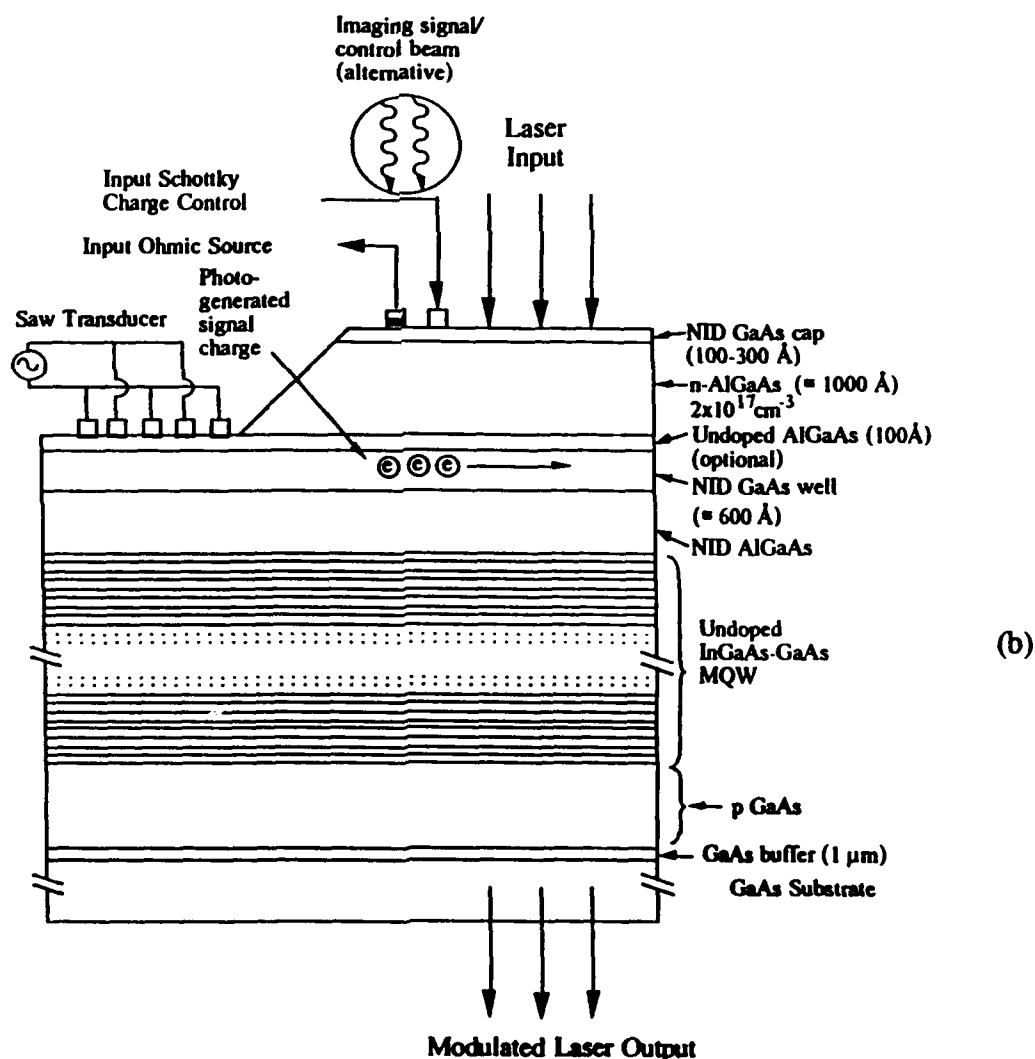
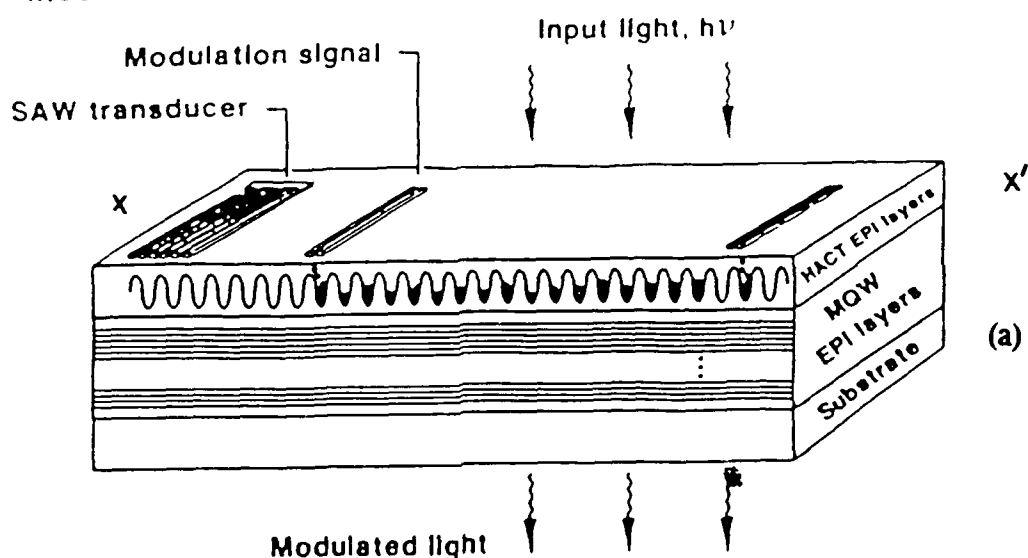


Fig 1. Heterostructure Acoustic Charge Transport (HACT) Controlled Multiple Quantum Well optical modulator structure; (a) 3-D schematic, (b) cross sectional view along x x'.

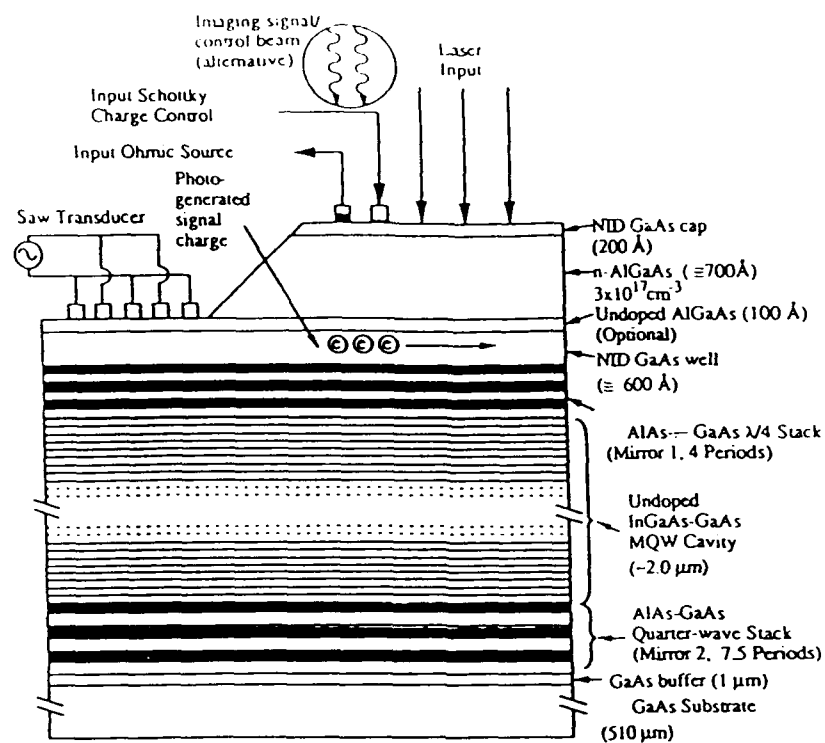


Fig 2. Heterostructure Acoustic Charge Transport (HACT) controlled Multiple Quantum Well optical modulator structure with a Fabry-Perot cavity.

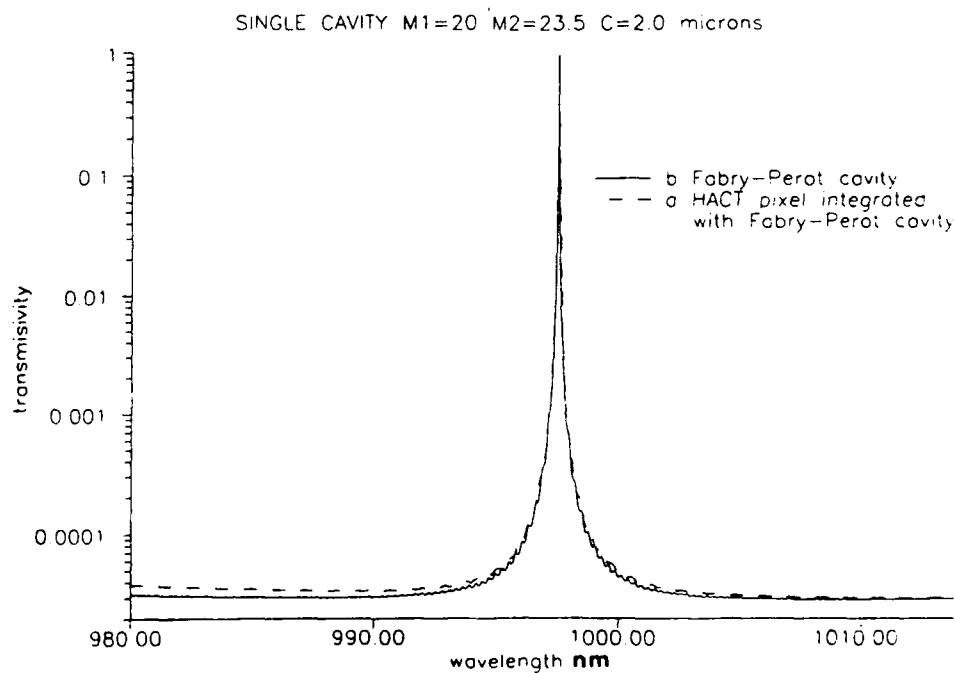


Fig 3. Transmission characteristics: (a) HACT pixel integrated with Fabry-Perot cavity (b) Fabry-Perot cavity.

A Novel High Contrast Multiple Quantum Well Spatial Light Modulator Based on Polarization Rotation

H. Shen,[†] M. Wraback,[‡] J. Pamulapati, M. Dutta, J. Kosinski, W. Chang, P. Newman

U. S. Army Research Laboratory
Electronics and Power Sources Directorate
AMSRL-EP-EF, Fort Monmouth, New Jersey 07703-5601
(908) 544-2978

Y. Lu

ECE Department
Rutgers University
Piscataway, New Jersey 08855-0909

Prior research on multiple quantum well (MQW) spatial light modulators (SLM) has concentrated on amplitude modulation, relying on a sufficient difference in the absorption coefficient between the on/off states at the operating wavelength to achieve useful contrasts. The change in the absorption coefficient is due to either the quantum confined Stark effect¹ (QCSE) or Wannier Stark localization². Unfortunately, the maximum obtainable change in the absorption coefficient is only about $2 \times 10^4 \text{ cm}^{-1}$, limited by broadening of the exciton peak.³ In addition, the thickness of the intrinsic region of a MQW modulator is limited to several microns to maintain a standard operating voltage. Therefore, the contrast ratio in a simple MQW SLM is typically limited to less than 10. To enhance the contrast ratio ($> 100:1$) a MQW can be integrated with an asymmetric Fabry-Perot (ASFP) cavity.^{4,5} Conversely, SLMs utilizing polarization rotation, such as liquid crystal and magneto-optic devices have achieved significantly higher contrast ratios ($> 10^4:1$), although they exhibit poor operating speeds. Due to symmetry considerations, polarization rotation is not possible for light incident normal to a MQW structure (lattice matched or pseudomorphic). However, an external perturbation, such as uniaxial stress along the x (or y) direction, breaks the rotation symmetry, mixing the heavy and light holes in the MQW and resulting in an anisotropic excitonic absorption.⁶ In combination with the QCSE, tunable polarization rotation can be achieved. In this paper we present the concept and report the first demonstration of such a device with an exceedingly high contrast ratio of 330:1.

Two p - i (MQW)- n structures grown on (100) GaAs have been used in this study. The i region consists of 100 periods of GaAs (100 Å and 150 Å for sample A and B respectively)/ $\text{Al}_x\text{Ga}_{1-x}\text{As}$ (60 Å, $x=10\%$ and 20%) MQWs. A 500 Å AlAs sacrifice layer used for epitaxial lift-off is grown below the active layer.⁷ The lift-off thin film is bonded to a transparent substrate (LiTaO_3) which has a direction-dependent thermal expansion. The host substrate is cut such that the thermal expansion, α_y , matches the thermal expansion, α_{MQW} , and the thermal expansion, α_x , is different from α_{MQW} . By choosing a proper bonding

temperature, T_0 , and operating temperature, T , a uniform uniaxial strain of

$$\epsilon = (a_x - a_{MQW}) \times (T - T_0)$$

is achieved.

Shown in Fig. 1 is the absorption spectrum for sample A bonded to LiTaO_3 at 300K and operating at 200 K. Sample B shows similar anisotropy at $T \neq T_0$. The solid (dashed) line is for light polarized along the x (y) direction. The peaks labeled 11H and 11L are for heavy and light hole exciton transitions. Near the exciton peak the absorption, α_x , is significantly different from α_y . This anisotropy corresponds to a compressive uniaxial strain equivalent to 0.1%. To prove the anisotropy is originating from the thermally induced uniaxial stress, we have performed measurements at $T = T_0$ and $T > T_0$. The former exhibits isotropic absorption and the latter is indicative of tensile stress.

To achieve polarization rotation, the incident light is polarized at 45° with x and y axes as shown in Fig. 2. The polarization of transmitted light is rotated by an angle of

$$\theta = \arctan \left[\exp \left(-\frac{\Delta\alpha d}{2} \right) \right] - 45$$

where $\Delta\alpha = \alpha_y - \alpha_x$ and d is the thickness of $i(\text{MQW})$ layer. θ can be modulated by applying a voltage to the $p-i(\text{MQW})-n$ structure or by optically addressing the device with a pulse. Since heavy- and light-holes have different polarization selection rules, they rotate the polarization in different directions. The maximum rotation we

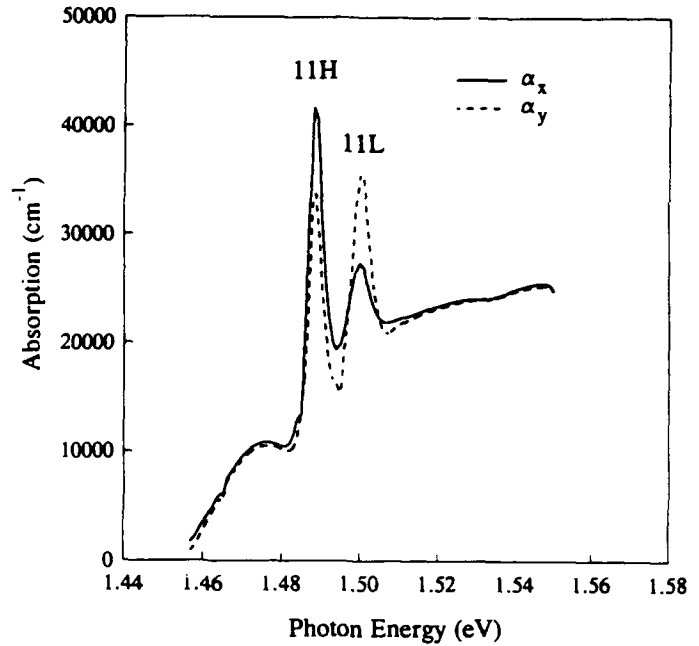


Fig. 1: Absorption spectrum from a sample under a 0.1% built-in uniaxial strain, α_x, α_y for polarization parallel (perpendicular) to the stress.

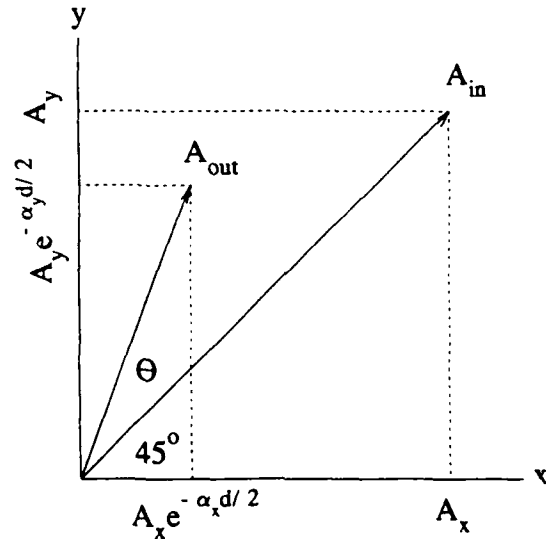


Fig. 2: Illustration of polarization rotation caused by an anisotropic absorption.

have achieved is $\pm 25^\circ$.

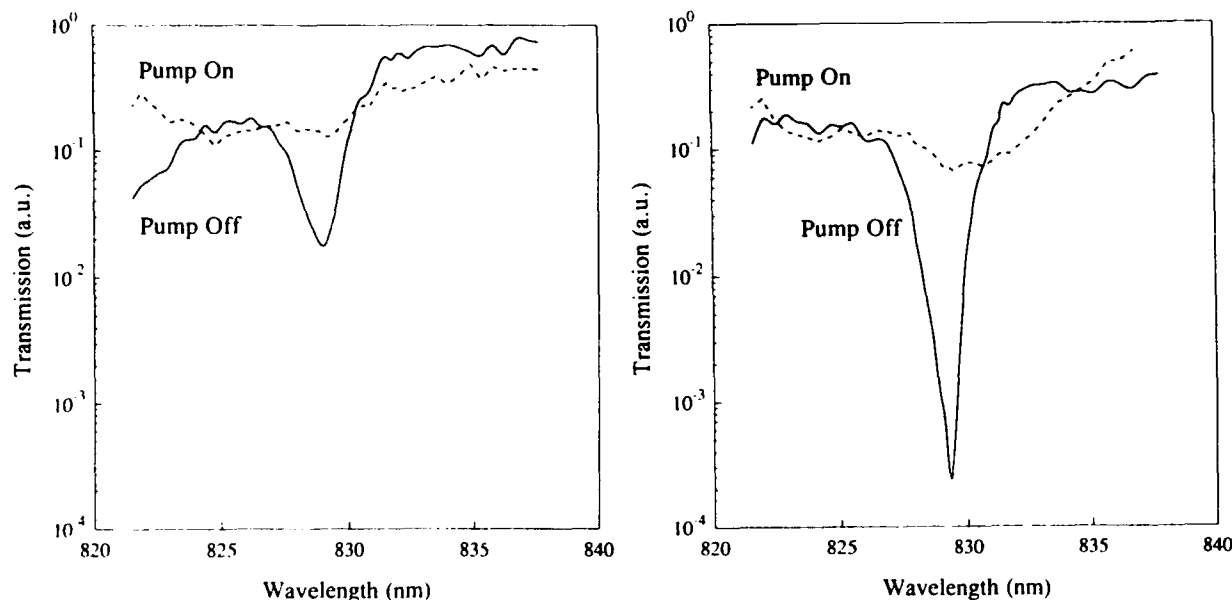


Fig. 3: Transmission as a function of wavelength for optical addressing. Solid (dashed) line is for off (on) state. a) amplitude modulation only, b) amplitude modulation with polarization rotation.

Figure 3(a) shows the transmission as a function of wavelength for optical addressing. The experiment is performed using a mode-locked Ti-Sapphire laser. The dashed line in Fig. 3(a) is the on-state when the gating pulse is on. The solid line is the off-state. In Fig. 3(a) no advantage due to polarization rotation has been achieved; therefore, the transmission exhibits simple amplitude modulation. The contrast ratio is only 8:1 at $\lambda = 829$ nm. To enhance the contrast ratio, a high quality polarizer is inserted in the path of the transmitted beam and is oriented perpendicular to the polarization of the off-state. By doing so, the transmitted light in the off-state is significantly reduced as shown in Fig. 3(b), resulting in a very high contrast ratio of 330:1.

In summary, we have presented a novel MQW SLM using thermally induced uniaxial stress and polarization rotation. We have achieved a controllable built-in uniaxial stress in the MQW device using a substrate possessing a direction dependent thermal expansion. We demonstrate a high contrast ratio of 330:1 in this device. Furthermore, the devices presented can be easily incorporated into an ASFP cavity, and the contrast ratio can be further enhanced.

References

- † Also at Geo Centers, Inc., Lake Hopatcong, New Jersey 07849.
- ‡ NRC-EPSD Research Associate.
1. D. A. B. Miller, D. S. Chemla, T. C. Damen, A. C. Gossard, W. Weigmann, T. H. Wood, and C. A. Burrus, **Phys. Rev. B** 32, 1043 (1985).
 2. J. Bleuse, G. Bastard, and P. Voisin, **Phys. Rev. Lett.** 60, 220 (1988)
 3. K. W. Jelley, R. W. H. Engelmann, K. Alavi, and H. Lee, **Appl. Phys. Lett.** 55, 70 (1989)
 4. M. Whitehead, A. Rivers, G. Parry, J. S. Roberts, and C. Button, **Electron. Lett.** 25, 984 (1989)
 5. K-K. Law, R. H. Yan, L. A. Coldren, and J. L. Merz, **Appl. Phys. Lett.** 57, 1345 (1990)
 6. H. Qiang, F. H. Pollak, Kai, Shum, Y. Takiguchi, R. R. Alfano, S. F. Fang, and H. Morkoc, **Appl. Phys. Lett.** 60, 2651 (1991)
 7. E. Yablonovitch, T. Gmitter, T. J. Harbison, and R. Bhat, **Appl. Phys. Lett.** 51, 2222 (1987)

Wednesday, March 17, 1993

Asymmetric Fabry-Perot MQW Modulators

SWB 10:30am-12:10pm
Grand Ballroom West

Constance J. Chang-Hasnain, *Presider*
Stanford University

Phase Characteristics of Reflection Electro-Absorption Modulators

Daxin Liu, S.M. Lord, M. Larson, J.A. Trezza, J.S. Harris Jr.,
Solid State Laboratories, Stanford University, CA 94305

B. Pezeshki, T.J. Watson Research Center, IBM, Yorktown Heights, NY 10694

Asymmetric Fabry-Perot(F-P) reflection modulators¹ with multi-quantum well cavities perform as excellent intensity modulators with high contrasts and large reflectivity changes. In addition to the intensity modulation caused by the absorption changes in the cavity, an accompanying phase modulation results from the refractive index changes that correlate with the absorption change through the Kramers-Kronig transformation^{2,3}. The phase properties are also strongly influenced by the Fabry-Perot effects. For instance, even without any changes in the refractive index, the phase of a reflection modulator may switch by 180 degrees at resonance⁴. Since parasitic phase changes in an intensity modulator can seriously degrade overall system performance, the phase properties of these devices merit consideration. In this paper, we present experimental results on the phase properties of a high contrast and low loss reflection modulator, and describe simple models that qualitatively explain the behavior.

The chirp parameter, α_c , is commonly used to measure the relative phase and intensity modulation in a device. For a pure phase modulator α_c is infinite, while a perfect intensity modulator has an α_c of zero. For a transmission device the chirp parameter is defined as:⁵

$$\alpha_c = \frac{\Delta n}{\Delta k} = 2 \frac{\Delta \Phi}{\Delta \ln(I)} \quad (1)$$

where Δn and Δk are the changes in the real and imaginary parts of the complex refractive index, $\Delta \Phi$ is the phase change of the modulated light, and I is the output intensity. A typical quantum well laser has α_c in the range of 1 to 3,⁶ while the chirp of quantum well modulators can be significantly lower.⁷ Although reflection modulators have the same index and absorption changes as transmission devices, the effective chirp parameter of a reflection modulator can be much lower, since the interference effects allow an infinite contrast ratio. From eq. (1), if the phase change $\Delta \Phi$ remains finite, but the intensity goes to zero, the effective chirp parameter also goes to zero.

To measure the phase characteristics of a reflection modulator, we used a Michelson interferometer with the device in one arm and a movable mirror in the other arm. The output of a tunable Ti:Sapphire laser was split by a non-polarizing beam splitter. One beam was focused on the device while the other was reflected from the reference mirror mounted on a piezoelectric transducer. Moving this mirror by scanning transducer voltage changed the optical length in the reference arm and therefore produced sinusoidal intensity oscillations at the center of the interference patterns at the output. The phase change as a function of reverse bias voltage at a given wavelength may be determined by comparing patterns taken at different biases to the pattern for the zero volt case.

Using this technique, we tested a normally-on intensity modulator. The back mirror consisted of 25.5 pairs of $\text{Al}_{0.33}\text{Ga}_{0.67}\text{As}$ / AlAs quarter-wave layers grown on an n^+ GaAs substrate, while the cavity had $92 \times 75\text{\AA}$ GaAs quantum wells with $93 \times 35\text{\AA}$ AlAs barriers. The top mirror was a six period $\text{Al}_{0.33}\text{Ga}_{0.67}\text{As}$ / AlAs quarter-wave stack with an AlGaAs half-wave layer on top. This half-wave layer was included to allow tuning the front mirror by etching after growth and fabrication. At the resonant wavelength of 8481\AA , this device exhibited a high contrast ratio ($> 100:1$) and very low insertion loss ($< 0.32\text{dB}$) when measured with a Ti:Sapphire laser. Fig. 1 shows the normalized reflectivity spectrum of this device around the resonance wavelength under several bias voltages. Fig. 2 shows both the normalized reflectivity and final phase change relative to the zero volt case as a function of device bias measured near the high contrast wavelength. The phase behavior is highly nonlinear, initially decreasing with bias, then rising sharply and then decreasing again. The effective chirp parameter is calculated to be 0.53 at 37V.

Although index changes are necessary for phase modulation in a transmission device, absorption changes alone can lead to phase changes in a F-P cavity. As the absorption is increased in a F-P cavity, the phase monotonically decreases below the resonance wavelength, increases above the resonance wavelength and switches by 180° at the resonance wavelength. This phase reversal is caused by the higher reflectivity back mirror dominating at low cavity losses and the front mirror dominating at high losses. To include the effect of index changes in this simple model, we simulated an ideal F-P device using the transmission matrix method⁸, and assumed that the absorption and index change uniformly at all wavelengths with a chirp parameter of one. This effectively shifts the resonance to longer wavelengths as the absorption increases. The behavior we simulated is qualitatively similar to the exact case if we assume the exciton always stays at shorter wavelengths than the cavity resonance. The simulated structure consists of a 6 period front mirror and a 25.5 period back mirror with the cavity treated as one slab of uniform material.

Fig. 3 shows the simulated phase versus wavelength of the reflected light for various cavity absorptions, while Fig. 4 a,b, and c show the reflectivity and the phase change versus the absorption coefficient in the cavity at three wavelengths. The phase change is relative to the absolute phase of the reflected light when the absorption in the cavity is very low. From Fig. 4a and Fig. 4b, we can see that when the modulator is operating at a wavelength shorter than or equal to the wavelength where the contrast ratio is maximum, λ_1 , the phase of the reflected beam decreases first as the absorption in the cavity increases, and drops steeply when the reflectivity is at its minimum. For wavelengths longer than λ_1 (Fig. 4c) the behavior is different; the phase decreases both before and after the matching condition, but rapidly increases at the reflectivity

minimum. Comparing Fig. 2 to Fig. 4 c, we see qualitative agreement. This indicates that the wavelength we used to measure the phase change is actually slightly above the maximum contrast wavelength. The change happens much faster in the experimental data since the absorption changes rapidly with voltage when the exciton gets close to the F-P wavelength. The numbers on Fig. 3 and Fig. 4c correspond to points of the same absorption and wavelength. Since the absorption changes qualitatively shift the phase versus wavelength behavior, and index changes simply shift the whole curves in wavelength, this approach can qualitatively predict the phase behavior when the absorption and index changes are known.

In conclusion, we interferometrically characterized a Fabry-Perot intensity modulator. Though the effective chirp can be reduced with a F-P cavity, the phase behavior is nonlinear. With a first order model, this phase behavior can be qualitatively predicted.

References

- 1 G. D. Boyd and G. Livescu, *Optical and Quantum Electronics* **24**, S147, (1992).
- 2 Y. H. Lee, J. L. Jewell, S. J. Walker, C. W. Tu, J. P. Harbison, and L. T. Florez, *Appl. Phys. Lett.* **53**, 1684, (1988).
- 3 G. Livescu, G. D. Boyd, R. A. Morgan, L. M. F. Chirovsky, and A. M. Fox, *Appl. Phys. Lett.* **60**, 1418, (1992).
- 4 B. Pezeshki, G. A. Williams, and J. S. Harris Jr., *Appl. Phys. Lett.* **60**, 1061 (1992).
- 5 T. H. Wood, R. W. Tkach, and A. R. Chraplyvy, *Appl. Phys. Lett.* **50**, 798 (1987).
- 6 F. Koyama and K. Iga, *IEEE Journal of Lightwave Tech.* **6**, 87, (1988).
- 7 M. S. Whalen, T.H. Wood, B. I. Miller, U. Koren, C. A. Burrus, and G. Raybon, *IEEE Photonics Tech. Lett.* **3**, 451, (1991).
- 8 H. A. Macleod, *Thin Film Optical Filters*, 2nd Ed. (Macmillan, New York, 1986).

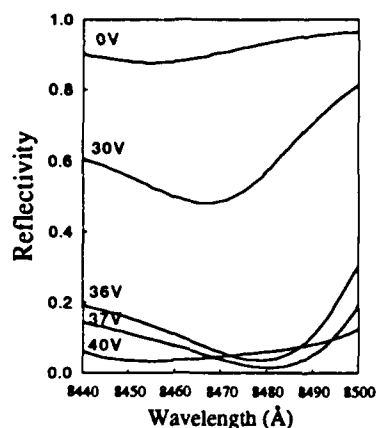


Fig. 1 Reflectivity spectrum of the asymmetric Fabry-Perot intensity modulator under study for various bias voltages.

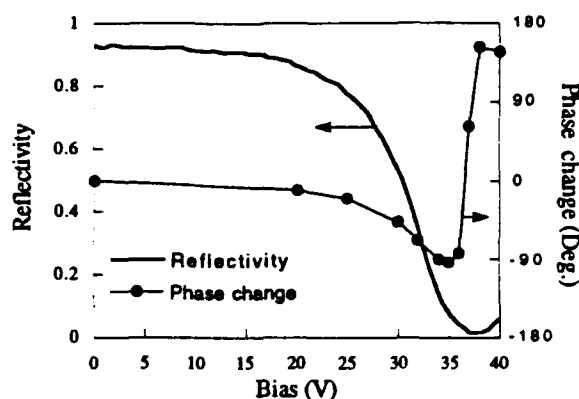


Fig. 2 Phase change relative to 0V and reflectivity versus bias voltage on the modulator. The dots are the measured data.

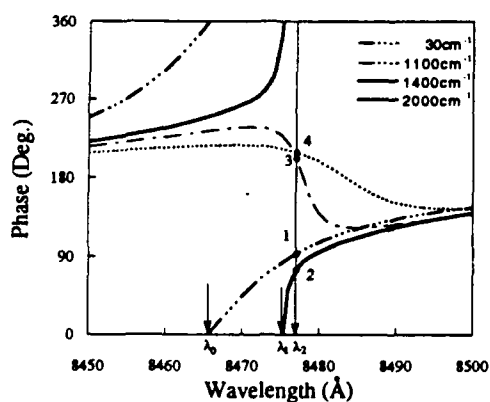


Fig. 3 Simulation of phase versus wavelength for four values of cavity absorption indicated in legend. λ_0 and λ_1 are the reflectivity minima when $\alpha=30\text{cm}^{-1}$ and $\alpha=1100\text{cm}^{-1}$, respectively. At λ_1 the contrast ratio is maximum. λ_2 is the wavelength which best fits our experiment as seen in Fig. 4c.

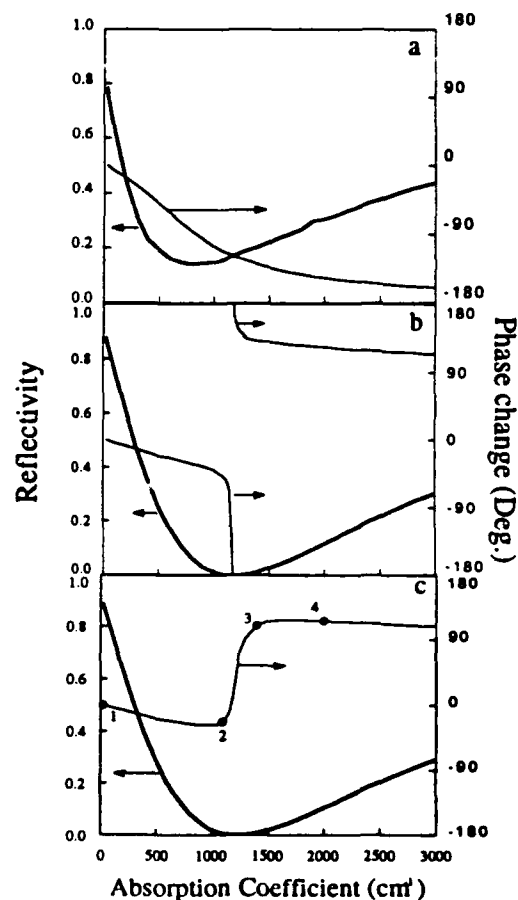


Fig. 4 Simulation results of the reflectivity and the phase change relative to $\alpha=30\text{cm}^{-1}$ versus the absorption coefficient in the cavity at (a) λ_0 , (b) λ_1 , and (c) λ_2 . The numbered dots in (c) correspond to the numbered dots in Fig. 3.

Ex-situ Cavity Phase Tuning of InGaAs/AlGaAs Multiple Quantum Well Based Inverted Asymmetric Fabry-Perot Reflection Modulators

Kezhong Hu, R. Cartland, Li Chen, K. Kaviani, P. Chen, and A. Madhukar

Photonics Materials and Devices Laboratory, the National Center for Integrated Photonic Technology, University of Southern California, Los Angeles, CA 90089-0241.

Phone: (213)740-4334; Fax: (213)740-7797.

A large array of light modulators is one of the key building blocks for optical computing and interconnection. Multiple quantum well (MQW) based asymmetric Fabry-Perot (ASFP) modulators¹⁻⁶ are a promising candidate for providing the basic surface normal switching function with high contrast and throughput, low switching energy and insertion loss. In addition, InGaAs/(Al)GaAs MQWs on GaAs substrates²⁻⁴ allow inverted cavity ASFP (I-ASFP) modulators^{3,4} in which the low reflectivity mirror is grown first followed by the active MQW region (including a GaAs phase matching layer) and ex-situ deposition of a metallic or dielectric high reflectivity mirror. The inverted geometry offers novel opportunities for face-to-face hybrid integration with Si based electronic circuits using flip-chip bonding techniques.⁷ Thus, smart pixels with versatile functionality can be achieved by incorporating the available highly developed Si technology.

In spite of the attractive features of the ASFP modulators, it is well known¹⁻⁶ that ASFPs demand tight control of the cavity phase (i.e. the effective optical path length (nd) of the MQW and the phase of the mirrors) to place the resonant mode, λ_{FP} , at an optimal distance ($\Delta\lambda$) from the exciton position, λ_{ex} . For a typical ASFP device operating at $\lambda_{op} \approx 1\mu m$, a 0.5% deviation in the (nd) of the MQW will cause λ_{FP} to shift by 50\AA , which is the typical band width of the ASFP devices. This means the absolute cavity thickness during growth needs to be controlled to within 0.5% error. To achieve a $\Delta\lambda$ of $\sim 200\text{\AA}$ (typically needed for optimal performance) within $\pm 50\text{\AA}$ also means that the realized exciton position also needs to be within 50\AA of the designed value. Such accuracy in "dead-reckoning" approaches are very difficult in the present day epitaxial growth systems. Moreover, theoretical uncertainty in the refractive index of the MQW imposes yet another challenge to the design of the cavity before the growth. In this paper, we demonstrate a novel technique of *ex-situ* cavity phase tuning for I-ASFP modulators through the incorporation and post-growth etching of a phase matching layer (which is part of the cavity) until the Fabry-Perot mode lies at a desired position prior to the deposition of the external high reflectivity mirror and accounting for the phase change introduced by the mirror. Using this technique, all the stringent requirements for the control of cavity phase turn out to be noncritical. As a result, all the device pixels over a wide area of the wafer, subject only to the relative

uniformity produced by the given growth system, become operative with uniform as-designed characteristics.

The I-ASFP structure used in this work was grown by molecular beam epitaxy (MBE) on a 2 inch semi-insulating GaAs substrate. The structure of the device consists of a 5.5 period Si-doped AlAs(830Å)/GaAs(700Å) Bragg mirror with reflectivity $\sim 60\%$ near 9800Å grown first, followed by an undoped GaAs (60Å) transition layer and a nominally intrinsic MQW structure having 50.5 periods of 81Å $\text{In}_{0.17}\text{Ga}_{0.83}\text{As}$ well and 88Å $\text{Al}_{0.26}\text{Ga}_{0.74}\text{As}$ barrier. Finally, a Be doped GaAs (1700Å) phase matching layer is grown on top of the MQW. During growth the substrate is rotated (at 24 rpm) to ensure a high uniformity in the central region of the wafer.

The as-grown sample was examined through a spatial scan of the reflectivity spectra with the light incident from the growth side of the wafer. In Fig. 1, panel (a), the "o" and the "+" symbols represent the λ_{FP} and λ_{ex} , respectively, as a function of distance from the wafer center. One can see that the central 1 cm diameter region of the wafer shows the highest uniformity in the λ_{FP} . Also, one can see that the exciton position shows uniformity over a much larger area.⁵ Finally, although the central area has excellent uniformity, it is useless for a modulator since the FP mode is almost 1000Å away from the exciton. However, this is so by design. Knowing the separation $\Delta\lambda$ in the as-grown structure, we can etch the phase-matching GaAs cap layer to achieve the $\Delta\lambda$ value needed prior to the deposition of the external mirror. In the present case we have employed gold mirrors that blue-shift the λ_{FP} by about 350Å. Consequently, the phase-matching GaAs needs to be etched just enough to blue shift the as-grown λ_{FP} by about 450Å, giving a final $\Delta\lambda$ after the gold mirror deposition of about 200Å, as desired.

The cavity phase tuning was done as follows. Before device processing, the top phase matching GaAs layer of the wafer was

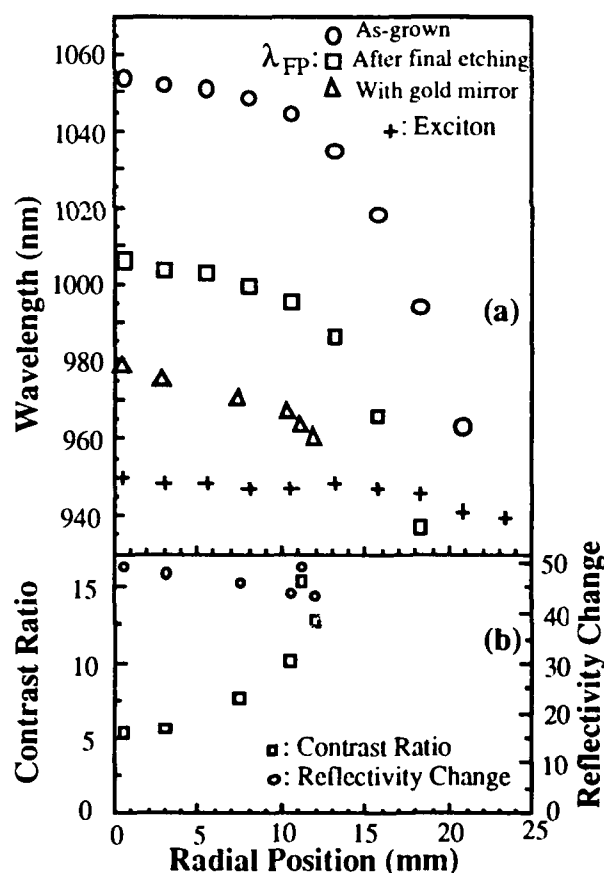


Fig. 1 (a) Uniformity data and ex-situ cavity phase tuning of inverted ASFP sample RG920728). (b) Contrast ratio and reflectivity change as a function of distance from the center of the wafer.

wet etched using a 3:1:50 volume ratio of $\text{H}_3\text{PO}_4:\text{H}_2\text{O}_2:\text{H}_2$ chemical etchant giving an etch rate of about 10-20Å/sec. The phase tuning was an iterative process. The wafer was etched, the reflectivity scan across the wafer conducted, and the blue-shifted FP mode mapped. The process was repeated until the desired λ_{FP} shift was achieved. The square symbols in Fig. 1, panel (a), show the blue-shifted FP mode after a total of 50 seconds of etching. A calculation⁴ showed that the desired 500Å blue shift of the FP mode corresponds to ~800Å of GaAs being etched, which is consistent with the etching rate of the etchant. Using this approach, the FP mode tuning with an accuracy of better than 20Å was achieved. Further dilution of the etchant would allow even better control. After tuning, the wafer was processed into 90µm x 120µm mesas with a pitch of 150µm and a thin SiN_x layer was deposited on the substrate side to serve as an anti-reflection coating. Finally, gold was deposited and lifted-off to serve as the high reflectivity (~94%) mirror and electrical contact pad on top of the mesa. The final FP mode (after the gold mirror deposition) is shown in Fig. 1(a) as triangles. Now the $\Delta\lambda$ is 200Å±100Å throughout the central 2.5 cm diameter of the wafer. Based on four I-ASFP samples that we have studied, we believe the FP mode shift due to the gold mirror can be predicted with an accuracy of 30Å.

The device characterization setup has been described in our earlier work.³ We have selected several pixels along one radial line to examine the modulation behavior. The measured contrast ratio and reflectivity change (at their individual operating wavelength) as a function of radial distance from the wafer center is plotted in panel (b) of Fig. 1. From the radial uniformity due to rotation, we conclude that the ~20,000 pixels in the central 4.5cm² area are all operative with contrast ratio greater than 5.4:1, reflectivity change greater than 43%, and insertion loss less than 3.3dB. In a smaller area (say 1cm²) about the central point of the wafer the $\Delta\lambda$ can be tuned to achieve contrast ratios ≥15:1 while maintaining a reflectivity change ~50% and insertion loss ≤3dB.

In Fig. 2 is shown the reflectivity spectra of pixel (73,44) for 0 and -13V biases. At 9634Å, a contrast of 18:1 and reflectivity change of 47% is obtained, with an insertion loss of 3.0 dB and 10dB contrast bandwidth as large as 50Å. This superior performance in an I-ASFP geometry is attributed to the superior absorption change available in the AlGaAs/InGaAs system.^{2,4}

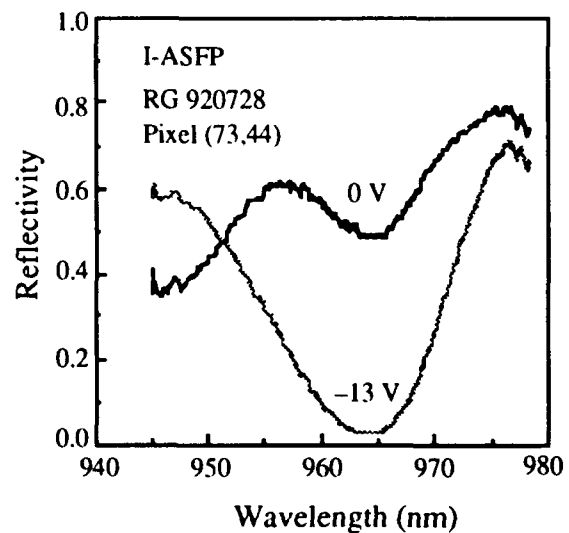


Fig. 2 Reflectivity spectra of pixel(73,44) at 0 and -13V biases for I-ASFP sample RG920728.

In most of the spatial light modulator (SLM) applications, one often requires the SLM array to be operated at the same wavelength and with the same switching voltage. Therefore, the device "transfer characteristics" is a more relevant criteria to examine the array uniformity. In Fig. 3 is plotted the reflectivity as a function of bias for four pixels out of a 12x1 linear pixel array. All the pixels are characterized at 9640Å. Good uniformity can be seen, the "on" state (zero bias) reflectivity being $52.0\% \pm 2.0\%$, and the "off" state (-14V bias) reflectivity being $3.0\% \pm 1.0\%$. The array shown here is located 12mm from the wafer center where the change in the FP mode as a function of location is still rather rapid due to the flux nonuniformity during growth (see Fig. 1a). A larger 2D uniform array can be obtained in the area closer to the center of the wafer where the flux uniformity is the best.

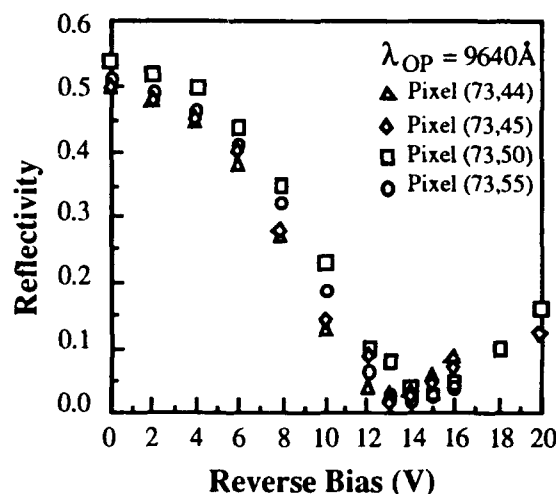


Fig.3 Transfer characteristics of four pixels in a linear 12X1 pixel array for I-ASFP sample RG920718.

In conclusion, we have demonstrated a novel and simple technique of *ex-situ* cavity phase tuning for inverted asymmetric Fabry-Perot modulators utilizing etching of a GaAs phase matching layer. Using this technique, all the stringent "dead-reckoning" requirements for the control of cavity the phase condition in the as-grown structure are released. Indeed, the phase-tuning can be made compatible with in-situ control by monitoring the λ_{FP} and λ_{ex} at various stages of the growth or alternatively via continuous monitoring during post growth etching, in-situ or ex-situ.

This work was supported by AFOSR-URI and by DRAPA.

1. R. H. Yan, R. J. Simes, L. A. Coldren, and A. C. Gossard, Appl. Phys. Lett. **56**, 1626 (1990).
2. B. Pezeshki, S. M. Lord, and J. S. Harris, Jr., Appl. Phys. Lett. **59**, 888 (1991).
3. K. Hu, L. Chen, A. Madhukar, P. Chen, C. Kyriakakis, Z. Karim, and A. R. Tanguay, Jr., Appl. Phys. Lett. **59**, 1664 (1991).
4. K. Hu, L. Chen, K. Kaviani, Q. Xie, K. C. Rajkumar, W. Chen, R. Cartland, P. Chen, and A. Madhukar, to appear in proceeding of the 21st international conference on the physics of semiconductors, Beijing, Aug. 1992.
5. K. K. Law, M. Whithead, J. L. Merz, and L. A. Coldren, Mater. Res. Soc. Symp. Proc. **240**, 609 (1992).
6. A. Jennings, P. Horan, B. Kelly, and J. Hegarty, IEEE Photon. Technol. Lett. **4**, 858 (1992).
7. C. Kyriakakis, Z. Karim, J. H. Rillum, J. J. Jung, A. R. Tanguay, Jr., and A. Madhukar, OSA Tech. Dig. Ser. **14**, 7 (1990).

Electroabsorptive Asymmetric Fabry-Perot Modulators with Symmetric Coupled Quantum Wells

D. S. Gerber, R. Droopad, and G. N. Maracas

Center for Solid State Engineering Research, Arizona State University,

Tempe, Arizona 85287-5706, USA

(602)-965-2551

The electroabsorptive asymmetric Fabry-Perot (ASFP) optical modulator has recently received attention for its use in electrically-addressable spatial light intensity modulator arrays due to its potentially high contrast ratio, large reflectance difference and low drive voltage¹. Most published results have been for modulators in which isolated rectangular quantum wells are used in the electrically-tunable absorbing region². In an effort to improve performance, the electroabsorptive properties of new bandgap engineered materials are being explored. It has been suggested that symmetric coupled quantum wells (SCQW) would allow reduced drive voltage due to an absorption edge which is more sensitive to an applied electric field than that of the commonly used rectangular quantum well (RQW)³. However, rapid shifting of the absorption edge with field does not ensure better performance if this is combined with a significant weakening of the transitions causing the absorption. We report here the first systematic comparison of ASFP modulators based on SCQWs and RQWs.

To determine if the SCQW offers an improvement over the RQW, the two types of wells must be designed to allow modulation at the same wavelength. We have chosen to compare a 100Å GaAs RQW with a 90Å GaAs/15Å Al_{0.3}Ga_{0.7}As/90Å GaAs SCQW, for which the longest wavelength peak in the absorption spectrum is at approximately 849 nm. First, the absorption coefficient, $\alpha(F, \lambda)$, of multiple quantum wells with 100Å Al_{0.3}Ga_{0.7}As barriers was measured as a function of wavelength and applied transverse electric field for both well types. Figures 1 and 2 show plots of this data for the RQW and SCQW, respectively. The calculations made for similar coupled well systems^{4,5} are used to identify and qualitatively explain the behavior of the excitonic transitions with electric field for the SCQW data. At zero field, the lowest energy transition in the SCQW is the $n=1$ electron to $n=1$ heavy hole transition, E_{1hh} , as in the RQW case. When an electric field is applied, it shifts rapidly to longer wavelengths, but also loses strength rapidly as the transition becomes spatially indirect due to separation of electron and hole into different wells in the coupled well system⁶. On the other hand, transitions which were spatially indirect without field become direct with field and can increase in strength. The longest wavelength transition of this type is the $n=1$ electron to $n=2$ heavy hole, E_{12h} , which first increases in strength and blue shifts before exhibiting a shift to longer wavelength with loss of strength⁵. The $n=2$ electron to $n=1$ heavy hole, E_{21h} , also has this behavior, and it is these two transitions which dominate the change in absorption at wavelengths below the absorption edge. The net effect in comparison with the RQW is that the absorption edge of the SCQW moves less rapidly to longer wavelengths with increasing electric field, but retains greater absorption strength due to the spatially direct nature of the transitions. This can be seen by comparing the absorption as a function of electric field at a series of wavelengths below the absorption edge for the RQW, figure 3, and the SCQW, figure 4. Modulation at wavelengths below the zero field absorption edge would require larger electric fields for the SCQW than the equivalent RQW, and this translates into greater drive voltage. This disadvantage could be offset, however, by the fact that the cavity of the SCQW modulator can be made shorter since there is a greater change in absorption coefficient. This reduces the drive voltage for a given electric field.

To assess the effect of this difference in electroabsorption behavior on performance, ASFP modulators employing the two well types were grown by molecular beam epitaxy. The devices were designed to be normally on for modulation at $\lambda=867$ nm. Distributed Bragg reflectors were grown for the top and bottom mirrors with design reflectances of 0.7 and 0.99, respectively. Of critical importance to performance is the wavelength separation, $\Delta\lambda$, between the zero field absorption edge and Fabry-Perot resonance². The wavelength position of the Fabry-Perot resonance varies radially on the wafer due to radial variations in layer thickness, while there is little variation in the position of the absorption edge, so devices with a range of $\Delta\lambda$ are present on each sample. For the comparison, we present the performance of RQW and SCQW devices both having $\Delta\lambda \approx 17$ -18 nm. The cavity lengths were chosen to be the minimum which still allows sufficient absorption to balance the mirrors and cause zero reflectance in the off state. Using the absorption data, the RQW modulator must have a cavity length of 7420 Å, while in the SCQW device it need be only 6134 Å due to the greater absorption change possible in the coupled well system. Figures 5 and 6 show plots of reflectance versus wavelength in the on and off states near the Fabry-Perot minimum for RQW and SCQW modulators, respectively. In both cases, there is a small mode pushing effect from electrorefraction⁷ which causes the Fabry-Perot minimum to move to a longer wavelength in the off state. The turn off voltage of the RQW device is $V_{\text{off}} = -14.9$ volts compared to $V_{\text{off}} = -15.6$ volts for the SCQW. The shorter cavity of the SCQW modulator was thus insufficient to offset the smaller shift of the absorption edge. We conclude from the absorption data that this is due to the dominance of the E_{12h} and E_{21h} transitions which have large absorption strength, but small shift, instead of the rapidly shifting E_{11h} transition which becomes so weak as to give a negligible contribution to any absorption change. Figures 7 and 8 show the reflectance difference, $\Delta R = R_{\text{on}} - R_{\text{off}}$, and contrast ratio, $A_R = R_{\text{on}}/R_{\text{off}}$, as a function of wavelength for the RQW and SCQW devices, respectively. It can be seen that both devices have a very high maximum $A_R \approx 600$ and large peak $\Delta R \approx 0.72 - 0.74$, indicating the high quality of the epitaxial growth. The high on state reflectance is a result of low residual absorption in the cavity at zero applied voltage. The very low off state reflectance of approximately 0.001 in both devices indicates that sufficient absorption is available in the cavity to balance the mirrors and that there is very little light scattering in the mirrors due to layer roughness. The insertion loss at peak ΔR of 1 dB and 1.25 dB for the RQW and SCQW devices, respectively, is quite low. Thus, the two devices have approximately the same performance aside from the drive voltage.

The SCQW does not appear to offer any advantage over the RQW for use in electroabsorptive modulators. The lowest energy transition, which shifts rapidly, becomes too weak in an applied field to play a role in modulation of the absorption coefficient below the zero field absorption edge. In general, the shift in wavelength, change in absorption strength and broadening in linewidth of several transitions all contribute to the change in absorption coefficient with field at a given wavelength. This work emphasizes the importance of (1) making measurements of the absorption coefficient as a function of wavelength and electric field and (2) comparing quantum wells with the same zero field wavelength in the search for materials with improved electroabsorptive properties.

References:

1. R. H. Yan, R. J. Simes, and L. A. Coldren, IEEE J. Quant. Electron., **27**, 1922 (1991).
2. G. D. Boyd and G. Livescu, Opt. and Quant. Electron., **24**, S147 (1992).
3. N. Debbar, S. Hong, J. Singh, and P. Bhattacharya, J. Appl. Phys., **65**, 383 (1989).
4. J. Lee, M. O. Vassel, E. S. Koteles, and B. Elman, Phys. Rev. B, **39**, 10133 (1989).
5. S. R. Andrews, C. M. Murray, R. A. Davies, and T. M. Kerr, Phys. Rev B, **37** 8198, (1988).
6. Y. J. Chen, E. S. Koteles, B. S. Elman, and C. A. Armiento, Phys. Rev. B, **36** 4562 (1987).
7. G. Livescu, G. D. Boyd, R. A. Morgan, L. M. F. Chirovsky, A. M. Fox, R. E. Leibenguth, M. T. Asom, and M. W. Focht, Appl. Phys. Lett., **60**, 1418 (1992).

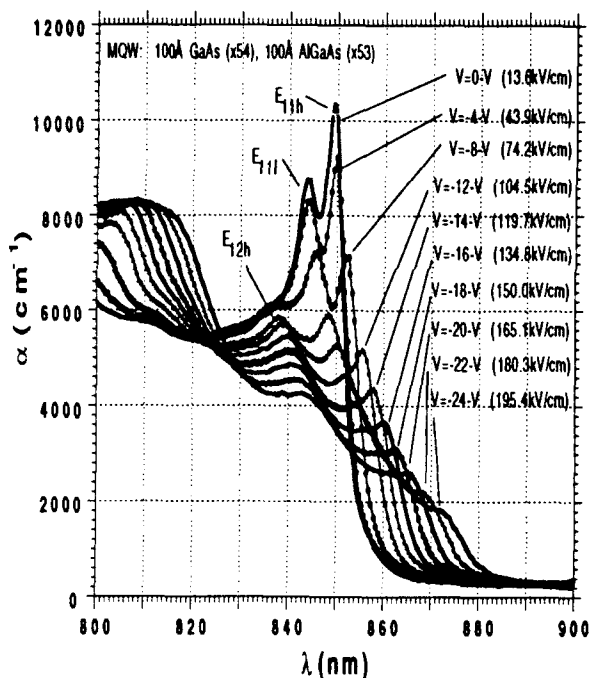


Figure 1: Absorption versus wavelength in the single rectangular quantum well.

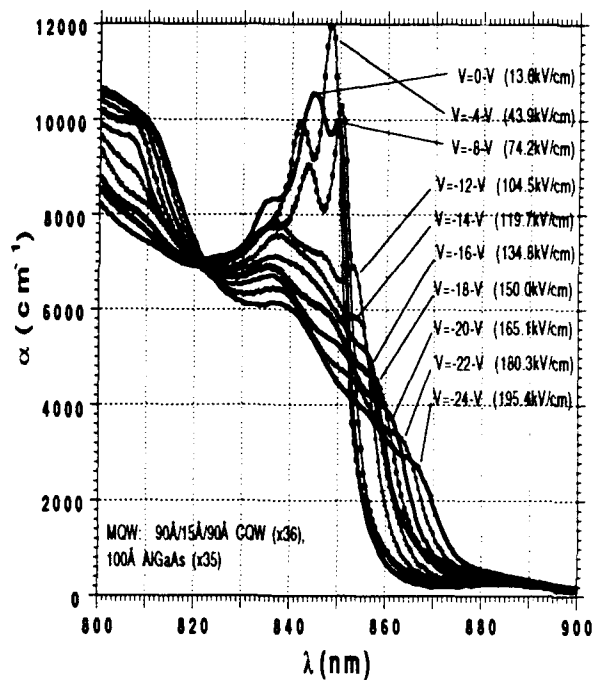


Figure 2: Absorption versus wavelength in the symmetric coupled quantum well.

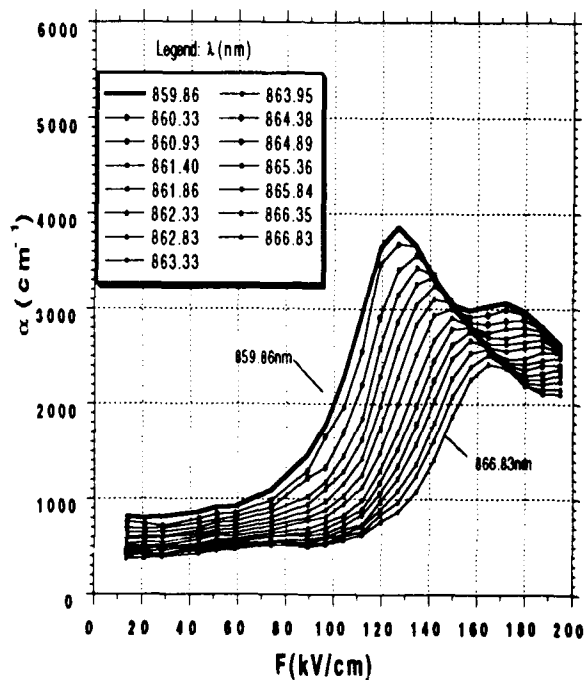


Figure 3: Absorption versus electric field in the single rectangular quantum well.

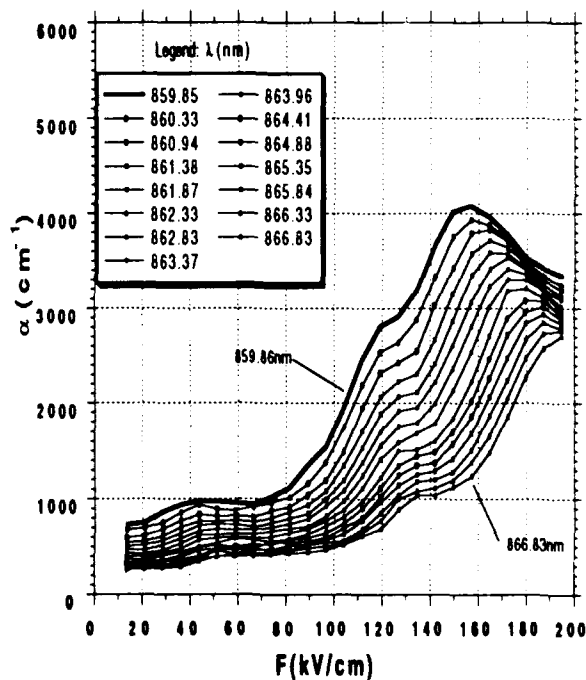


Figure 4: Absorption versus electric field in the symmetric coupled quantum well.

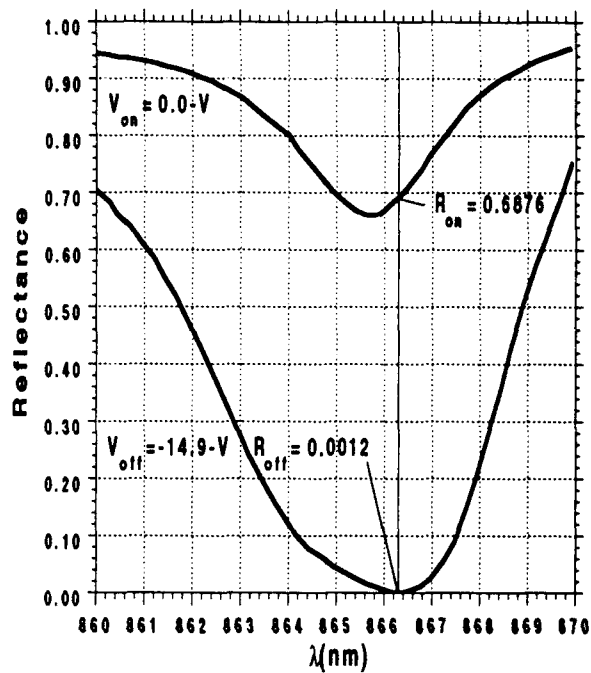


Figure 5: Reflectance in on and off states in the single rectangular quantum well.

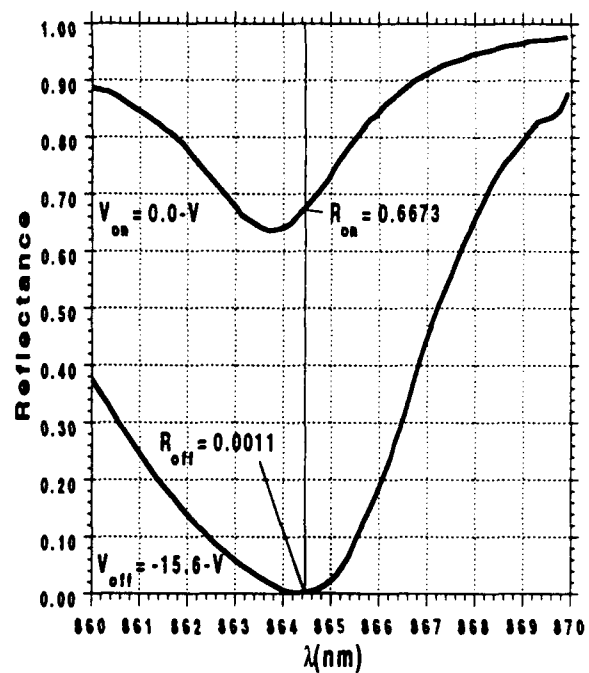


Figure 6: Reflectance in on and off states in the symmetric coupled quantum well.

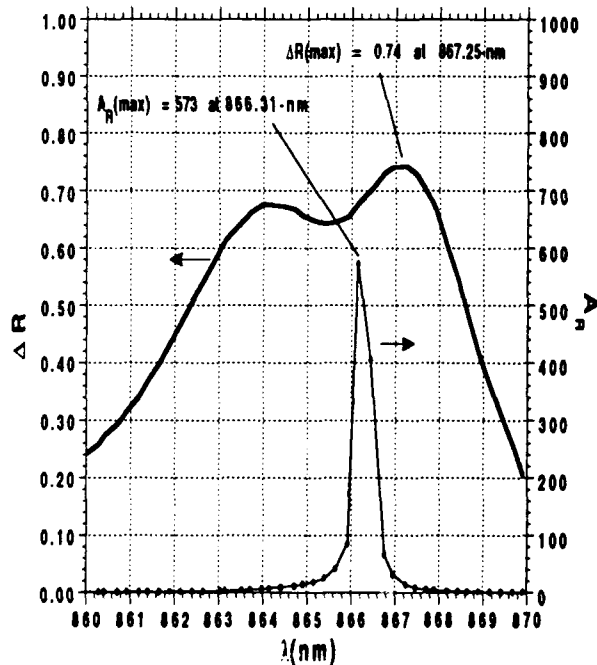


Figure 7: Reflectance change and contrast ratio in the single rectangular quantum well.

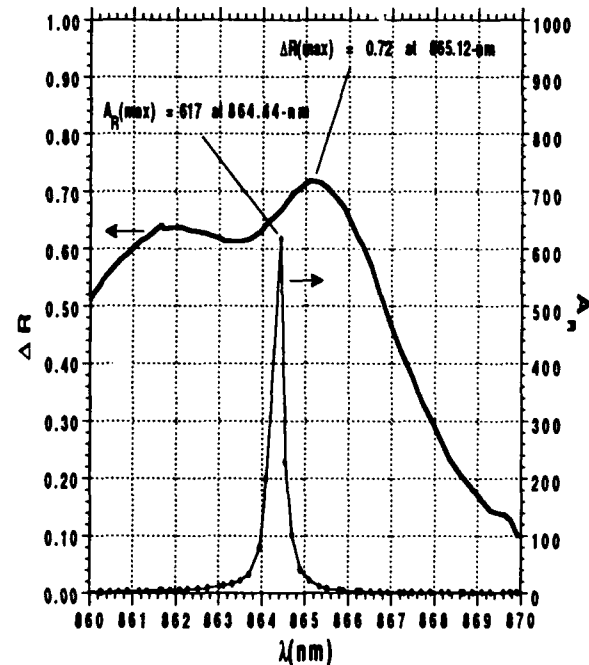


Figure 8: Reflectance change and contrast ratio in the symmetric coupled quantum well.

A Design Model for Reflection Mode MQW Modulators Based on Minimization of Power Penalties

C. Fan, M. W. Hansen, D. W. Shih, and S. C. Esener

University of California, San Diego
Department of Electrical and Computer Engineering, 0407
La Jolla, CA 92093
Tel. (619) 534-6226

The quantum-confined Stark effect and the Wannier-Stark effect in multiple-quantum-well (MQW) materials have been used in Fabry-Perot étalons to modulate the total reflected power. High contrast ratio modulators which use asymmetric Fabry-Perot (ASFP) cavities have been reported¹⁻³ with AlGaAs/GaAs and GaAs/InGaAs MQW materials. In addition to contrast ratio, however, power budgets should be examined in many opto-electronic interconnection systems. In this paper, we present a model to evaluate modulator performance through the contrast ratio and the total power penalty.

Contrast ratio and insertion loss are often used as figures of merit for electro-optic modulators. They are defined as the power ratio of output-high versus output-low, and the ratio of total input power versus the maximum power output, respectively. Ideally, one would like to have high contrast ratio as well as low insertion loss in a modulator. In an ASFP modulator design, however, there is a trade-off between the two; both contrast ratio and insertion loss increase with the increase of front mirror reflectivity (Fig. 1). Design parameters of an ASFP modulator are cavity length (L_{cav}), front and back mirror reflectivity ($R_{f,b}$), and material properties (residual absorption (α_0) and electro-absorption coefficient ($\Delta\alpha$)). A high contrast ratio can be achieved by

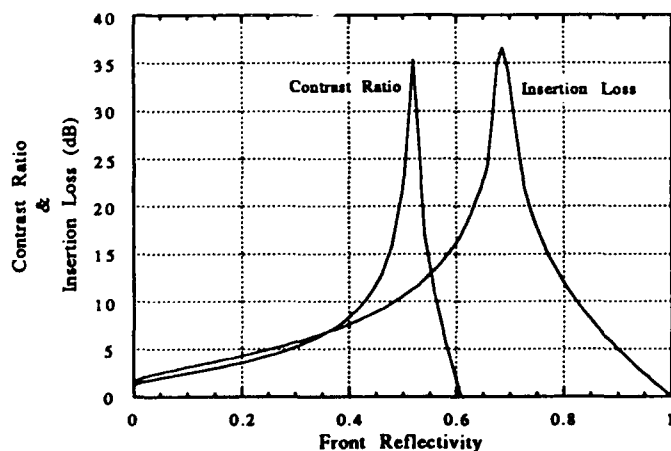


Fig. 1 Contrast ratio and insertion loss vs R_f

having a very low output-low condition. To do this with an ASFP structure, the optical beams reflected from the front and the back mirrors interfere destructively. Therefore, even when residual absorption is neglected, the maximum reflected power at the output-high state is lower than the total input power with the presence of a front mirror. This results in the insertion loss increasing with the front mirror reflectivity.

In order to obtain an optimum design, one could examine the situation from the perspective of power budget, since both contrast ratio and insertion loss can be related to a system through

power penalties. The power penalty is defined as additional signal power required at the input to guarantee the same signal performance at the output when a power loss mechanism is introduced or the noise level has increased. For example, the insertion loss is a power loss by definition and it can be directly translated to signal power penalty. The effect of contrast ratio or its inverse, extinction ratio, on the power budget is observed through the noise level in the receiver. Due to a non-zero extinction ratio in modulators, the noise floor in the receiver is higher. Extra signal power must be provided to guarantee the same signal performance with reference to the noise level at the receiver output. This is the power penalty associated with non-zero extinction ratio (detailed analyses can be found in Ref. 4). Summing up the two extra power terms, one obtains the total power penalty associated with a modulator⁵.

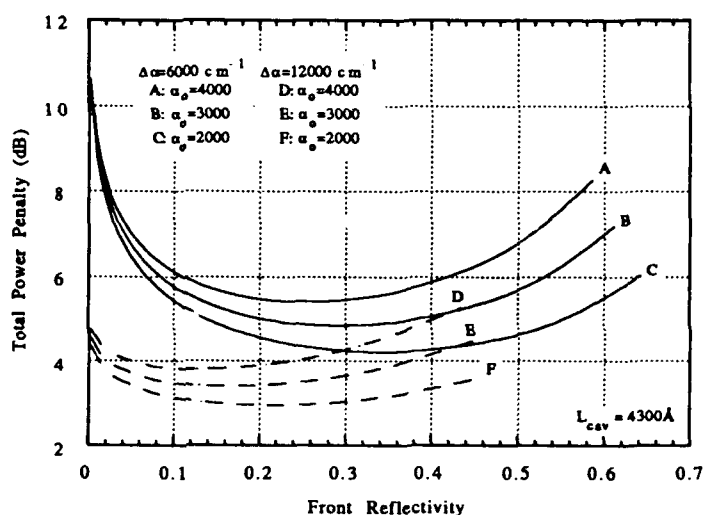


Fig. 2 Total power penalty vs R_f

Since the power penalty increases with the increase of insertion loss and extinction ratio, it is expected that there is an optimum modulator design, i.e. a set of parameters, mainly R_f , L_{cav} , α_0 and $\Delta\alpha$, for which the power penalty is minimized. Following the analytic expressions given in Ref. 4 & 6, the relationship of total power penalty versus front mirror reflectivity takes the form as shown in Fig. 2 for various modulator parameters⁷. There is indeed a region on each curve where the power penalty reaches a minimum. This minimum value depends greatly on the material properties.

For a given material, on the other hand, the minimum power penalty varies with the cavity length and front mirror reflectivity. Fig. 3 illustrates that the minimum point decreases with the increase of cavity length and shifts toward the lower front-mirror reflectivity. The power penalty at high front mirror reflectivity is mostly from the loss associated with the front mirror. With long cavity and low front mirror reflectivity, the minimum point reaches a value determined by the residual absorption.

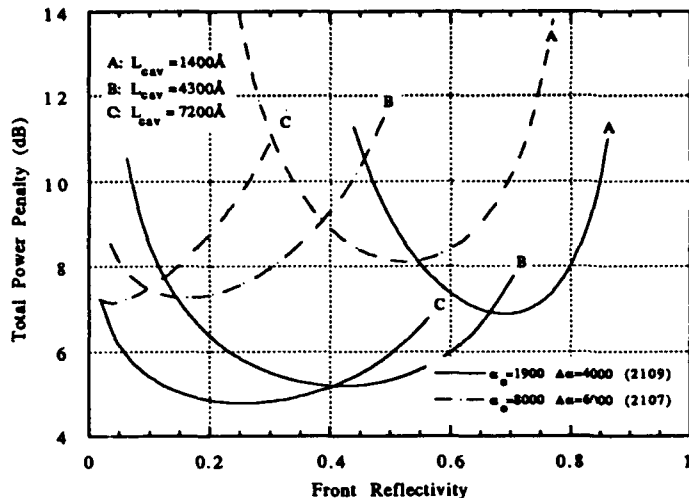


Fig. 3 Power penalty vs R_f with cavity length variation

application has to have an electro-absorption coefficient of at least 8000/cm and a residual absorption of at most 2000/cm, if the cavity length is given.

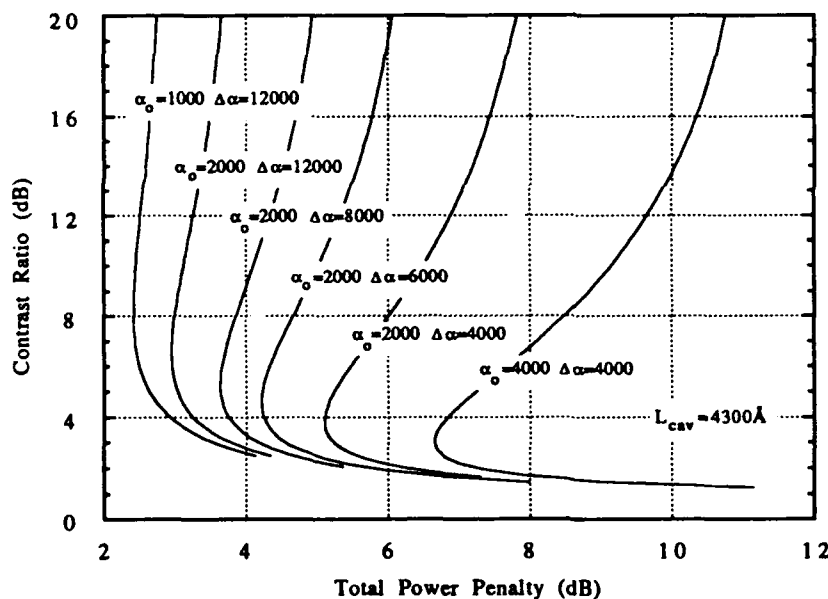


Fig. 4 Contrast ratio vs power penalty with material parameter variation

optimum design using a graph such as Fig. 5,⁸ where the predicted modulator performances are plotted with the cavity length as a variable. One can see that there is an optimum cavity length, below which the modulator performance is significantly worse, and above which the performance is not significantly better. For an example, see the curves lettered B in Fig. 5. In any case, the design parameters should always be chosen such that the predicted performance falls on the upper part of the chart (Fig. 4 or 5), using the contrast ratio value where power penalty is a minimum as the divider.

Fig. 4 predicts modulator performances from material properties. Performances are measured in terms of both contrast ratio and total power penalty. It provides a tool to determine whether a material is suitable for a specific application. For example, if a system specifies a 4 dB power margin and 8 dB contrast ratio for a modulator, the material used for this

One can generate a set of similar plots with different cavity lengths to search for an optimum set of design parameters. More often, perhaps, the material properties are given. One can then look for the

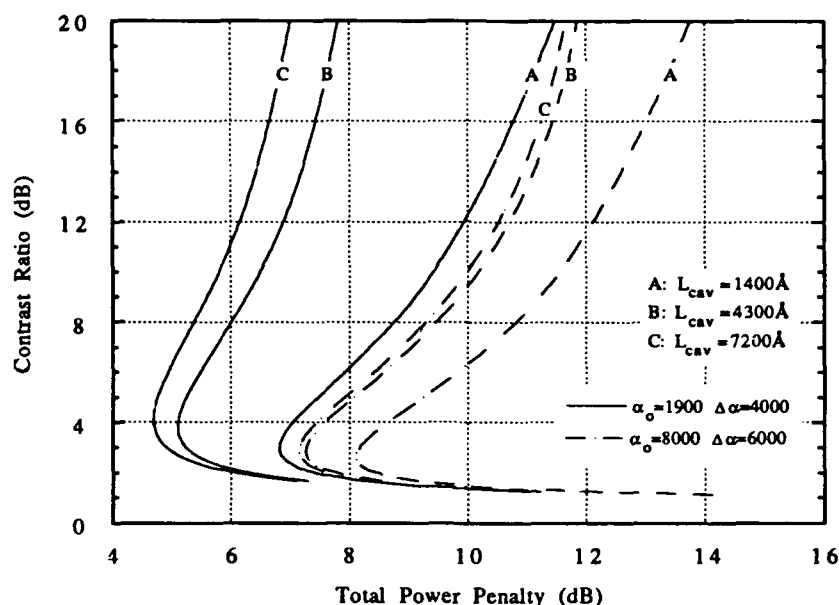


Fig. 5 InAlGaAs/InGaAs ASFP modulator performance

In summary, a design model has been developed based on the minimization of total power penalty. It provides a means to evaluate modulator material as well as structure design. It is shown that there is always an optimum modulator design for any given material if the power budget is the primary concern. For applications, such as multi-link interconnection systems, where the contrast ratio is deemed important, the model provides a tool to budget the power.

References

1. R. H. Yan, R. J. Simes, and L. A. Coldren, *IEEE Photon. Technol. Lett.*, **1**, 273(1989).
2. M. Whitehead, A. Rivers, G. Parry, J. S. Roberts, and C. Button, *Electron. Lett.*, **25**, 984(1989).
3. B. Pezeshki, D. Thomas, and J. S. Harris, Jr., *Appl. Phys. Lett.*, **57**, 1491(1990).
4. R. J. Hoss, "Fiber Optic Communication - Design Handbook", Chapt. 6, Prentice-Hall, New Jersey, 1990.
5. In this work, the signal power fluctuation introduced in modulators due to a non-zero extinction ratio is not included in calculating the total power penalty.
6. R. H. Yan, R. J. Simes, and L. A. Coldren, *IEEE J. Quantum Electron.*, **27**, 1922(1991).
7. PIN photodetectors are used in the receiver. APDs result in high power penalties.
8. InAlGaAs/InGaAs MQW materials, shown in Fig. 3,5, were grown on GaAs substrates in our laboratory with a compositionally-step-graded buffer. The material properties were reported in MRS spring meeting, San Francisco, 1992. The modulator results were presented at OSA annual meeting, Albuquerque, New Mexico, Sept. 1992.

Active Anti-Reflection Coating Electro-Optic Modulator

Amjad Obeidat, Jacob Khurgin, Shaozhong Li
Department of Electrical and Computer Engineering
The Johns Hopkins University
Baltimore, MD 21218 U.S.A.

Electro-optical switches and modulators based on multiple quantum wells (MQW) have been receiving increasing attention due to their potential applications in optical logic, interconnects, and all optical signal processing [1], [2]. A prime example of such devices is the Asymmetric Fabry-Perot (AFP) modulator [3].

A typical AFP modulator consists of a single dielectric mirror and a half wavelength active layer containing multiple quantum wells (MQW) (Fig. 1 (a)). An AFP can be designed so that its overall reflectivity is nearly zero [4]. The absorption of the active layer can be changed by applying an external bias. This unbalances the anti-reflection condition and causes the reflectivity to rise, yielding a large modulation contrast. One possible drawback of the AFP modulator is the fact that only the single half-wavelength layer is active while the remaining layers are passive and serve only as a mirror.

We propose a scheme for an Active Anti-Reflection Coating (A-ARC) in which each period of the anti-reflection coating incorporates MQW's (Fig. 1 (b)). This structure is quite similar to the AFP with the exception that the single active layer has been eliminated and all the high index layers have been made active. This results in a much larger absorption length than that of an AFP. Figure 2 shows the absorption curves for both an AFP and an A-ARC. Both devices contain 30 double layers. A double layer is a high index quarter-wavelength layer on top of a low index quarter-wavelength layer. The A-ARC has an additional low index layer on top while the AFP has on top an active layer of $5\lambda/2$ thickness. The increase in the AFP active layer thickness was needed to give both devices comparable absorption lengths. In both devices the quantum well material is GaAs with a thickness of 95 Å, and the barrier material is $\text{Al}_{0.29}\text{Ga}_{0.71}\text{As}$ with a thickness of 80 Å. The operating wavelength

is 850 nm which corresponds to the exciton peak. In the A-ARC, the low index material is $\text{Al}_{0.38}\text{Ga}_{0.62}\text{As}$ with a thickness of 634.77 Å per layer, and the high index layer thickness is 605 Å which corresponds to 3 wells and 4 barrier segments.

It is clear in figure 2 that the A-ARC matches the performance of the AFP. Both devices have a wide and flat zero reflectivity region centered roughly around an absorption of $\alpha = 0.9 \mu\text{m}^{-1}$. We observe that to obtain a useful ON-OFF reflectivity contrast of about 20%, a change in absorption of about $\Delta\alpha = 0.6 \mu\text{m}^{-1}$ is required. One of the A-ARC advantages is its smaller device thickness while maintaining the same performance as the AFP. For the case above, the thicknesses are $t_{\text{AFP}} = 4.222 \mu\text{m}$ while $t_{\text{A-ARC}} = 3.783 \mu\text{m}$.

The major A-ARC advantage is its inherent tolerance to manufacturing variations since the active medium is not concentrated in one layer. Variations in the active layer thickness can degrade the device performance significantly. In the A-ARC, if one of the active layers overgrown (undergrown) then the next active layer may be undergrown (overgrown) by the same amount preserving the same overall device thickness and absorption length. This is not possible with the AFP since there is only one active layer. Figure 3 shows various reflectivity vs. absorption curves for different A-ARC's. All devices have 30 double layers. Different layer thickness variations were introduced to different devices. The variations were compensated for by the next layer and so on. We can see that there is negligible performance degradation compared to the unaltered device.

In conclusion, we have shown a new modulator configuration with improved performance characteristics. The A-ARC has a greater efficiency in the utilization of space and material over an AFP. It also has a built-in mechanism for the correction of growth error. This makes an ideal candidate for building modulator arrays where such performance uniformity is imperative.

References

1. H. M. Gibbs, *Optical Bistability: Controlling light with light*. New York: Academic, 1985.
2. N. Peyghambarian and H. M. Gibbs, *J. Opt. Soc. Amer. B.* **2** (1985) 1215.

3. H. M. Gibbs, S. L. McCall, T. N. Venkatesan, A. C. Gossard, A. Passner, and W. Wiegmann, *Appl. Phys. Lett.* **35** (1979) 451.
4. K. W. Goossen, J. E. Cunningham, and W. Y. Jan, *Appl. Phys. Lett.* **60** (1992) 727.
5. H. G. Winful, J. H. Marburger, and E. Garmire, *Appl. Phys. Lett.* **35** (1979) 379.

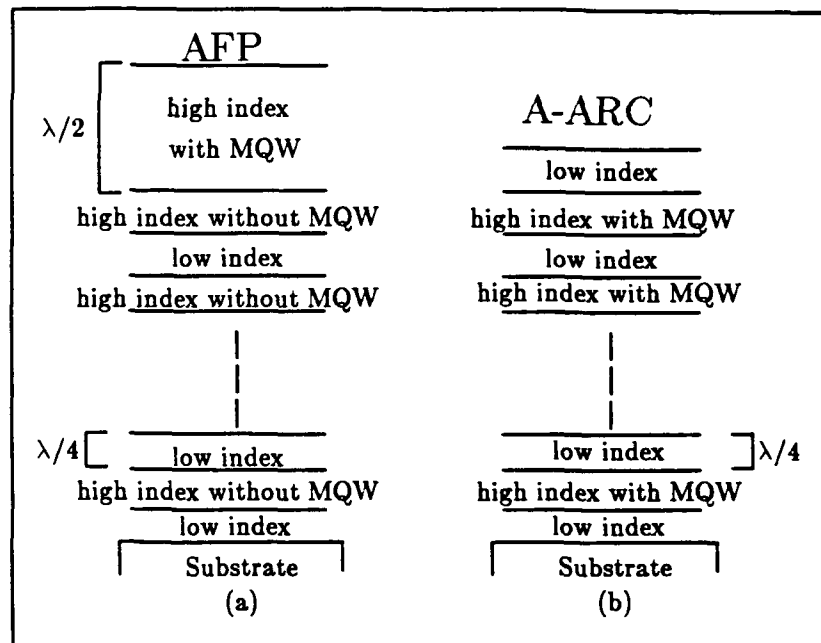


Fig. 1. The configuration of (a) an AFP and (b) an A-ARC.

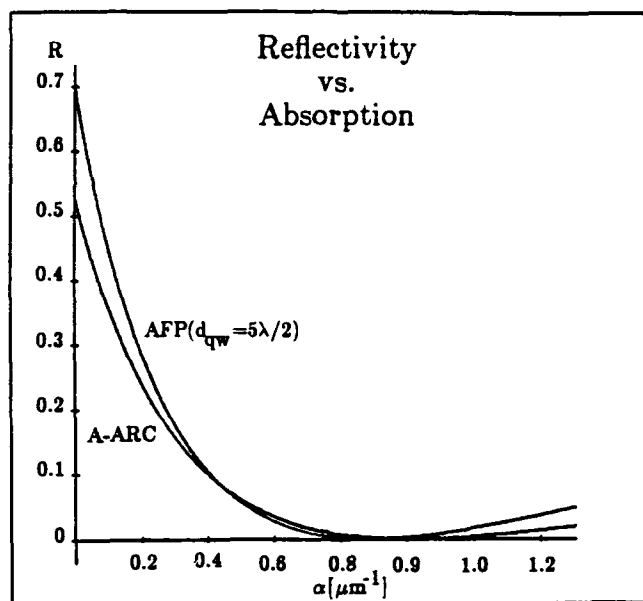


Fig. 2. Reflectivity vs. absorption curves for an AFP and an A-ARC.

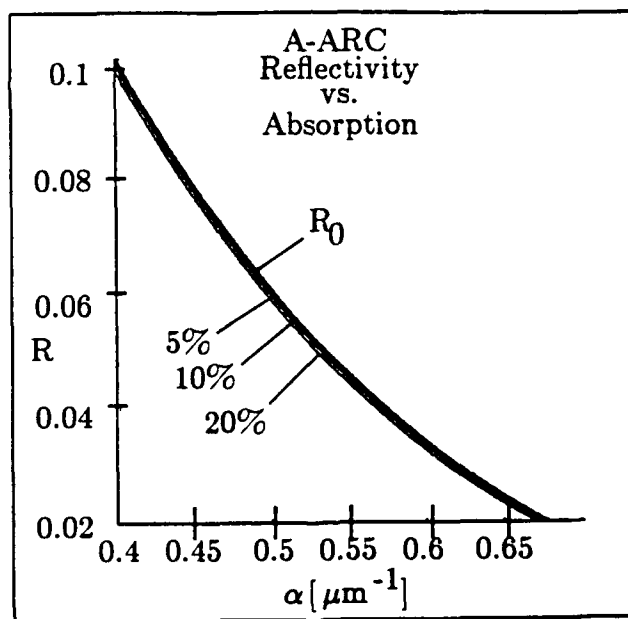


Fig. 3. Reflectivity vs. absorption curves for 4 different A-ARC modulators. The percentage associated with each curve represents the amount of overgrowth in a high index layer. The next high index layer was undergrown by the same amount until all of the layer thicknesses have been changed in that manner. R_0 is the curve for the unaltered A-ARC. Note that all four devices have the same overall thickness.

Wednesday, March 17, 1993

Optical Interconnects and other SLM Applications

SWC 1:30pm-3:10pm
Grand Ballroom West

Uzi Efron, *Presider*
Hughes Research Laboratory

Potential Field Computation for Robotic Path Planning Using a Microchannel SLM

Max B. Reid

NASA Ames Research Center
Mail Stop 269-3 / Moffett Field, CA 94035 / (415)604-4378

A microchannel SLM is employed to demonstrate the optical calculation of potential field maps for mobile robot navigation. In one MSLM mode, written patterns expand spatially, and this characteristic is used to create an extended two dimensional function representing the influence of the goal in a robot's workspace. The optical calculation time scales favorably in comparison to digital electronic computation.

Introduction

The MSLM consists essentially of a photocathode, a microchannel plate (MCP), a mesh electrode, and an electrooptic crystal, as shown in Figure 1.[1-3] An input light intensity distribution is converted by the photocathode to a spatial electronic current distribution, which is amplified on the order of 1000 times by the MCP. This electron current is incident on a thin dielectric mirror which coats the backsurface of the crystal. The deposited surface charge density, σ_s , creates an electric field across the electrooptic crystal, which in turn rotates the polarization of a coherent readout light beam.

A second method of writing patterns on the MSLM involves first depositing a uniform charge distribution on the surface of the crystal and then removing, or depleting, charge from areas to be written. For a given input light distribution, patterns written in the two modes are very nearly reverse contrast images. However, if the electron deposition/depletion process is continued beyond $\approx 90\%$ modulation, the deposited pattern will grow to fill the entire active area of the electrooptic crystal, while the depleted pattern remains relatively confined. In this work, we demonstrate that the spatial spread of charge across the surface of the electrooptic crystal may have practical application, allowing analog calculation of complicated two dimensional spatial functions which are very time consuming to compute using standard digital techniques. The particular application considered here is the calculation of two dimensional potential field maps suitable for use in autonomous robotic path planning.

Spread of MSLM Patterns Due to Secondary Electron Redistribution

Electrons leaving the MCP output electrode are accelerated by the grid electrode to potential V_a , which is on the order of 2 kV, and the energy of primary electrons striking the dielectric mirror is well approximated by

$$E_p = e(V_a + V_g), \quad (1)$$

where e is the electron charge and the gap voltage is given by

$$V_g = V_b - V_a - V_x, \quad (2)$$

V_b being the voltage applied to the crystal and V_x the voltage drop across the crystal caused by accumulated charge.

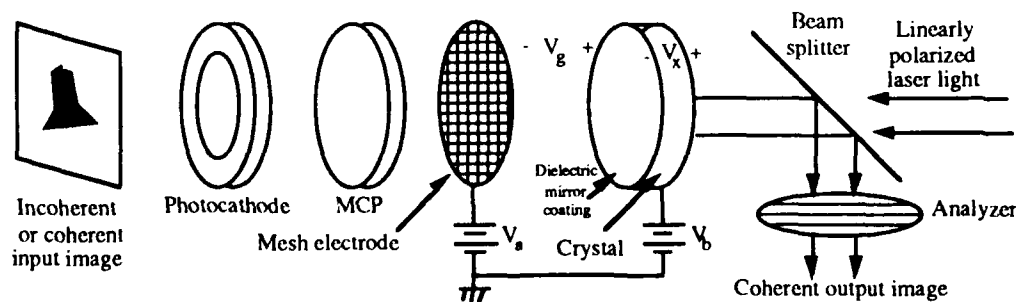


Figure 1: Basic operation of the microchannel spatial light modulator.

If only primary electrons emitted from the MCP were involved in the MSLM writing process, charge would accumulate on the mirror until $E_p = 0$ in Eq. (1), requiring $V_x = V_b$. However, on average, each primary electron creates a number, δ_s , of secondary electrons which are emitted from the dielectric mirror surface.[4] With $\delta_s > 1$, the net current reaching the mirror would be negative from the relation

$$I_{net} = I_p(1 - \delta_s), \quad (3)$$

where I_p is the primary electron current. However, δ_s is reduced to a lower effective value δ_e by the presence of a positive gap voltage, V_g . The great majority of secondary electrons are attracted back to the mirror, as only those secondaries with $V_s > V_g$ can cross the gap to be collected on the grid electrode.

A stable equilibrium occurs when $\delta_e = 1$ and $I_{net} = 0$. The basic MSLM equilibrium model is summarized as follows: for each primary electron striking the dielectric mirror, approximately two secondary electrons are emitted. On average, exactly one of these secondaries has enough energy to reach the grid. Other secondaries are pulled back to the mirror surface. The entire surface is assumed to be at a uniform potential and no transverse effects are felt.

In practice, electrons traversing the gap are affected by the distribution of charge already deposited on the dielectric mirror surface. Calculations show that the transverse displacement of primary electrons caused by non-uniform transverse fields on the crystal surface is negligible because of the primary's high initial velocity. A much more likely cause of growth in the deposition region is the redistribution of secondary electrons, which results when a secondary emitted from one spot on a target is attracted by transverse fields to another location on the target instead of either being collected on the grid or returned to the location of its emission. For typical patterns, the energy required for a secondary to reach the grid before it is accelerated back to the undeposited region ranges from $E_{s,min} \approx 10$ eV to $E_{s,min} \approx 100$ eV, with the higher energies required for secondaries emitted near the edge of the pattern. These values are considerably greater than the average secondary electron energy which is only $E_s \approx 2 - 3$ eV. The fraction of secondary electrons collected at the grid is reduced by redistribution to $\delta_c \approx 0$. This conclusion results in the prediction that the total charge accumulated on the surface of the mirror will grow approximately linearly with time, directly proportional to the primary current.

Potential Fields for Path Planning

We consider one class of path planning problem, that of determining a series of motions for a robot to execute to move from an initial location to a designated goal location in a bounded two dimensional workspace.[5] A robot's workspace may be partially filled with obstacles, regions which it cannot traverse due to physical or other constraints. In potential field path planning, the robot is assumed to be a positively charged object, the goal is a negatively charged region which exerts an attractive force, and obstacles are positively charged regions which exert repulsive forces on the robot. Each location in the workspace is considered to have an associated potential energy, and the robot follows the gradient of the potential.

Figure 2 shows an algorithm for computing a local-minima-free potential field map. The obstacles are considered maximum potential regions which do not exert forces beyond their boundaries. The goal location is the source of an expanding low potential region which starts in a small area and grows uniformly until it reaches an obstacle. Upon reaching an obstacle, the goal's "field" spreads around the obstacle. The field stops expanding when it has filled the entire workspace. The completed pattern in Fig. 2d contains no local minima, and a robot located behind the obstacle will follow a path such as that shown in the figure.

Optical Calculation of Potential Fields

A high speed analog optical calculation of field maps suitable for robotic path planning can be performed using a microchannel spatial light modulator. Let the workspace be represented by the output pattern of the MSLM. The workspace is initially uniformly written in depletion mode and then the goal is written in deposition mode. At this point, an image of the MSLM output shows the goal at a value of zero, while the remaining area of the workspace is at the maximum 8-bit gray-scale value of 255. A series of alternating deposition/depletion writing cycles follows. The goal region is written for a time t_e , during which time the deposited region expands.

When the expanding deposited area reaches the location of an obstacle, some of the area written falls within the borders of the obstacle. This charge is removed by writing in depletion mode for a time t_p . All obstacles are written back to full intensity before an image is taken of the output pattern. The procedure terminates after the area written

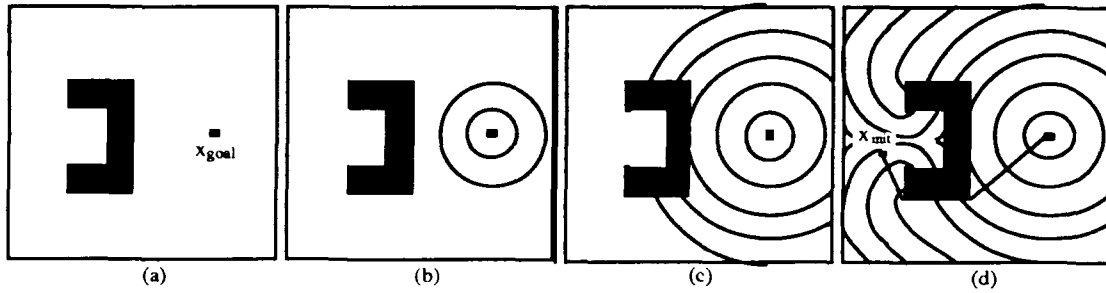


Figure 2: Potential field map calculation algorithm employing expanding goal region. a) Initial goal and obstacle locations. b) First two equipotential lines show expanding goal region. c) Expanding goal region is forced to proceed around obstacles. d) Final equipotential map. Highest potentials are directly behind the obstacle.

to full modulation via electron deposition spreads to cover the entire active area of the electrooptic crystal, excluding the regions occupied by obstacles. The potential field map is formed by averaging the images taken at the end of each write cycle, and contains no local minima. Any electrons which spread into the bounds of obstacles are removed, while electrons which spread around the edges of the obstacles are allowed to accumulate.

Using feedback, the area illuminated during deposition mode writing during each cycle is the area which was fully modulated via deposition after the previous cycle. This leads to exponential growth in the area written via deposition (the goal region), and therefore to a logarithmic relation for the total optical writing time

$$t_{\text{calc}} \propto \frac{\sigma_{\text{sat}}}{J_p} \ln(N), \quad (4)$$

where J_p is the primary electron current density, σ_{sat} is the charge density required for full amplitude modulation, and N is the total number of resolution cells in the 2D workspace, given by electrooptic crystal active area divided by the area of the smallest resolvable spot on the MSLM. Using current commercial MSLMs with MCP strip currents limited to about $10 \mu\text{A}$, t_{calc} is on the order of 10 seconds. Experimental versions of MSLM have been demonstrated with MCP strip currents as high as $300 \mu\text{A}$. Use of such MCPs would decrease t_{calc} to a few tenths of a second, allowing potential field map updates at a few hertz.

We see from Eq. (4) that the optical writing time scales as $\ln(N)$. The full potential field calculation algorithm includes electronically implemented functions of frame-grabbing, image thresholding and inversion, and display of a feedback pattern on an electronically addressed SLM. Each of these operations scales linearly with the size of images, i.e., as $O(N)$. In addition, each of these operations is repeated M times during the calculation of a potential field map, where M scales as $O(\ln N)$. The electronic operations therefore determine the ultimate limit on system computation speed. In the limit of large N , the order of the computation time for the hybrid optical/electronic system is $O(N \ln(N))$. Comparable potential field map computations performed using conventional digital electronics scale at best as $O(N^{3/2})$. The advantage of optical calculations therefore lies in the domain of large, high resolution potential field maps.

Experimental Results

A common obstacle used in robotics research [5] was used to demonstrate the procedure in the single obstacle case. This is a "C" or "U" shaped object, as shown in Figure 3a. Five intermediate output images are seen in Figure 3, starting just after the goal was written in Figure 3b. Output images after 20, 40, 60, and 80 iterations are shown in Figures 3c-f. In Figure 4c, the goal region has just expanded to the edge of the obstacle. The deposited area spreads around the obstacle in Figures 3d and 3e, and has almost filled the entire workspace in Figure 3f.

After the output image stopped changing, the sequence of images stored during the writing process was averaged to produce the potential field map. The potential field map is a gray-scale image with values ranging from 0 at the goal to 255 within the bounds of the obstacle. Figure 4a shows a contour plot where the first equipotential line surrounding the goal represents a gray-scale value of 15, and each successive line is separated by a gray-scale value of 16. Notice that the highest potential values in the field are those directly behind the obstacle from the goal. We have simulated the path that a simple "point robot" would follow when started at any initial position in the workspace. A point robot is assumed to occupy only one resolution cell of the workspace at a time. The robot

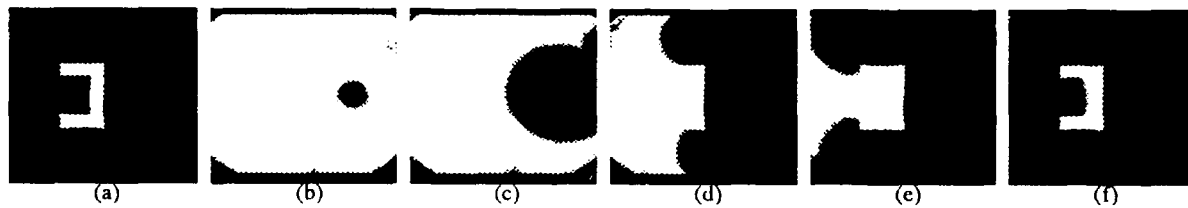


Figure 3: Intermediate MSLM output images taken during optical potential field calculation. a) "C" shaped obstacle. b) Initial goal pattern. c) Output after 20 iterations of deposition/depletion write cycle. d) 40 iterations. e) 60 iterations. f) 80 iterations.

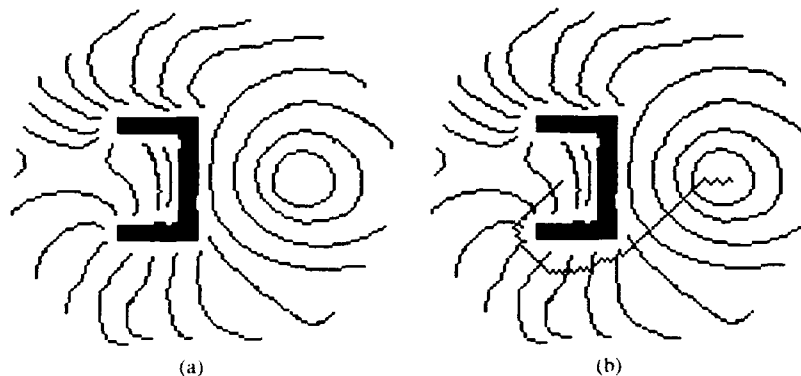


Figure 4: Optically calculated potential field for "C" obstacle. a) Equipotential contour plot of gray-scale field map. b) Path followed by a simulated "point robot" using simple gradient descent through the optically calculated potential field map. Path is roughly perpendicular to equipotential lines.

follows the potential map using simple gradient descent. An example of a path generated for the "C" obstacle is shown in Figure 4b. Optically calculated fields have also been produced for multiple obstacle workspaces, and the potential field maps have been used to guide a roving robot through an obstacle-strewn landscape.

Conclusions

We have experimentally shown that the writing mode characteristics of the MSLM can be used to calculate potential field maps suitable for robotic path planning. Optics is well suited for this application because the hybrid optical/electronic calculation scales as $O(N \ln(N))$, where N is the number of resolution cells in the robot's workspace, whereas conventional digital electronic techniques scale as $O(N^{3/2})$ or worse. Map updates at several hertz for 128×128 pixel fields are feasible using existing technologies. The bandwidth of optical potential field calculations may be increased most easily by increasing the area of the electrooptic crystal and by increasing the maximum strip current of the microchannel plate. Further research aimed at optimizing MSLM technology for this application is warranted, as is research into performing similar calculations using alternative SLM technologies.

Acknowledgement

This research was supported by the NASA Office of Aeronautics and Space Technology under RTOP 506-59-31.

References

1. C. Warde and J. Thackara, "Operating modes of the microchannel spatial light modulator," *Opt. Eng.* **22**, 695-703 (1983).
2. A.D. Fisher, "Techniques and devices for high-resolution adaptive optics," Ph.D. dissertation (Massachusetts Institute of Technology, Cambridge, Mass., 1981).
3. T. Hara, Y. Ooi, Y. Suzuki, and M.H. Wu, "Transfer characteristics of the microchannel spatial light modulator," *Appl. Opt.* **28**, 4781-4786 (1989).
4. B. Kazan and M. Knoll, *Electronic Image Storage* (Academic Press, New York, 1968).
5. J.C. Latombe, *Robot Motion Planning* (Kluwer Academic Publishers, Boston, 1991).

Generalised dynamic holographic interconnects using spatial light modulators

D.C.O'Brien, T.D. Wilkinson, R.J. Mears, W.A. Crossland. Cambridge University Engineering department, Trumpington St, Cambridge, UK. CB2 1PZ (tel. +44 223 332674).

1 Introduction

Applications such as optical neural networks often require a programmable weighted optical interconnect between 'neurons'. This can be achieved using a Stanford matrix vector multiplier crossbar geometry [1], or a matrix-matrix crossbar geometry [2]. In this type of interconnect each input is optically connected to all outputs, and the undesired connections are blocked using a shutter array (usually a electrically addressed spatial light modulator (EASLM)) between them. This gives a programmable interconnect. Non binary weights can be achieved by using a 'grey scale' EASLM or a number of pixels (a 'maxi-pixel') as a variable aperture shutter. The loss in such interconnects increases rapidly with the number of routes, N , due to the intrinsic N way optical power split in the crossbar. Crosstalk between channels is a function of the contrast ratio of the shuttering device, and there is poor tolerance to variation in pixel performance across the cell. Alternatively, a fixed weighted interconnect can be achieved using a computer generated hologram (CGH) [3]. The weights can take an analogue value, but are fixed when the hologram is designed. The holographic technique preserves optical power, and there is tolerance to small faults in the recording as information about a particular route is distributed over the whole hologram surface. Routing uses the complete aperture of the hologram, creating small Gaussian spots in the transform plane, allowing densely packed output detectors. The holographic architecture does not suffer from the poor loss scaling of the shuttered interconnects mentioned above.

In this paper we present a demonstration of a reprogrammable holographic weighted interconnect using a Ferroelectric Liquid Crystal EASLM as the recording device. This combines the programmability of the shuttered interconnect with the advantages of the holographic technique. A one to many weighted interconnect is performed, simulating a single channel of a matrix-matrix interconnect.

2 Description

CGHs are designed to route to a square array of output points, corresponding to a detector array placed in the Fourier (replay) plane of the hologram, with varying connection weights. The hologram is replayed on an EASLM which is illuminated with a collimated beam. The beam emerging from the hologram is transformed using a lens. The transformed (replay) field is captured using a camera and frame grabber.

The hologram is illuminated using a collimated beam ($\lambda = 633\text{nm}$). A laser is launched into a single mode fibre (N.A.=0.1), and the optical field from the cleaved end is collimated with an achromat ($f=125\text{mm}$, F.no=0.12). The resultant plane wave illuminates the EASLM.

The EASLM is a 128×128 ferroelectric liquid crystal device produced by THORN EMI CRL [4]. It is designed as an amplitude modulation device, but can be used to provide binary phase modulation: The polariser and analyser are set at $\pi/2$ to each other and aligned so that the input polarisation selected by the polariser bisects the angle the liquid crystal optic axes switch through (twice the tilt angle of the crystal). This creates binary phase modulation, independent of the tilt angle and the relative phase lag (δ) between the two optic axes. The transmission through the modulator is given by $0.5\sin^2(2\theta)(1 - \cos(\delta))$, and is $1.5 \pm 0.1\%$ for the particular device used, including a polariser loss of $60 \pm 5\%$. This is almost entirely avoidable, if $\delta = \pi$ and $\theta = \pi/4$. Liquid crystals with this tilt angle (θ) exist [5], and the optical thickness of the liquid crystal can be altered to achieve the $\delta = \pi$ condition. The loss measured in the cell used is unrepresentative, and device producers consider optimising the cells for phase operation to be straightforward.

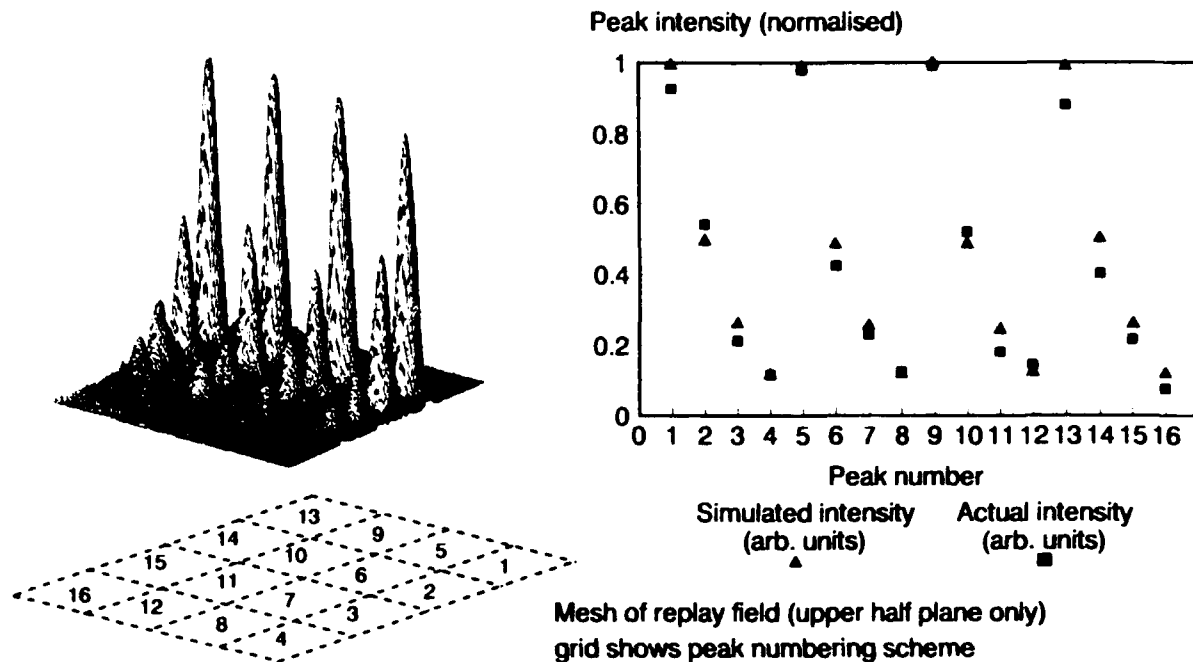


Figure 1: Results for 4x4 weighted interconnect

The holograms are calculated using a Direct Binary Search (DBS) algorithm [6] with simulated annealing, and have 32x32 coding pixels. The targets spots are on fixed pitch for the holograms described, corresponding to two pixels apart in the target array. The algorithm works in two stages: In the first stage the algorithm finds an approximation to a fixed height target. This creates a good positional fit to the target, with a large error in the heights of the peaks. The algorithm then changes, so that approximation is scaled to become a 'best fit' (in a least squares sense) to the target. This increases the emphasis on the relative heights of the peaks in the simulated hologram, and the error in peak height can reduce by a factor of up to 10 as a consequence. The holograms become slightly 'dithered' in appearance, and the noise spreads over the whole of the hologram replay field in this second stage. Simulation results for the two stage technique compare favourably with results reported for other algorithms [7]

3 Experiments

A series of holograms were simulated, using 32x32 coding pixels. The target array was specified in the upper half plane of the hologram replay field. There must be at least one axis of symmetry, and leaving the algorithm to find the best natural symmetry in the lower half creates the best holograms.

Figure 1 shows a 4x4 interconnect with weights 1,2,4 and 8 arranged in a regular pattern. The graph shows the simulated peak heights, compared with those measured from the grabbed image. The simulated heights closely match the original target, showing that the algorithm functions well. The measured heights are in good agreement with those predicted, with a mean absolute error of approximately 0.05. This would allow 10 levels of amplitude to be specified with certainty.

In a neural network the connection patterns required are likely to be random, so a series of randomly specified holograms were designed.

Figure 2 shows the replay for a typical 4x4 binary weighted interconnect with randomly chosen peak

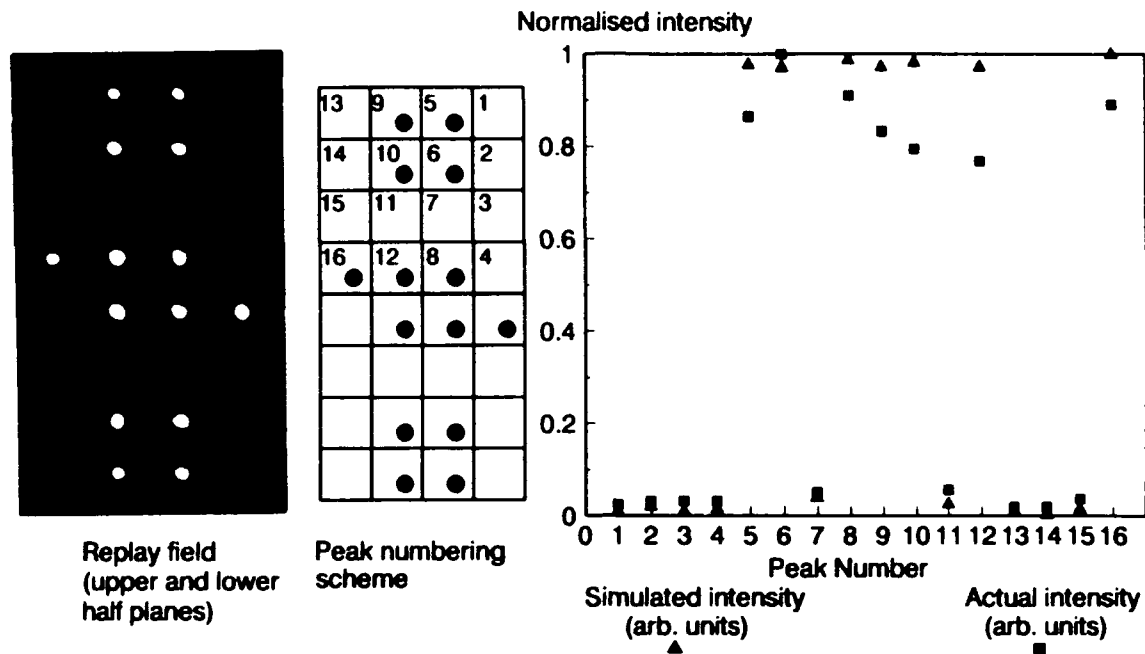


Figure 2: Results for 4x4 binary weighted interconnect

amplitudes (either 0 or 1). The whole of the replay field is shown, showing the rotational symmetry between upper and lower half planes. The zero order spot (which would be at the rotational centre of the picture) is not visible and is $> 20\text{dB}$ down on the bright spots. This indicates the two EASLM pixel states are close to π radians apart in phase. The interconnect has a good noise margin (0.7) between connected and unconnected cells.

As target spots are specified further from the optic axis their intensity is reduced from that predicted by the transmission envelope of the system. This envelope is governed by the pixel transmission function, and is a sinc squared distribution for 'ideal' pixels. This fall off can be compensated for by boosting the target levels of outer pixels by the correct proportion. The holograms above use spots close to the optic axis and are uncorrected. Figure 3 shows a typical 8x8 binary weighted interconnect hologram, which uses all of the replay plane, and is 'sinc' corrected for this reason. This gives a great improvement in peak uniformity over a similar uncorrected hologram, and much improved noise margin (approximately 0.5 compared with 0.1). The interconnect functions well, showing good use of available recording bandwidth.

4 Discussion

The results show that it is possible to create useful (8x8) binary holographic interconnects with good (approx 0.5) noise margin. As less points are connected weights can be specified more accurately, as would be expected.

The cause of the variation in performance between predicted and actual connections is unclear. The contribution from dead space is proportional to the relative areas of dead and active space. In this case about 0.1% of the incident optical energy passes through uncontrolled areas of the SLM, so has little effect. Other experiments show that the envelope function is not a simple sinc distribution as would be expected, indicating variation in pixel behaviour across the device. External components such as polarisers are likely to contribute to multiple reflections and transmission variation, which are both likely to effect results. The variation is likely to be a combination of these and other factors. Work is underway to improve control of spot amplitude using compensation techniques and improved external components.

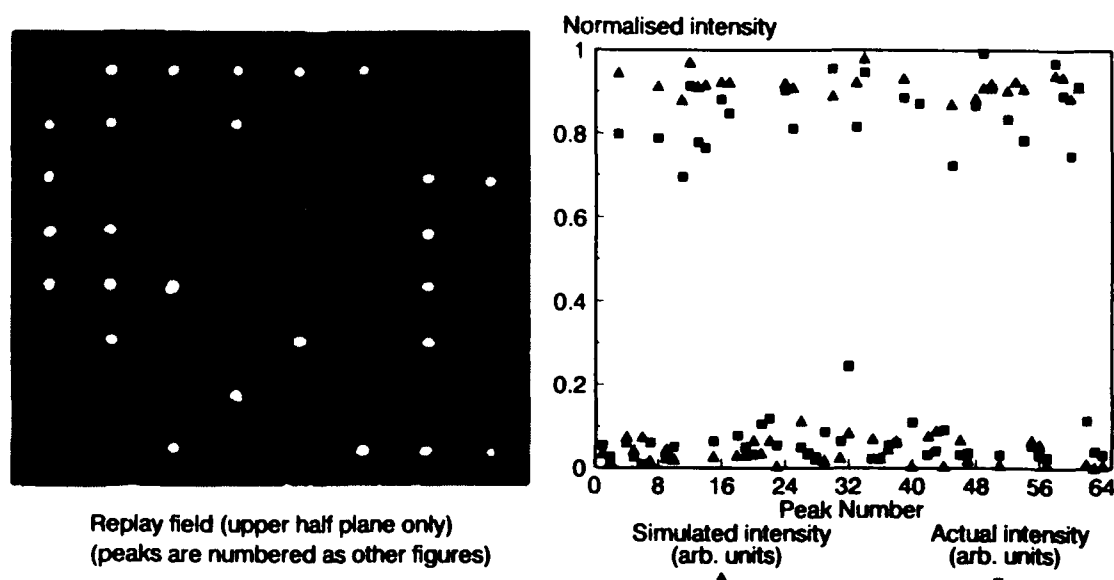


Figure 3: Results for 8x8 binary weighted interconnect

5 Conclusions

The demonstration indicates it is possible to create dynamic holographic interconnects with multilevel weights which closely match those desired. The potential for better intensity control exists, and work is continuing to improve the performance of such interconnects.

References

- [1] J.W.Goodman, A.R.Dias, and L.M.Woody. Fully parallel, high speed incoherent method for performing discrete fourier transforms. *Optics Letters*, 2(1):1-3, 1978.
- [2] M.J.Birch, W.A.Crossland, A.G.Kirk, T.J.Hall, and D.G.Vass. The design of scaleable optical crossbar structures using felc/vlsi technology and free space optics. In *LEOS 1992 Summer Topical Meeting Digest on Smart Pixels*, August 1992.
- [3] M.P.Dames, R.J.Dowling, P.Mckee, and D.Wood. Efficient optical elements to generate intensity weighted spot arrays: design and fabrication. *Applied Optics*, 30(19):2685-2691, 1991.
- [4] M.F.Bone, D. Coates, W.A.Crossland, P.Gunn, and P.W. Ross. Ferroelectric liquid crystal display capable of video line address times. *Displays*, pages 115-118, 1987.
- [5] Chisso Corp., Fine chemicals division, 2 Kamariya, Kanazawa-ku, Yokohama, 235 Japan. *Chisso Chemical 2004*.
- [6] M.A.Seldowitz, J.P.Allebach, and D.W.Sweeney. Synthesis of holograms by direct binary search. *Applied Optics*, 26(14):2788-2798, 1987.
- [7] P.E. Keller and A.F. Guicho. Design and analysis of fixed planar holographic interconnects for optical neural networks. *Applied Optics*, 31(26):5512-5526, 1992.

Implementation of a Polarization Sensitive Silicon Retinula Array

Ido Bar-Tana and Kristina M. Johnson
Optical Computing Systems Center
University of Colorado at Boulder
Boulder, CO 80309, (303)492-0785

1. Introduction

This paper describes the implementation of a polarization sensitive silicon retinula array. The biological and machine vision motivation for a polarization sensitive retinula array is described in section 2. The theory of specular reflection, upon which the retinula array is based, is described in section 3. Section 4 describes the implementation concepts and realization of the polarization sensitive retinula array, including a description of the VLSI chip and the optical system.

2. Motivation

2.1. Biological

The initial motivation for this work stemmed from biological evidence on the use of polarization by various migrating birds and insects^{1,2,3,4}; the partial polarization of skylight is used by migrating birds for navigation and orientation; the photoreceptors of crickets are polarization sensitive⁴ and homing pigeons have the ability to orient themselves spatially by discriminating the orientation of polarized light³. In most cases, studies show that these phenomena are due to polarization sensitive visual receptors⁵.

2.2. Machine Vision

Classification techniques based on the polarization of reflected light by materials can be used to distinguish between metallic and dielectric surfaces. These techniques have applications in machine vision such as printed circuit board inspection and enhancement of higher-level object recognition. The implementation of the polarization retinula array is optimized towards such tasks and the circuit operation at each pixel is based on the Fresnel reflection model⁶, as described in the following section.

3. Theory

The principle behind classifying metals from dielectrics lies in the fact that unpolarized light, reflecting obliquely from a smooth surface, will be

partially polarized due to specular reflection. Specular reflection arise from lightwaves that reflect a single time from material microfacets that are significantly larger than the wavelength of incident light. The specular plane is the plane defined by the incident and reflected directions of specularly reflected light⁶. Light reflecting from a dielectric has a higher component of specular reflection than metals. *Specular reflection thus acts as a converter between the material type and the degree of polarization.* Polarizers can be used to change the degree of polarized light into intensity, which in turn can be converted to an electrical signal by photodetectors and circuitry. This process is shown in figure 1.

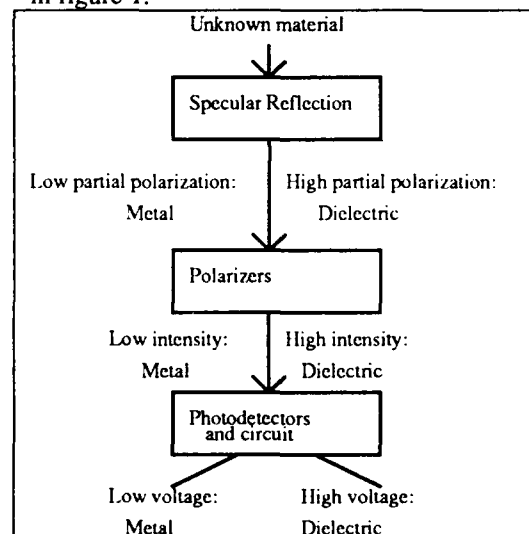


Figure 1: Classifying material type from detected intensity of polarized light.

3.1. The Fresnel reflection model⁶

The transmitted radiance through a polarizer oriented at θ with respect to the specular plane of incidence is given by:

$$I_t = \frac{1}{2} I_d + \frac{F_{\parallel} \cos^2 \theta + F_{\perp} \sin^2 \theta}{F_{\parallel} + F_{\perp}} I_s \quad (1)$$

where I_s is the magnitude of the component due to specular reflection, I_d is the magnitude of the component due to diffused reflection, F_{\perp} is the Fresnel coefficient for the polarization component perpendicular to the specular plane and F_{\parallel} is the Fresnel reflection coefficient for the polarization component parallel to the specular plane. From equation (1) we get:

$$\begin{aligned} I_{\max} = I_{\theta=90} &= \frac{1}{2} I_d + \frac{F_{\perp}}{F_{\parallel} + F_{\perp}} I_s \\ I_{\min} = I_{\theta=0} &= \frac{1}{2} I_d + \frac{F_{\parallel}}{F_{\parallel} + F_{\perp}} I_s \\ \text{Fresnel Ratio} &\equiv \frac{F_{\perp}}{F_{\parallel}} = \frac{I_{\max} - \frac{1}{2} I_d}{I_{\min} - \frac{1}{2} I_d} \approx \frac{I_{\max}}{I_{\min}} \end{aligned} \quad (2)$$

where the last approximation in equation (2) is valid for $I_d \ll I_{\min}$, which is true for most surfaces of interest. The value of the Fresnel ratio is the key to distinguishing between metals and dielectrics: *for a wide range of angles, the value of the Fresnel ratio of dielectrics is substantially higher than that of Metals.*

3.2. Simulations

A CCD camera connected to a frame grabber and digitizer was used to take four frames of an object illuminated with unpolarized light, each passed through a different polarizer orientation: 0° , 45° , 90° , 135° . These orientations are generally not with respect to the specular plane, resulting in an approximation to I_{\max} and I_{\min} . The Fresnel ratio was then calculated on a pixel by pixel basis. Using a hard threshold, a binary image was produced, in which a white pixel corresponds to metal, and a black pixel to dielectric. However, hardware implementation of a system that holds and handles four images is not practical. Further simplification of the algorithm, using only two orientations of the polarizer, at 0° and 90° , yielded results almost as accurate as the four orientations case.

4. Implementation

With only two inputs, the output from a pixel reduces to the following expression:

$$V_{out} = \begin{cases} 5v, & \max\left(\frac{V_1}{V_2}, \frac{V_2}{V_1}\right) > kI_{thresh} \\ 0v, & \max\left(\frac{V_1}{V_2}, \frac{V_2}{V_1}\right) < kI_{thresh} \end{cases} \quad (3)$$

where V_{out} is the output voltage, which can be a logical 0 or 1, V_1 and V_2 are the input voltages (representing the two input intensities from the two photodetectors), k is a constant and I_{thresh} is an adjustable threshold current, thresholding between a signal corresponding to dielectric ($V_{out}=5v$) and a signal corresponding to metal ($V_{out}=0v$).

4.1. Approach

To implement the above function electronically, the algorithm shown in figure 2 is used.

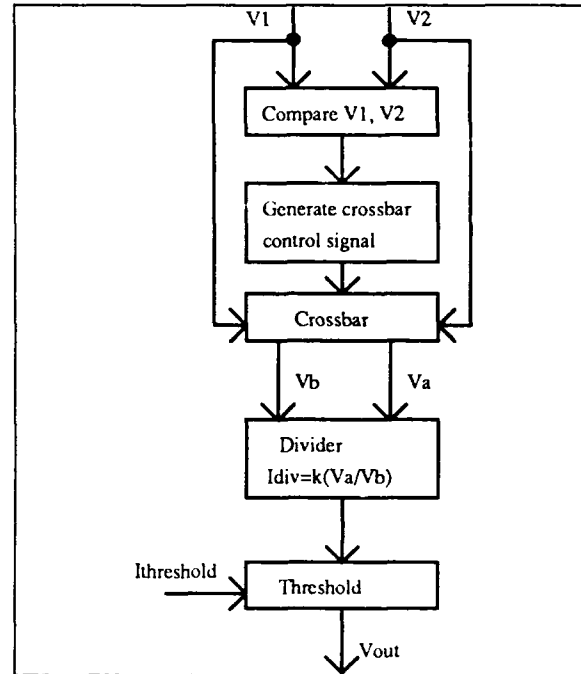


Figure 2: Algorithm for implementing the Fresnel reflection model

The combination of the comparator and crossbar blocks assure that the higher of the two input voltages is directed to the Va line of the divider, and the lower of the input voltages - to the Vb line. The crossbar either passes the two voltages such that input V1 is directed to Vb and V2 is directed to Va (the bar state) or crosses them such that V1 is directed to Va and V2 is directed to Vb (the cross state). The state of the crossbar is controlled by the output of the comparator. This assures that the divider will always generate an output current proportional to:

$$I_{div} \propto \max\left(\frac{V_1}{V_2}, \frac{V_2}{V_1}\right) \quad (4)$$

Finally the output from the divider is thresholded to generate a binary output, Vout as shown in equation (3).

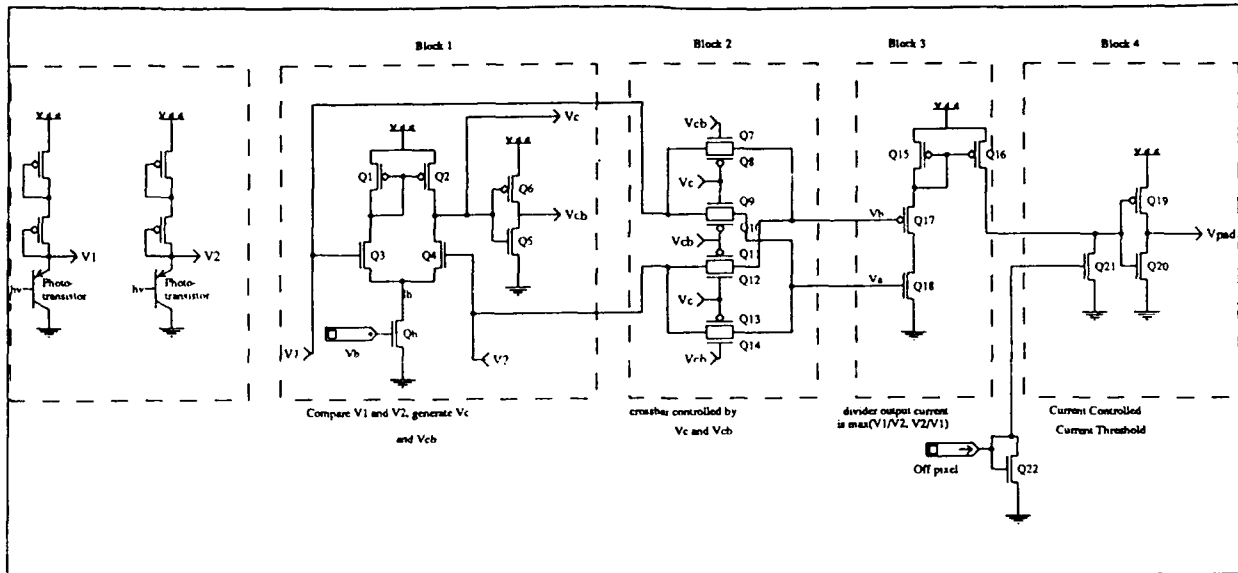


Figure 3: Circuit diagram

4.2. Circuit Description

The circuit is composed of blocks corresponding to those shown in figure 2. What follows is a description of the electrical circuit in each block shown in figure 3.

Block 1: the comparator and crossbar control voltage is a simple transconductance amplifier, connected to an inverter. The comparator receives two voltage inputs, V1 and V2 (from the two photodetectors on the pixel) and generates an output that is fed to an inverter and the crossbar. The voltage V1 generates a current that is mirrored by the current mirror Q1-Q2. V2 generates a current that is subtracted from the output node of the comparator (marked Vc). If V1 is higher than V2, the input node of the inverter is charged, resulting in a high on that node, and vice versa. The inverter generates the inverted voltage of Vc, denoted as Vcb. These two voltages, as well as V1 and V2, are the inputs to the crossbar.

Block 2: the crossbar generates outputs Va and Vb. It is composed of four pass gates, each gate consisting of two complementary transistors which are controlled by Vc and Vcb. If Vc is high (Vcb low) the inner pass gates are closed (short) and the outer pass gates are open (cut) - corresponding to the cross state. If Vc is low (Vcb high) the outer pass gates are closed and the inner pass gates are open, corresponding to the bar state.

Block 3: the divider is a modified transconductance amplifier that performs crude analog division over a

limited voltage range. It is based on the simple transconductance amplifier (used as a comparator in block 1) which performs the function:

$$I_{out} = I_b \tanh\left(\frac{k(V1-V2)}{2}\right) \quad (5)$$

where I_{out} is the output current from the amplifier, I_b is the bias current (shown in block 1) and k is a constant. Starting with equation 5, we assume the following simplifications:

1. The voltage range is such that $\tanh(x) \approx x$, resulting in:

$$I_{out} \propto I_b(V1-V2) \quad (6)$$

2. If V2 is low, we can discard its transistor (Q4 in block 1), and we arrive at the divider circuit shown in block 3. The resulting output is $I_{out} \propto I_b V1$

3. Over a limited range, I_b is in direct proportion to Vb, resulting in $I_{out} \propto Vb V1$

4. Lastly, in order to get a division, we replace the NFET transistor associated with V1 with a PFET transistor. The resulting circuit generates an output current, I_{out} , that depends on Vb/Va, when assumptions 1,2,3 are valid. If Vb > 0.8v or Va < 0.2v, the resulting output current is low. Simulations and experiment confirmed that the operating range of the divider is approximately between 0.2v and 0.8v

Block 4: the Threshold circuit is composed of an inverter and a bias threshold current feeding into the off-array transistor. The output of the divider charges the input node of the inverter while the threshold current causes the node to discharge. If the divider output is lower than the drain current of Q21, the input node of the inverter will discharge, causing a high at the output, Vpad, and vice versa.

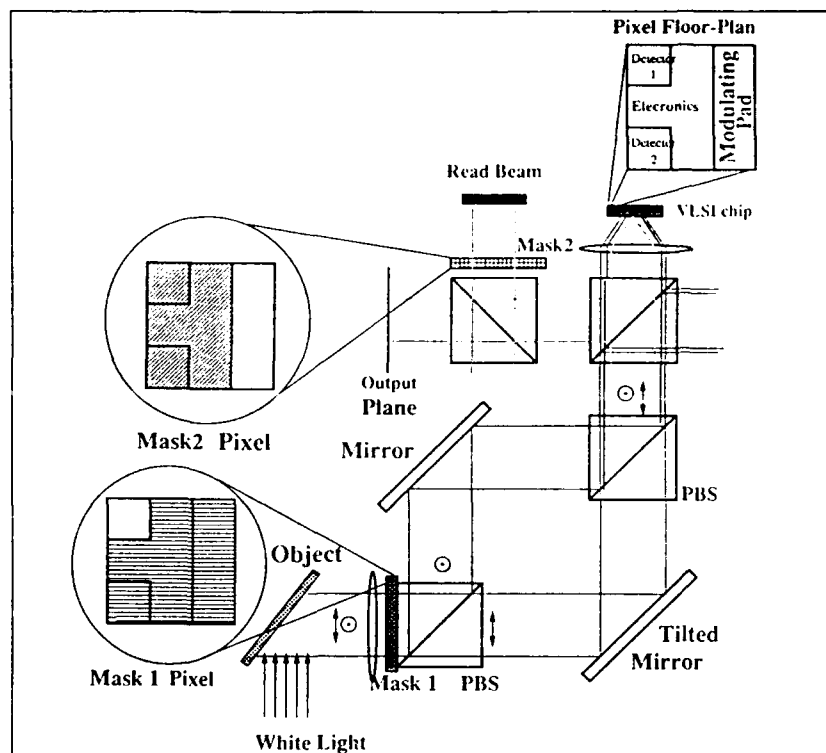


Figure 4: System Layout

4.3. System description

The optical system of the polarization sensitive retinula array is shown in figure 4. The input image, illuminated obliquely by unpolarized white light, is passed through a mask and a broadband polarizing beamsplitter (PBS). The mask filters the image spatially into pixels such that only the photodetectors will be illuminated. The PBS generates two copies of the image, with orthogonal polarizations. The orthogonally polarized images are then recombined, with one image being slightly tilted (by the mirror) such that when they are focused onto the VLSI chip pixel, light from each image will illuminate the corresponding photodetector. The circuit at each pixel calculates the output as described in section 4.2, and produces a binary voltage output onto the modulating pad. The chip has a thin layer of ferroelectric liquid crystal (FLC) on top of it, which is sensitive to the voltage of the modulating pad⁷. The liquid crystal modulates the polarization state of an optical read beam according to the electrical output of the circuit. The FLC acts as a waveplate, capable of rotating the orientation of its fast axis

upon application of an electric field. An additional mask filters the read beam spatially such that only the modulating pad of the circuit is exposed to it.

A test chip with the electronic and optical detectors has been fabricated (on a 2.0 μ m n-well process) and tested. A 32x32 array composed of the tested pixels is being designed.

5. Acknowledgment

The authors acknowledge Dr. John Lazzaro for initial discussions on animal vision using polarization and Dr. Douglas McKnight and David Jared for useful discussions and suggestions.

6. References

1. Frank R. Moore, "Sunrise, skylight polarization, and the early morning orientation of night-migrating Warblers", in *The Condor*, 88:493-498
2. John B. Phillips and Jerry A. Waldvogel, "Celestial polarized light patterns as a calibration reference for sun compass of homing pigeons", in *j. theor. Biol.* (1988) 131 55-67
3. Juan D. Delius, Robert J. Perchard and Jacky Emmerton "Polarized light discrimination by pigeons and an electroretinographic correlate", in *j. of Comparative and Physiological Psychology*, 1976, Vol. 90, No. 6, 560-571
4. Thomas Labhart, "Polarization-opponent interneurons in the insect visual system", in *Nature*, Vol. 331 4 Feb. 1988
5. S.R. Young and G.R. Martin, "Optics of retinal oil droplets: a model of light collection and polarization detection in the avian retina", in *Vision Res.* Vol. 24, No. 2. pp. 129-137, 1984
6. Lawrence B. Wolff, "Polarization-based material classification from specular reflection", in *IEEE trans. on pattern analysis and machine intelligence*, Vol. 12, No. 11, Nov 1990
7. Kristina M. Johnson, Douglas J. McKnight, Ian Underwood "Smart Spatial Light Modulators Using Liquid Crystals on Silicon", to appear in *J. Quan. Elec.*, Feb. 1993

Programmable Diffractive Optical Elements

Jeffrey A. Davis, Don M. Cottrell, Robert M. Bunch,
Werner V. Brandt, Heidi M. Schley-Seebold, and Jarod Guertin
Department of Physics
San Diego State University
San Diego, CA 92182
(619) 594-6158

1. Introduction

Diffractive optical elements can be written onto spatial light modulators (SLM's) yielding several advantages. First, new ideas can be quickly tested before incurring the expense of making higher quality elements. Secondly, a variety of new applications involving dynamic optical elements may become useful. We report new kinds of optical elements written onto the programmable magneto-optic spatial light modulator (MOSLM)

The main differences between diffractive optical elements and SLM's are the limited number of pixel elements and phase encoding capability for the SLM. In our case, the MOSLM only has 128x128 pixels and can only encode a binary phase grating.

In order to focus a beam of light, the phase of the incident optical beam $\phi(x,y)$ must be altered as a function of x and y . This phase function is given, using small angle approximation theory, by

$$Z^*(x,y;f) = e^{i\phi(x,y)} = e^{ik \left(\frac{x^2+y^2}{2f} \right)} \quad (1)$$

where f is the focal length of the lens and $k = 2\pi/\lambda$. The fixed pixel size forces a Nyquist limit in the encoded phase patterns and results in a minimum focal length given by $f = (N\Delta^2 / \lambda)$. Using a MOSLM with a pixel size of $\Delta = 75 \mu\text{m}$ and $N = 128$, the minimum focal length at a wavelength of $0.6328 \mu\text{m}$ is 1.138 m.

2. Derivative lenses

Spatial differentiation can be performed by imaging an input pattern with a binary optical element consisting of Fresnel lenses having identical focal lengths but different center locations. These lenses form overlapping images having different transverse locations in the image plane. If the two lenses have a relative

phase shift of π radians, the images will be subtracted resulting in an image which is differentiated in the direction of the shifted lens positions.

Figure 1A shows a conventional Fresnel lens which forms the image of an input object $g(x,y)$. Next the pattern is imaged with an optical element consisting of two Fresnel lenses having identical focal lengths f , but different center locations and written as $Z^*(x + a; f) - Z^*(x - a; f)$ as shown in Fig. 1B. Each lens images the object to a different transverse location in the image plane. By subtracting the lenses, the two images will be subtracted resulting in the first order derivative of the image as

$$g(x + a, y) - g(x - a, y) \approx 2a \frac{\partial g}{\partial x} \quad (2)$$

By shifting the two lenses in the vertical direction, the y derivative can be formed. Using a combination of four appropriately shifted lenses written as $Z^*(x + a, y + a; f) + Z^*(x - a, y - a; f) - Z^*(x + a, y - a; f) - Z^*(x - a, y + a; f)$ and shown in Fig. 1C, the cross derivative image is formed as $(\partial^2 g / \partial x \partial y)$. Experimental results will be shown.

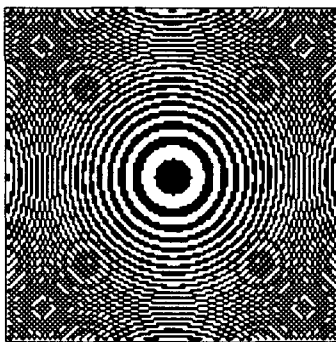


Fig. 1A. Conventional
Fresnel lens

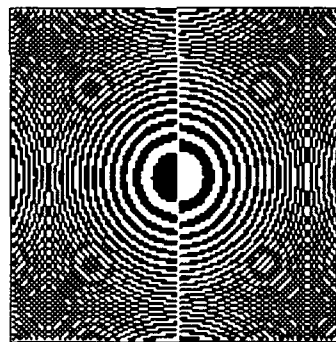


Fig. 1B Derivative lens
forming $\partial g / \partial x$

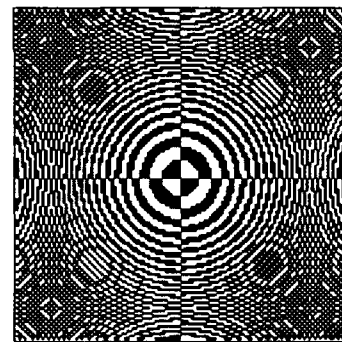


Fig. 1C. Derivative lens
forming $(\partial^2 g / \partial x \partial y)$

3. Anamorphic optical elements

Anamorphic optical elements have different focal lengths for the horizontal and vertical axes as $Z^*(x; f_x) Z^*(y; f_y)$. These lenses can be used in optical systems in which the magnification for the horizontal axis is different from the vertical axis. Two applications are of interest. Anamorphic imaging systems are used to image an object onto a recording medium having different physical dimensions. Anamorphic Fourier transform systems allow scaling of the Fourier

transform to increase the resolution of one axis relative to the other. Programmable spatial light modulators (SLM's) can be used where the magnification of the optical system must be varied with time.

Some anamorphic lenses are shown in Fig. 2 and include (A) a cylindrical lens which only focuses in the horizontal direction, (B) a lens which has different positive focal lengths in the x and y directions, and (C) a lens which has a positive focal length in the x direction and a negative focal length in the y direction.

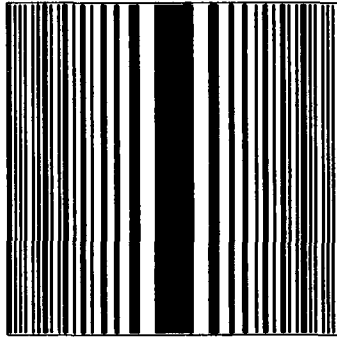


Fig. 2A. Cylindrical lens which focuses in horizontal axis

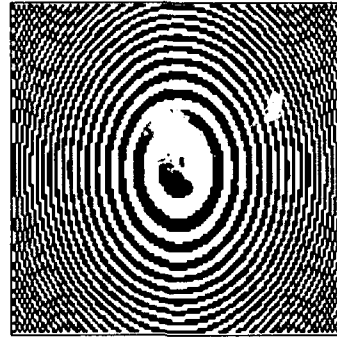


Fig. 2B Lens with different positive horizontal and vertical focal lengths

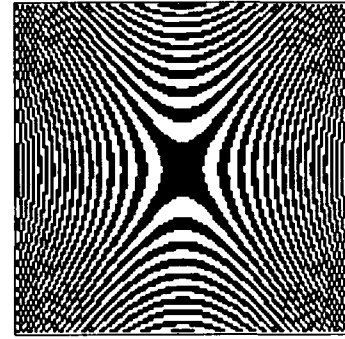


Fig. 2C. Lens with positive vertical and negative horizontal focal lengths

We show experimental results in which the horizontal and vertical magnifications can be varied to distort the output image relative to the input object.

4. Nondiffracting Bessel function beams

Non diffracting beams having an electric field Bessel function profile can be created by passing the beam through a transmission function¹ of the form $t(r) = \exp(i\Phi(r))$ where $\Phi(r) = -2\pi r/r_0$ and r_0 is a constant. This creates a beam having a Bessel function profile whose width stays constant over a distance given by $L = Dr_0/\lambda$ where D is the size of the hologram. The beam width is given (in the small angle approximation) by $W = 0.766r_0$. Assuming that the pattern is written onto a SLM where $D = N\Delta$, $r_0 = q\Delta$, and q is an integer, we can rewrite the expressions for L and W as

$$L = Nq\Delta^2/\lambda ; \quad W = 0.766q\Delta \quad (3)$$

Figure 3A shows the pattern associated with $q = 4$. When written onto the MOSLM, this results in a nondiffracting beam having a width of $230\text{ }\mu\text{m}$. By changing the value for q , the beam diameter and nondiffracting propagation distance can be changed. By shifting the pattern horizontally as shown in Fig. 3B, the axis of the beam can be translated. By forming the pattern shown in Fig. 3C, the propagation direction of the beam can be tilted relative to the plane of the SLM. Experimental results will be shown which agree with theoretical predictions.

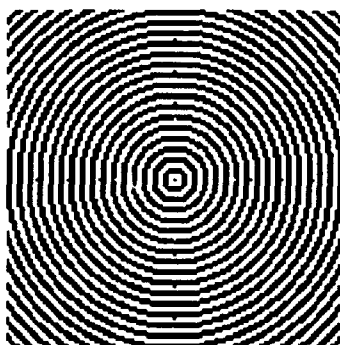


Fig. 3A. Bessel function pattern with $q = 4$

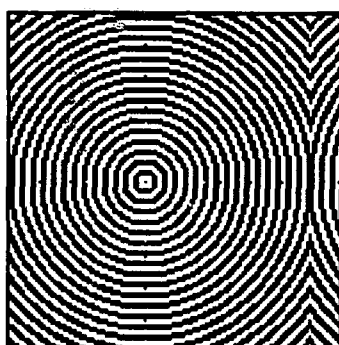


Fig. 3B. Bessel function pattern with shifted beam axis

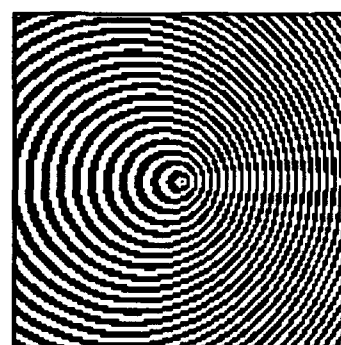


Fig. 3C. Bessel function pattern with tilted beam axis

5. Conclusions

We show a variety of new kinds of diffractive optical element designs which demonstrate the versatility of this field. More importantly as discussed in the introduction, use of SLM's for encoding these patterns offers two advantages. First the SLM serves as a programmable low cost testbed for more complicated nonprogrammable binary optical elements. Finally the programmability of this system allows real time image processing in which the optical element can be changed rapidly offering dynamic applications.

6. References

1. J. Turunen, A. Vasara, and A.T. Friberg, "Holographic generation of diffraction-free beams", *Appl. Opt.*, 27, 3959-3962, (1988)

A Self-amplified Beam-Steering Technique for Programmable Optical Interconnections

Hua-Kuang Liu

Center for Space Microelectronics Technology
Jet Propulsion Laboratory
California Institute of Technology
Pasadena, California 91109

Shaomin Zhou and Pochi Yeh

Department of Electrical and Computer Engineering
University of California, Santa Barbara, CA 93106

A self-amplified angularly multiplexed beam-steering technique for programmable interconnection and optical computing applications is presented. The technique utilizes an electrically-addressed spatial light modulators for the dynamic writing of specific computer-generated holographic gratings and the two-beam coupling energy transfer effect in photorefractive crystals for self-amplification in the steered beams. In comparison with other dynamic optical array generation and optical interconnection methods reported in literature [1-8], our new technique has the unique advantages of large array size, pattern combination capability, high-gain self-amplification, and intensity uniformity of the steered beam. The low space band-width product of the liquid crystal television spatial light modulator (LCTV-SLM) will not limit the beam quality of our technique since it is used only to generate the angularly multiplexed reference beam.

Our new technique may be described by the two processes as illustrated with the assistance of Fig.1. First, in the storage process, an Ar⁺ laser beam is collimated by lenses L₁, L₂, and pin-hole spatial filter (SF) combination and then passed through the polarized beam splitter(PBS). The reflected component is changed from the ordinary beam to an extra-ordinary beam with a half wave plate, and used to image the original 2-D grating elements through the photorefractive crystal via mirror M, and lenses L₅ and L₆. Here, The 2-D grating elements are the phase-only optical elements (i.e. Dammann grating) which can be recorded in the crystal with a high modulation depth leading to high diffraction efficiency. The transmitted extraordinary beam is used to illuminate the computer-generated hologram (CGH) on the LCTV-SLM for the generation of the reference plane

wave (or waves) in the time domain for the angularly multiplexed holographic recording and reconstruction in the photorefractive crystal in the spatial domain. Secondly, in the reconstruction process, the reconstructed 2-D beam configurations can be obtained on the back focal plane of the Fourier transform lens, FL, as the crystal is illuminated by an extraordinary plane wave(or waves).

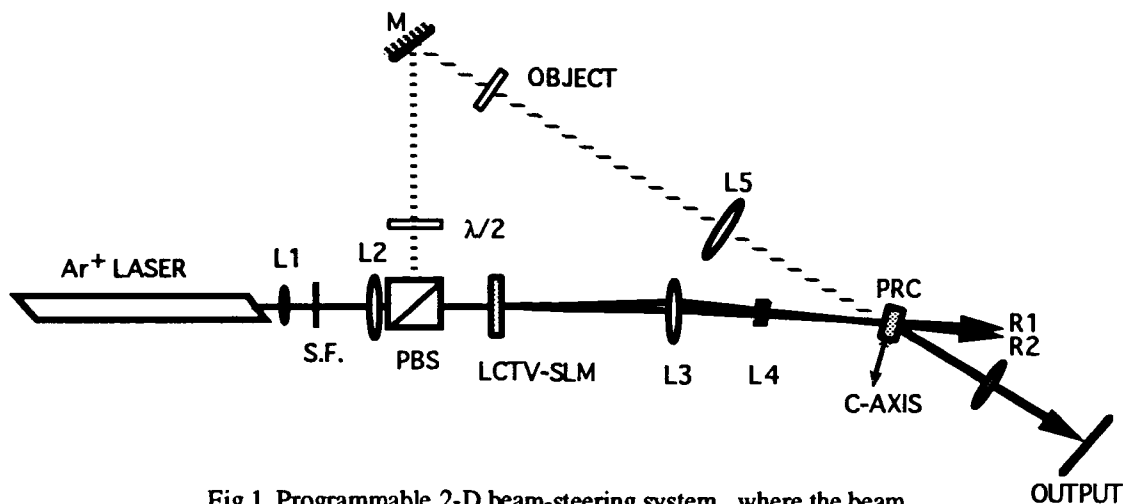


Fig.1 Programmable 2-D beam-steering system, where the beam marked with dashed line exist only in recording procedure

In the theoretical discussion of the technique, the generation of the reference plane wave of different propagation direction, the required minimum angular separation between the reference beams for the avoidance of cross-talk among the steered beams, the beam combination configurations, the effective interaction regime, the optimization of the recording procedure, and the self-amplification conditions of the steered beam will be analyzed in detail.

Furthermore, interesting experimental results using a LCTV-SLM and a lithium niobate photorefractive crystal demonstrated that arbitrary beam patterns with high amplification gain and uniform intensity can be achieved by the new technique. To show the feasibility of the new technique, the designed arbitrary patterns and the experimental results of the steered beams are shown in Figures 2 and 3 respectively. These results indicate that the technique viable for applications to multichannel photonic switching, and optical interconnection in electronics and optical neural network.

Part of the research described in this paper was performed by the Center of Space Microelectronics Technology, Jet Propulsion Laboratory, California Institute of Technology, and was jointly sponsored by DARPA and NASA Code SMI, through an agreement with the National Aeronautics and Space Administration.

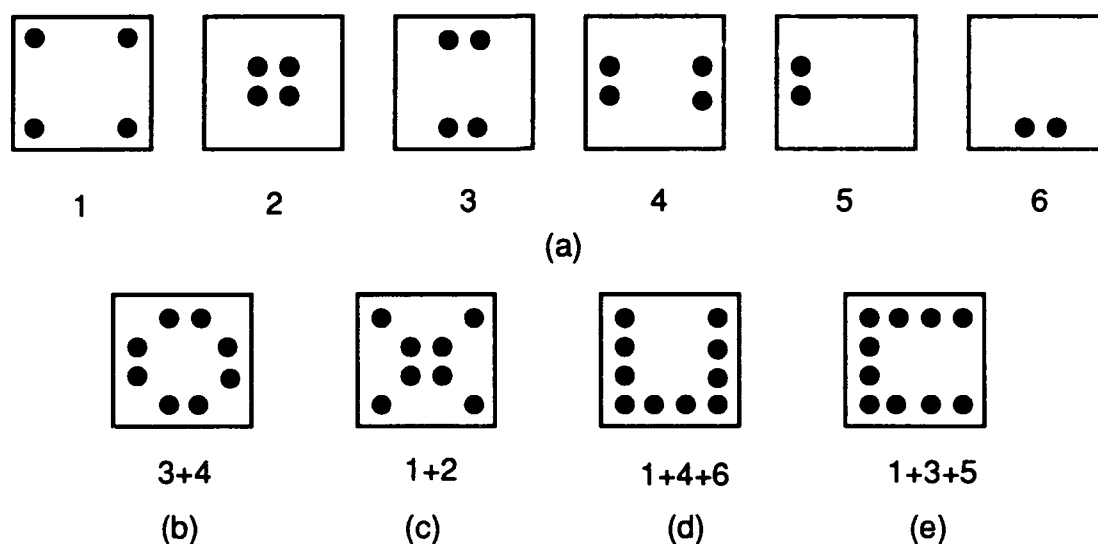


Fig.2 Scheme of the combination capability, (a) elementary patterns 1-6, (b) - (e) designed arbitrary patterns combined with elementary patterns

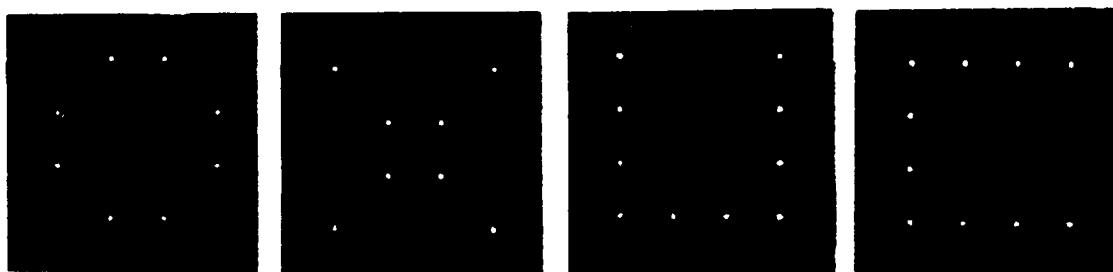


Fig.3 Experimental results corresponding to figure 2 (b) - (e).

References:

1. Y.-Z. Liang, D.-Z. Zhao, and H.-K. Liu; " Multifocus dichromatic gelatin hololenes ", Appl. Opt. **22**, 3451 (1983).
2. S. K. Case and V. Gerbig; " Efficient and flexible laser scanners constructed from volume holograms ", Opt. Commun. **36**, 94 (1981).
3. A. Marrakchi, S. F. Habiby, and J. R. Wullert II; " Generation of Programmable coherent source arrays using spatial light modulators ", Opt. Lett. **16**, 931 (1991).

4. E. C. Tam, S. Zhou, and Q. Song; " Spatial light modulator-based real-time multiple beam splitter ", Technical Digest of the OSA 1991 Annual Meeting, 146 (1991).
5. J. Amako and T. Sonehara; " Kinoform using electrically controlled birefringent liquid-crystal spatial light modulator ", Appl. Opt. **30**, 4622 (1991).
6. E. S. Maniloff and K. M. Johnson; " Dynamic holographic interconnects using static holograms ", Opt. Eng. **29**, 225 (1990).
7. C. Denz, G. Pauliat, G. Roosen, and T. Tschidi; " Phase-coded hologram multiplexing for high capacity optical data storage ", Photorefractive Materials, Effects, and Devices Topical Meeting, 1991 Tech. Digest Series **14**, 122, July 29-31, 1991, Beverly, Massachusetts.
8. H. Yamazaki and M. Yamaguchi, " Experiments on multichannel holographic optical switch with the use of a liquid crystal display ", Opt. Lett. **17**, 1228 (1992).

Wednesday, March 17, 1993

New Materials

SWD 3:30pm-5:00pm
Grand Ballroom West

Tracy D. Hudson, *Presider*
U.S. Army Missile Command

Self Assembly SLM for Molecular Computing

Harold Szu, Ann Tate*, David Cullin*, Marianne Walch^, David Demske+, Joseph

Garcia, Sonlinh Phuvan#, Nicholas Caviris#

Naval Surface Warfare Center, Dahlgren Division, R44, +R13, ^R301, #B40

Silver Spring, MD 20903; *N507 Dahlgren, VA 22448

Spatial Light Modulator (SLM) useful Molecular Computing is made on a bacteriorhodopsin (BR) molecule film suspended in a viscous liquid medium, similar to a wet photograph but having adaptive and finer pixels.

The natural synergism between the thermal diffusion of BR molecule (induced externally by a write-laser) and its photochromism (generated internally by electronic transitions) is demonstrated in an edge-enhanced laser-image application.

Keywords: Molecular Computing, Nonuniform Pixel, Bacteriorhodopsin, Spatial Light Modulator, Image Processing

I. Introduction

Photochromisms of bacteriorhodopsin (BR) are observed in Russia Dead Sea, and other marsh area near San Francisco bay, known as the purple membrane light effect. Since that discovery about a decade ago, the BR molecules, extracted from the wild type and its mutants via the recent advancement of genetic engineering biotechnology [1-4], are enjoying much desirable storage attributes with a demonstrated resolution of 5000 line pairs per mm, better than a high resolution photograph film.

Assuming that the size of molecular pixels could be made about 60 \AA from the BR monomer, then an exceedingly high image definition on the order of a hundred million of pixels is possible within a 100 cm^2 BR optically flat film. Since a flat film is generally difficult to make, by serendipity, we have observed a non-flatness in a wet film, in the liquid phase, which has an edge enhancement effect. If this fact is understood, one can imagine the great potential that, based on the molecular self-assembly [5], an edge-enhancement image of millions' pixels occurs

naturally with a finer resolution and a higher dynamic range without hour's computing time of a digital computer.

In this paper we demonstrated such a liquid BR film that is diffusion-limited similar to a wet photograph but having adaptive and finer pixel density at wherever it is needed. The resulting edge-enhanced image storage, after a chemical fixation, is due to the synergism between a write-laser induced diffusion of BR molecules in the liquid phase and a read-laser photochromic property of BR molecules.

2. Optical Experiments

The optical experimental design is to use a two laser system. One of these lasers (which we call the imaging laser) is used to "write" the image to the BR solution. It is not necessary that this light be absorbed by the BR as we are only interested in the local heating caused by the laser illumination, thus we choose the 488 nm line of the Ar⁺ laser as our image illumination source (the BR ground state only weakly absorbs at this wavelength). After illumination with the image laser beam we are left with a nonuniform distribution of BR molecules in our film and there is a buildup of BR molecules at the edges of where the powerful laser image hits the solution due to diffusion from a region of higher temperature (the bright image area) to the lower temperature surroundings. Now if we pass a laser beam through the solution that the BR ground state will absorb, (we are using both the 632.8 nm and 543.5 nm HeNe lines as our readout laser sources), we will see the reconstructed image with edge enhancement. This edge enhancement is due to the fact that there are now a greater number of ground state BR absorbers at the image boundary than are present inside the image or in the surrounding diffusion-limited medium.

According to the Einstein theory, the mean square vector displacements of an *i*th BR molecule is given $\langle |x_i|^2 \rangle = 6D_i t_i$, where the diffusion constant D_i is proportional to the local temperature T_i as $D_i = k_B T_i / 6\pi \eta a_i$ with the size a_i of the BR molecule. A detergent treatment of the purple membrane can be used to break the membrane fragments of micron sizes into smaller units of BR molecules with a size of close to 60 Å⁰. Then, the laser-driven thermal diffusion becomes enhanced by a factor of 100 to 1000 fold. Consider a 0.3×10^{-3} degree increase in the local

temperature T above the ambient room temperature 300 Kelvin: $\Delta T/T = 0.3 \times 10^{-3} / 300 = 10^{-6}$. Therefore, diffusion over the original width of the spot borderline is

given by $\langle |r_i|^2 \rangle / \langle |r|^2 \rangle = 10^{-6}$, which, upon taking the square root, gives the line width broadening at most about 10^{-3} , namely a 0.1% increase in the line width. The heating will no doubt blur the edge somewhat. However, it is anticipated that the advantage of the nonlinear edge-piling effect of denser BR at the edge will outweigh the linear diffusion-blurring.

3. Applications

In one envisioned application, the incoherent IR image of an engine hot spot is converted to a laser image by means of a Spatial Light Modulator. The laser image is directed to a BR film for edge enhancement. The edge intensified image is produced by the synergism between the write-laser induced diffusion of BR molecules and the read-laser photochromism at the locations of excess BR molecules. The heat generated by a powerful laser-image can lower the barrier of thermal diffusion of BR molecules through a highly viscous liquid medium, while the dark side BR remains to be diffusion-limited. Therefore, the relatively higher diffusion barrier at the dark and colder area of the image can trap the BR molecules near the intensity edge and produce a nonlinear accumulation effect of BR molecules at the intensity edges, before the final solidification of the BR film. Thus the image of the hot engine and tailpipe is enhanced relative to its cold background.

4. Conclusions

One of the central attractions but also a major challenges of molecular computers is the information processing capability present at the molecular level. We have shown in this paper that molecular implementations of collective computing is possible. Theoretically, we have extended [5] the concept of control theory and neural nets to the thermodynamic free energy principle and proved for MC a similar minimization principle. Thus the Lyapunov-style energy convergence theorems [9] are valid for both neural nets and MC with some minor refinements.

The convergence can insure the reliability of the processing. Experimentally, we have demonstrated a special case of the theorem by exploiting laser imaging. A wet film used to store the laser image is initially having a uniform density of BR molecules suspended in a diffusion-limited viscous medium. As a result of laser-driven thermal diffusion, edge-enhancement occurs naturally due to the accumulation of BR molecules at the diffusion edge. This proof of concept experiment reveals the great potential for image processing and pattern recognitions [6-8].

References

- [1] N. Hampp and C. Brauchle, "BR & its Functional Variants: Potential Applications in Modern Optics," In: Photochromism, Studies in Organic Chemistry Vol.40, ed. H. Dubr, H. Bouas-Laurent; Elsevier Publ. 1990.
- [2] O. Werner, B. Fischer, A. Lewis, I. Nebenzahl, "Saturable Absorption, Wave Mixing, and Phase Conjugation with Bacteriorhodopsin", *Optics Letters*, V,15, p.117, Oct. 1990;
- [3] H. Takei, A. Lewis, Z. Chen, I. Nebenzahl, "Implementing receptive fields with excitatory and inhibitory optoelectrical responses of bacteriorhodopsin films," *Appl. Opt.* Vol. 30, pp. 500-509, 1991;
- [4] R. R. Birge, "Photophysics and molecular electronic applications of rhodopsins," *Ann. Rev. Phys. Chem.* Vol. 41, pp. 693-733, 1990.
- [5] H. Szu, A. Tate, D. Cullin, M. Walch, D. Demske, J. Garcia, S. Phuwan, N. Cavaris, "Self-Organization of Molecular Computing," *IJCNN-92 Beijing*, Nov.1-5, 1992
- [6] H. Szu, "Brownian Motion of Elastically Deformable Bodies," *Phys. Rev. A* 11, pp.350-359, 1975.
- [7] H. Szu, J. Blodgett, L. Sica, "Local Instances of Good Seeing," *Opt. Commun.* Vol. 35, pp. 315-322, 1980;
- [8] H. Szu, J. Blodgett, "Self-reference Spatiotemporal Image-Restoration Technique," *J. Opt. Soc. Am.*, Vol. 72, pp. 1666-1669, Dec. 1982.
- [9] H. Szu, "Neural Networks Based on Peano Curves and Halry Neurons," *Telemetric and Informatics*, Vol. 7, pp. 403-430, 1990 (Pergamon Press)

Photoanisotropic Organic Volume Holograms for Spatial Light Modulation

Tizhi Huang, Samuel Weaver, Steve Blair, and Kelvin Wagner

Optoelectronic Computing Systems Center

Department of Electrical and Computer Engineering, University of Colorado at Boulder
Boulder, CO 80309-0425

Introduction

In optical processing it is often required to transform the information to be processed into a coherent modulation carried on a laser beam. This light modulation can be accomplished with a conventional spatial light modulator (SLM) based on a detector-modulator sandwich, which can be operated in real-time. Information can be either electrically or optically loaded into an SLM and can be updated at will. This class of spatial light modulators have been widely used in optical systems, but they are typically limited to low spatial frequency images in the range of 10-40 lp/mm. For applications which require high frequency image modulation, such as synthetic aperture radar (SAR) processing and joint transform correlation (JTC), these low resolution SLMs are inadequate. In this paper we present an alternative technique for modulating high resolution images based on an easily fabricated dye-polymer holographic film.^[1] These materials have extremely high resolution because the photoinduced changes of the material properties are recorded at the molecular level. We have measured MTF of azo/polymer systems out to 75° with no noticeable rolloff in diffraction efficiency. In addition these materials have real-time dynamic holographic recording capabilities.

Photoanisotropic organic materials are produced by uniformly distributing a photoresponsive dye molecule throughout the volume of a polymer host. These dye molecules undergo reversible photochemically induced transformations that allows the dynamic recording of holograms. Since the optical field produces a modulation of the material properties at the molecular level, and diffusion of the photoactive species is minimal, the resolution capabilities of these materials is very large. The probability of absorbing a photon by a highly anisotropic dye molecule depends on the orientation of its principal absorption oscillator axis with respect to the polarization direction of the acting light. This will result in more molecules whose absorption axes are parallel to the polarization direction undergoing the transformations than the molecules which have other orientations. As a result, some degree of ordering of the molecular orientation of the isomers can be achieved, which leads to birefringence, dichroism, and optical activity. On a time scale of a few seconds the nonequilibrium population distribution of dye molecules relaxes back to the isotropic distribution of thermally stable isomers, thereby erasing the hologram and allowing a new recording cycle to be initiated. This macroscopic photoanisotropy enables the recording not only of intensity distribution information, but also the spatial variation of the polarization direction.

We have used the MO/PVA films for several optical processing applications including, photoanisotropic incoherent-to-coherent optical conversion (PAICOC), optical SAR processing, and real-time joint transform correlation.

Photoanisotropic Incoherent-to-Coherent Optical Conversion

The PAICOC process is based on an incoherent erasure of a holographic grating and subsequent readout.^{[2],[3]} It may be seen as a combination of recording the interference of two coherent plane waves in a photoanisotropic material and erasing part of the recorded orientational population

distribution by reordering the dye molecules with the help of a third incoherent erasure beam modulated by an image. This process is illustrated in Fig. (1), and can be qualitatively described in more detail as follows. Two coherent plane waves intersect inside the photoanisotropic MO/PVA

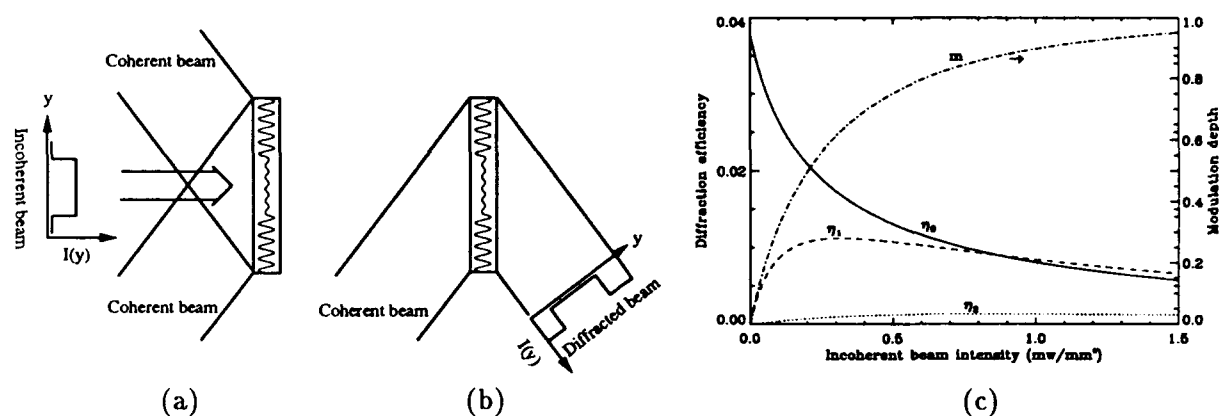


Figure 1: (a). PAICOC writing. (b). PAICOC readout showing contrast reversal. (c). Diffraction efficiency and modulation depth versus incoherent erasing beam intensity.

film forming a holographic grating. The variations in the intensity induce a spatially varying ordering of the isomeric population distribution in the film due to the molecular anisotropic transition probabilities, so that the information of the total field is stored in the form of a hologram. A third incoherent image is used to illuminate this hologram. The grating produced by the coherent interfering fields is erased in the bright areas of the incoherent image, so that nothing will be diffracted when using a Bragg matched readout beam. As a result, the diffraction produces a coherent negative replica of the incoherent erasure image. The experimental results of both binary and gray level images are given in Fig. (2). Fig. (2)(a) is for a U.S. Air Force resolution target



Figure 2: The converted negative coherent images. (a). U.S. Air Force resolution target. (b). A student picture, from a negative.

which shows excellent image quality and contrast ratio. Fig. (2)(b) is produced from the negative of a student picture, and shows good gray level performance and demonstrates the image inversion caused by the PAICOC process. The image resolution exceeds 28 lp/mm and the sample size was $3.5\text{cm} \times 3.5\text{cm}$, giving an overall image resolution of 1000×1000 pixels.

Real-time Joint Transform Correlation

Joint transform correlation is performed first by recording the interference between the Fourier transforms of two objects as a hologram, then reading out this hologram with a plane wave and optically Fourier transforming the diffracted field with a lens. This requires a very high resolution linear response from the thin holographic media that is beyond the capability of conventional SLMs, but nearly ideal for the dye-polymer holograms. Since the interference between the Fourier transforms of the two objects results in a fringe pattern containing the product of the amplitude of one with the conjugate of the other, the Fourier transform of the diffracted beam results in the production of the correlation of the two inputs. The correlation result between a high resolution synthetic aperture radar (SAR) image of Los Angeles airport and the SAR image of the entire Los Angeles area is illustrated in Fig. (3). The correlation output can recognize the airport by locating the correlation peak. The ratio of peak to next highest sidelobe is 4.3.

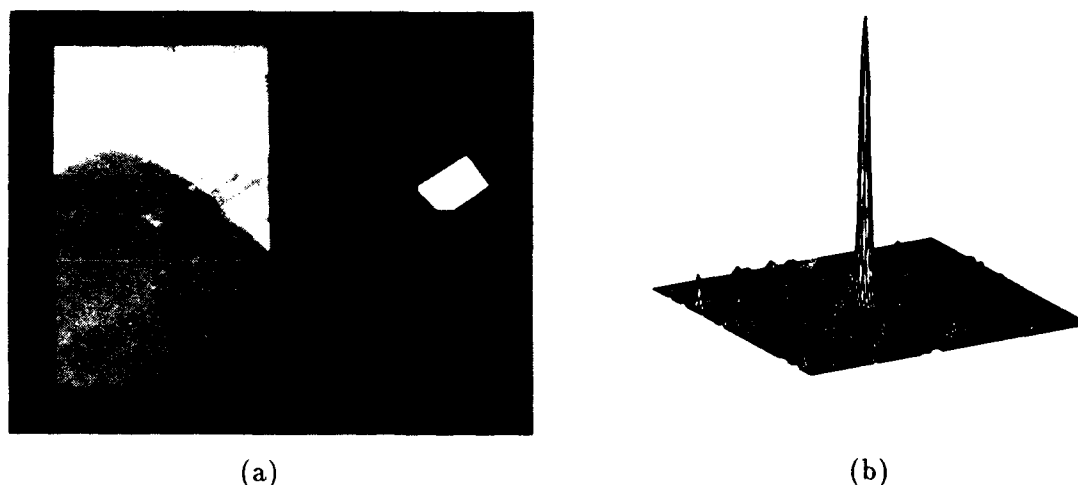


Figure 3: The correlation result of a high resolution SAR image. (a). SAR images of Los Angeles airport and entire Los Angeles area. (b). Correlation output.

Real-time SAR Image Generation

Another optical processing application which is well-matched with the material properties of the organic photorefractive material is the real-time processing of high-resolution SAR data.^[4] The requirements for a real-time optical SAR processing input medium include a very high space-bandwidth product, a real-time holographic response, and a storage time of at least one second without rewriting, which corresponds to the full frame acquisition time of a full synthetic aperture. Systems are being developed using the organic material as the input to an optical image generator for both the rectangular (strip-map) and the tomographic (spotlight) formulations of the SAR data. Experimental results have been obtained using the organic material as the real-time input to an optical processor using strip-map data from the Shuttle Imaging Radar-A (SIR-A) mission. Fig. (4)(a) shows the optical processor which achieved these results. The film-based SIR-A data is imaged onto the organic material which is also illuminated with a reference beam, holographically recording the SAR data on the real-time organic holographic media. Blocking the radar data and illuminating the organic material with the reference beam, a SAR image is formed from the light diffracted by the organic hologram using the high-resolution tilted-plane anamorphic image

generator. The processed SAR image is shown in Fig. (4)(b). The three large objects shown in

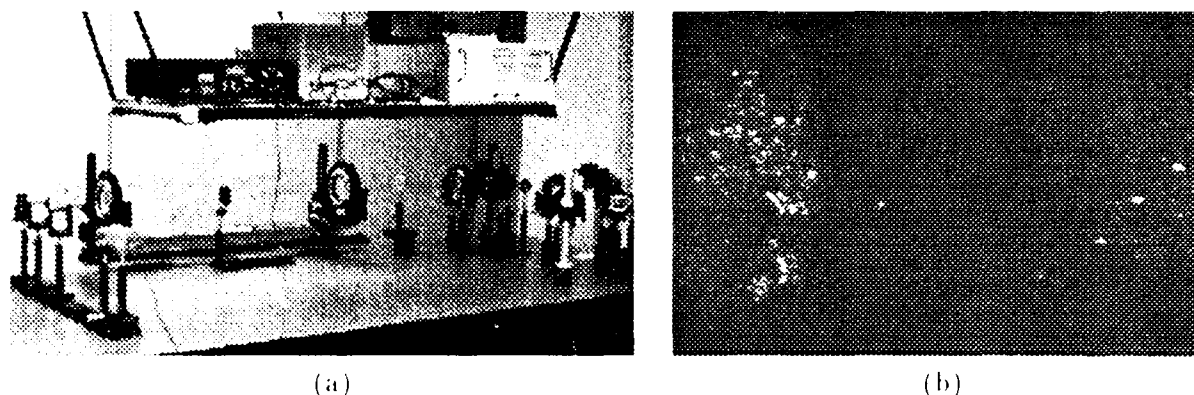


Figure 4: (a). High-resolution tilted-plane anamorphic SAR image generator using the organic holographic material as the input medium. (b). SAR image formed using data written on the organic medium. The coastline of Santa Barbara and three oil derricks are shown.

The figure are oil derricks located off the coast of Santa Barbara, which are used to focus the system because their response is similar to that of point targets. The real-time recording system demonstrated an image quality approaching the diffraction limit imposed by the radar system and a contrast ratio of greater than 700:1. The output image plane exhibited 1200 resolvable spots across an aperture of 1.2 inches. The resolution of the organic material is high enough that the spatial extent of the SAR data could be reduced by a factor of 5 in each dimension. This will result in a nearly hundred-fold decrease in the volume required to build an optical strip-map SAR image generator.

Summary

MO/PVA films have been investigated as optically addressed spatial light modulators for recording and processing high resolution images. The MO/PVA films are relatively easy to fabricate in large sample size, and demonstrate high quality and good diffraction efficiency. Using this real-time holographic technique, we have performed several optical processing functions including photoanisotropic incoherent-to-coherent optical conversion, real-time joint transform correlation, and real-time SAR image generation.

This work was supported by Martin Marietta Corporation and C.S. Draper Labs.

References

- [1] T. Todorov, L. Nikolova, N. Tomova, and V. Dragostinova, IEEE J. Quantum Electron. **22**, 1262 (1986).
- [2] J. W. Yu et al, Photorefractive Materials and Their Applications II, Springer-Verlag, (1989).
- [3] T. Huang and K. H. Wagner, "Photoanisotropic incoherent to-coherent optical conversion," Appl. Opt., to be published.
- [4] S. Weaver and K. H. Wagner, Proc. SPIE 1704, 105 (1992).

Optical Data Processing With Bacteriorhodopsin And Its Genetically Modified Variants

C. Bräuchle, N. Hampp

Institut für Physikalische Chemie, Universität München,
Sophienstraße 11, D-8000 München 2, Germany (089)-5902302

D. Oesterhelt

Max-Planck-Institut für Biochemie, Am Klopferspitz 18,
D-8033 Martinsried, Germany (089)-85782387

1. Structure and Function of Bacteriorhodopsin

BR from *Halobacterium halobium* [1] is embedded as a twodimensional crystallin lattice of BR-trimers in the lipid bilayer of the cell membrane. BR consists of a single polypeptide chain of 248 amino acids which is arranged in seven transmembrane α -helices. A retinal molecule bound via a Schiff base to lysine-216 forms the chromophoric group. Under illumination BR creates a proton gradient across the cell membrane which is used by a membrane-bound ATP-ase for ATP synthesis. Proton transport through the cell membrane is closely connected to the photocycle of BR [2]. Under illumination with light of about 570 nm the photochemical reaction of B \rightarrow J is induced. From the J-state BR passes through a couple of shortlived intermediates to the M-state in about 50 μ s. The M-intermediate has the longest lifetime which is about 10 ms for wildtype BR in suspension. From the M-state BR can relax to the B-state either thermally or photochemically. The photochemical transition from M \rightarrow B is initiated by the absorption of a photon of, e.g. 412 nm by the M-intermediate.

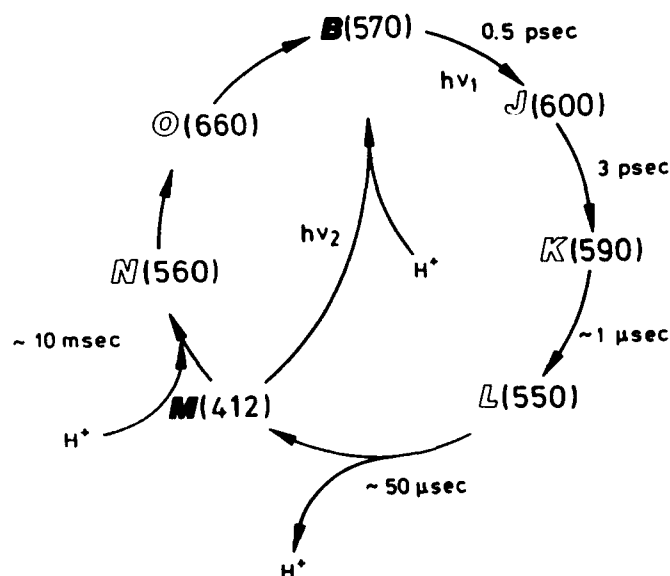


Fig. 1: Photocycle of Bacteriorhodopsin

2. Dynamic Optical Filtering With Spatial Light Modulators (SLM)

Light controlled modulation of the local absorption of a BR film is obtained by the combined use of yellow (B→M) and blue (M→B) light. Therefore, BR films can be used as intensity dependent SLM [3-5]. As an example Fig. 2 shows the edge-enhancement of the letter E and the set-up used with BR. Blue light illuminates the object, i.e. a transparency with the letter E, is then fourrier transformed by a lense, passes through a BR film without absorption and is retransformed. The CCD-camera sees an unchanged letter E. However, when the second beam of yellow light enters the common light pass - assuming for simplicity no object in this beam - the FTL lense will focus the beam on the 0th order fourrier component of letter E in the fourrier plane on the BR film. This will initiate a B→M transformation and the blue light will be blocked by M in the 0th order. Thus the CCD-camera will see an edge-enhanced letter E. From this example it is obvious that all kinds of logical operations can be performed between the two inputs at λ_1 and λ_2 which drive the different states of BR (B→M, M→B) used as processor states. More examples and the special properties of the BR mutant D96N used in these experiments will be given in the talk.

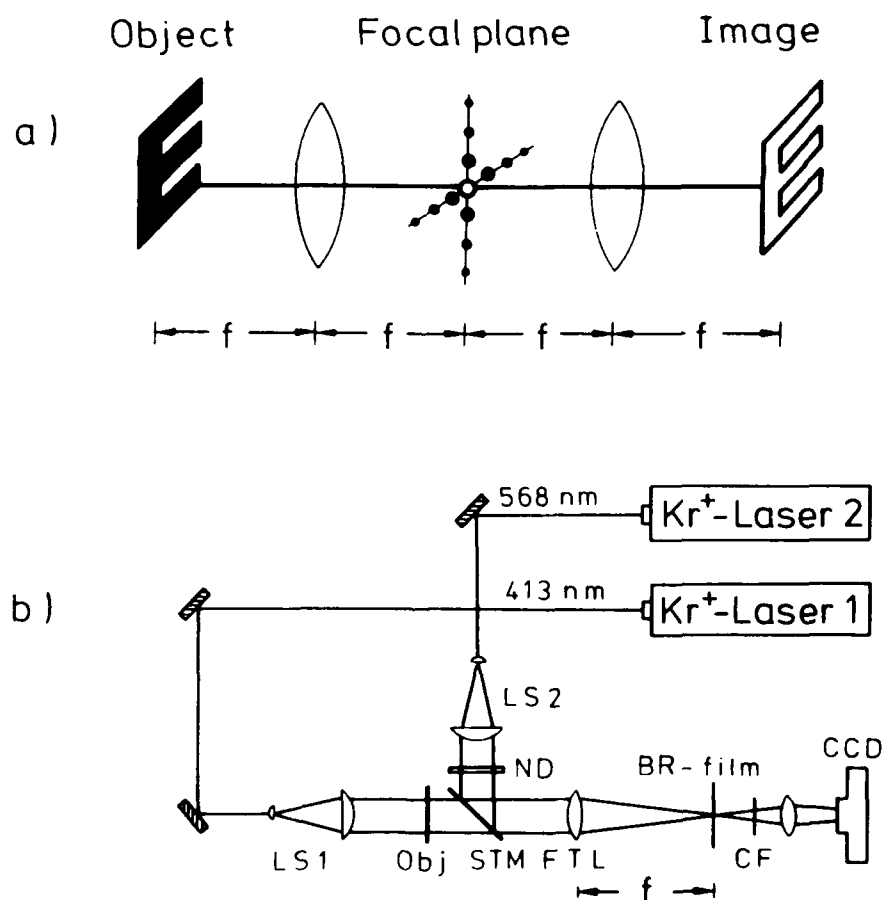


Fig. 2: a) Principle of edge-enhancement by suppression of the 0th order Fourier component. b) Set-up for the dynamical spatial filtering with BR film.

3. Optical Pattern Recognition

In Fig. 3 an optical set-up [6] for real-time pattern recognition with a dual-axis joint-fourier-transform correlator (DA-JFT) is shown. Since again BR will work as a processing medium two lasers are used with $\lambda_1 = 413 \text{ nm}$ and $\lambda_2 = 530 \text{ nm}$. With the split beam of λ_1 , two optical axis are installed containing object 1 (master pattern) and object 2 (filter pattern). Both objects are post-lense fourier-transformed into the same fourier plane and recorded into the BR-film. Since the light in both axis is mutually coherent overlapping parts of the fourier spectra will form a hologram. These overlapping parts identify common patterns of both objects. The hologram (M-type) is read out with the beam of λ_2 of the second laser. The retransformation with lenas FTL3 leads to light spots on the frame of the CCD camera indicating the location and the degree of correlation between common patterns of object 1 and 2. Fig. 4 shows one of our typical experimental results [4-6].

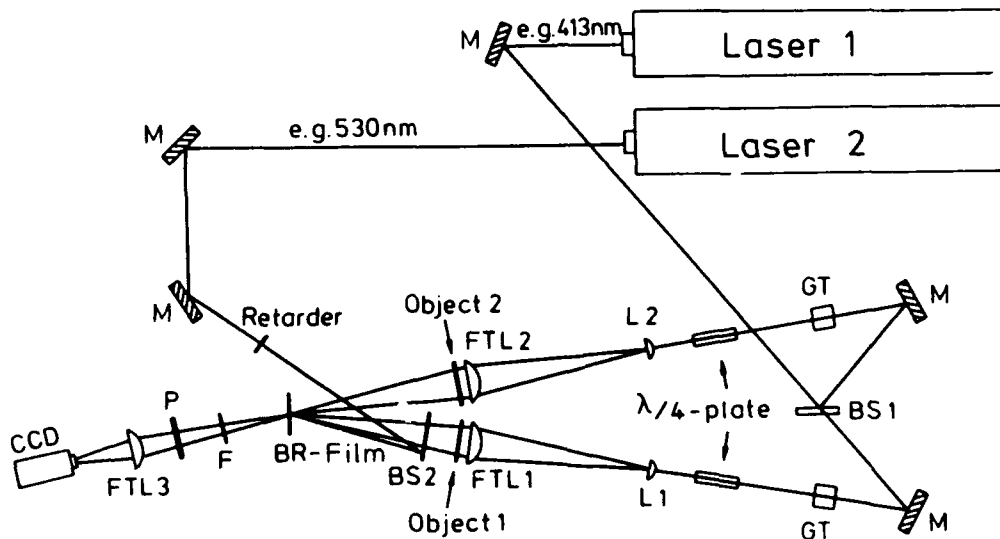


Fig. 3: A dual-axis joint-fourier-transform correlator for pattern recognition with a BR-film as processing medium.



Fig. 4: Holographic pattern recognition with BR-films. On the left side the "master" pattern is shown, on the right side the correlation signal together with the "search" pattern.

4. References

- [1] D. Oesterhelt, W. Stoeckenius, *Nature* 233, 149 (1971)
- [2] R. R. Birge, *Annu. Rev. Phys. Chem.* 41, 683 (1990)
- [3] R. Thoma, N. Hampp, C. Bräuchle, D. Oesterhelt, *Opt. Lett.* 16, 651 (1991)
- [4] C. Bräuchle, N. Hampp, D. Oesterhelt, *Adv. Materials*, 3, 420 (1991) and references therein
- [5] D. Oesterhelt, C. Bräuchle, N. Hampp, *Quarterly Review of Biophysics* 24 425 (1991) and references therein
- [6] N. Hampp, R. Thoma, D. Oesterhelt, C. Bräuchle, *Appl. Opt.* 31, 1834 (1992)

Optically Driven Optically Addressed Spatial Light Modulator.

Janine V. Reardon and Don A. Gregory

Department of Physics

The University of Alabama in Huntsville

Huntsville, AL 35988

(205) 895-6276 EXT. 314

1 Introduction

Organic based materials have been developed that can record an intensity distribution in the form of an amplitude or a phase distribution and can be written and read multiple times(1, 2, 3, 4, 5.). These materials show great promise as SLM modulation media. Although the chemistry of these organic materials is fairly well understood, the process of inducing anisotropy in these materials by photons, the method by which information is stored by these materials, has not yet been the subject of careful examination. The aim of this paper is to present an investigation of these materials and construct a model for these systems. This model will be used to experimentally modify properties of these materials, such as response time, contrast, and resolution.

2 Spectral Analysis

The spectral transmittance of a $120\mu m$ thick dye doped copolymer film developed by Physical Optics Corporation is shown in Fig. 2.1. Strong absorption is present in a region below 560 nm. Transmission in the region above 600 nm and below 100 nm is observed to be as great as 80%. A window of transmission is also present between $3\mu m$ and $5\mu m$ as can be seen in Fig. 2.2. This material is therefore well suited to be written with the 514 nm line of an Argon Ion laser and read with either a HeNe laser at 632.8 nm or an infrared diode laser.

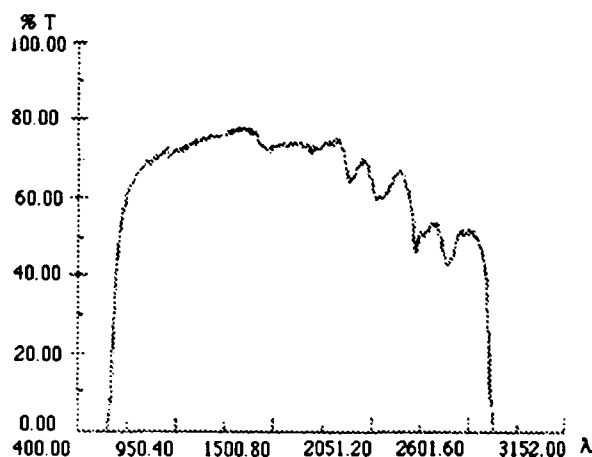


Figure 2.1. Visible spectral transmittance of POC film.

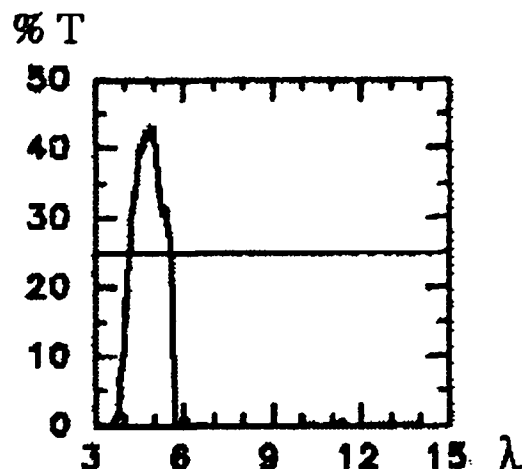


Figure 2.2. Infrared spectral transmittance of POC film. (Data obtained by David Chenault on the UAH Physics department spectropolarimeter).

3 Resolution and Response Time

The POC dye doped copolymer films have been examined for resolution and response time. Two thicknesses have been investigated thus far: $92\mu m$ and $120\mu m$. Measurements of surface flatness indicate adequate uniformity of thickness within the central 1 cm radius of each sample.

All images written in the copolymer film are in the form of anisotropic refractive index distributions induced by the intensity distribution of the optical write field. Images are read from the material by passing a probe beam through the sample which is placed between crossed polarizers. A resolution of 14 lp/mm at a 5:1 contrast ratio was measured for this material with an intensity of $< 10 \text{ mw/cm}^2$.

Response times of these thick films are on the order of seconds with the low intensity optical write field used in the experiments so far. Shorter response times have been observed in thinner films at the same optical write field intensity. The low intensity requirements of these films indicates that the mechanism by which anisotropies are induced in these films is not a thermal process.

4 Polarimetry

The object of this phase of the research is to determine the mechanism by which the interaction of an optical field with a doped material induces an anisotropic change in the material. Samples have been examined in the system shown in Fig. 4.1.

With this system, input and output polarization state pairs were measured. The amount of birefringence and dichroism has been calculated for each sample and the amount of depolarization determined.

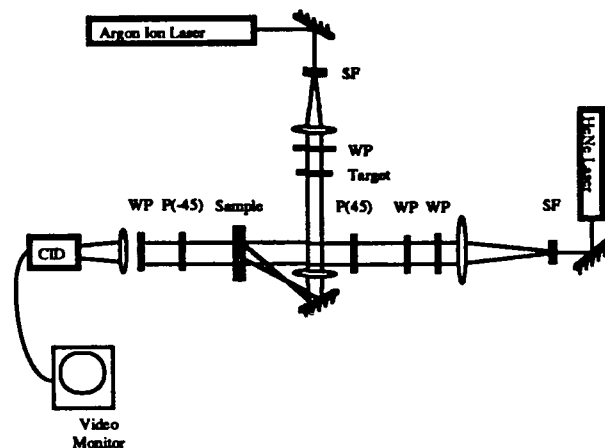


Figure 4.1. Polarimeter.

Stokes vectors measured for the POC copolymer films at 632.8 nm indicate that the linearly polarized write beam induces two effects in the copolymer film. The most prominent of the two is linear birefringence. A small amount of diattenuation also appears to be present. These two processes are theorized to be attributed to the alignment of the dopant molecules with the electric field of the optical write field and the stressing of the polymer material by the movement of the dopant molecules.

5 Conclusions

A theoretical model of the interaction of these materials with optical fields has been developed. To this end, the optically induced dichroism and birefringence have been measured. An experimental measurement of the theoretically predicted optical field induced rotation of the dopant molecules will be conducted in the next phase of this research and a better model of the part that each component of the material plays in the process will be

formulated. The preliminary results indicate that the optically induced birefringence in the dye doped copolymer films can be attributed to nonthermal processes. Also, the amount of photoinduced birefringence in the material has been measured and found to be substantial. These preliminary results indicate that this material shows great promise as an optical modulation material.

6 References

1. N. M. Burykin et al., "Photoinduced anisotropy in bio-chrom films," Opt. Comm. **54** (2) 68-70 (1985). N. Hampp et al., "Diffraction efficiency of bacteriorhodopsin films for holography containing bacteriorhodopsin wildtype BR_{WT} and its variants BRD85E and BRD96N," J. Phys. Chem. **96** 4679-4685 (1992).
2. N. Hampp et al., "Biological photochrome bacteriorhodopsin and its genetic variant Asp96 → Asn as media for optical pattern recognition," Appl. Opt. **31** (11) 1834-1841 (1992).
3. Z. Chen et al., "Bacteriorhodopsin oriented in polyvinyl alcohol films as an erasable optical storage medium," Appl. Opt. **30** (35) 5188-5196 (1991).
4. T. Todorov et al., "Photochromism and dynamic holographic recording in a rigid solution of fluorescein," Opt. Quan. Elec. **13** 209-215 (1981).
5. T. Todorov, L. Nikolova, and N. Tomova, "Polarization holography. 1: A new high-efficiency organic material with reversible photoinduced birefringence," Appl. Opt. **23** (23) 4309-4312 (1984).

Amako, Jun — STuA1
Athale, Ravindra A. — STuC

Banas, David B. — SMD4
Bar-Tana, Ido — SWC3
Barbier, Pierre R. — SMB1
Blair, Steve — SWD2
Brandt, Werner V. — SWC4
Brauchle, C. — SWD3
Brocklehurst, J. R. — SMD1
Bryan, R. P. — SMA1
Buchholz, J. C. — STuA4
Bunch, Robert M. — SWC4
Burns, D. C. — STuA2
Buydens, L. — SMC2

Cartland, Robert F. — SWB2
Caviris, Nicholas — SWD1
Chang, W. — SWA4
Chang-Hasnain, Constance J. — SWB
Chavel, P. — SME3
Chen, Li — SWB2
Chen, P. — SWB2
Cheung, S. K. — SWA3
Chirovsky, L. M. F. — SMD2
Chiu, T. H. — SWA2
Collings, N. — SMD1, SME6
Cotter, Lisa K. — SMB2
Cottrell, Don M. — SWC4
Crossland, W. A. — SMD1, SWC2
Cullen, D. — SWA3
Cullin, David — SWD1
Cunningham, Jim D. — SMB2

D'Asaro, L. A. — SMD2
Davis, Jeffrey A. — SWC4
de Bourgrenet, J. L. — STuA3
Demeester, P. — SMC2
Demske, David — SWD1
Doroski, D. — SMB4
Drabik, Timothy J. — SMB2
Droopad, R. — SWB3
Dutta, M. — SWA4

Efron, Uzi — SWC
Esener, S. C. — STuB4, SWB4

Fan, C. — STuB4, SWB4
Fan, J. — STuB1
Fisher, Arthur — SMA
Focht, M. W. — SMD2
Freund, J. M. — SMD2
Fu, W. S. — SMA1
Fukushima, Seiji — SMB5

Gaalerna, Stephen D. — SMB2, SMD4
Garcia, Joseph — SWD1
Gerber, D. S. — SWB3
Glass, A. M. — SWA2
Gourlay, J. — SME8
Gregory, Don A. — SWD4
Grider, David E. — SMD6
Gross, M. A. — SME2
Grot, Annette C. — SMA2
Grudkowski, T. — SWA3
Guertin, Jarod — SWC4

Guilfoyle, Peter — SMD6
Guth, G. D. — SMD2

Hampp, N. — SWD3
Handschy, Mark A. — SMB2, SMD4, SME5
Hansen, M. W. — SWB4
Hara, Tsutomu — SMA3, SME7
Harris, J. S., Jr. — SWB1
Hibbs-Brenner, M. K. — SMC3
Hirai, Masakatsu — SME4
Hori, T. — SME7
Hsu, W. F. — SMC3
Hu, KeZhong — SWB2
Huang, Tizhi — SWD2
Hudson, Tracy D. — SWD

Ichikawa, Hiroyuki — SME1
Inaba, Yasushi — SME4

Jain, F. — SWA3
Jared, David A. — SMD5
Jenkins, B. Keith — STuB3
Jewell, J. L. — SMA1
Jin, M. S. — STuB2
Johnson, Kristina M. — SMB3, SMB4, SMD5, STuA, SWC3

Kaviani, K. — SWB2
Kenan, R. P. — SME2
Khurgin, Jacob — SWB5
Kobayashi, Yuji — SMB5, SME7
Kohda, Shigeto — SME4
Koppa, P. — SME3
Kosinski, J. — SWA4
Kuszelewicz, R. — SME3

LaComb, R. — SWA3
Lambeth, David N. — SMC1
Larson, M. — SWB1
Laskowski, E. J. — SMD2
Lee, John N. — SMB
Lee, Sing H. — STuB, STuB2
Lehman, J. — SMC3
Leibenguth, R. E. — SMD2
Lentine, Anthony L. — SMD2, SWA
Li, Shaozhong — SWB5
Liu, Daxin — SWB1
Liu, Hua-Kuang — SWC5
Liu, J. J. — SMC3
Liu, Jian-Yu — SMB3
Lord, S. M. — SWB1
Lu, Y. — SWA4
Luo, Jiafu — SMA2

Madhukar, A. — STuB3, SWB2
Mansoorian, B. — STuB4
Mao, Chongchang — SMB3
Maracas, G. N. — SWB3
Marsden, G. — STuB4
McArdle, Neil — SME1
McKnight, Douglas J. — SMB3
McOwan, P. — SME8
Mears, R. J. — SMD1, SWC2
Miceli, William J. — SMD
Miller, David A. B. — SWA1

Miura, Hirotuna — STuA1
 Moddel, Garret — SMB1
 Mukherjee, S. D. — SMC3
 Mukohzaka, Naohisa — SMB5, SME7

Neifeld, Mark A. — SMC4
 Newman, P. — SWA4

O'Brien, D. C. — SWC2
 O'Hara, A. — STuA2
 Obeidat, Amjad — SWB5
 Oesterheld, D. — SWD3
 Olbright, G. R. — SMA1
 Oudar, J. L. — SME3
 Ozguz, V. H. — STuB2, STuB4

Pamulapati, J. — SWA4
 Papuchon, M. — SME3
 Parfenov, A. V. — STuA4
 Partovi, A. — SWA2
 Pei, S. S. — SMD2
 Pezeshki, B. — SWB1
 Phuvan, Sonlinh — SWD1
 Pocholle, J. P. — SME3
 Psaltis, Demetri — SMA2

Raffy, J. — SME3
 Reardon, Janine V. — SWD4
 Reid, Max B. — SWC1
 Roe, M. G. — SME5
 Ross, William E. — SMC1
 Ruden, P. P. — SMC3

Sacks, R. — SWA3
 Sawchuk, A. A. — SMC3
 Schehrer, K. L. — SME5
 Schirber, L. — SME5
 Schley-Seebold, Heidi M. — SWC4
 Schnell, J. P. — SME3
 Sharp, Gary D. — SMB3, SMB4
 Shen, H. — SWA4
 Shih, D. W. — SWB4
 Slagle, Timothy M. — SMD3
 Smith, L. E. — SMD2
 Sneh, Anat — SMB3
 Sonehara, Tomio — STuA1
 Stockley, J. E. — SMB4
 Summers, C. J. — SME2
 Suzuki, Yoshiji — SMA3
 Szu, Harold — SWD1

Taboury, J. — SME3
 Taghizadeh, Mohammad R. — SME1
 Takemori, Tamiki — SMB5
 Tanguay, Armand R., Jr. — STuB3
 Tate, Ann — SWD1
 Toyoda, H. — SME7
 Tran, T. K. — SME2
 Trezza, J. A. — SWB1

Underwood, I. I. — SME8, STuA2

Van Zeghbroeck, Bart — SMD6
 Vass, D. G. — SMD1, SME8, STuA2

Wagner, Kelvin H. — SMD3, SWD2
 Walch, Marianne — SWD1
 Wang, J. H. — STuB2
 Warde, Cardinal — SMC
 Weaver, Samuel — SWD2
 Wilkinson, T. D. — SWC2
 Woodward, T. K. — SMD2
 Worboys, M. R. — SMD1, SME8
 Wraback, M. — SWA4
 Wu, Ming H. — SMA3

Xue, W. — SME6

Yamauchi, Noriyoshi — SME4
 Yeh, Pochi A. — SWC5
 Yoshida, Narihiro — SMB5, SME7

Zhou, Shaomin — SWC5